UNIVERSIDAD NACIONAL AUTÓNOMA DE MÉXICO

PROGRAMA DE MAESTRÍA Y DOCTORADO EN INGENIERÍA
INGENIERÍA CIVIL – ESTRUCTURAS

SEISMIC BEHAVIOR OF INNOVATIVE PRECAST CONCRETE BEAM-COLUMN CONNECTIONS

TESIS
QUE PARA OPTAR POR EL GRADO DE:
DOCTOR EN INGENIERÍA

PRESENTA:
VLADIMIR ENRIQUE RODRÍGUEZ MORENO

TUTORES PRINCIPALES:
JOSÉ ALBERTO ESCOBAR SÁNCHEZ, II-UNAM
HÉCTOR GUERRERO BOBADILLA, II-UNAM

COMITÉ TUTOR:
AMADOR TERÁN GILMORE, UAM
ÓSCAR LÓPEZ BÁTIZ, CENAPRED
SONIA ELDA RUIZ GÓMEZ, II-UNAM

CIUDAD UNIVERSITARIA, CDMX, DICIEMBRE, 2023

JURADO ASIGNADO:

Presidente:	Dr. Óscar López Bátiz
Secretario:	Dr. Amador Terán Gilmore
1 er. Vocal:	Dr. José Alberto Escobar Sánchez
2 do. Vocal:	Dra. Sonia Elda Ruiz Gómez
3 er. Vocal:	Dr. Héctor Guerrero Bobadilla

Lugar o lugares donde se realizó la tesis: INSTITUTO DE INGENIERÍA

TUTOR DE TESIS:

Dr. José Alberto Escobar Sánchez

FIRMA

CONTENT

LIST OF FIGURES

LIST OF TABLES

PUBLICATIONS

Published papers:

- Rodríguez V, Guerrero H, Alcocer SM, Tapia-Hernández E. "Rehabilitation of heavily damaged beam-column connections with CFRP wrapping and SFRM casing", *Soil Dynamics and Earthquake Engineering*, Vol. 145, 2021.
- Rodríguez-Moreno V, Guerrero H, Escobar JA, Terán-Gilmore A. "Cyclic behavior of a slit damper proposed for precast concrete beam-column connections", *Engineering Structures*, Vol. 294, 2023.

Papers to be published:

- Rodríguez-Moreno V, Guerrero H, Escobar JA, Terán-Gilmore A. "Proposal of a low-damage precast beam-column connection equipped with a slit damper", *Engineering Structures*. To be submitted in 2023.

International conference papers:

- Rodríguez V, Guerrero H, Escobar J, López O. "Experimental evaluation of CFRP wrapping for seismic rehabilitation of a heavily damaged concrete beam", *12th National Conference on Earthquake Engineering*. Salt Lake City, Utah, United States of America.
- Rodríguez-Moreno V, Guerrero H, Escobar JA, Terán-Gilmore A, Gómez JJ. "Proposal of an easy-repair precast beam-column connection equipped with a slit damper", *18th World Conference on Earthquake Engineering*. June-July 2024, Milan, Italy, Mexico. To be presented.

National conference papers

- Rodríguez Moreno V, Guerrero H, Escobar Sánchez JA, López Bátiz O, Suárez González M. "Estudio de la resistencia de conexiones trabe-columna prefabricadas", *XXIII Congreso Nacional de Ingeniería Sísmica*. February 2022, Juriquilla, Querétaro, Mexico.
- Rodríguez Moreno V, Rodríguez Díaz DF, Suárez González M, Guerrero Bobadilla H. "Diseño por estados límite de servicio de elementos presforzados sujetos a

flexión", *XXIII Congreso Nacional de Ingeniería Estructural*. November 2022, Zacatecas, Zacatecas, Mexico.

- Rodríguez-Moreno V, Guerrero H, Escobar JA, Terán-Gilmore A. "Ensayo cíclico de una conexión trabe-columna híbrida prefabricada de concreto reforzado", *XXIV Congreso Nacional de Ingeniería Sísmica*. November 2023, Guadalajara, Jalisco, Mexico.

Divulgation publications

- Rodríguez Moreno V, Guerrero Bobadilla H, Escobar Sánchez JA. "Propuesta de disipador multiperforado para conexiones trabe-columna prefabricadas de concreto reforzado", *Gaceta del Instituto de Ingeniería, UNAM*. No. 157, November-December 2022.

Others

- Mecalco Díaz G, Rodríguez Díaz D, Gallegos Suárez A, Suárez González M, Rodríguez Moreno V. "Guía de diseño de un edificio con marcos prefabricados". Comité de Investigación y Normatividad ANIPPAC, 2021.
- Chapter in: "Guía de los Prefabricados de Concreto y el Aislamiento Sísmico". Subcomité de la Guía de Aplicación de Dispositivos de la Respuesta Sísmica. Comité de Investigación y Normatividad, ANIPPAC, 2023.

Awards

- Winner of "Contest for the best technical papers on precast concrete", for the paper "Experimental tests of precast reinforced concrete beam-column connections", Event: *Mes del Prefabricado*. Awarded by ANIPPAC-ANIVIP, August 2021, Mexico.
- Winner of "Miguel A. Urquijo Award", for the paper "Experimental tests of precast reinforced concrete beam-column connections". Awarded by the College of Civil Engineers of Mexico, 2023, Mexico.

DEDICATION

To my loving wife, Laura, and our beautiful children, Bárbara and Joaquín

To my parents, Olga Moreno and Joaquín Rodríguez

ACKNOWLEDGMENTS

First, I would like to express my sincere gratitude to Dr. Héctor Guerrero Bobadilla. He has been like a second father to me. His patience, guidance, and constant support have been crucial in developing this project and will be for future projects.

The recommendations and comments of the members of my advisory committee, Dr. José A. Escobar, Dr. Amador Terán, Dr. Óscar López, and Dr. Sonia Ruiz, are greatly appreciated. I want to express special thanks to Dr. Amador for his help, which has tremendously improved the quality of this study and various publications.

I want to thank the National Association of Prestress and Precast Manufacturers (ANIPPAC) and various members: Leticia Amador, Juan Carlos Delgado, Manuel Suárez, and David Rodríguez. They have supported me throughout my doctoral studies, and their passion for prestressed and precast concrete has been inspiring.

I would like to recognize Osvaldo Contreras and Juan José Gómez from CENAPRED, Juan Carlos Alvarez, Paola Gil, and Cyprien Lubin from II-UNAM for their help during the experiments.

The kind donations of specimen P-SD-1 from ITISA and the slit dampers from Dampo Systems are highly appreciated.

Acknowledgments are expressed to Mexico's National Center for Disaster Prevention (CENAPRED) and the Institute of Engineering of UNAM (II-UNAM) for providing the facilities to conduct the experiments.

The scholarship provided by CONACyT to conduct my doctoral studies is also most recognized.

Finally, I am most grateful to my wife, Laura, for all her support, encouragement, and love throughout the years; to our beautiful children, Bárbara and Joaquín, for they are our life; and to my extraordinary parents, Olga and Joaquín, for their unconditional love and support. I wouldn't be anywhere close to where I am without anyone of them.

ABSTRACT

Precast reinforced concrete structural systems offer widely known advantages, i.e., high-quality control of the precast elements, accelerated construction, reduction in formwork and on-site work, etc. Despite all the well-known advantages of precast construction, mistrust in using these systems in high seismic regions is still common. This mistrust has resulted, amongst others, from the lack of experimental data and design provisions in building codes for precast structures. Although many experimental and analytical studies have been carried out through the years, the general lack of knowledge of these systems has remained a common problem.

The upcoming Mexican City Building Code (MCBC-2023), to be published at the end of 2023, is set to adapt the approach of ACI 318 (2019), which establish that high ductility moment-resisting frames that do not emulate cast-in-place concrete behavior can be used for seismic regions if they satisfy specific requirements. This change alone may open areas of opportunity for improvement and innovation in the precast industry, since the use of precast structural systems is ever-growing in the countries like Mexico. At the same time, the design philosophy of buildings is shifting to limiting consequences and damage to structural components. As a result, the use of energy dissipation devices has received renewed attention.

Based on the above reasons, this thesis aimed at developing innovative low-damage precast concrete beam-column connections that exploit the inherent advantages of precast construction while having superior seismic performance and predictable behavior. The proposed precast structural system is a non-emulative connection equipped with a slit damper, which is a passive energy dissipation device. Some of the advantages of the proposed system include maintaining the less ductile elements, such as the beams and columns essentially elastic, i.e., with little to no damage; predictable behavior; reduction of waste of raw materials; less use of formwork and finishing materials; and provide opportunities to recycle its precast elements, since they are easier to disassemble, once it has reached the end of its life cycle.

In this thesis, an experimental program carried out on multiple innovative precast beam-column connections is described. Though the first part of the program did not render the desired results, it set the basis for developing a prototype of a precast beam-column connection equipped with a slit damper. Due to the success of this prototype, the experimental program was expanded upon with cyclic tests of isolated slit dampers, and a design method was proposed for these devices. The program then culminated with testing two full-scale beam-column connections equipped with slit dampers with an optimized shape. One of the specimens developed a global ductility ratio of 10, while the concrete elements remained undamaged up to a drift ratio of 0.035 rad. A method for designing beam-column connections equipped with slit dampers was also proposed.

RESUMEN

Los sistemas estructurales prefabricados de concreto reforzado ofrecen muchas ventajas tales como alto control de calidad, construcción acelerada, reducción en uso de cimbra y trabajos en obra, etc. A pesar de todas estas ventajas, la desconfianza en el uso de estos sistemas en regiones de alta sismicidad sigue siendo común. Esta desconfianza es el resultado de, entre otros, la falta de datos experimentales y disposiciones de diseño en los códigos de construcción para estructuras prefabricadas. Aunque se han realizado muchos estudios experimentales y analíticos a lo largo de los años, y algunos países han incluido a las estructuras prefabricadas en sus códigos de construcción, la falta de conocimiento de estos sistemas sigue siendo un problema en general.

En las próximas Normas Técnicas Complementarias para Diseño y Construcción de Estructuras de Concreto (NTCC-2023), que se publicará a fines de 2023, se adaptará el enfoque de ACI 318 (2019), el cual establece que los marcos resistentes a momento de alta ductilidad que no emulan el comportamiento del concreto colado en sitio se pueden usar para regiones sísmicas si cumplen requisitos específicos. Este cambio por sí solo puede abrir áreas de oportunidad para la mejora y la innovación en la industria de los prefabricados, ya que el uso de sistemas estructurales prefabricados es cada vez mayor en países como México. Al mismo tiempo, la filosofía de diseño de estructuras está siendo enfocada hacía la limitación de daños a los elementos estructurales y, como consecuencia, el uso de dispositivos de disipación de energía ha recibido una atención renovada.

Con base en las razones anteriores, esta tesis tuvo como objetivo el de desarrollar conexiones trabe-columna de concreto prefabricado innovadoras de bajo daño que exploten las ventajas inherentes de los prefabricados y que tengan un desempeño sísmico superior. El sistema estructural propuesto aquí es una conexión no emulativa equipada con un disipador multiperforado, que es un dispositivo pasivo de disipación de energía. Algunas de las ventajas del sistema propuesto incluyen mantener los elementos menos dúctiles, como las trabes y columnas, esencialmente elásticos, es decir, con poco o ningún daño; tener comportamiento predecible; reducir el desperdicio de materiales; reducir el uso de materiales para cimbras y acabados; y brindar oportunidades para reciclar los elementos prefabricados una vez que la estructura ha llegado al final de su vida útil ya que son más fáciles de desmontar.

En esta tesis se describe un programa experimental de ensayes de conexiones trabe-columna prefabricadas innovadoras. Aunque la primera parte del programa no arrojó los resultados deseados, sentó las bases para desarrollar un prototipo de una conexión trabe-columna equipada con un disipador multiperforado. Debido al éxito de este prototipo, se amplió el programa experimental con ensayos cíclicos de disipadores multiperforados aislados, y se propuso un método de diseño para estos dispositivos. El programa culminó con la prueba de dos conexiones trabe-columna a escala real equipadas con estos dispositivos. Uno de los especímenes desarrolló una ductilidad global de 10, mientras que los elementos de concreto permanecieron sin daño hasta una distorsión de 0.035 rad. También se propuso un método para diseñar conexiones trabe-columna equipadas con disipadores multiperforados.

1

Introduction

1.1 Background

Precast reinforced concrete structural systems offer widely known advantages, i.e., high-quality control, a significant reduction in formwork and on-site work, greater durability, accelerated construction, etc. [1,2]. The working conditions in a plant favor the mass production of high-quality structural elements and provide a safer environment for precast plant workers, especially in regions with extreme weather. Precast construction is also in tune with the demands of today's society, such as achieving sustainability and seismic resiliency [3].

Despite all the well-known advantages that precast construction offers, for decades, there has been mistrust in the use of precast systems in areas of high seismicity. A common misconception of these systems is that they tend to be less ductile and present less stable inelastic behavior than conventional cast-in-place structures [4]. This belief has resulted from the lack of experimental data and design provisions in building codes for precast structures. Additionally, the poor performance of precast structures in past earthquakes has discouraged their use for a long time. Nowadays, it is recognized that most failures in precast structures, as in conventional cast-in-place structures, can be avoided with proper design, detailing, and

construction of the connections between the elements. However, the lack of experimental data of precast systems has remained a common problem.

Design misconceptions, especially at the connections, and inadequate construction procedures are often the reason for precast concrete buildings exhibiting poor structural performance. Therefore, one of the most important objectives of the precast industry is to find economical and practical methods for connecting the precast elements while ensuring adequate stiffness, strength, ductility, and stability [5,6]. There are still many areas of opportunity for improvement and innovation in the precast industry. The use of precast concrete is ever-growing worldwide, as well as the interest in researching innovative techniques and seismic structural systems.

On the other hand, the general design philosophy of structures is changing. Interest in limiting damage to structural components has increased exponentially in the last years, especially since the observed damages in recent earthquakes. Consequently, using proved technologies, such as passive energy dissipation devices, has received renewed attention, leading to the belief that non-emulative precast construction is a real possibility in seismic-prone regions.

Based on the above reasons, this thesis studies an innovative precast structural system: a non-emulative precast concrete beam-column connection equipped with a slit damper, which is a passive energy dissipation device. This study aimed at developing a precast moment-resistant framing system that exploits the inherent advantages of precast construction (such as higher quality contr; while keeping the less ductile elements, such as the beams and columns essentially elastic, i.e., with little to no damage. The proposed system is in line with society's goal of achieving sustainability as it should contribute to the recycling of materials; the reduction of finishing materials, waste of raw materials, formwork, and on-site labor; and provide opportunities for recycling the precast components once the structure has reached the end of its life cycle.

1.2 Objectives and Scope

This study's main objective is to develop innovative low-damage non-emulative precast concrete beam-column connections that exploit the inherent advantages of precast construction while having superior seismic performance and predictable behavior.

The specific objectives of this study were:

- To conduct a literature review to understand the seismic behavior of precast concrete structures.
- To assess the seismic behavior of cast-in-place and conventional precast beam-column connections under cyclic loading.
- Propose innovative precast beam-column connections that, compared with cast-in-place and conventional precast systems, have improved seismic performance and accelerated construction.
- To assess the seismic behavior of precast beam-column connections equipped with slit dampers under cyclic loading and propose a comprehensive design methodology considering these systems' non-linear behavior.
- To assess the cyclic behavior of slit dampers under incremental and uniform loading tests, propose a design method that determines the key structural design parameters of these devices, and propose numerical analysis methods for reasonably predicting their hysteretic response.
- To propose numerical analysis methods for modeling precast concrete beam-column connections with available software, both with frame and solid elements, for predicting their cyclic response.

1.3 Development of the Research Project

A literature review was conducted first. It was found that many innovative non-emulative precast systems have been proposed in the past three decades. Experimental, numerical, and analytical research was conducted but these connections were seldom implemented in practice despite offering many advantages such as accelerated construction, less on-site work and waste of materials and, most of all, superior seismic performance. Certainly, non-emulative construction represents an important area of opportunity for the precast industry that has long been ignored. The work carried out by important researchers in the field, such as Nigel Priestley, John Stanton, Suzanne Nakaki, and Robert Englekirk, has inspired some ideas for this research project.

Taking the results from the literature review, in February 2020, the construction of a first test specimen began at the National Center for Disaster Prevention (CENAPRED, Mexico). The specimen was designed to have a passive hysteretic damper, referred to hereafter as an I-damper, which dissipates energy through shear deformation. However, by the end of the month, the Mexican government announced the first Covid-19 case. Shortly after, many academic and economic activities were paused. With limited resources and significantly less access to the laboratory, activities resumed in June 2020. By September, the first test was carried out.

Results of the first test were not satisfactory; therefore, two variations of the proposed I-damper were proposed and tested. However, these specimens shared many of the same complications. To solve the shortcomings of the first three specimens, a prototype beam-column connection equipped with a slit damper was then proposed and tested. Some of the same components, used in the first three tests, were used for recycling and saving purposes. The specimen showed wide and stable hysteresis loops and adequate deformation capacity. This prototype specimen was named P-SD-0.

Due to the promising results of specimen P-SD-0, efforts were shifted to the study of slit dampers as isolated components. In March 2022, an experimental program, consisting of eight slit dampers subjected to incremental and uniform cyclic loading tests began. The results of this program gave the basis for developing an improved method for designing these devices and an improved version of a beam-column connection.

Finally, in 2023, with the experience gained during the prior three years, the project culminated with the cyclic testing of a full-scale beam-column connection equipped with a slit damper with optimized geometry. Once this test had concluded, the damaged slit damper was removed and replaced with a new one, thus verifying the system's repairability. The specimen was then retested. The results showed that the tested specimen had great performance, which is considered appropriate for reliable application in seismic regions.

1.4 Thesis Outline

This thesis contains nine chapters, with this introduction serving as the first. The second chapter is an extensive literature review covering related topics, such as the behavior of

precast systems and beam-column connections, and the previous research regarding these topics available in the literature. A short commentary on building codes and common practices is also offered.

The main contents of the project are presented in Chapters 3 through 8.

- Chapter 3 shows the results of four cast-in-place beam-column connections subjected to incremental cyclic loading. One of the tests was carried out in 2017, and the rest in 2019. All of them were conducted in the Large Structures Laboratory (LEG) of Mexico's National Center for Disaster Prevention (CENAPRED). The results help contextualize the reader on the cyclic behavior of conventional beam-column connections and allow comparisons with conventional and innovative precast connections.
- Chapter 4 shows the results of four conventional precast beam-column connections subjected to incremental cyclic loading. All of the tests were conducted in 2017 in the facilities of CENAPRED. Similarly to Chapter 3, this chapter aims at comparing the cyclic behavior of conventional precast connections with the innovative connections proposed in the following chapters, primarily in terms of deformation and energy-dissipating capabilities.
- Chapter 5 describes an experimental program for developing innovative precast concrete beam-column connections with passive energy-dissipating devices. Although the results of this project stage were not the desired ones, they served as the basis for developing a new slit damper, proposed for precast beam-column connections, which would render satisfactory results. The results and the shortcomings of the proposed systems are presented and discussed. The tests were conducted also in CENAPRED.
- Chapter 6 shows the bulk of the project. A small-scale precast beam-column sub-assembly was built and tested following the tests of Chapter 5. The specimen was subjected to incremental cyclic loading. The results of this test were promising, with broad and stable hysteretic loops and adequate deformation capacity. The system's ease of application and design are discussed here. After that, two tests were conducted on a full-scale precast beam-column subassembly equipped with a larger and

improved slit damper. After the first test, the damaged damper was replaced with a new one and installed with an alternative configuration. These tests clearly showed the benefits of using passive energy devices in precast structures, namely: low damage on concrete elements even at high displacement demands and adequate deformation capacity, having developed a maximum global ductility ratio of 12. It was found, however, that the predictability of the cyclic behavior of the proposed system is one of its most significant advantages. This feature is discussed extensively as the results are shown.

- Chapter 7 describes an experimental program of eight isolated slit dampers subjected to incremental or uniform cyclic loading. Here, slit dampers with uniform and non-uniform struts were studied. It is seen that using non-uniform struts improves the deformation and energy-dissipating capacities drastically. Also, a method is proposed to calculate the strength and elastic stiffness of the slit damper with uniform or non-uniform struts. This method provides more precise results than the previous methods available in the literature. Finally, finite element analyses were performed, simulating three different damper configurations studied experimentally. It is shown that the proposed damper's hysteretic response could be accurately predicted using the combined non-linear isotropic and kinematic hardening model available in Abaqus [7].
- Chapter 8 shows modeling methods in FEM software of precast beam-column sub-assemblies equipped with slit dampers. Specimens P-SD-0 and P-SD-1 were modeled with solid elements. The concrete and steel components were mainly modeled with elastic or elastic-perfectly plastic materials. The slit dampers, on the other hand, were modeled with the non-linear isotropic and kinematic hardening model described in Chapter 7. The results show that the proposed cyclic hardening parameters could accurately predict the cyclic response of the beam-column sub-assemblies.

Finally, Chapter 9 presents the conclusions and further work.

2

Literature Review

2.1 Precast Reinforced Concrete Systems

Precast concrete, by definition, is prepared, poured, and cured at a location other than its final destination. An element made of precast concrete is finite in size and, therefore, must be joined to other elements at the erection site to form a complete system [8]; which, if properly connected, must be capable of resisting gravity and accidental loads, such as those generated by seismic or wind action. Advantages of precast structures include high-quality control of the precast elements, a significant reduction in formwork and on-site labor, greater durability, accelerated construction, etcetera [1].

Despite the well-known advantages of precast construction, for decades, there has been mistrust in the use of precast systems in areas of high seismicity, since there is an erroneous idea that they tend to be less ductile and that they present less stable inelastic behavior than conventional reinforced concrete structures [4]. This belief has resulted from the lack of experimental data and, consequently, the lack of design provisions for precast structures in building codes for many years, even though interest in precast construction in North America occurred during the decade of the 1950s [9]. Added to that, the poor performance of precast structures in past earthquakes, such as in Romania and Armenia, has effectively discouraged

their use for a long time. Nowadays, it is clear that most failures in precast structures, as in conventional structures, can be avoided with proper detailing, design, and construction procedures of elements and connections.

Precast moment-resisting frames are assembled on-site, joining the precast beams and columns with different techniques. As a result, beam-column connections may be vulnerable to severe lateral loading if they are not adequately designed and assembled. Thus, the challenge in precast construction lies in developing economical and practical methods of joining precast elements together that guarantee adequate stiffness, strength, ductility, and stability [5].

Precast connections can be divided into two general categories, emulative and non-emulative. Emulative connections are designed to perform similarly to cast-in-place connections in terms of strength, stiffness, and energy dissipation [10]. These connections are further divided into ductile and strong. Ductile connections are designed to yield in flexure and form plastic hinges at the connections across the precast elements, as shown in Figure 2-1. Strong connections are designed to develop flexural yielding within precast elements at preselected locations adjacent to or away from the joints, i.e., away from the region where the precast elements are connected. An example of a strong nonyielding beam-column connection is shown in Figure 2-2, where post-tensioned strands are combined with conventional reinforcement to force the plastic hinge away from the connection. A more practical form of relocating the hinge away from the connection is shown in Figure 2-3. In this example, proposed by Eom et al. [11], strengthening the beam's region adjacent to the joint is achieved through different kinds of methods, such as introducing U-shaped bars, 90° hooked bars, straight bars, etc. The beam is strengthened over a length towards the center of the beam so that the moment demand at the beam-column interface is less than its capacity. More strengthening methods can be found in [11].

The two approaches to emulative construction described above are shown in Figure 2-4. A typical ductile system, such as the one shown in Figure 2-1, can be represented by Figure 2-4a, where the location of the plastic hinges is at the ends of the beams adjacent to the joint. The two systems shown in Figure 2-2 and Figure 2-3 can be represented with Figure 2-4b. In this case, the plastic hinge is relocated away from the beam-column connection. Strong

connections should be capacity-designed to remain essentially linear-elastic while the plastic hinges develop elsewhere [10].

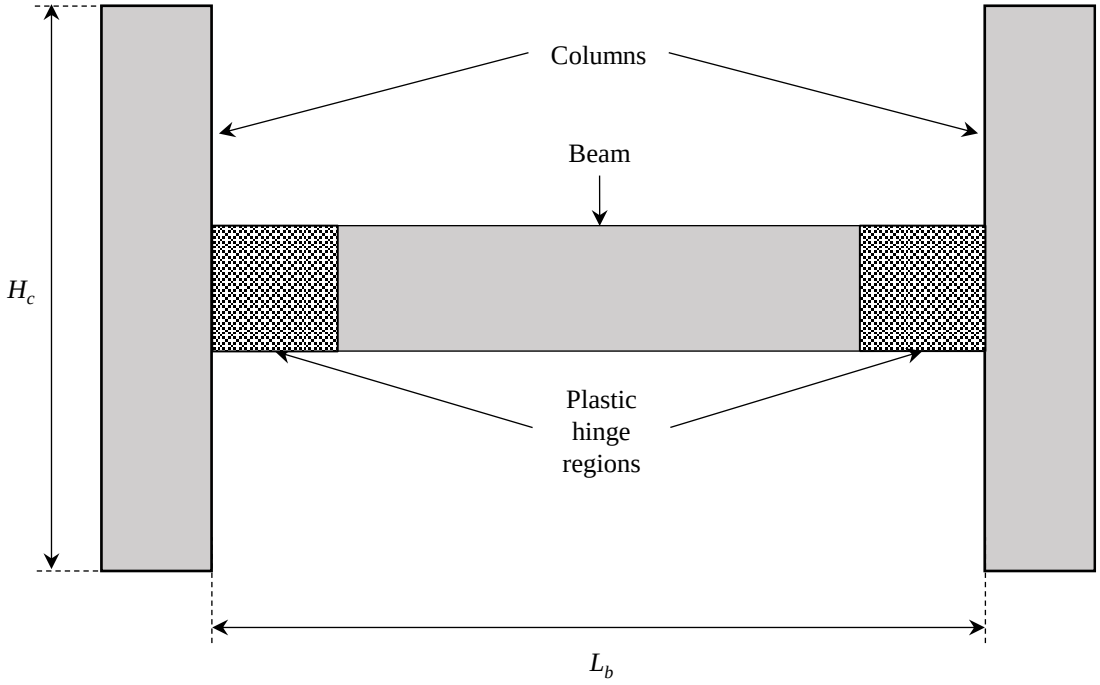

Figure 2-1. Typical beam-column frame.

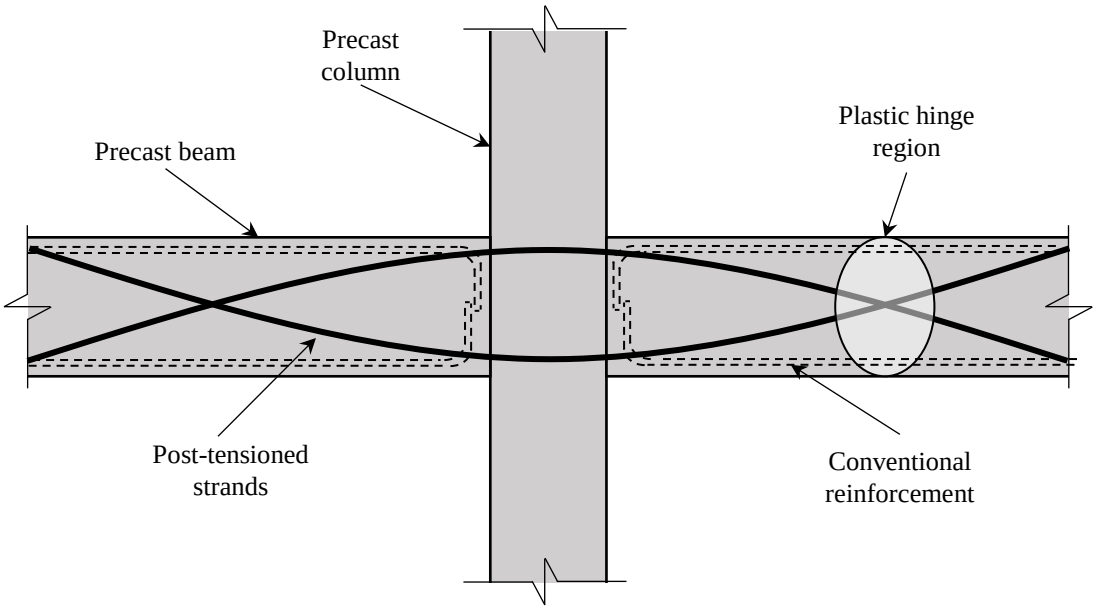

Figure 2-2. Strong nonyielding beam-column connection (adapted from [12]).

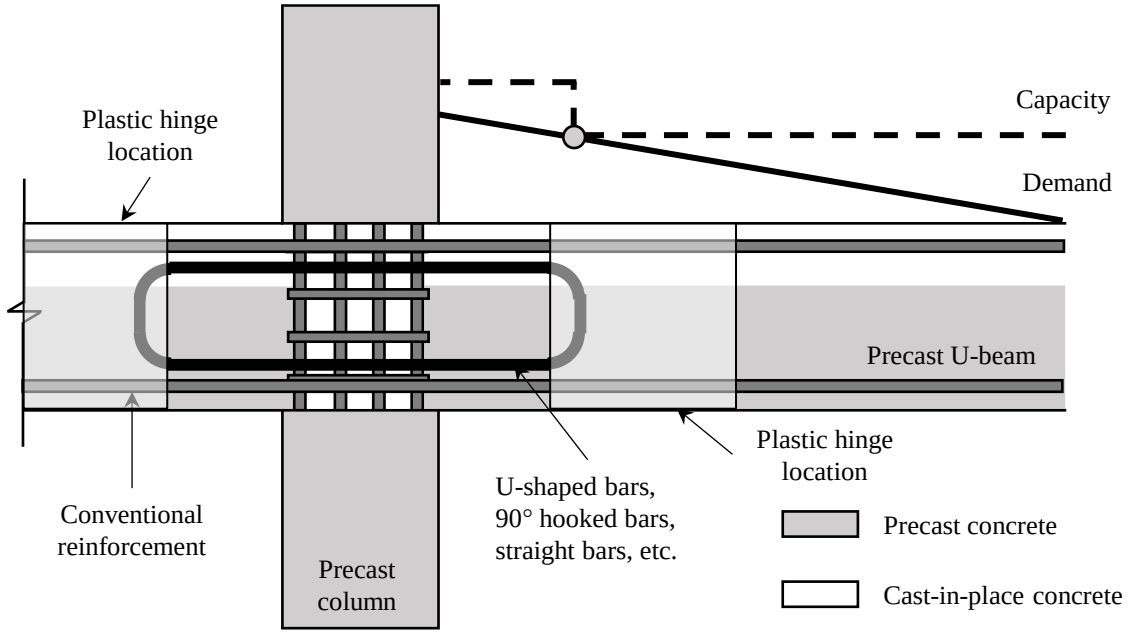

Figure 2-3. Relocation of the plastic hinge in a precast beam [11].

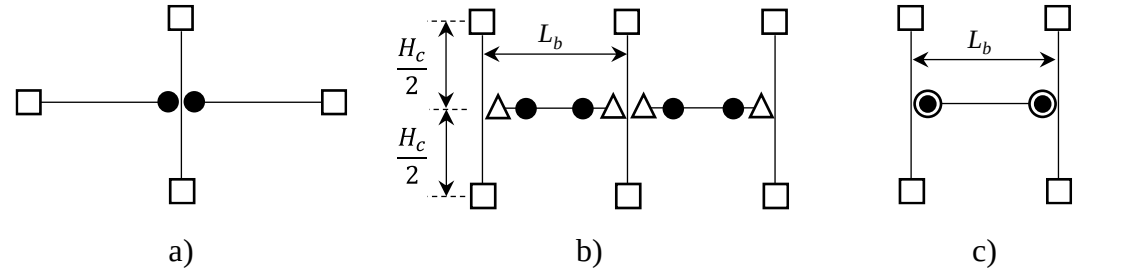

Figure 2-4. Precast connections (adapted from [12]).

Non-emulative construction uses the properties of the connections between the precast elements with the intention of sustaining severe non-linear deformations. This mechanism is shown in Figure 2-4c, where the connections are energy-dissipating devices. The non-linear rotations of the structure are concentrated at the ends of the precast elements in the joint regions, avoiding inelastic behavior of the elements [10].

One of the most successful non-emulative systems is the hybrid moment frame. This system was developed and tested during the NIST and PRESSS program in the nineties [13,14]. The hybrid moment frame uses unbonded post-tensioned strands as the main reinforcement, providing the system with self-centering capabilities. Damping, i.e., energy-dissipating capacity, is provided by mild steel. A typical beam-column connection for a hybrid moment frame is shown in Figure 2-5. When the frame sways, the end of the beam rocks against the column, where a single crack opens alternatively at the top and bottom of the beam when subjected to cyclic loading. The post-tensioning steel, designed to remain elastic, provides a restoring force that re-centers the structure with minimal residual displacements and closes any opened cracks [13]. The unique properties of the hybrid moment frame result in flag-shaped hysteresis loops, such as those shown in Figure 2-6.

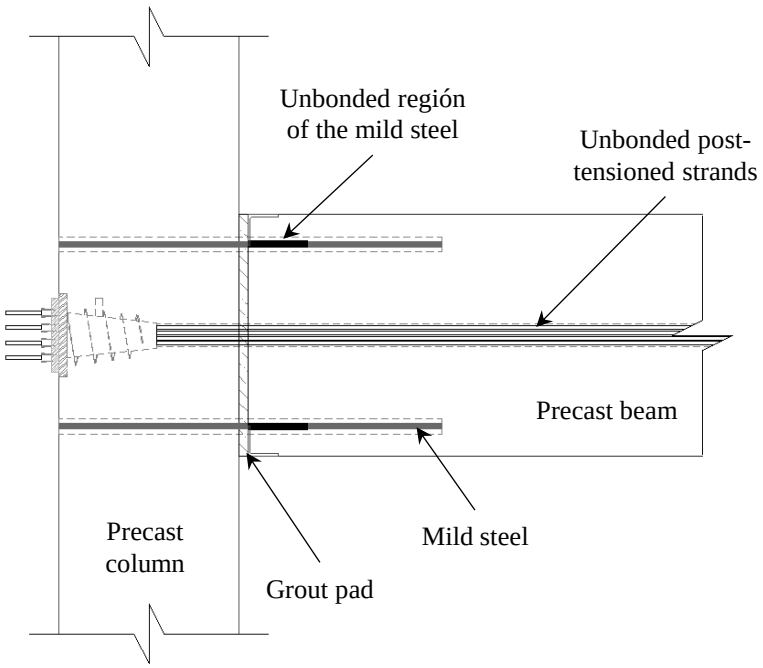

Figure 2-5. Typical beam-column connection for a hybrid moment frame [13,14].

Combining unbonded post-tensioned strands and mild steel has also been applied to column-to-foundation and wall-to-foundation connections [10]. Further, alternatives to the mild steel inside the concrete sections have been proposed in the form of external energy dissipation devices such as that proposed by Marriot et al. [15]. External devices can be easily replaced if damaged during a seismic event.

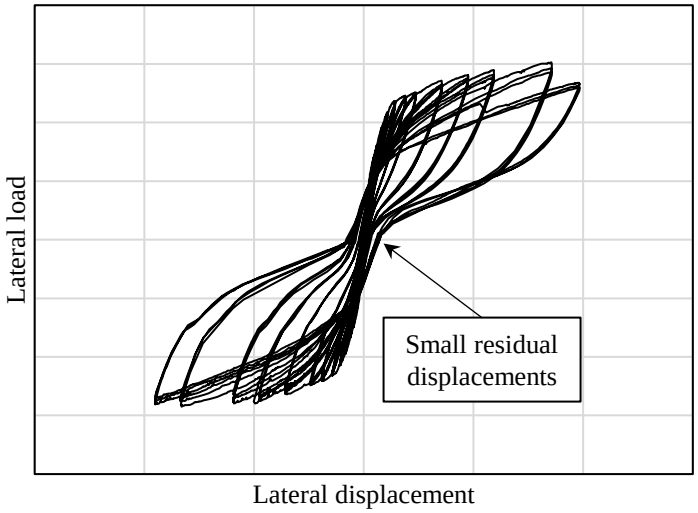

Figure 2-6. Scheme of typical hysteretic behavior of a hybrid moment frame.

Although many non-emulative systems have been proposed, some of which are covered in Section 2.4, most building codes have not taken the approach of emulating cast-in-place concrete. The American Concrete Institute (ACI) code first included precast and prestressed concrete provisions in its 1963 edition [16]. However, it did not address the seismic design of precast and prestressed structures, nor did it include non-emulative construction. It was not until 2002 that seismic provisions were included for the design of precast and prestressed structures in areas of high seismicity [17]. In the case of frames with non-emulative connections, these were allowed as long as they were validated experimentally, following the guidelines of ACI 374.1 [18]. Later, ACI 318-08 [19] included provisions for using structural walls joined by non-emulating connections, provided they were experimentally validated with the guidelines of ACI ITG 5.1 [20].

2.2 Advantages and Disadvantages of Precast Systems

2.2.1 Advantages

Structural systems made from precast reinforced concrete elements have numerous advantages for the construction industry, among which are: ensuring high-quality control in the precast members, reduction in formwork and on-site work, greater durability, accelerated

construction, aesthetic finishing and structural shapes, as well as providing social and economic benefits [1,2].

The controlled conditions in precast plants ensure high-quality precast members, which is challenging to achieve on-site. The working conditions in a plant favor the mass production of high-quality structural elements since they are built indoors, minimizing adverse effects, such as environmental ones [21]. The profitability and quality control of precast systems have led to their use worldwide, including in areas of high seismicity [10] and especially in regions with extreme weather or where labor is expensive.

2.2.2 Disadvantages

According to Park [18], the main disadvantage is developing affordable and effective means to join the precast elements to resist seismic actions. In many cases, innovative emulative system proposals rarely progress beyond the prototype due to the high cost of their development [12]. In addition, the construction procedures of the connections may generally be unknown and must be carried out with high-quality control, so it is necessary to have qualified personnel specifically trained for this activity. Of course, the latter can be considered an advantage as it guarantees high-quality structures.

Compared with conventional monolithic structures, precast structures have significantly lower tolerances for assembling the structural elements and their reinforcements. It is also possible that special machinery is necessary to lift heavy precast elements [22].

2.3 Behavior of Precast Structures in Past Earthquakes

2.3.1 Romania (1977)

The 1977 Romanian earthquake registered a magnitude of 7.2 and had its epicenter in the Vrancia mountains, 165 km from the city of Bucharest. In that city, 35 buildings collapsed, causing approximately 1,500 deaths. Of the 35 collapsed buildings, 32 were multi-story and built before World War II when seismic design codes were not yet established. The three remaining buildings were more recent [23].

At the time, all residential buildings were conventional reinforced or precast concrete, but only one of the 35 collapsed buildings combined precast and cast-in-place elements. This

building had ten stories, and its failure was attributed to inadequate construction procedures and the use of poor-quality concrete [23].

Most of the precast structures with shear walls showed minimal damage. However, it is relevant to mention that these structures had periods between 0.6 and 0.7 seconds, while the earthquake ground motions had a period around 1.5 seconds [24], so there might not have been issues with resonance.

2.3.2 México (1985)

The September 19, 1985, Mexico earthquake has been the most important seismic event in the country's history. This earthquake originated in Michoacán, 400 km from Mexico City, and an estimated 10,000 people died, and 250,000 were left homeless [25,26]. Hundreds of buildings collapsed, most of these being reinforced concrete moment-resisting frames between six and fifteen stories high. Approximately 180 buildings collapsed, and 85 were severely damaged. Of these, 143 were concrete frames; 85 had flat slabs; 10 were steel frames; 17 were masonry; and the remaining ten were constructed with other structural systems [26]. According to Fintel [26], most collapsed buildings failed by column shear, resulting in excessive story drifts, which caused the slabs to fall on each other.

There were some precast concrete buildings at that time. Most of them were medium height, between four and eight stories, where the primary lateral force-resisting system comprised moment-resisting frames. In most cases, the connection between beams and columns was made by cast-in-place concrete, placing the top reinforcement of the beams in place and giving continuity to the bottom reinforcement by welding [27].

Five of the hundreds of collapsed buildings contained precast concrete elements as part of their structural system. Inspection of these buildings indicated that the collapses were caused by failures unrelated to the precast elements or their connections [28]. On the other hand, many buildings and parking lots that used precast elements withstood the earthquake without damage. The collapse of the general hospital maternity ward is of particular interest. This building was six stories with cast-in-place columns and precast tees as the flooring system. The collapse was attributed to the failure of the columns and not to the behavior of the precast or prestressed elements nor their connections with the columns. The previous affirmation was

confirmed by the inspection of the collapsed building, where it was observed that the connections presented virtually no damage [26]. However, it is argued that the low stiffness of the precast floor system may have concentrated the shear forces on some columns, contributing to their failure [28].

Finally, it is worth mentioning that by 1985, 40% of the bridges in Mexico City were built using precast reinforced concrete elements. No bridges, cast-in-place or precast, were reported with damage during the earthquake [26].

2.3.3 Armenia (1988)

In 1988, an earthquake with a magnitude of 6.9 hit the city of Spitak. The city was almost completely destroyed. All their schools, hospitals, public facilities, and homes were destroyed. Of the residential buildings, only one precast concrete structure with shear walls withstood the earthquake without damage [24]. In the city of Leninakan (32 km from the epicenter), there were significant casualties due to the collapse of modern residential buildings; most of these being nine-story reinforced concrete precast frames [24].

To the east of the epicenter, the city of Kirovakan suffered significantly less damage than the city of Leninakan. None of the 108 five- and nine-story prefabricated buildings collapsed or sustained significant damage, although 88 of them had to be repaired or reinforced. It is believed that the difference in the behavior of the precast buildings is due to the soil characteristics of each city. Kirovakan lies on firm soil, while Leninakan lies on 300 meters of alluvial deposits, which are generally associated with heavy earthquake damages [24]. Rodríguez [27] points out that in addition to the amplification problems due to the soil conditions of Leninakan, the connections between precast elements were inadequate.

2.3.4 Japan (1995)

On January 17, 1995, in Kobe, one of the strongest earthquakes (M_w 7.2) that Japan has experienced was recorded. The earthquake affected old and new buildings designed according to the established codes at the time [29]. Multiple reinforced concrete buildings constructed before 1971 (the year in which the design codes were updated) collapsed or suffered significant damage. Only two buildings built between 1971 and 1981 collapsed or suffered severe damage, and no building built after the code revision in 1981 collapse [29].

Most building collapses designed and constructed before 1981 were attributed to inadequate transverse reinforcement, torsional failures due to eccentricities of mass and stiffness, and soft story problems [29]. The collapse of a significant number of low and medium-height structures was caused by the loss of one or more levels due to the concentration of inelastic deformations in those levels. The combination of this phenomenon and the non-ductile detailing of the columns and connections caused the failure of many columns [30].

Regarding precast and prestressed structures, the Japan Prestressed Concrete Engineering Association (JPCEA) [31] reported that the 163 buildings built with elements of this type did not present damage. Most of these buildings presented excellent behavior in the face of the earthquake. Muguruma et al. [29] attribute the good performance of precast buildings to the fact that: 1) they were designed for seismic forces greater than those assigned for other types of structural systems; 2) they were generally regular in plan and elevation and had a uniform distribution of mass and stiffness; 3) the concrete used was of high strength and quality, and the construction was done with greater quality control; and 4) the precast and prestressed structures of the time were relatively new.

2.3.5 New Zealand (2010-2011)

The February 22, 2011 earthquake in Christchurch, with a magnitude of M_w 6.2, was part of a sequence of aftershocks caused by the Canterbury earthquake in September 2010 with a magnitude of M_w 7.1 [32]. Most of the reinforced concrete structures, particularly those capacity-designed, behaved as expected during the earthquake, forming plastic hinges at the ends of the beams and the base of walls and columns. Although only two reinforced concrete buildings collapsed, many damaged buildings were considered too expensive to repair [32].

Older reinforced concrete buildings generally exhibited poor structural performance, presenting inelastic deformations due to brittle failure mechanisms. However, buildings built before 1970 with significant redundancy and reasonable regularity in plan and elevation presented acceptable behavior [32].

Many buildings in New Zealand were built during the 1980s with medium to high-rise precast concrete elements. Although the behavior of these buildings was acceptable, unexpected problems were observed, such as excessive residual displacements, collapse of precast stairs,

and elongation of beams due to the development of plastic hinges. The latter has serious implications for the performance of precast floor systems since they can move out of their supports [33,34]. Although there are more than 250,000 m^2 installed of hollow core slabs in the city of Christchurch, Kam et al. [35] reported very few cases of damage due to incompatibility of deformations between beams and precast floor systems. However, the most extreme case of damage due to incompatibility occurred in a 17-story frame-based concrete building that exhibited plastic behavior, leaving the precast floor system vulnerable.

On the other hand, before the Canterbury-Christchurch sequence, low-damage precast systems were implemented, generally called PRESSS (Precast Seismic Structural Systems) technology. These systems consisted of ductile connections between the precast elements that did not emulate cast-in-place concrete behavior. The first building built to these standards was a four-story hospital completed in 2010. This building withstood the seismic sequence from September 4 to June 13, 2011, with no observable damage. Kam and Pampanin [32] considered that the use of this technology in precast systems may increase in the future, given the importance of design for damage control.

2.3.6 Additional Comments

Precast reinforced concrete structures have performed adequately against severe earthquakes worldwide. In few cases, there has been poor behavior, such as in the city of Leninakan, Romania. Most cases of severe damage or collapse are attributed to typical problems also found in conventional cast-in-place structures and not to the precast construction or its connections themselves. Of course, at the time of occurrence of each described earthquake, the number of precast structures was much lower compared to that of cast-in-place structures and relatively newer, as observed by Muguruma et al. [29], after the Kobe earthquake.

Design misconceptions and inadequate construction procedures are often the reason for precast concrete buildings exhibiting poor structural performance. However, as observed in past seismic events, satisfactory performance can be expected if proper design and detailing are done, and care is taken to assemble the precast elements properly. In addition, projecting a precast structure with a regular shape (within reason) both in plan and elevation would avoid serious torsional effects, contributing to their good behavior [29].

Despite the above, isolated cases of past bad experiences have generated doubts about the behavior of precast structures built in areas of high seismicity [27]. For a long time, it has been considered that precast structures tend to be less ductile and develop less stable inelastic behavior [4]. Although experimental evidence demonstrates the adequate seismic performance of precast structures, there are still many areas of opportunity for their improvement and innovation. The following section describes experimental research programs carried out in the last 30 years dedicated to providing precast structures with sufficient stiffness, strength, stability, and ductility, mainly in beam-column connections.

2.4 Precast Reinforced Concrete Beam-Column Connections

One of the most important objectives of precast reinforced concrete systems is to find economical and practical methods to connect precast structural elements that ensure adequate stiffness, strength, ductility, and stability [5,6]. Most concrete buildings are based on moment-resisting frames exclusively or in combination with other structural systems, such as shear walls. In many countries around the world, using structural walls is not common, so beam-column connections are particularly interesting to researchers and precasters. Over the past 30 years, significant progress has been made in developing innovative connections, particularly in New Zealand, the United States, and Japan. If there is experimental evidence of the success of innovative precast systems and comprehensive guidelines are developed, practicing engineers are more inclined to use them. The most reliable way to assess the behavior of emulative and non-emulative precast connections is through experimental validation. The following sections describe some of the most relevant studies on precast beam-column connections.

2.4.1 Experimental studies on precast emulative beam-column connections

A typical precast beam-column connection that emulates cast-in-place concrete behavior is shown in Figure 2-7. The connection is formed by a precast or cast-in-place column with a precast U-shaped beam resting on the column's cover concrete or a temporary support. Once the beams and the flooring system are placed, the reinforcement of the beam's core is set on the precast U-beam and anchored to the joint. Then, the beam's core, the topping concrete of the flooring system, and the joint are cast simultaneously. The U-shaped beams are pre-tensioned in a precast plant with high-strength steel strands and are designed to support the

beam's weight and the construction loads. The prestressing strands only span the length of the beam and are not anchored to the joints. This system became very popular in New Zealand. It was mainly used in low-rise buildings in which the lateral loads are resisted by other elements, such as cast-in-place structural walls or moment-resisting frames. However, in the 1980s, its use expanded to taller buildings and as part of the lateral load-resisting system.

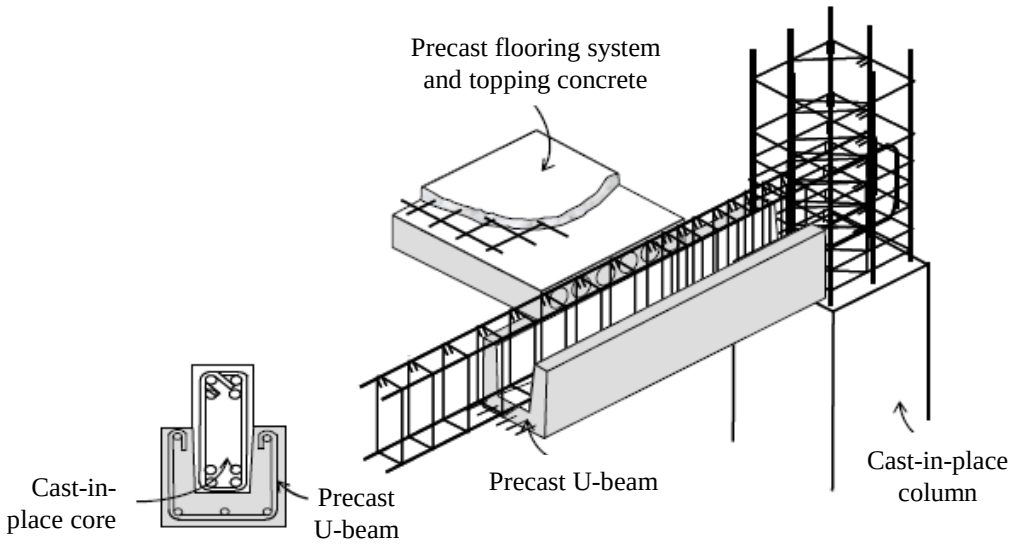

Figure 2-7. U-beam detail for precast frames (adapted from [6] and [36]).

Naturally, many questions were raised about the ability of the U-beams to meet the ductility demands produced during seismic events. For this reason, Park and Bull [6] tested three exterior full-scale beam-column connections subjected to cyclic loading to evaluate the seismic performance of the composite system. One of the specimens was not detailed for seismic loading, while the other two were. The only difference between the last two was that in one of the beams, an unbonded area of the longitudinal reinforcing steel was left inside the U-section, adjacent to the face of the column, to improve the behavior of the plastic hinge. According to the results, the specimens designed to resist seismic loads presented acceptable behavior with adequate load-carrying and deformation capacities. The unbonded area within the U-section of one of the beams helped to improve the behavior of the plastic hinge. The study showed that the cast-in-place and precast concrete composite system is a practical and

suitable solution for seismic zones as long as appropriate detailing for ductile behavior is used.

The use of U-beams in precast frames was further studied by Lee et al. [37]. In their system, the stirrups are placed inside the U-beam and closed at the top with a tie. The cast-in-place and precast concrete work together as a composite section under gravity and seismic loads. Additionally, the columns were manufactured in a single piece with windows at story level, where the beams are supported for the subsequent casting of the beam's core and the joint region (see Figure 2-8). Although the system was ideal for fast and efficient construction, the results showed that it had poor energy dissipation capacity and presented severe diagonal cracking and spalling of the concrete at the connection.

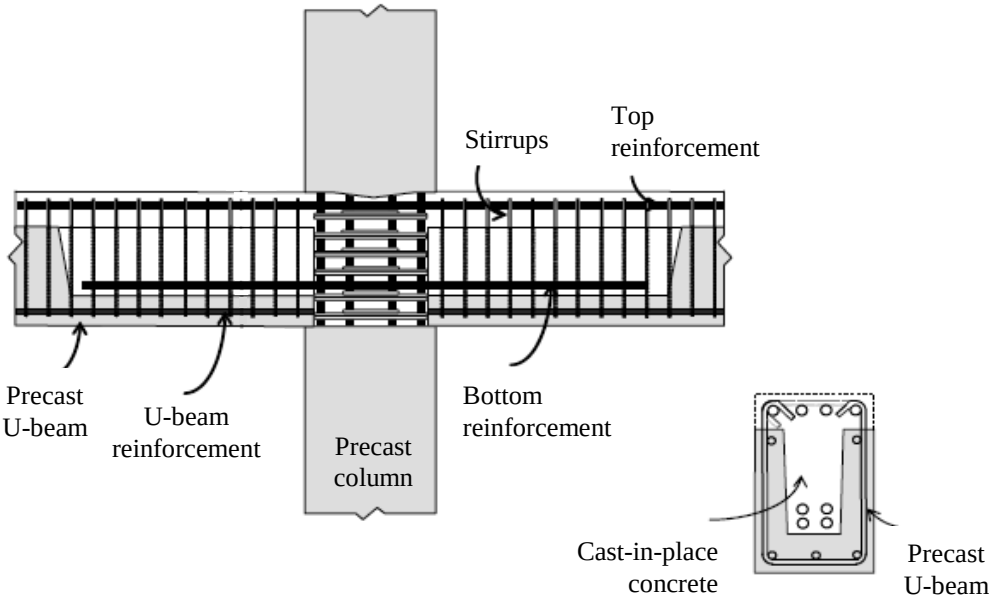

Figure 2-8. U-beam detail for precast frames proposed by Lee et al. [37] (adapted from [37]).

Park et al. [36] further assessed the strength of connections with U-shaped beams. The results showed that the connections had good load and deformation capacity. However, there was a decrease in the energy dissipation capacity due to the sliding of the longitudinal reinforcement inside the U-beam. It was observed that the support length of the beam on the column cover concrete significantly reduced the joint's effective shear area, which caused

the cracks and deformations (due to shear) to be greater than those of a similar monolithic connection.

Ochs and Ehsani [38] proposed strong connections with welded plates at the beam-column interface (see Figure 2-9). In addition, complementary U-shaped bars were placed to strengthen the beam over a length equal to 1.5*d*, where *d* is the effective depth of the beam, and relocate the plastic hinge. The observed damage occurred where expected, i.e., away from the connection; however, all the tested specimens failed similarly. In all cases, the welded bars fractured at different displacement demands, mainly attributed to the brittleness introduced by welding the bars to the plates.

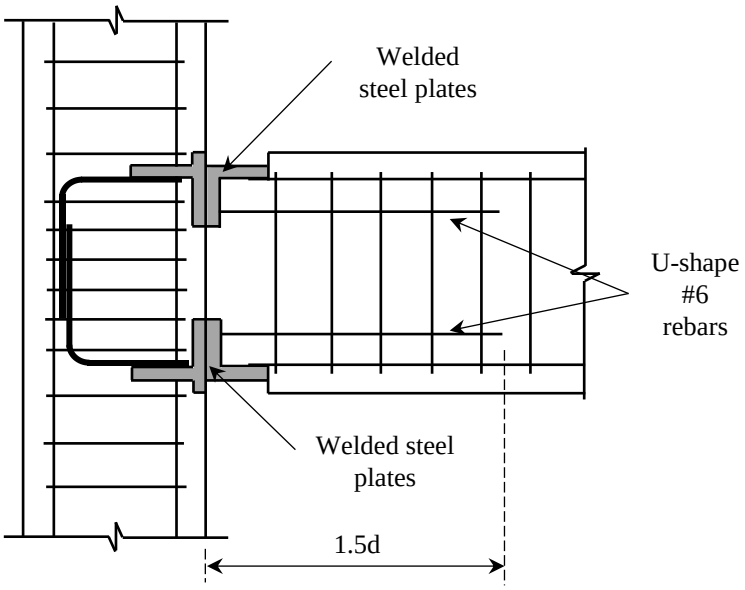

Figure 2-9. Connection proposed by Ochs and Ehsani [38] (adapted from [38]).

Ertas et al. [39] studied the behavior of four ductile beam-column connections and one monolithic connection. Three of the proposed precast connections required cast-in-place concrete; the other was a bolted connection. One of these specimens is shown in Figure 2-10. Specimen GOK-W, similar to a connection studied in Chapter 4, consisted of a precast beam supported on a concrete corbel and joined by welding. The continuity of the lower reinforcement was provided by welding it to the steel plate at the end of the beam. The top longitudinal reinforcement was introduced in the column window, where concrete was later poured.

All specimens, except for GOK-W, presented load-carrying and energy dissipation capacities adequate for seismic zones, and they reasonably emulated cast-in-place concrete behavior presenting hysteretic behavior similar to the monolithic connection. The bolted connection (Mod-B) performed better than the others and allowed rapid manufacturing and assembly. Similar to what was observed by Ochs and Ehsani [38], the poor behavior of the GOK-W specimen was attributed to the change in the mechanical properties of the reinforcement due to welding.

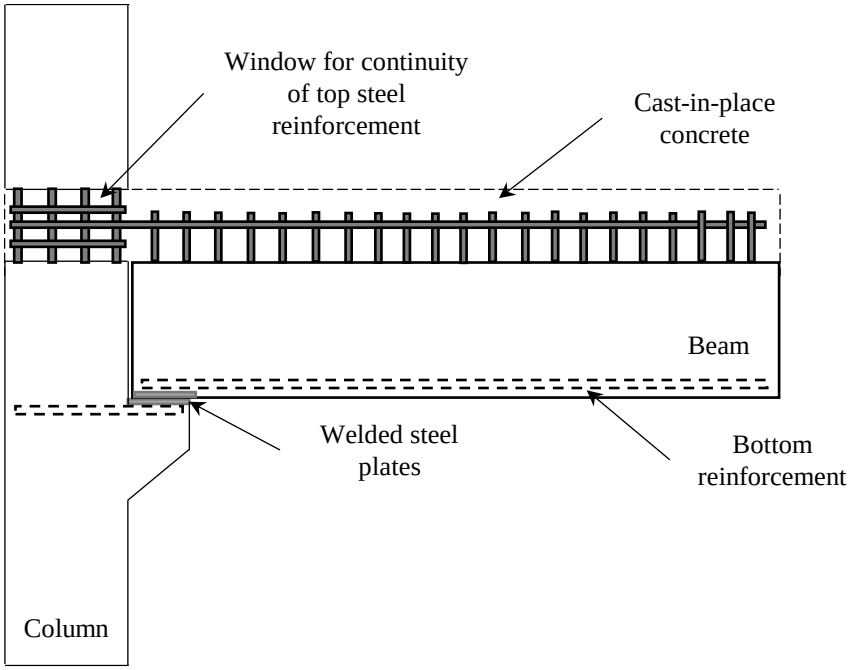

Figure 2-10. Specimen GOK-W studied by Ertas et al. [39] (adapted from [39]).

It has been recognized that welding should be avoided or minimized in connections or where plastic hinges are expected to develop. The Mexico City Building Code (MCBC) [40] and its Complementary Technical Norms for the Design and Construction of Concrete Structures 2020 (NTC-C-20) [41] do not allow, for medium or high ductility structures, that there be any rebar overlaps, welded or mechanical, inside the joints, at a distance of twice the depth of the member from the joint, and in those regions where plastic hinges are assumed to develop. The restrictions on welded connections are because the mechanical properties of the reinforcing steel are affected by the heat and the subsequent uncontrolled cooling. In this

process, the steel hardens significantly, affecting its ductility, which is not desirable for the seismic behavior of structures [42,43].

Regarding welded connections in precast structures, Girgin et al. [29] proposed to detach a portion of the longitudinal reinforcement near the welded connection from the concrete. This solution significantly increased the energy dissipation capacity of their tested beam-column specimens while avoiding buckling and premature rupture of the longitudinal rebars. However, additional transverse reinforcement is required in the region near the connection to prevent excessive deformation or shear failure.

Parastesh et al. [44] developed a ductile connection suitable for seismic zones. Their proposal allowed fast and efficient construction, eliminating the need for formwork, bolts, welding, and minimizing cast-in-place concrete. The columns were fabricated with a window at the story levels, where four diagonal bars were placed to guarantee stability. The ends of the beams, i.e., the plastic hinge regions, were U-shaped sections with diagonal stirrups. The bottom longitudinal reinforcement was spliced in the cast-in-place area, and the top reinforcement was continuous through the joint, extended into the beam on the other side, and later grouted. The results demonstrated that the proposed connections had higher flexural strength and initial stiffness than similar cast-in-place specimens. Stiffness degradation was acceptable up to a 4% drift, and flexural cracks were concentrated in the plastic hinge regions of the beams. The ductility ratios and the dissipated hysteretic energy were higher than those of the cast-in-place counterparts.

2.4.2 Experimental studies on precast non-emulative beam-column connections

The first major research program focused on the seismic performance of precast seismic structural systems in the United States was initiated at NIST (National Institute of Standards and Technology) in 1989 [4]. The aim was to develop design standards for precast reinforced concrete beam-column connections for seismic regions [4,45]. This program was initially carried out in three phases.

The first phase [4] consisted of two cast-in-place beam-column connections designed with the 1985 Uniform Building Code (UBC) specifications [46] for seismic zone 2 and two cast-in-place connections for seismic zone 4. Additionally, two precast connections were also

studied. The beams of the precast specimens were connected to the columns using two post-tensioned bars. Typical sections of the zone 4 specimens are shown in Figure 2-11. All the tested specimens represented an interior connection of a moment-resisting frame. The specimens were pinned at the base of the columns and roller supported at the free ends of the beams and at the top of the columns. A reversible cyclic loading protocol was applied at the tip of the column. The results of this phase of the project demonstrated that the post-tensioned precast connections are as strong and ductile as the cast-in-place connections and they are a viable option for structures built in seismic zones. However, the prefabricated connections' energy dissipation capacity, accumulated and per cycle, was not satisfactory, dissipating approximately 20 and 30% less energy, respectively, than the cast-in-place connections designed for zone 4.

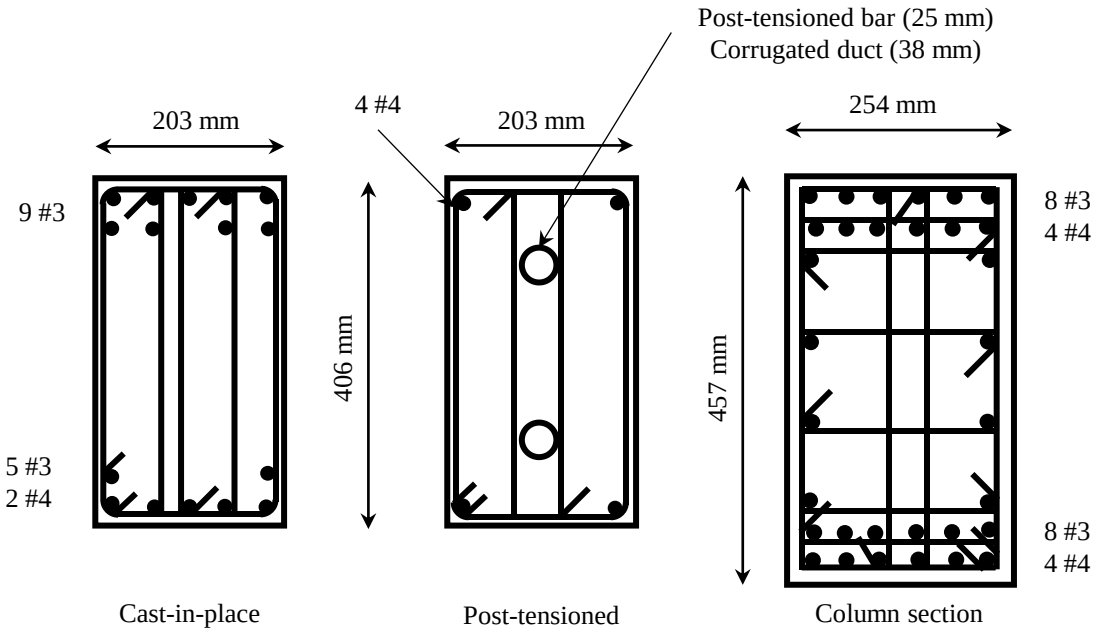

Figure 2-11. Zone 4 beams and columns studied by Cheok and Lew [4] (adapted from [4]).

To improve the energy dissipation capacity of precast beam-column connections, the second phase of the NIST project [45] consisted of testing six precast connections with different characteristics from those of the first phase. Two post-tensioned connections were tested. In this case, the post-tensioned bars were placed closer to the beams' centroid to improve energy

dissipation. The four remaining connections were prestressed using fully bonded 13 and 11-mm strands. The quantity and position of the strands were varied to evaluate their effects. In general, the energy dissipation capacity of the connections was improved, particularly that of the prestressed specimens. The energy dissipation per cycle of the precast connections was approximately 60% of that of the first-phase cast-in-place connections. However, the precast connections' total accumulated energy was higher due to larger ductility and deformation capacity.

Two prestressed precast connections with partially bonded strands were tested as part of the third phase of the NIST project. Overall, these specimens did not display good performance. However, the authors recommended using these connections in regions where energy dissipation is not a problem since they generally showed elastic behavior. The typical section of the prestressed zone 4 specimens studied for phases II and III is shown in Figure 2-12. It is observed that the prestress strands were closer to the centroid of the section.

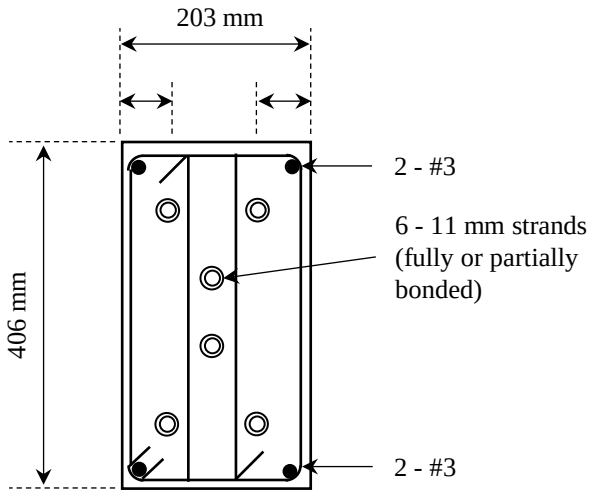

Figure 2-12. Zone 4 beams for phases II and III (adapted from [45]).

A fourth phase of the NIST project was later initiated to investigate the hybrid moment frame system [13]. Phase IV was further divided into two sub-phases, A and B. The objective of Phase IVA was to test the concept of the hybrid moment frame and determine the most promising archetype design. The results of this sub-phase were used to determine the specimen details for Phase IVB. According to Stanton et al. [13], the primary lessons learned from Phase IVA were that: the hybrid system performed well, maintaining its integrity to

very large drifts; strands, rather than high-strength bars, should be used for the post-tensioning steel because of its higher yield strain and ability to remain elastic at high elongations; the strands should be placed a mid-depth of the beam and should remain unbonded for most of its length; the post-tensioning steel should be contained within a single duct; and the energy-dissipating rebars should be placed at the top and bottom of the beam and should have a small debonded length at the beam-column interface to avoid strain concentrations and risk premature fracture.

In Phase IV, four precast interior beam-column specimens were tested under cyclic loading. Two of them were designed so that the ratio of the moment contribution from the mild steel to that from the post-tensioning steel was 35%, and the other two were designed to have a ratio of 47%. The strands were jacked to a stress of approximately $0.44f_{pu}$. Typical beam sections of the tested specimens are shown in Figure 2-13.

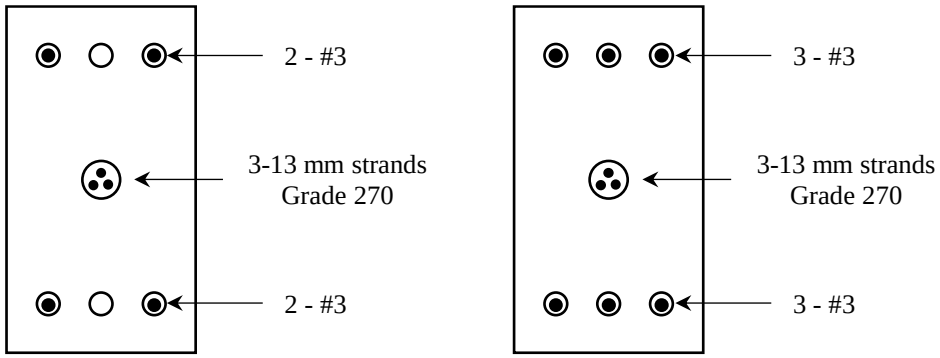

Specimen M-P-Z4 Specimen O-P-Z4

Figure 2-13. Typical beam sections of the tested hybrid specimens for Phase IV.

The hybrid specimens failed at drift ratios between 0.029 and 0.034 rad, less than what the two previously tested cast-in-place specimens reached. However, the hybrid specimens retained an average of 55% of their peak strength because the strands were undamaged even at failure of the specimen. Failure was defined as the point at which the strength dropped below 80% of the maximum measured load. The tested specimens also displayed minimal damage and no loss of shear strength. Hybrid moment frames have become one of the most successful precast structural systems regarding seismic performance; however, their use has been minimal. They are mainly used in New Zealand and the United States. Design

specifications for unbonded post-tensioned precast special moment frames have been developed by the Joint ACI-ASCE Committee 550 [47].

In general, structures perform better when some mechanism with ductile behavior is introduced. In concrete and steel structures, this mechanism is provided by plastic hinges at the ends of the beams. By 1994, there were already several proposals for cast-in-place emulating precast connections. However, some of them required characteristics that compromised the most important benefit of precast structures: speed of construction. Nakaki et al. [48] developed a connection that would take advantage of the inherent attributes of precast systems by allowing the beams and columns to be independently fabricated and joined at the column face with ductile connectors (see Figure 2-14), thus eliminating casting of concrete on site. These connectors contained steel rods that yielded at a well-defined strength, thus limiting the loads that can be transferred to less ductile components.

In the experimental program carried out by Nakaki et al. [48], two conventional cast-in-place beam-column connections and a precast connection equipped with their proposed ductile connectors were tested. The specimens were subjected to quasi-statically applied reversible cyclic loads. The precast connection achieved drifts of up to 4.5% with significantly less strength degradation and visual damage than the cast-in-place specimens. The load-displacement curve of the proposed system presented significant pinching of the hysteresis curves at drift ratios close to zero. This was attributed to the horizontal expansion of the specimen because as the ductile rods yielded in tension, the system had to overcome the post-yield deformation by yielding the rods in compression, and once contact was restored, the system's stiffness was also restored.

Overall, the ductile connectors prevented the precast components from entering a range of inelastic behavior. The most important advantage of this connection was that the inherent advantages of precast systems were maintained by avoiding concrete casting on-site. However, the system's low tolerances for on-site installation were a disadvantage.

Palmieri et al. [49] proposed multiple connections to provide precast systems with stable inelastic behavior. They found that the beam-column connections can be detailed to exhibit acceptable behavior when used in lateral load-resistant systems designed for seismic zones. The studied connections were designed to develop an elastic-nonlinear response through

post-tensioning steel or with a configuration that ensures that the longitudinal reinforcement to yield in tension and compression. The specimens had acceptable behavior at 2% drift, and severe damage occurred at around 4%. The load-displacement curves of the tests were used to model five- and 15-story frames and evaluate their response under seismic ground motions. The frames with precast connections behaved similarly between them and presented higher displacements than the cast-in-place model. It should be noted that the latter was modeled with an idealized bilinear behavior and not based on experimental results.

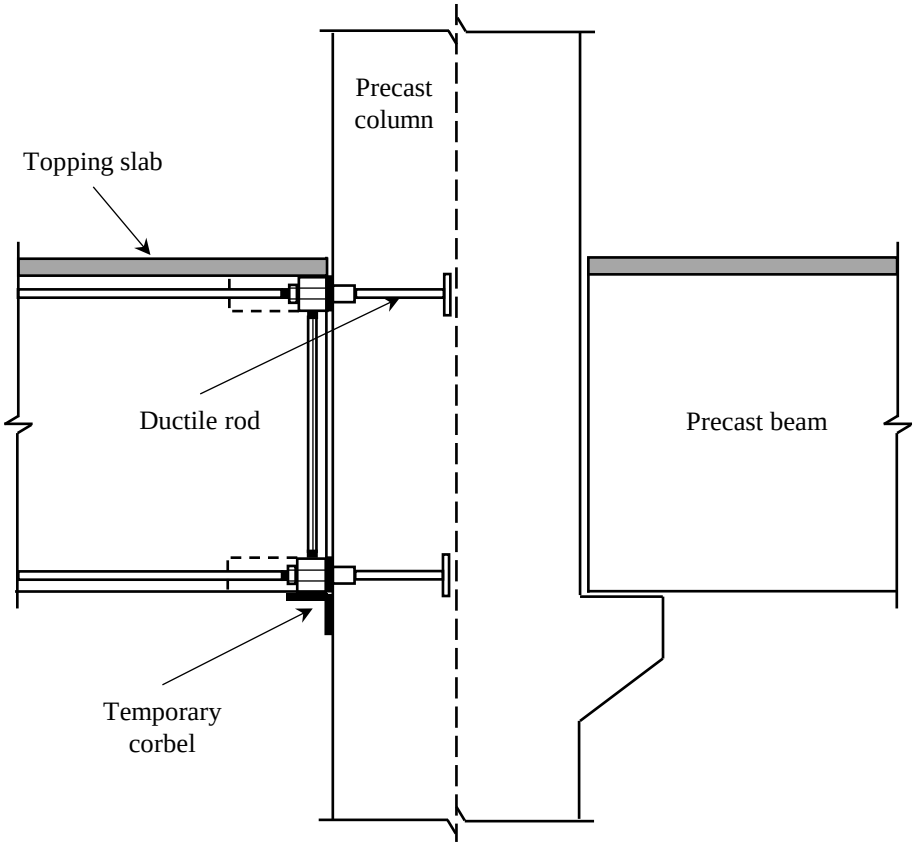

Figure 2-14. Beam-column connection proposed by Nakaki et al. [48] (adapted from [48]).

2.5 Building Codes on Precast Structures

In many countries around the world, structures are commonly designed with force-based seismic design methods. The design forces are obtained based on the ductility and overstrength that the structural elements may develop. The MCBC [40] and its Complementary Technical Norms for Earthquake Design (NTC-S-2020) [50] indicate that

for force-based methods (static or dynamic analysis), ductility is considered through the seismic behavior factor, *Q*, and the overstrength factor, *R*, which reduce the spectral ordinates of the elastic spectra. The seismic behavior factor depends on the structural system and its materials and reflects the capacity of the structure to incur inelastic deformations stably.

The NTC-S-2020 [50] divides conventional concrete frames into high, moderate, or low ductility structures, as shown in Table 2-1. Values for *Q* and maximum allowable drift ratios, θ_{max}, are assigned to each category. Precast concrete frames can only be designed as low and moderate ductility structures. This has been the case for decades, probably attributed to the belief that precast frames are less ductile.

Precast structures with their connections in critical areas or at the joints must be considered as low ductility structures. These structures are designed with the same criteria used for cast-in-place concrete structures, considering the load conditions that occur throughout the life cycle of the precast structure from the manufacturing, transportation, and assembly of the members to the completion of the structure and its conditions under service. In composite sections formed with precast and cast-in-place concrete, the parts must be interconnected to act as a unit, and their design should consider the effects of propping, or lack of propping, deflections, and cracking.

Table 2-1. Seismic behavior factors and maximum distortions for concrete structures, according to [50].

Structural system	Ductility	Condition	*Q*	θ_{max}
Concrete frames	High	-	4	0.030
	Moderate	-	3	0.020
	Low	-	2	0.015
Precast concrete frames	Moderate	With monolithic joints and ductile connections located outside of critical zones	3	0.020
	Low	With connections in critical areas or at nodes	2	0.015

In the case of precast structures designed for medium ductility ($Q = 3$), they must be able to emulate cast-in-place concrete behavior and have ductile connections outside critical areas. The connections of the precast elements must be made in a section where the design bending moments due to seismic loads are not greater than 70% of the total bending moments due to

dead, live, and accidental loads at the critical section of the element or within two depths of the critical section.

ASCE 7-22 [51] does not consider a separate category for precast moment-resisting frames. Cast-in-place and precast structures are divided into three categories: special, intermediate, and ordinary reinforced concrete moment frames, as shown in Table 2-2. The response modification coefficient, *R*, and overstrength factor, Ω_0, are also shown. Precast structures can be designed as anyone one of these seismic force-resisting systems. According to ACI 318-19 [52], special moment frames are those cast-in-place that comply with sections 18.2.3 to 18.2.8 and sections 18.6 to 18.8; and precast that comply with sections 18.2.3 to 18.2.8 and with section 18.9.

Table 2-2. Design coefficients and factors for seismic force-resisting systems, according to [51].

Seismic force-resisting system	Response modification coefficient, *R*	Overstrength factor, Ω_0
Special reinforced concrete moment frames	8	3
Intermediate reinforced concrete moment frames	5	3
Ordinary reinforced concrete moment frames	3	3

In section 18.9, ACI 318-19 [52] gives general requirements for special moment frames with ductile connections (section 18.9.2.1) and strong connections (section 18.9.2.2) constructed using precast concrete. Additionally, special moment frames constructed using precast concrete that does not satisfy the above (section 18.9.2.3) can be used if they satisfy the following [52]:

1. ACI 374.1 [18] requirements.
2. Details and materials used in the test specimens shall be representative of those used in the structure.
3. The design procedure used to proportion the test specimens shall define the mechanism by which the frame resists gravity and earthquake effects and shall establish acceptance values for sustaining that mechanism. Portions of the mechanisms that deviate from code requirements shall be contained in the test specimens and shall be tested to determine upper bounds for acceptance values.

ACI 374.1 [18] defines the minimum experimental evidence that shall be provided to validate the use, in regions of high seismic risk for structures assigned to satisfy high seismic performance or design categories, of a weak beam/strong column moment frame that do not satisfy the requirements of the sections mentioned above. Thus, ACI 374.1 [18] can be used to validate non-emulative beam-column connections of special moment frames. This standard is used to evaluate the seismic performance of the innovative beam-column connections proposed in this thesis.

Apart from restricting the use of precast frames with high ductility, NTC-S-2020 [41] requires that precast connections must comply with the requirements of section 7.7.4. The most important points are summarized below.

1. When a connection is part of the structural system resistant to lateral actions, it must resist not less than 1.3 times the design value of the internal forces and moments that it transmits, for the beam-column connection, and 1.4 times for the column-to-column connection.
2. In connections that are part of the structural system resistant to lateral actions, the compressive strength of the concrete, f'_c, used in the connections between precast elements required to transmit tension and compression forces, must be at least equal to the greater of the connecting precast elements.
3. The reinforcing steel placed in the connections of precast elements, required to transmit tension and compression forces, must have a yield stress not greater than 412 MPa and be adequately anchored within the connecting members.
4. Transverse reinforcement must be placed in the connections with the diameter and spacing specifications indicated in the same standards for cast-in-place structures to ensure the required strength and confinement of the connection, according to the ductility category used for design.
5. In any case, the connections will be detailed to minimize cracking due to forces by volumetric changes.

The upcoming NTC-C-2023, to be published at the end of this year, is set to adapt the approach of ACI 318-19, mainly that high ductility moment-resisting frames that do not emulate cast-in-place concrete behavior can be used for seismic regions if they satisfy the

same requirements of section 18.9.2.3 of ACI 318-19 [52]. Additionally, most of the restrictions in NTC-C 2020 [41] for precast structures are to be removed. The changes in the upcoming NTC-C-2023 will encourage improvement and innovation in the precast industry.

3

Experimental Tests of Cast-in-Place Reinforced Concrete Beam-Column Connections

3.1 Introduction

Beam-column connections and their joints are critical regions that play an important role in structural integrity and often define the overall behavior of reinforced concrete framed buildings [53,54]. If adequately detailed, the joints of a structure provide seismic resistance by enabling the adjoining members, i.e., beams and columns, to develop their ultimate strength and deformation capacity while remaining elastic and presenting minimal damage. Joint deformation in seismic design has been historically disregarded in many parts around the world.

After events like the 1985 Mexico earthquake, design and construction flaws were evident, such as: minimal transverse reinforcement in the joint regions, which is one of the most common problems. Unfortunately, poorly designed and detailed reinforced beam-column joints are still prevalent today. Consequently, researchers are still very interested in the cyclic behavior of concrete joints and their adjoining members. Most research is focused on the

shear strength of the beam-column joint, the effect of their reinforcement, and eccentric beam-column connections.

A particular interest in studying the seismic performance of precast reinforced concrete beam-column connections has arisen in Mexico. In 2017 and 2019, an experimental program was carried out to study the seismic performance of cast-in-place concrete beam-column connections. These connections served as benchmarks for comparing their cyclic behavior to that of conventional and innovative precast beam-column connections. The results of four cast-in-place beam-column connections are shown in this chapter, with particular emphasis on deformation and energy-dissipating capacities. The connections were subjected to reversible incremental cyclic loading applied quasi-statically.

3.2 Experimental Program

3.2.1 Test specimens

The test specimens represented an exterior "T" connection of a reinforced concrete frame building model studied by Guerrero et al. [55] (see Figure 3-1). They covered half the span of the beam (L_b = 5000 mm) and half the height of the column above and below the joint (L_c = 3300 mm). At the time, the model building was designed according to the 2004 Mexican City Building Code (MCBC-2004) [56] and its Complementary Technical Norms for Seismic Design (NTC-S-2004) [57] and Complementary Technical Standards for Design and Construction of Concrete Structures (NTC-C-2004) [58].

The test matrix consisted of four cast-in-place beam-column connections. The beams had a length of 5000 mm and a cross-section of 450 mm x 810 mm, while the columns had a length of 3300 mm and a 600 mm x 600 mm cross-section. At the time of planning these tests, the more current 2020 MCBC [40] was published and used to design the beam-column specimens. A seismic modification factor of Q = 2, appropriate for low-ductility elements. It is significant to mention that the detailing requirements of the NTC-C-2020 [41] for concrete structures are similar to those specified in ACI 318-19 [52] and ACI 352R-02 [59].

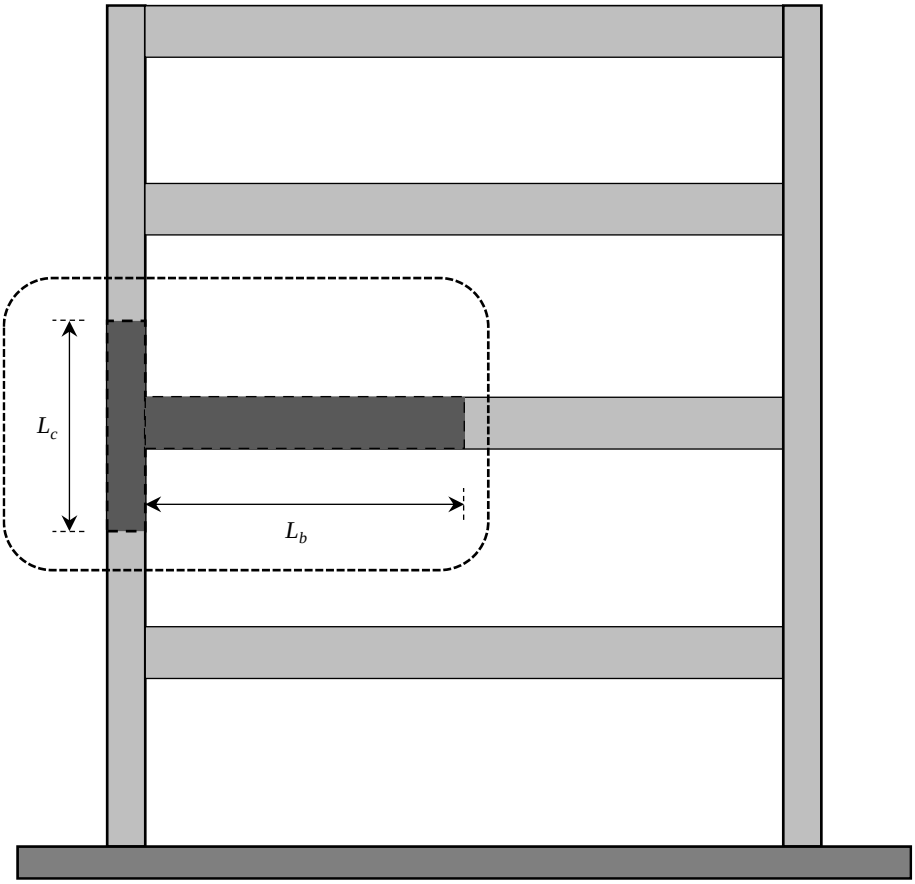

Figure 3-1. Exterior beam-column connection of a concrete frame.

The beams shared the same geometric characteristics and the same amount of longitudinal reinforcement of two #12 rebars at the top and four #8 bars at the bottom. Transverse reinforcement consisted of #3 stirrups with variable spacing. The tested specimens and some of their characteristics are shown in Table 3-1, where ρ is the longitudinal reinforcement ratio. As can be seen, their main difference was the stirrup spacing at 300, 150, and 75 mm. The specimens' joint shear strength was adequate and complied with the minimum transverse reinforcing ratio required by the NTC-C-2020 [41]. It is worth mentioning that when designing low-ductility moment-resistant frames, the NTC-C-2020 [41] does not strictly require checking the joints' shear strength or the minimum transverse reinforcement ratio. The columns were detailed to satisfy the strong column-weak beam design philosophy. Th typical beam section of the cast-in-place (CIP) specimens is shown in Figure 3-2.

The materials used were concrete with an average compressive strength of f'_c = 55.2 MPa, measured from samples, and Grade 42 [60] reinforcing steel.

Table 3-1. Cast-in-place (CIP) test specimens.

Specimen	Construction	$\rho_{(+)}$	$\rho_{(-)}$	Stirrup spacing (mm)
CIP-1A	Cast-in-place	0.0062	0.0069	300
CIP-1B				300
CIP-2				150
CIP-3				75

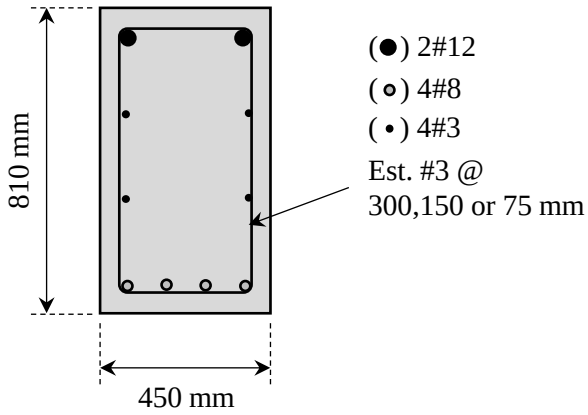

Figure 3-2. Typical beam section of the CIP specimens.

3.2.2 Test setup

It was assumed that the connection could be isolated, as shown in Figure 3-3, because the zero moment points, or inflection points, due to seismic actions, are located around the middle of the columns and girders. The drifts, θ, obtained by applying a load on the column are equivalent to those obtained if the load was applied at the end of the beam. The load V applied during the tests (Figure 3-3b) represents the shear force resulting from the deformation of the beam at the center of the span if the lateral load was applied at the end of the column.

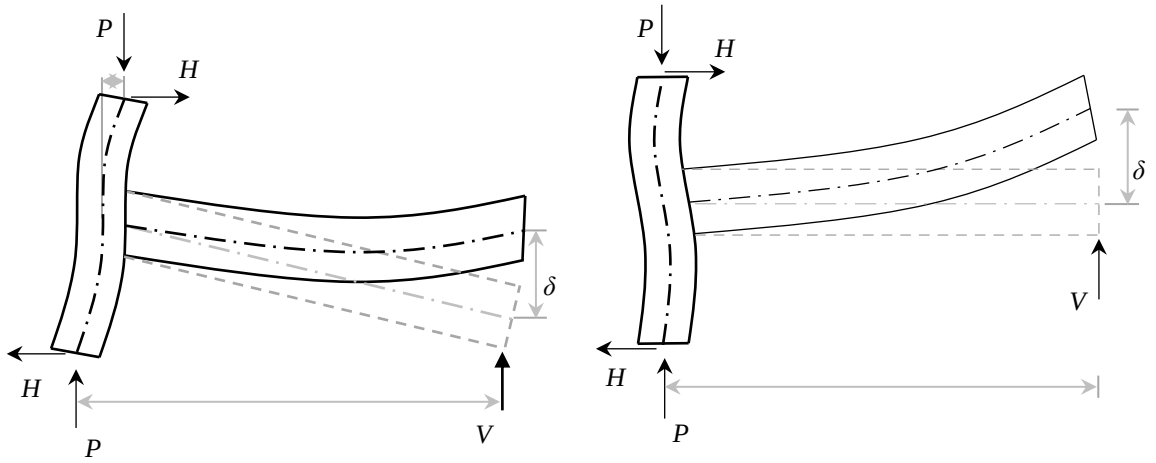

a) Actual isolated connection b) Connection in the test position

Figure 3-3. Isolated beam-column connection.

Similar to other studies [61–63], the beams were oriented vertically and the columns horizontally. This was done for convenience and easeness of the tests. Displacements were applied at the beam's tip using two hydraulic actuators connected in series, and the forces necessary to achieve the target displacements were measured with two load cells installed on each actuator. It is mentioned that two actuators were connected in series to reach large displacement strokes, as required by the tests. The columns were anchored to the reaction slab through four post-tensioned steel bars, while the actuators were similarly anchored to the reaction wall. Figure 3-4 shows the general setup.

It is significant to mention that the contribution to the beam's flexural strength due to the presence of the floor system was not considered. According to ACI 374.1 [18], having a slab connected to the beam of a specimen is not required for testing purposes. It is recognized that the presence of a slab increases beam strength and column shear demands; however, if the strong column-weak beam design philosophy is satisfied, the results should be acceptable. Similarly, ACI 374.1 [18] does not require an axial load to be applied to the column simultaneously with the lateral load; therefore, it was not applied here.

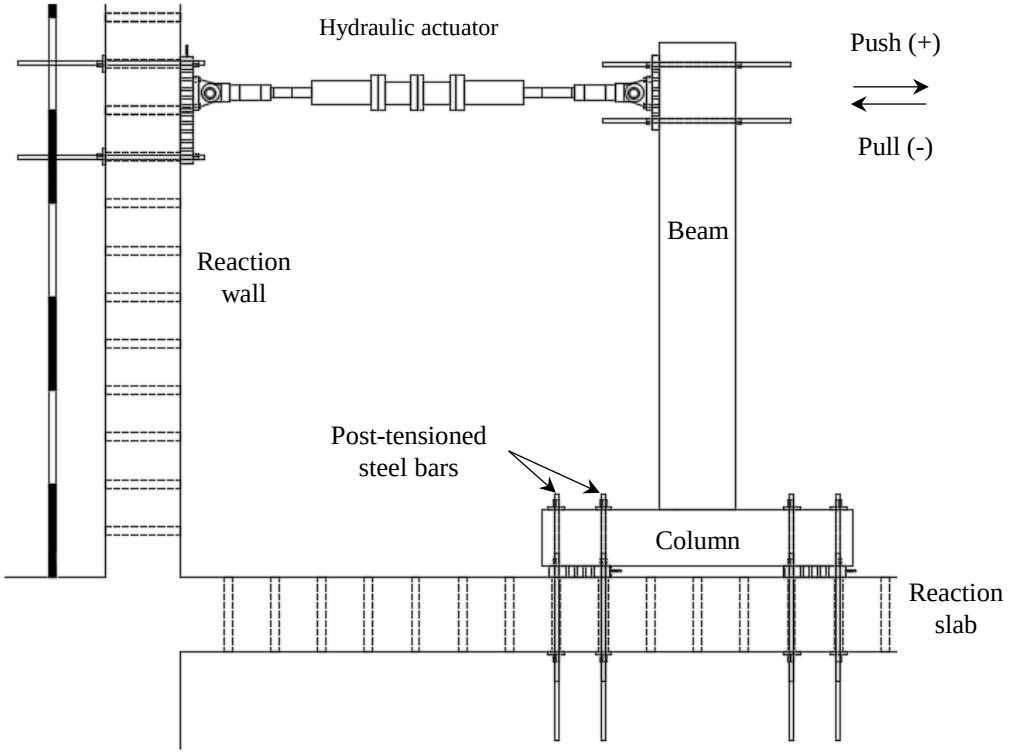

Figure 3-4. Test setup.

3.2.3 Loading protocol

Two displacement-controlled loading protocols were proposed for the experimental program. The first protocol, shown in Figure 3-5a, was applied to all specimens except for CIP-1B, which was loaded with the protocol shown in Figure 3-5b. These protocols were developed according to the recommendations of ACI 374.2 [64] and ACI 374.1 [18], respectively. The first consisted of two cycles for each target displacement followed by one cycle at 50% of the immediately preceding displacement.

Similarly, the second protocol consisted of three cycles for each target displacement followed by one cycle at 50% of the immediately preceding displacement. The effects of applying a different protocol for specimen CIP-1B are discussed in the following sections. Figure 3-5 also shows the equivalent drift ratios as percentages, calculated as the relationship between the horizontal displacement of the beam at the level of the applied load and the distance from this point to the center of the column. According to FEMA P-795 [65], a component's displacement or drift capacity is reached when the strength decays by 20%. However, ACI

374.2 [64] indicates that researchers should not necessarily adopt this point as the definition of collapse, as different structural systems do not respond the same. Instead, a strength decay of 25%, indicated in ACI 374.1 [18], was adopted in this study to be consistent with the tests carried out in Chapters 5 and 6.

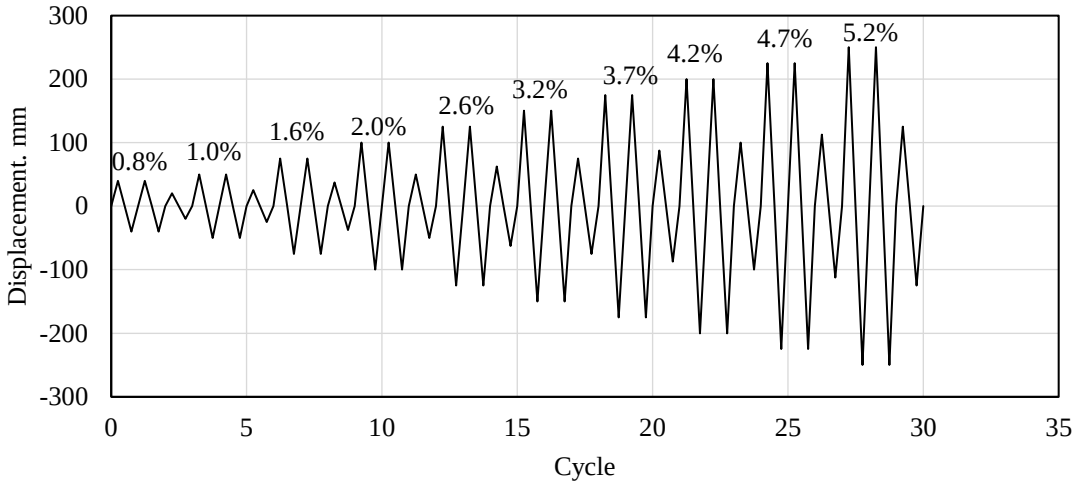

a) Typical loading protocol

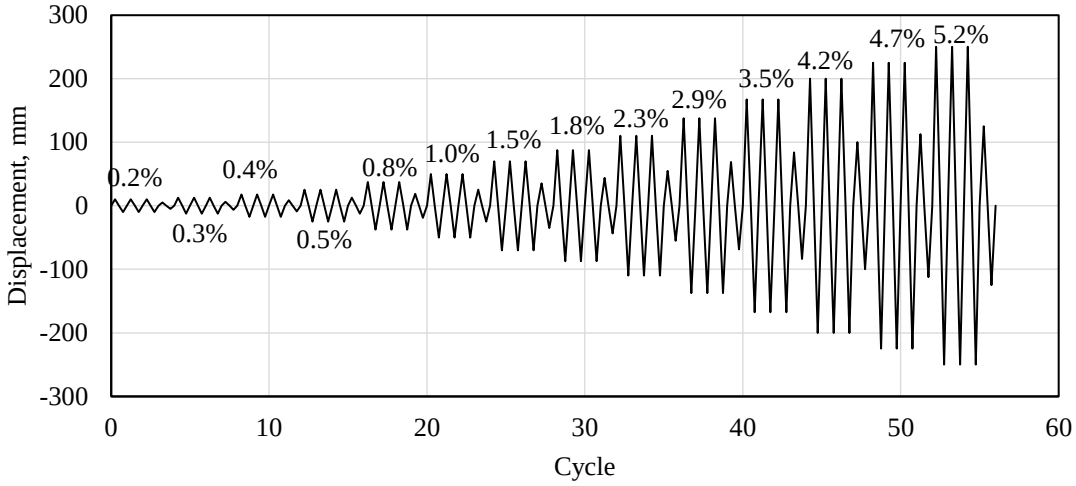

b) Loading protocol for specimen CIP-1B

Figure 3-5. Applied loading protocols.

It is worth mentioning that ACI 374.1 [18] gives the minimum experimental evidence for special moment frames that do not satisfy certain requirements of ACI 318-19 [52]. When performing these tests, since specimens CIP-1A and CIP-1B were the same, it was decided

that the former be tested with the protocol on ACI 371.1 [18] to assess the possible differences in their response.

3.2.4 Instrumentation

Specimens were instrumented with linear variable differential transducers (LVDTs) to assess local displacements. As shown in Figure 3-6, horizontal LVDTs (H1-H5) were placed along the beam's length to measure horizontal displacements (see Figure 3-6a). Two LVDTs (H1 and H2) were located at the beam's tip for redundancy purposes. Diagonal LVDTs were placed on the lateral face of the beam (D1-D6) and the joint area (D7 and D8) to measure shear deformations (see Figure 3-6b). Figure 3-6c shows a picture of the typical setup of the beam-column specimens. Test specimens were also instrumented with strain gauges (SGs) on longitudinal and transverse reinforcement. However, rebar strains are not discussed in this chapter.

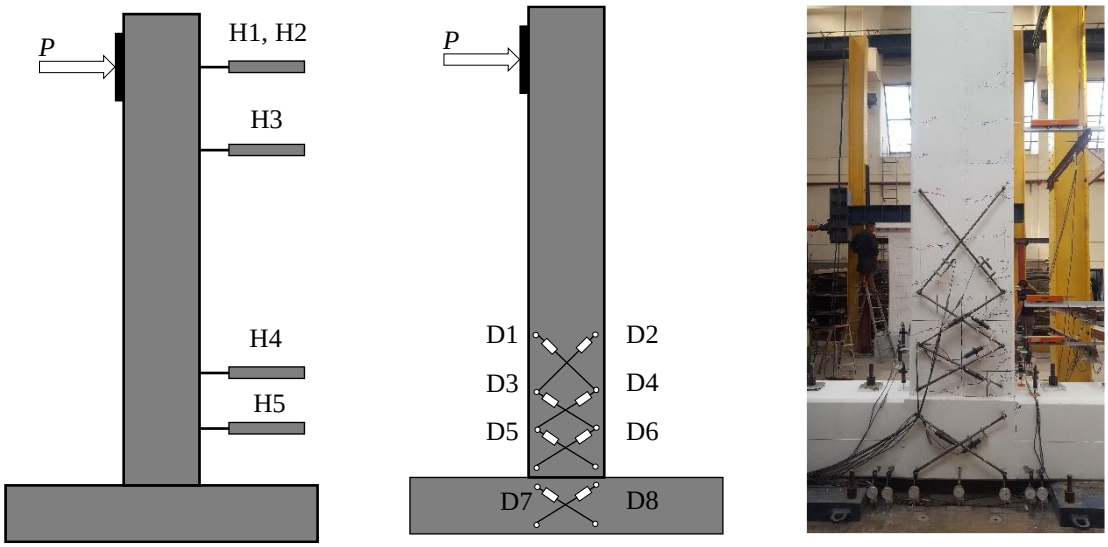

a) Horizontal LVDTs b) Diagonal LVDTs c) Picture of the actual setup

Figure 3-6. Typical instrumentation of a beam-column specimen.

3.3 Results

3.3.1 Failure modes and observed damage

The damage presented by the specimens at an approximate drift ratio of 0.03 is shown in Figure 3-7. The failure modes of the four specimens were similar, mainly by flexure. Some specimens exhibited severe damage with significant flexural and shear cracking, concrete crushing and spalling, and even buckling of the longitudinal rebars. The four lower rebars of specimen CIP-1A (see Figure 3-7a) buckled around 3% drift, which was attributed to the low level of confinement (with a stirrup spacing of 300 mm). Specimen CIP-1B, which had the same stirrup spacing, also presented buckling of the same rebars, as shown in Figure 3-8, but at slightly higher drift demands, close to 3.5%.

Flexural and shear cracking on specimen CIP-3 was observably lower than the other three specimens. The joint region especially presented less diagonal cracking than the rest and did not extend significantly on either side of the column. The smaller stirrup spacing contributed to the good performance of specimen CIP-3 because it avoided the buckling of the longitudinal rebars even at large drifts, which allowed them to develop their post-elastic strength appropriately in both loading directions. It will be seen in the following section that specimen CIP-3 displayed stable hysteretic behavior with significantly less pinching in the hysteresis loops.

3.3.1 Hysteresis curves

The measured moment-drift ratio curves are shown in Figure 3-9. The beam moments were obtained by multiplying the measured load at the tip of the beam by the lever arm. The drift ratio was obtained as the ratio between the lateral displacement of the beam at the load application point and the distance from this point to the column centerline. The backbone curves are shown in continuous red lines, and the calculated ultimate moment, $M_{u,c}$, is shown with dashed lines for illustration purposes. The calculated flexural strengths were based on the actual material properties of the steel and concrete. An average compressive strength of 55.2 MPa was used for all specimens, and a factor of 1.25 was applied to the yield stress (412 MPa) of the reinforcing steel to account for strain hardening as recommended in ACI 352R-02 [59].

a) CIP-1A

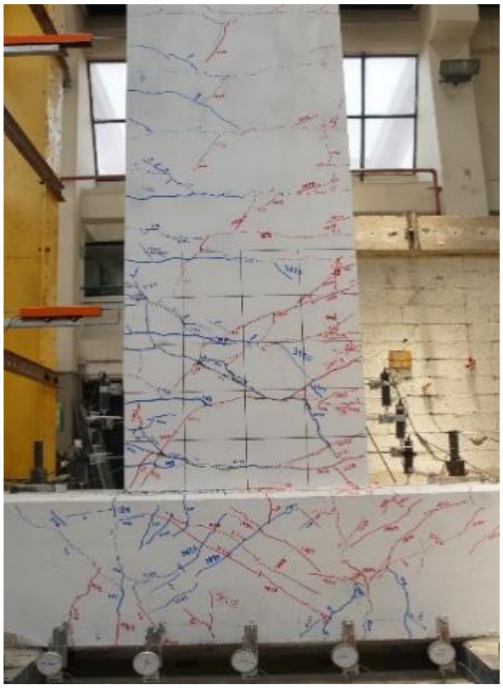

b) CIP-2B

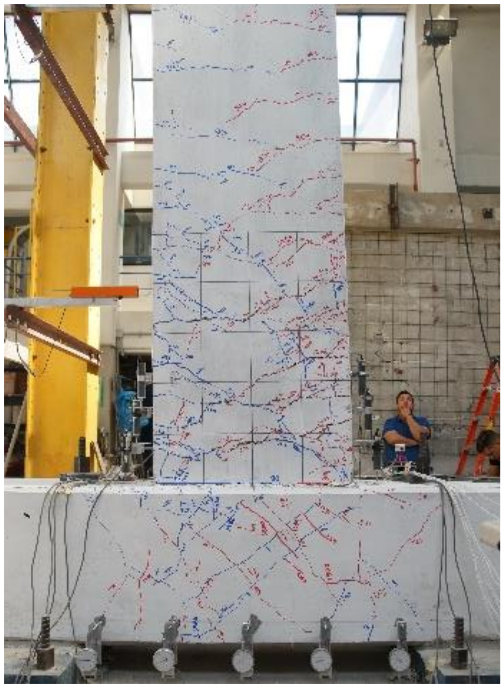

c) CIP-2

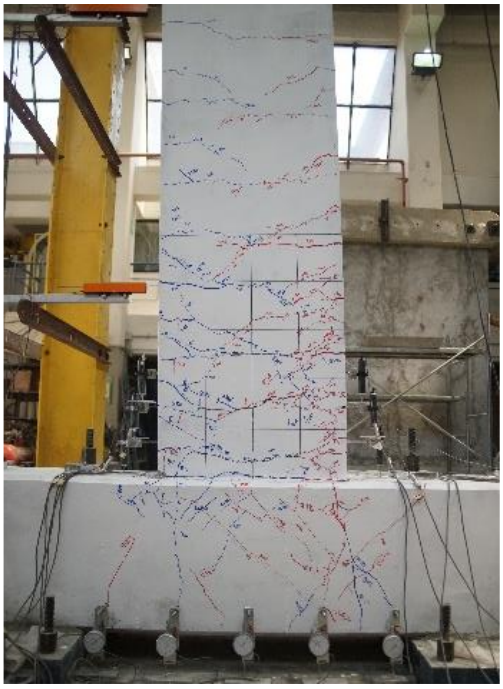

d) CIP-3

Figure 3-7. Damage of CIP specimens at 3% drift.

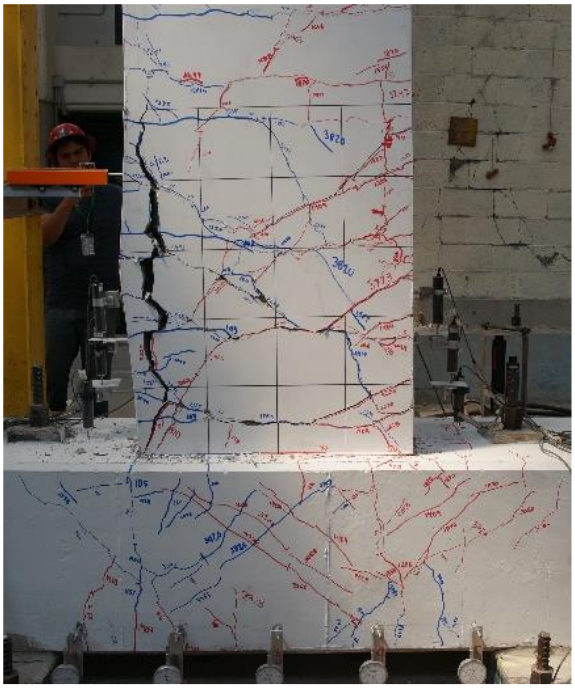

Figure 3-8. Concrete spalling due to rebar buckling in specimen CIP-1B (3.5% drift).

All specimens showed adequate hysteretic behavior, with broad and stable loops and some pinching behavior appearing on cycles with drift demands greater than 3%. Flexural strengths after specimen yielding increased in all cases. Specimen yielding occurred at drifts between 0.6 and 0.8%. The maximum measured moments, $M_{u,exp}$, and the calculated ultimate moments, $M_{u,c}$, are shown in Table 3-2. Flexural strengths were the same for all specimens as they had the same reinforcement ratios. It can be seen that the maximum experimental moment was between 1.13 and 1.23 times the calculated flexural strength. The average of these values, i.e., the average overstrength, was approximately 1.18. Specimen CIP-1B exhibited the lowest overstrength, which could be attributed to the different applied loading protocol.

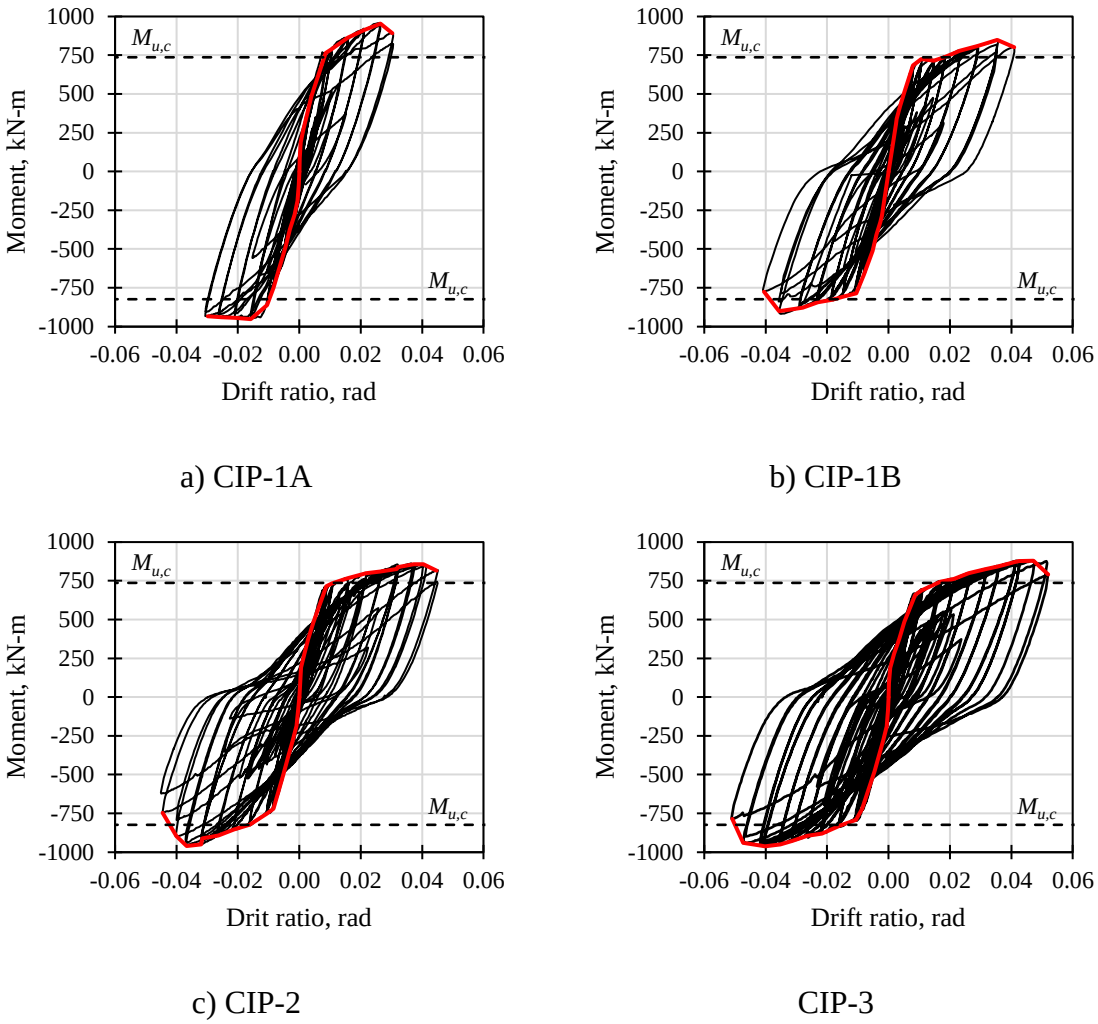

a) CIP-1A b) CIP-1B

c) CIP-2 CIP-3

Figure 3-9. Moment-drift ratio curves.

In Figure 3-10a comparison of the backbone curves is shown. All specimens displayed similar initial stiffnesses. Regarding load-carrying capacity, all specimens, except for specimen CIP-1A, behaved similarly. Loads were maintained above the calculated flexural strength in the push direction but fell below this threshold in the positive direction at drifts above 4%.

The cracking moment, M_{cr}, considering a modulus of rupture (f_r) equal to $0.63\sqrt{f_c'}$ [41] and gross section properties is also shown normalized to the calculated ultimate moment ($M_{u,c}$) in Figure 3-10. The theoretical M_{cr} was $0.3M_{u,c,}$ with a corresponding drift ratio of 0.05%. Graphically, it can be seen that the change in stiffness due to crack initiation could be

accurately predicted. From the experimental backbone curves, it was seen that the change in stiffness occurred at an average drift of 0.06%, which is close to the theoretical value of 0.05%.

The NTC-C-2020 [41] allows calculating the modulus of rupture of high-strength concrete, i.e., concrete with compressive strength equal to or greater than 40 MPa, as $0.85\sqrt{f_c'}$ if no experimental evidence is available; however, in the case of the tested specimens, this value overestimates M_{cr}. Therefore using $0.63\sqrt{f_c'}$ to estimate the modulus of rupture was appropriate and is also the value recommended by ACI 318-19 [52].

Table 3-2. Comparison of flexural strengths.

Specimen	Direction	$M_{u,exp}$ (kN-m)	$M_{u,c}$ (kN-m)	$M_{u,exp}$ / $M_{c,u}$ (average)
CIP-1A	(+)	957	736	1.23
	(-)	954	824	
CIP-1B	(+)	849	736	1.13
	(-)	919	824	
CIP-2	(+)	862	736	1.17
	(-)	960	824	
CIP-3	(+)	880	736	1.18
	(-)	963	824	

The yielding drifts (θ_y), ultimate drifts (θ_u), and the average global ductility ratios (μ) are listed in Table 3-3. The global ductility ratio is defined as the ratio of the maximum displacement or drift to the yield displacement or drift. As mentioned, the main difference between the specimens was the stirrup spacing.

From Table 3-3, it can be seen that as the stirrup spacing was closed, the ductility ratio increased. Specimen CIP-3, with a stirrup spacing of 75 mm, developed the highest average ductility ratio of 8.1 while exhibiting the lowest damage. Of course, it is well known that adequate confinement of the plastic hinge region of a beam improves its overall seismic behavior, e.i., better deformation and energy-dissipating capacities. Also, it must be recognized that, in general, the low longitudinal reinforcement ratio in the beams contributed to the appropriate behavior of the tested specimens, as an increase of strength tends to reduce

ductility [12]. For example, specimens CIP-1A and CIP-1B were designed with low-ductility detailing requirements and developed acceptable ductility ratios: 4.9 and 5.6, respectively.

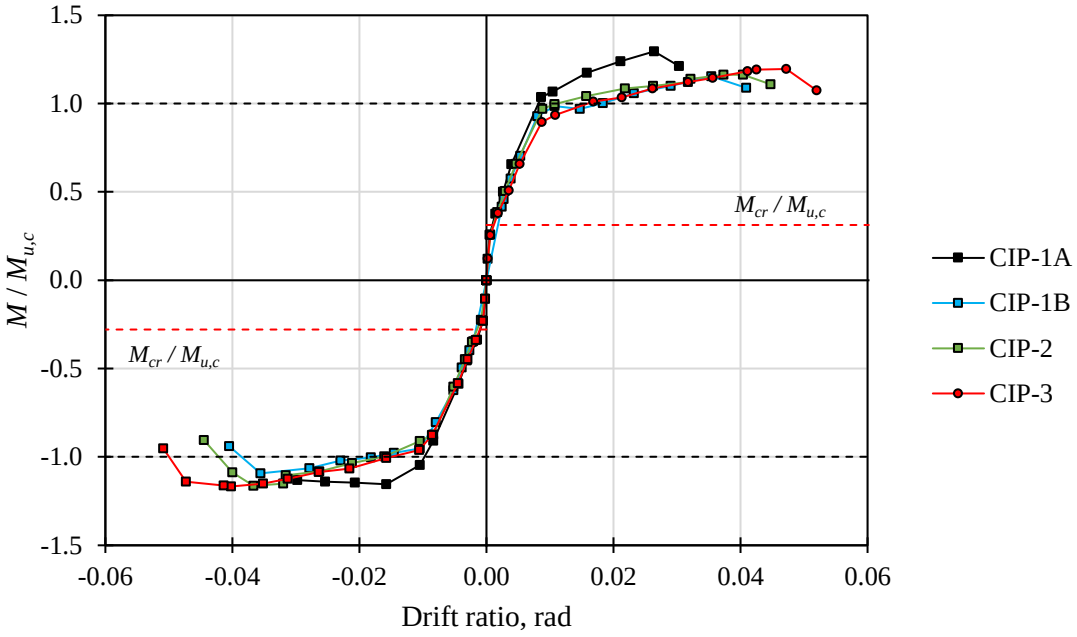

Figure 3-10. Comparison of backbone curves.

Table 3-3. Global ductility ratios.

Specimen	Direction	θ_y (rad)	θ_u (rad)	μ (average)
CIP-1A	(+)	0.6	3.0	4.9
	(-)	0.6	3.0	
CIP-1B	(+)	0.7	4.1	5.6
	(-)	0.8	4.1	
CIP-2	(+)	0.6	4.5	6.3
	(-)	0.8	4.5	
CIP-3	(+)	0.6	5.2	8.1
	(-)	0.7	5.1	

3.3.2 Ductility and energy dissipation

The energy dissipation capacity of the specimens was evaluated with the relative energy dissipation (β_i). The relative energy dissipation is the ratio between the area of the hysteresis loop of interest and the idealized area of a parallelogram defined by the initial stiffness during

the first cycle of the test and the maximum load presented during the cycle for which β_i is calculated (see Figure 3-11). The following equation is given by ACI 374.1 [18]:

$$\beta_i = \frac{A_h}{(P_1 + P_2)(\theta'_1 + \theta'_2)} \tag{3-1}$$

where A_h is the area of the hysteretic loop, P_1 and P_2 are the maximum loads and θ'_1 and θ'_2 are the inelastic drift ratios in the positive and negative directions, respectively.

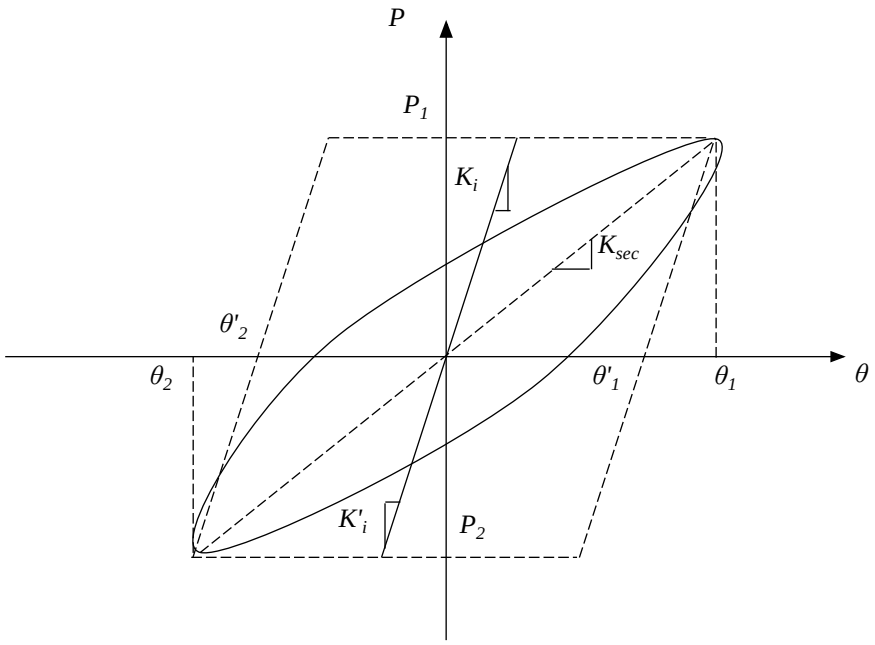

Figure 3-11. Secant stiffness and idealized parallelogram.

The relative energy dissipation ratios of the tested specimens are shown in Figure 3-12. The reported values correspond to the second cycle of each target displacement. According to ACI 374.1 [18], the relative energy dissipation ratio must be evaluated for the third cycle of the target displacement; however, only two cycles were applied during the tests described here. Specimen CIP-1A exhibited less deformation capacity than the other specimens but still had a maximum relative energy dissipation ratio close to 35%. The rest were closer to 40%, developed around a 0.03 drift ratio or above. Specimens CIP-1B and CIP-2 showed noticeable degradation in their energy dissipation capacity after a drift ratio of 0.035 rad. Specimen CIP-3, in contrast, peaked at around 0.045 rad.

According to ACI 374.1 [18], the relative energy dissipation ratio must not be less than 12.5% for the third cycle at a drift ratio of 0.035. This value is shown only for reference in Figure 3-12, as the only specimen tested with the loading protocol based on ACI 374.1 [18] was specimen CIP-3. Also, the tests carried out on the proposed innovative precast beam-column connections in Chapters 5 and 6 were evaluated with this acceptance criterion. From the figure, it is clearly seen that for a drift ratio of 0.035 rad, all specimens had exhibited a relative energy dissipation ratio above 12.5%.

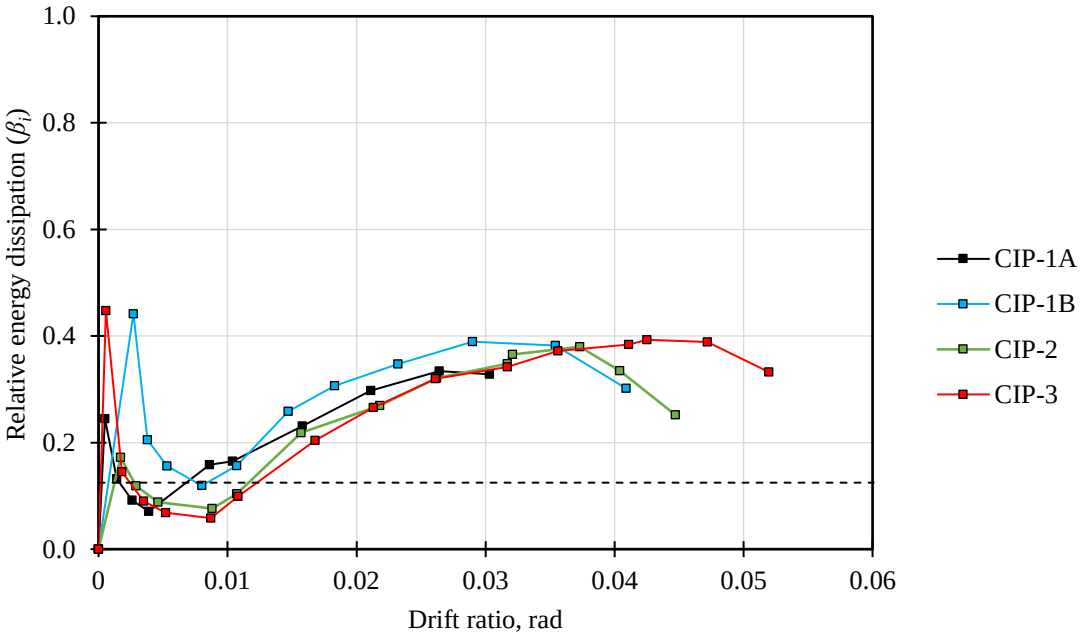

Figure 3-12. Relative energy dissipation ratio.

Another way to evaluate the performance of the tested specimens is with the cumulative ductility ratio, defined by Teran et al. [66] as

$$NE_{H\mu} = \frac{E_{H\mu}}{P_y \delta_y} \tag{3-2}$$

where $E_{H\mu}$ is the accumulated plastic energy, and P_y y δ_y are the load and the displacement at yield, respectively.

The cumulative ductility ratio is shown in Figure 3-13. It is evident that specimens CIP-2 and CIP-3 could dissipate more plastic energy, as they could accumulate larger displacements. However, between these two, specimen CIP-2 had the largest for the same cumulative displacements, which might be mainly attributed to the fact that specimen CIP-2 developed more damage during the test. This observation is also consistent with specimen CIP-1A, that for the same cumulative displacements, dissipated more plastic energy than the others and is the specimen that presented the most damage at the same drift ratios. Specimen CIP-1B, although equal to CIP-1A regarding transverse reinforcement ratios, dissipated less plastic energy for the same cumulative displacements. This was because CIP-1B accumulated more displacements due to applying three cycles for each target displacement without necessarily developing the same damage until the latter stages of the tests. The above can be considered one of the more evident effects that the different loading protocols had on the specimens.

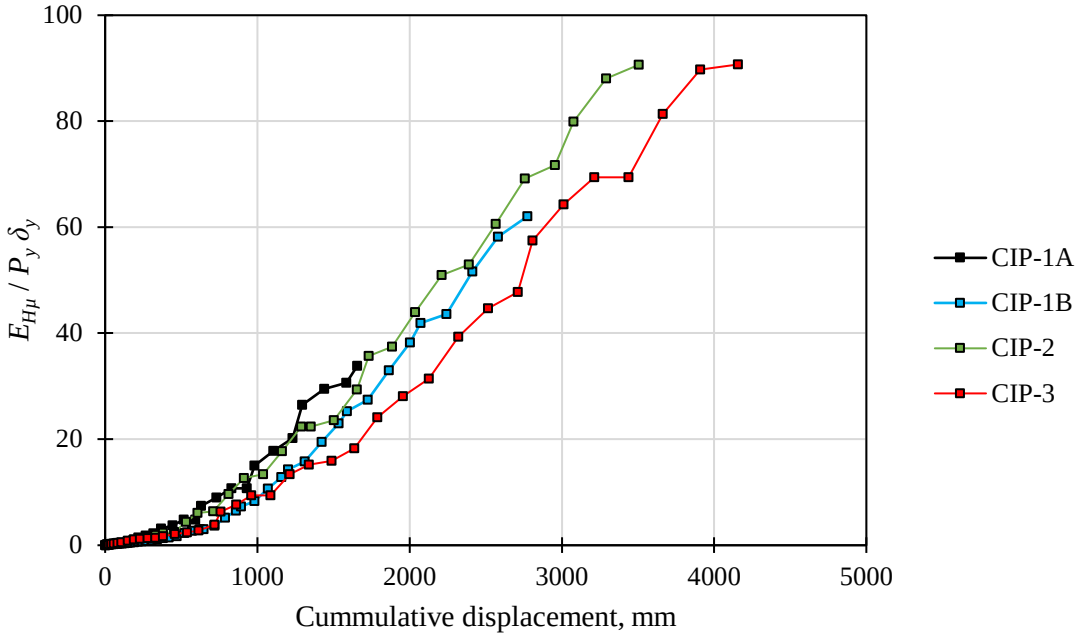

Figure 3-13. Cumulative ductility ratio for CIP specimens.

3.3.3 Equivalent viscous damping

The equivalent viscous damping ratio, ζ_{eq}, can be obtained by equating the measured energy dissipated per cycle (E_D) under an experimental load cycle with that of an equivalent viscously damped one degree-of-freedom oscillator, expressed as [67]:

$$\zeta_{eq} = \frac{1}{4\pi}\frac{E_D}{E_{S0}} \tag{3-3}$$

where E_D is the measured energy dissipated per cycle, and E_{S0} is the straining energy stored in an elastic mass-spring oscillator.

The equivalent viscous damping ratios are plotted against the ductility ratios in Figure 3-14a. Before yielding, i.e., ductility ratios below 1, the specimens were able to dissipate small amounts of hysteretic energy, with equivalent damping ratios below 10%, even when considered to be within the elastic range. As expected, damping increased as the deformation increased. After yielding, damping ratios for all specimens increased similarly up to approximately 20% for a ductility ratio of 5. After that, specimens CIP-1B and CIP-2 dropped off, and specimen CIP-3 did not drop below 20%, even at a ductility ratio of approximately 8.

The equivalent viscous damping ratio against the normalized effective stiffness is plotted in Figure 3-14b. In this figure, each point represents a feasible damping ratio for a given normalized effective stiffness. As can be seen, damping ratios vary approximately linearly and inversely proportional to the effective stiffness, i.e., effective stiffness decreases as the specimens undergo larger deformations. This figure will be used to compare the damping ratios of the cast-in-place specimens with those developed by the conventional precast specimens studied in Chapter 4. It will be seen that the precast specimens behave similarly to the specimens studied here, and because of that, an equivalent viscous damping model was proposed in Chapter 4. A damping model was also proposed for the innovative precast beam-column connections studied in Chapter 6.

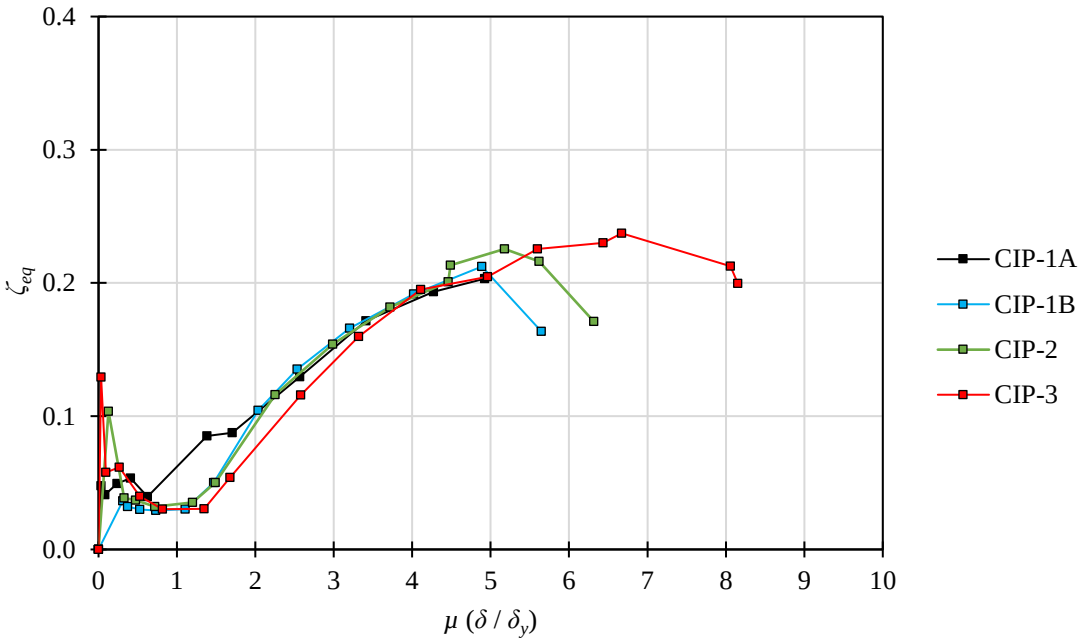

a) Equivalent viscous damping with ductility ratios

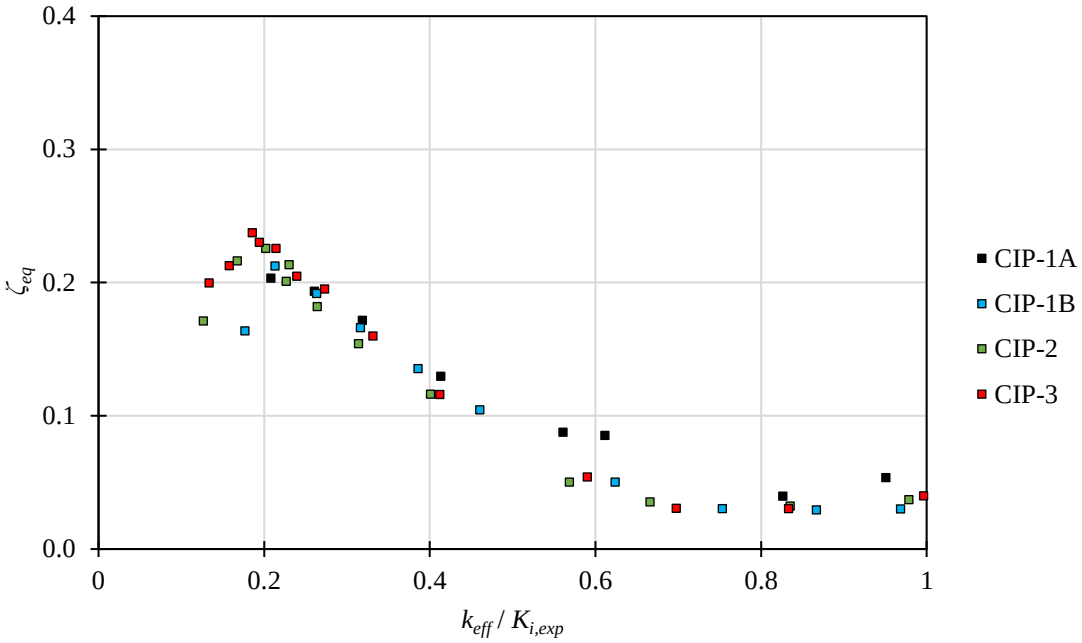

b) Equivalent viscous damping with normalized effective stiffness

Figure 3-14. Equivalent viscous damping for CIP specimens.

3.4 Conclusions

In this chapter, four full-scale exterior cast-in-place beam-column connections with longitudinal reinforcement ratios between 0.0062 and 0.0069 and stirrup spacing of 300, 150 and 75 mm were subjected to reversible incremental cyclic loading applied quasi-statically. Based on the results, the following conclusions are offered:

1. The hysteresis loops remained stable throughout most of the tests, with some pinching behavior at cycles above 0.03 target drift. It must be said that the selected reinforcement ratios were significantly smaller than those commonly used in practice. Experiments with higher reinforcement ratios should be studied to assess the effect on the cyclic behavior of beam-column connections.
2. Damage on the joints was minimal. Specimen CIP-3, which had the smallest stirrup spacing (75 mm), displayed less cracking on the beam and the joint than the other specimens.
3. The theoretical ultimate flexural strengths were achieved in all cases, and the load-carrying capacity remained stable even in the final stages of the tests. The load at crack initiation was predicted with great precision. The overstrength developed by the specimens was, on average, 1.18.
4. Three of the tested specimens dissipated close to 40% of their idealized energy-dissipating capacity, that is, the ratio of the hysteresis loop area to the area of an idealized parallelogram with elastic-perfectly plastic behavior.
5. Equivalent viscous damping ratios were above 20% in all cases, with a maximum of 23% developed by specimen CIP-3.

Some key structural characteristics of the tested cast-in-place specimens were obtained experimentally and discussed in this chapter. They will be used to assess their cyclic behavior compared to precast beam-column connections in the following chapter.

4

Experimental Tests of Conventional Precast Reinforced Concrete Beam-Column Connections

4.1 Introduction

Historically, earthquakes in Mexico and many other countries have caused extensive damage [68–70]. Recently, the September 2017 Puebla-Morelos earthquakes caused significant damage to numerous buildings in Mexico City and other smaller communities [71–73]. The need for more effective lateral load-resisting structural systems is evident. Designing efficient structural solutions is the main objective of structural and seismic engineering [74]; however, these require experimental and numerical validation. Experimental tests are currently the most reliable method to evaluate and validate the seismic performance of conventional and innovative structural solutions.

Precast reinforced concrete systems (PRCS) are an attractive alternative, given their advantages over conventional systems, such as better quality control of the precast members, accelerated construction, reduction in formwork and on-site labor, greater durability, and quick investment recovery. The working conditions in a precast plant also favor the mass production of structural elements, and there is less risk of interruption of activities due to

weather conditions or others. The cost-effectiveness and quality control of precast systems has led to their increased popularity throughout the world, including in areas of high seismicity [10] and, especially, in areas with extreme weather and expensive labor [8].

The use of PRCS in high seismic areas has been limited for various reasons. For decades, they were believed to be less ductile and present less stable inelastic behavior than traditional cast-in-place reinforced concrete structures [4]. The poor performance of some precast structures in past earthquakes, such as in the 1977 Romania earthquake [23] and the 1988 Armenia earthquake (1988) [24], had effectively discouraged their use for a long time, even when the reason for their poor performance was due to deficient design or construction practices that could be avoided. Added to the above, the scarcity of design guidelines, particularly design provisions for the seismic design of precast structures and their connections, had limited their use [5].

The seismic performance of PRCS is highly dependent on the characteristics of the connections between the precast members. It is now known that the poor performance of precast buildings, as well as conventional cast-in-place buildings, has often been attributed to poorly designed and poorly constructed connections [10]. Precast concrete frames are built by assembling precast elements on site and are generally connected by monolithic emulating techniques. For that reason, the connections might be left vulnerable to severe seismic loads. Therefore, one of the main challenges of precast construction lies in finding economical and practical methods to connect precast elements, ensuring adequate stability, stiffness, strength, and ductility [5].

Many studies have evaluated the seismic performance of precast beam-column connections. One of the first notable investigations was carried out by Park and Bull [6]. At the time, precast concrete was growing in popularity in New Zealand for its use in lateral moment-resisting frames. Naturally, concerns were raised by some designers and building officials. In their study, Park and Bull [6] reviewed seismic design considerations for precast prestressed concrete beam shells. Three full-scale exterior beam-column connections were tested under cyclic loading to evaluate the seismic performance of the precast U-beams acting as a composite section with cast-in-place concrete cores. The results showed good seismic behavior as long as special ductility provisions were met. However, when special seismic

detailing was not implemented, the studied connections were considered only suitable for gravity frames where other elements, such as walls or bracing, provided lateral resistance.

The use of U-beams in precast frames was further studied by Lee et al. [37]. In this system, the stirrups were placed inside the U section and connected to the cast-in-place concrete so that composite action was achieved under gravity and seismic loads. The columns could be fabricated as a single piece with windows at the story levels, where the beam shells are supported for the following casting of the core, the floor topping concrete, and the joint region. Although the system was ideal for fast and efficient construction, the results showed that the system had poor energy dissipation capacity and had severe diagonal cracking and concrete spalling at the connection.

More recently, Parastesh et al. [44] proposed a ductile connection suitable for seismic zones. Their proposal allowed for fast and efficient construction, eliminating the need for formwork or welding, and minimizing cast-in-place concrete. The columns were manufactured with a free space in the joint area where four diagonal bars were placed to guarantee the stability of the columns during the construction process. The beams in the plastic hinge area had a precast U-shaped cross-section with diagonal stirrups on the side faces. The lower longitudinal reinforcement of the beam was lapped within the cast-in-place area with the bars running through the joint and extending into the beam on the opposite side or topped off with 180-degree bends in the case of exterior connections. The top reinforcement was continuous along the beams and within the joints and cast with a layer of grout. To validate the proposed system, Parastesh et al. [44] tested two monolithic specimens and six precast specimens under cyclic loading. The results of this study demonstrated that the precast specimens had higher flexural strength and initial stiffness than the monolithic specimens. Stiffness degradation was acceptable up to 4% drift, and flexural cracks were concentrated in the plastic hinge region of the beams. The ductility ratios and the dissipated hysteretic energy were higher than those of the monolithic specimens. The precast specimens dissipated 30% more hysteretic energy, which was attributed to the formation of wide cracks in the region of the beam-column connections.

Efforts have also been made to develop non-emulative connections between precast members. Non-emulative construction uses the unique properties of the connections between

the precast elements to sustain severe non-linear deformations while avoiding excessive damage to the precast elements. The hybrid moment frame is among the most successful PRCSs [10]. This system combines unbonded post-tensioned tendons and conventional reinforcing steel. The tendons give the hybrid frame the ability to self-center while the reinforcing steel provides dissipation to the system through yielding [13]. The hybrid frame has several properties superior to cast-in-place frames, such as reduced cyclic loading damage, negligible residual displacements, and high deformation capacity [75]. In return, the energy dissipation capacity is reduced due to a flag-type hysteretic behavior, resulting in possible greater displacements during a seismic event. This system and other non-emulating techniques were developed during the NIST (National Instituto of Standards and Technology) program [4] and some were tested for the culmination of the PRESSS (Precast Seismic Structural Systems) project in a five-story, two-bay building [76].

After conducting a literature review, it has been observed that numerous precast beam-column connections, both emulative and non-emulative, have presented acceptable cyclic behavior and, in some cases, surpassed the cast-in-place connections in terms of seismic performance. While efforts are made to develop innovative PRCSs, studying the experimental behavior of conventional precast structures is essential since most precast buildings have been built with emulating techniques that have not been yet validated extensively.

Considering the above, an experimental program was initiated in Mexico in 2017. The objective was to study the seismic performance of precast reinforced concrete beam-column connections. Among these were conventional cast-in-place, conventional precast used in the industry, and innovative precast connections. Between 2017 and 2019, cast-in-place and conventional precast connections with low longitudinal reinforcement ratios were studied. The results of the cast-in-place connections were discussed in Chapter 3. The results of the conventional precast specimens are reported in this chapter, while those of the innovative precast connections are presented in Chapter 5. Particular emphasis on deformation and energy-dissipating capacities is paid.

Based on the experimental results and the number of tested specimens (four), it cannot be concluded that the general response of the precast specimens was superior to that of the cast-

in-place specimens. However, they showed good hysteretic behavior with broad and stable hysteresis loops. In general, it can be said that the precast specimens showed similar load-deformation and energy-dissipating capacities to the cast-in-place specimens described in Chapter 3.

4.2 The Studied Precast Beam-Column Connections

Two precast beam-column connections were studied. The first consisted of precast U-beams and precast columns with story-level windows. The precast components were connected at the joints with wet connections. Unlike the systems proposed in [36,37], the precast beams are not introduced into the column windows; instead, they are supported on temporary metallic supports, which are later removed after the cast-in-place concrete reaches its nominal strength (see Figure 4-1). The floor system is generally supported on the concrete corbels of the bearing beams. When needed, column-to-column connections are made at the mid-height of the columns using high-strength grout and connecting steel bars.

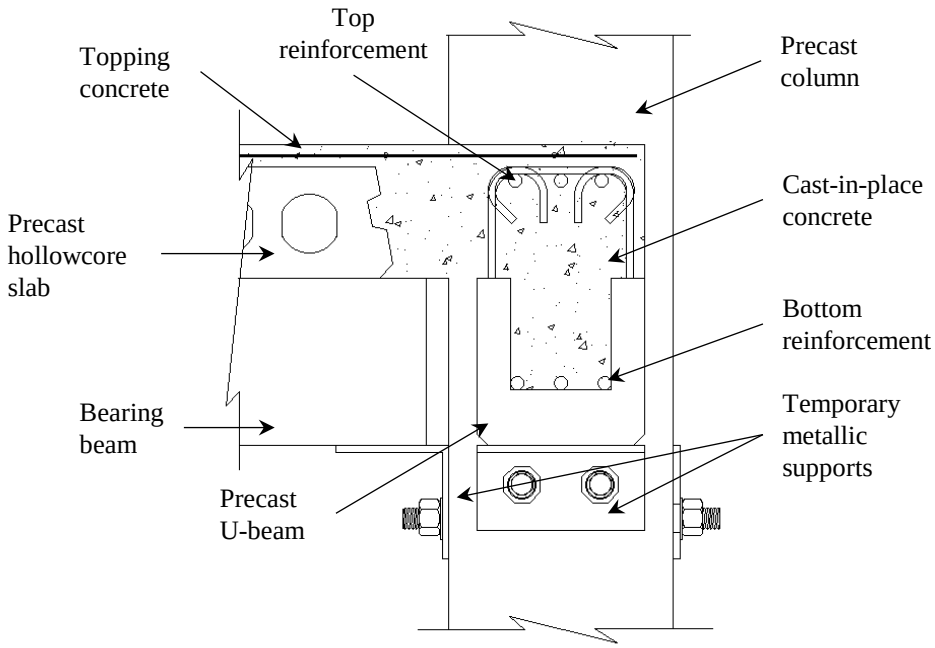

Figure 4-1. Precast beam-column with U-beams.

The second precast beam-column connection consisted of a welded connection at the bottom of the beam and a wet connection at the top, similar to that shown in [39]. The precast column was fabricated with a concrete corbel at story level, where a steel plate was anchored with welded rebars, as shown in Figure 4-2. A steel plate was also anchored with welded rebars at the bottom of the beam. In this type of connections, once the columns are erected, the beams are supported on the concrete corbel, and the steel plates are welded together. At the top of the beam, the longitudinal reinforcement is inserted in a duct left in the column, and the transverse reinforcement is closed with cross ties. Subsequently, the top of the beam, the column duct, and the topping concrete is poured. This type of connection is practical and is commonly used in some regios in Mexico; however, its seismic performance has been questioned in the past and, therefore, it should be studied.

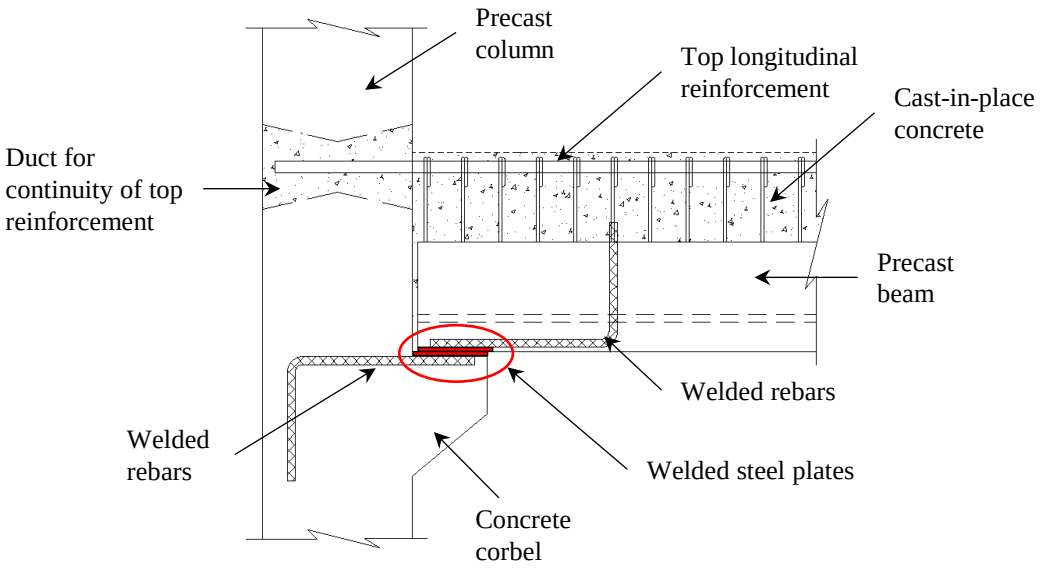

Figure 4-2. Precast beam-column with welding.

4.3 Experimental Program

4.3.1 Test specimens

Similarly to the specimens described in Chapter 3, the precast specimens described here represented an exterior "T" connection of a reinforced concrete frame building model studied by Guerrero et al. [55]. They covered half the span of the beam (L_b = 5000 mm) and half the height of the column above and below the joint (L_c = 3300 mm).

The test matrix consisted of four precast beam-column connections. Three of them were similar to the precast system with U-beams described in the previous section (Figure 4-1), and the remaining specimen had a welded connection at the bottom of the beam and a wet connection at the top (Figure 4-2). The beams had a cross-section of 450 mm x 810 mm, while the columns were 600 mm x 600 mm. The specimens were designed according to NTC-C-2020 [41], and the NTC-S-2020 [50]. Low-ductility detailing was considered. Detailing requirements in Mexico are similar to those in ACI 318-19 [52] and ACI 352R-02 [59].

The tested specimens and some of their characteristics are shown in Table 4-1. The beams shared the same geometric characteristics and the same amount of longitudinal reinforcement (i.e. two #12 rebars at the top and four #8 rebars at the bottom). Transverse reinforcement consisted of single #3 stirrups with variable spacing (300, 150 and 75 mm). The precast beams and columns had the same longitudinal reinforcement as the cast-in-place specimens described in Chapter 3, however, the effective depth for positive moment was reduced due to the precast U-shaped section. The welded specimen was provided with the same effective depth as the U-beams. The interior surfaces of the U-beams were roughened to ensure proper bonding between the precast and cast-in-place concrete.

The top longitudinal reinforcement of specimen P-COR-1 was covered with cast-in-place concrete in a small duck within the joint region, where the rebars were introduced, and at the top of the beam over its length. Bottom reinforcement continuity was given with a welded connection. During the production of specimen P-COR-1, steel plates were anchored to the concrete corbel of the column and another to the bottom end of the beam. These steel plates were later aligned and welded together.

The specimens' joint shear strength was adequate and complied with the minimum transverse reinforcing ratio required by the NTC-C-2020 [41]. The columns were detailed to satisfy the strong column-weak beam design philosophy.

The materials used were concrete with an average compressive strength of f'_c = 55.2 MPa, measured from samples, and Grade 42 [60] reinforcing steel.

Table 4-1. Conventional precast test specimens.

Specimen	Construction	Atribute	Stirrup spacing (*s*), mm	Scheme
P-UB-1	Precast	U-beam	300	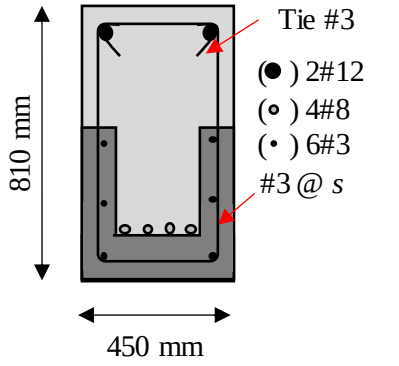
P-UB-2	Precast	U-beam	150	
P-UB-3	Precast	U-beam	75	
P-COR-1	Precast	Concrete corbel and welded connection	150	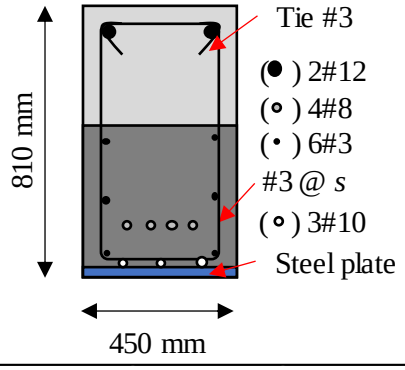

4.3.2 Test setup

The test setup was similar to the setup described in Chapter 3. For convenience, the test setup is shown again in Figure 4-3. The beams were oriented vertically, while the columns horizontally. Similar test setups can be seen in [61–63]. It was assumed that the beam-column sub-assembly could be isolated in this way because the zero moment points, or inflection points, due to seismic actions are located close to the mid-height of the columns and mid-span of the beam. Displacements were applied at the beam's tip using two hydraulic actuators connected in series. The columns were anchored to the reaction slab through four post-tensioned steel bars, and the actuator was similarly anchored to the reaction wall.

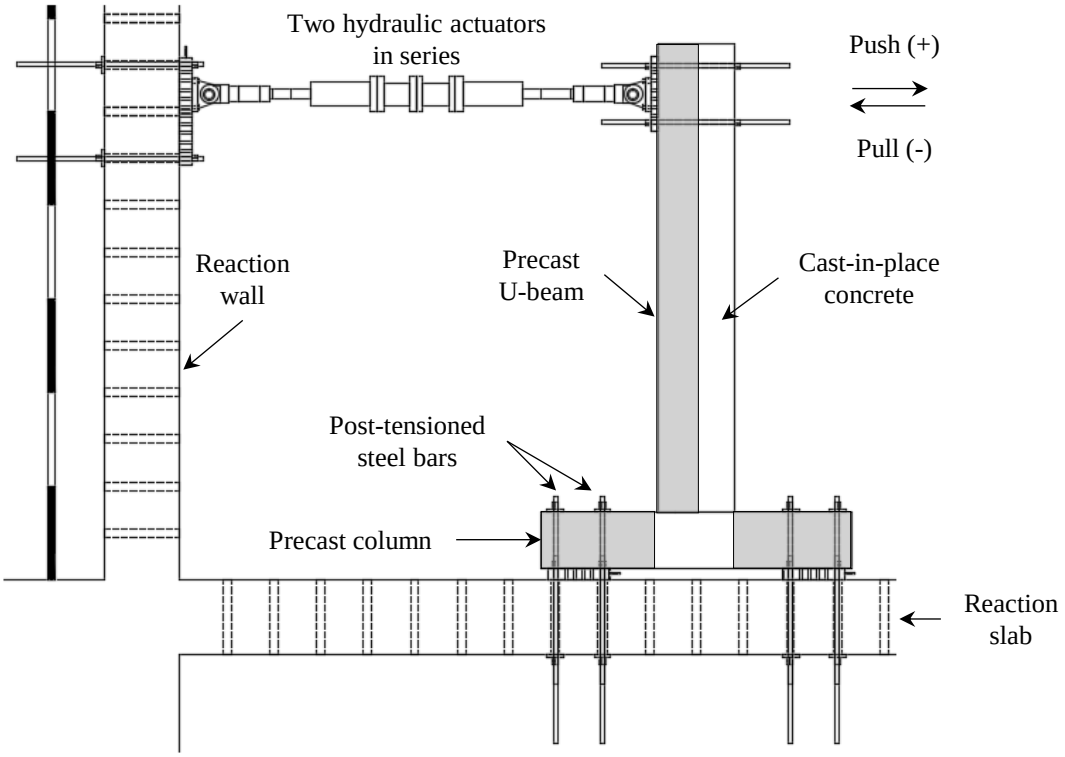

Figure 4-3. Test setup.

4.3.3 Loading protocol

A displacement-controlled loading protocol was developed for the experimental program. The same protocol, shown in Figure 4-4, was applied to all specimens. The equivalent drift ratios are shown as percentages. The loading protocol was developed according to the recommendations by ACI 374.2 [64], which consisted of two cycles for each target displacement followed by one cycle at 50% of the immediately preceding displacement.

The drift ratio was calculated as the relationship between the horizontal displacement of the beam at the load point and the distance from the column centerline to the load point. FEMA P-795 [65] defines the component's displacement or drift capacity as that to a strength decay of 20%. However, ACI 374.2 [64] indicates that this criterion should not necessarily be adopted as the definition of collapse. In this study, failure was defined as the point when a decay of 25% of the specimen's maximum load-carrying capacity was reached, as indicated in ACI 374.1 [18]. This criterion was adopted to be consistent with the tests carried out in Chapters 5 and 6.

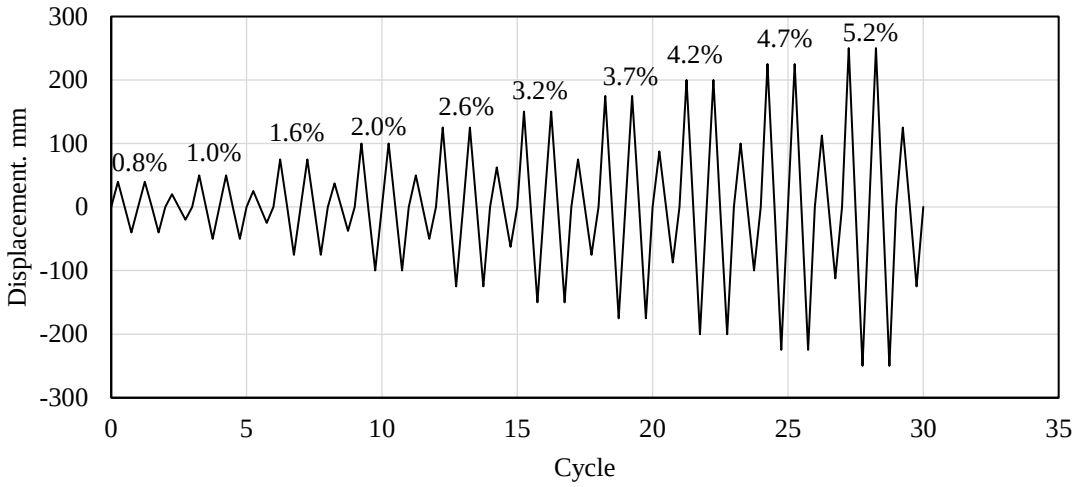

Figure 4-4. Loading protocol.

4.3.4 Instrumentation

Specimens were instrumented with linear variable differential transducers (LVDTs) to assess local displacements. As shown in Figure 4-5, horizontal LVDTs (H1-H5) were placed along the beam's length to measure horizontal displacements (see Figure 4-5a). Diagonal LVDTs were placed on the lateral face of the beam (D1-D6) and in the joint area (D7 and D8) to measure shear deformations (see Figure 4-5b). Test specimens were also instrumented with strain gauges (SGs) on longitudinal and transverse reinforcement. However, rebar strains are not discussed in this chapter.

4.4 Results

4.4.1 Failure modes and observed damage

The damage presented by the specimens at a drift close to 3% is shown in Figure 4-6. The failure modes of the four specimens were similar, mainly by flexure. Specimen P-UB-1 (300 mm stirrup spacing) exhibited severe damage on the cast-in-place portion of the beam with rebar buckling, significant flexural and shear cracking, and concrete crushing and spalling. Damage on the precast U-beams was less severe. The precast U-beam itself functioned as a confining element of the longitudinal rebars. Similar observations can be made of P-UB-2 (150 mm strirrup spacing).

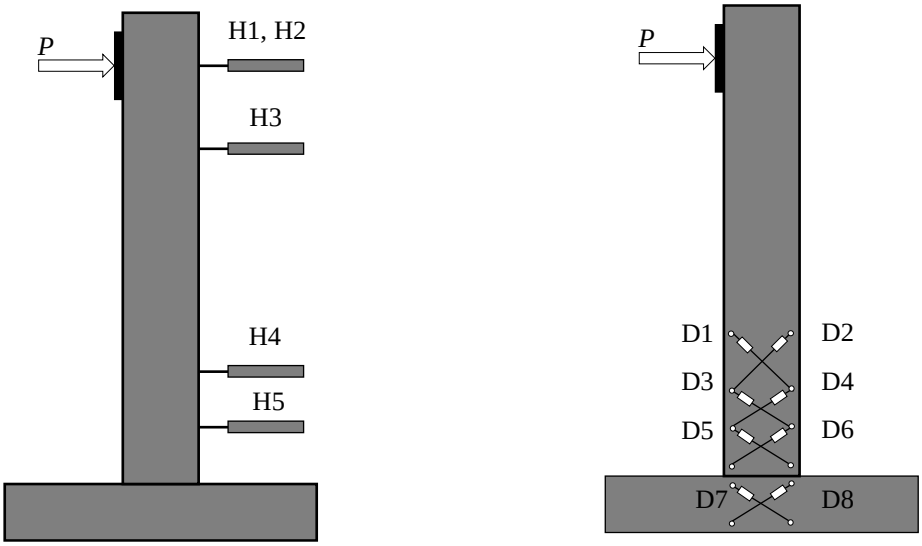

a) Horizontal LVDTs b) Diagonal LVDTs

Figure 4-5. Instrumentation of the beam-column specimens.

In contrast, specimen P-UB-3 performed excellently, with the beam exhibiting similar flexural cracking but less damage due to shear. This is because specimen P-UB-3 had the closest stirrup spacing of the three (75 mm). Also, the reduced level of damage is explained by the concentration of the plastic deformation of the longitudinal beam reinforcement at the beam-column interface, where a cold joint was formed. In precast construction, in the regions where precast concrete is joined to cast-in-place concrete, an unintentional crack is often formed at the interface of both concretes; therefore, it is logical to see inelastic concentration in that region.

Specimen P-COR-1 exhibited significant damage on the beam and corbel. Vertical cracks were formed on the lateral faces of the beam at the interface where the precast beam met the cast-in-place concrete (see Figure 4-7). At first sight, they could be caused by a lack of adherence between the two types of concrete. Unfortunately, the test was concluded prematurely, so it was impossible to corroborate this inference. Concrete crushing was also observed at the beam-column interface, where the precast section of the beam was not attached to the column by a wet joint. In the beam, there was also cover concrete spalling where the corbel ends due to the high compressive stresses in that area. Similarly, the corbel cover concrete also detached, but no significant damage was observed in the interior of the

corbel. Also, one of the welded rebars inside the beam fractured at a drift close to 2.6% (see Figure 4-7).

a) P-UB-1

b) P-UB-2

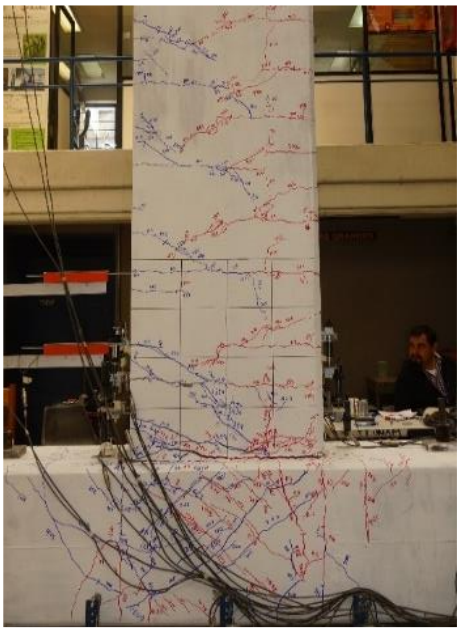

c) P-UB-3

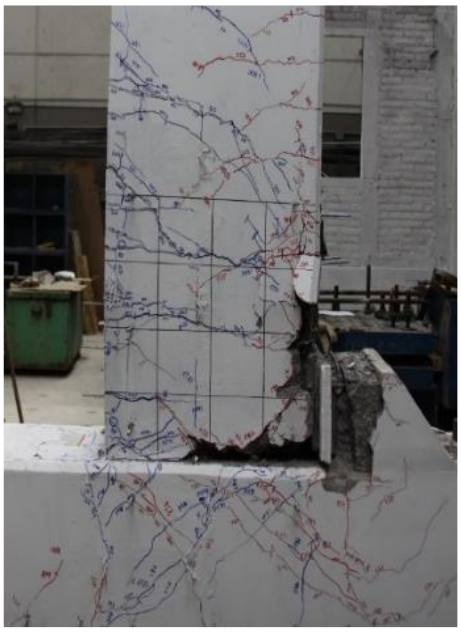

d) P-COR-1

Figure 4-6. Damage at drifts close to 3%.

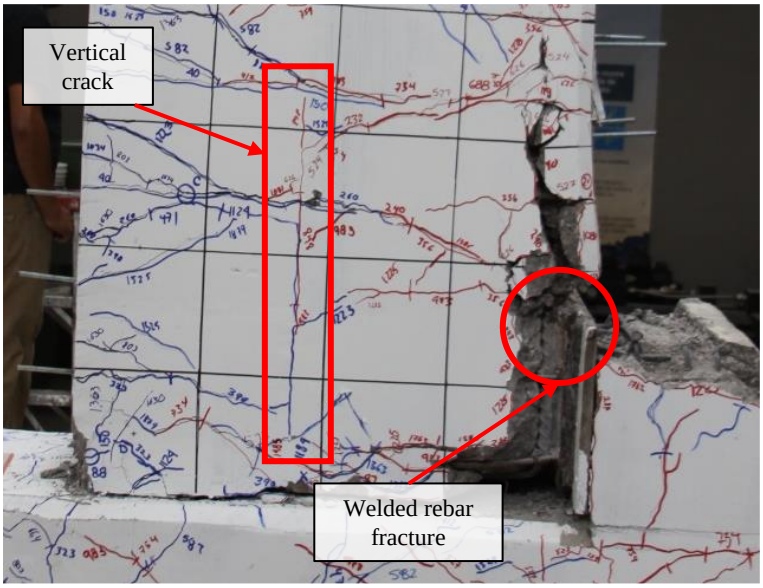

Figure 4-7. Damage on specimen P-COR-1.

4.4.2 Hysteresis curves

The measured moment-drift ratio curves are shown in Figure 4-8. The beam moments were obtained by multiplying the measured load at the tip of the beam by the lever arm. The drift ratio was obtained as the ratio between the lateral displacement of the beam at the height of the load application and the distance from this load point to the column centerline. The backbone curves are also shown in red. The calculated ultimate moment, $M_{u,c}$, is shown with dashed lines. The calculated strengths were based on the actual material properties of the steel and concrete. A factor of 1.25 was applied to the nominal yield stress, f_y, of 412 MPa to account for strain hardening, as recommended by [59].

Specimens P-UB-1 and P-UB-2 showed good hysteretic behavior with broad and stable loops. Some pinching behavior was observed, especially at higher drift demands. All specimens developed their predicted flexural strengths; however, the U-beam specimens did not show a significant increase in their flexural strengths after yielding. Rather, loads remained almost constant up to the final stages of the tests. In contrast, specimen P-COR-1 showed significant overstrength. The maximum measured moments and the calculated ultimate moments are shown in Table 4-2. For the U-beam specimens, it can be seen that the maximum experimental moment was between 1.02 and 1.07 times the calculated flexural

strength for the U-beam specimens. The average overstrength developed by specimen P-COR-1 was 1.28, closer to the overstrength developed by the cast-in-place specimens studied in Chapter 3.

Specimen P-UB-3 reached the failure criteria around 4.0% drift in the pull direction. The failure was due to one of the #12 longitudinal rebars fracturing prematurely. This occurred due to a manufacturing error since the top reinforcement was bent with a smaller radius than the minimum specified by the standard [41]. After this point, specimen P-UB-3 lost its load-carrying capacity drastically for negative bending, while for positive bending, the specimen could sustain its strength up to a 4.0% drift.

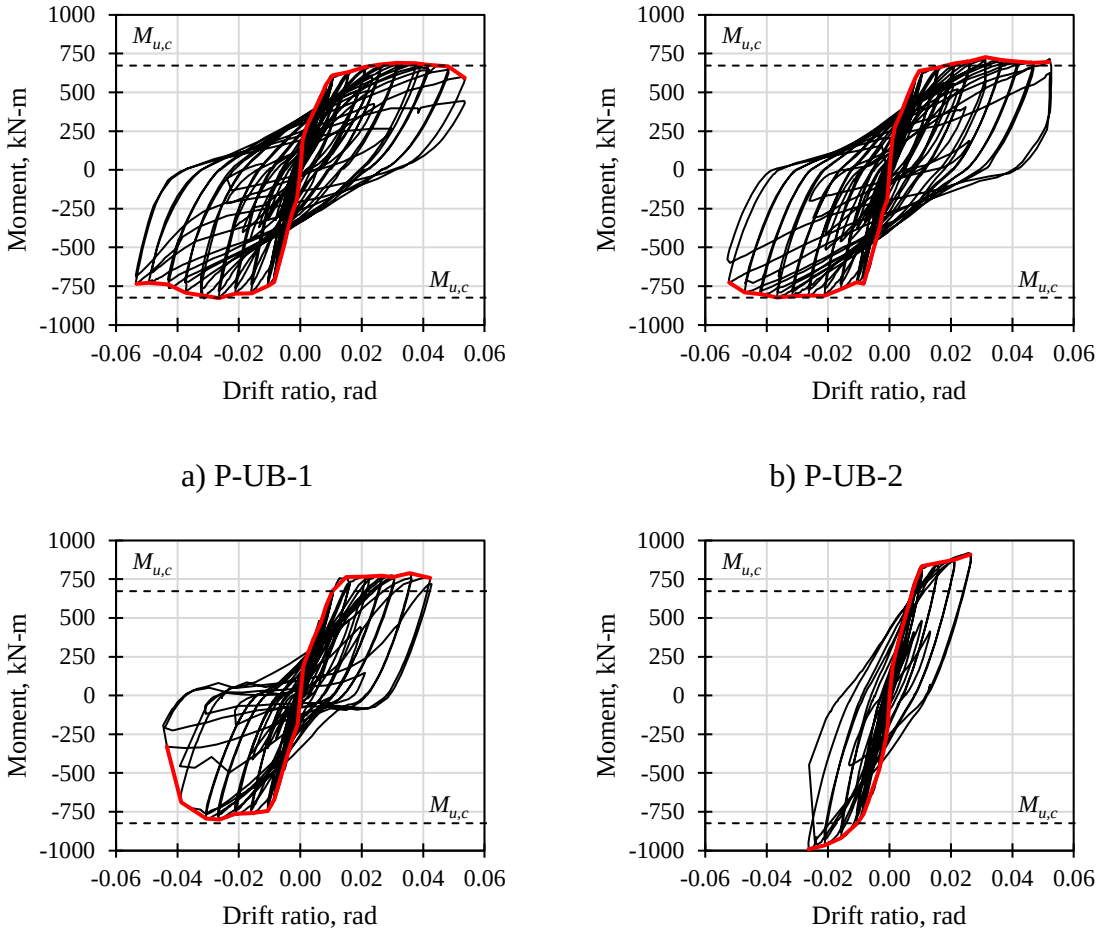

a) P-UB-1

b) P-UB-2

c) P-UB-3

d) P-COR-1

Figure 4-8. Moment-rotation curves.

Specimen P-COR-1 failed abruptly due to fracturing of one of the welded rebars inside the beam at a drift close to 2.6% (see Figure 4-7).

Table 4-2. Comparison of flexural strengths.

Specimen	Direction	$M_{u,exp}$ (kN-m)	$M_{u,c}$ (kN-m)	$M_{u,exp}$ / $M_{c,u}$ (average)
P-UB-1	(+)	690	673	1.02
	(-)	829	824	
P-UB-2	(+)	727	673	1.04
	(-)	827	824	
P-UB-3	(+)	788	673	1.07
	(-)	801	824	
P-COR-1	(+)	919	673	1.28
	(-)	991	824	

In Figure 4-9, a comparison of the backbone curves is shown. All specimens displayed similar initial stiffnesses. Regarding load-carrying capacity, the U-beam specimens behaved similarly, maintaining their strength almost constant up to the end of the tests. The cracking moment, M_{cr}, considering a modulus of rupture (f_r) equal to $0.63\sqrt{f_c'}$ [41] and gross section properties, is also shown. This was normalized to the calculated ultimate moment ($M_{u,c}$). The theoretical M_{cr} was around $0.34M_{u,c}$ in the positive direction and $0.28M_{u,c}$ in the negative direction, both with a corresponding drift ratio of 0.05%. The difference in the cracking moment ratios is due to the different flexural strengths in the push and pull directions. Graphically, it can be seen that the change in stiffness due to crack initiation could be accurately predicted.

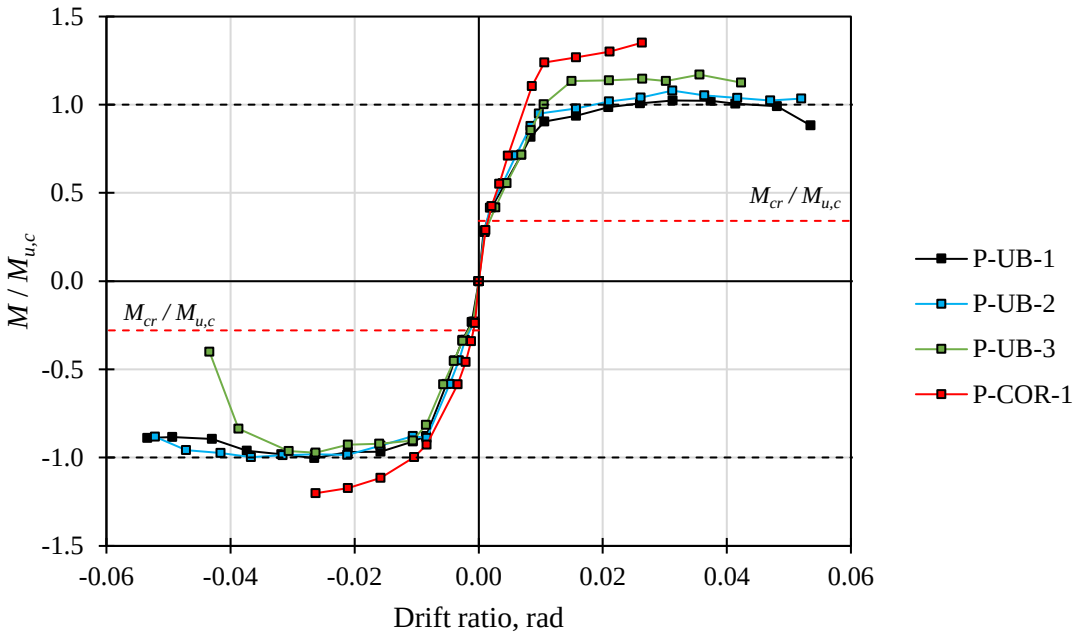

Figure 4-9. Comparison of backbone curves.

The yield drifts (θ_y), ultimate drifts (θ_u), and global ductility ratios (μ) are listed in Table 4-3. As mentioned, the main difference between the U-beam specimens was the stirrup spacing. Specimens P-UB-1 and P-UB-2 developed similar ductility ratios. In contrast, specimen P-UB-3, which had stirrups at 75 mm, presented a ductility ratio significantly lower than the other two, mainly due to the manufacturing defect explained above.

Specimen P-COR-1 developed the lowest ductility ratio. This was expected since the welded corbel system has been deemed to be less ductile than other cast-in-place and precast systems by some researchers and practicing engineers. However, it can be considered for use in low to moderate seismic regions because it is still a practical solution for precasters, and its lack of ductility can be solved with better capacity design concepts. Relocation of the plastic hinge should also be considered. Eom et al. [11] present various methods for relocating the plastic hinge away from the connection in precast frames. An example is shown in Chapter 2. Unbonding the longitudinal reinforcement over a certain length adjacent to where the welded connection starts is also an alternative that has been explored with successful results recently by Girgin et al. [77].

Table 4-3. Global ductility ratios.

Specimen	Direction	θ_y (rad)	θ_u (rad)	μ (average)
P-UB-1	(+)	0.7	5.4	7.2
	(-)	0.8	5.3	
P-UB-2	(+)	0.8	5.2	7.0
	(-)	0.7	5.2	
P-UB-3	(+)	1.0	4.2	4.1
	(-)	1.0	3.9	
P-COR-1	(+)	0.8	2.6	3.6
	(-)	0.7	2.6	

4.4.3 Ductility and energy dissipation

The energy dissipation capacity of the specimens was evaluated using two different concepts. First, the relative energy dissipation ratio (β_i) was assessed as described in [18]. Second, the cumulative ductility ratio, which considers the specimens' structural characteristics, was obtained. The former concept is addressed first.

The relative energy dissipation is the ratio between the area of the hysteresis loop in interest and the idealized area of the parallelogram defined by the initial stiffness during the first cycle of the test and the maximum load during the cycle for which the energy dissipation is calculated:

$$\beta_i = \frac{A_h}{(P_1 + P_2)(\theta'_1 + \theta'_2)} \tag{4-1}$$

where A_h is the area of the hysteretic loop, P_1 and P_2 are the maximum loads, and θ'_1 and θ'_2 are the inelastic drift ratios in both directions.

The relative energy dissipation ratios of the tested specimens are shown in Figure 4-10. The reported values correspond to the second cycle of each target displacement. Specimen P-COR-1 exhibited less deformation capacity than the other specimens but still had a relative energy dissipation ratio close to 40%. For specimens, P-UB-1 and P-UB-2, the developed energy dissipation ratio peaked at around 40%, just above 0.035 drift ratio. After that, their energy dissipation capacity consistently dropped to the ultimate drift ratio. Due to its

manufacturing defect and premature failure, specimen P-UB-3 had the smallest maximum ratio of 31%.

According to ACI 374.1 [18], the relative energy dissipation ratio must not be less than 12.5% for the third cycle at a drift ratio of 0.035. This value is shown only for reference since none of the precast specimens were tested using the loading protocol based on ACI 374.1 [18]. However, the tests carried out on the proposed innovative precast beam-column connections in Chapters 5 and 6 were evaluated with this criteria, and it is worth noting that none of the conventional precast connections dropped below the 12.5% threshold.

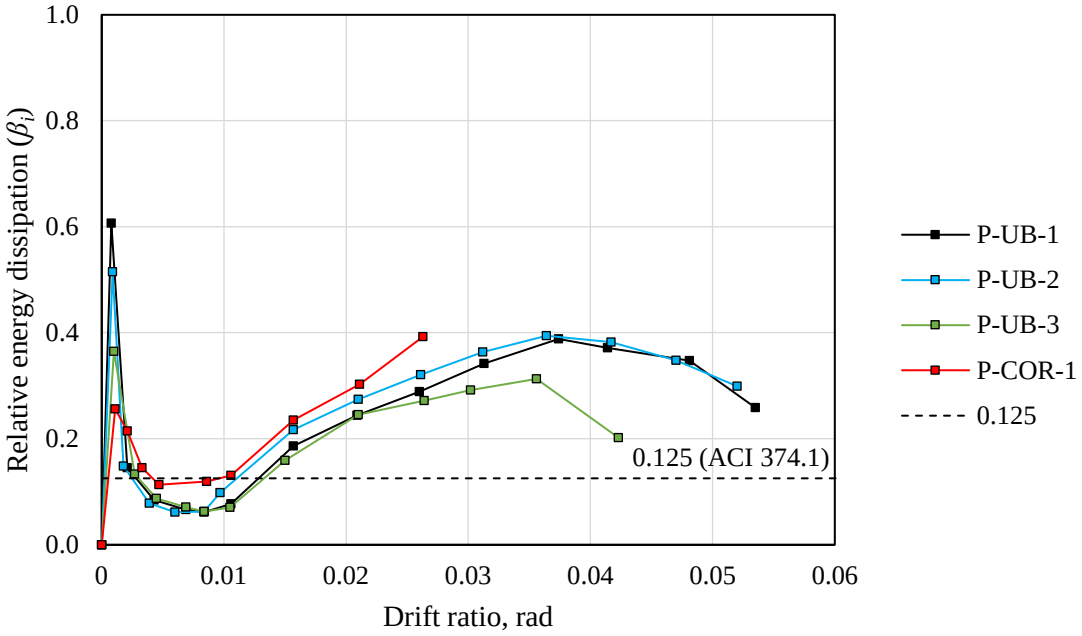

Figure 4-10. Relative energy dissipation ratio.

The cumulative ductility ratio, as defined by Teran et al. [66], was obtained as follows:

$$NE_{H,\mu} = \frac{E_{H,\mu}}{P_y \delta_y} \tag{4-2}$$

where $E_{H,\mu}$ is the accumulated plastic energy, and P_y y δ_y are the load and the displacement at yield, respectively.

The cumulative ductility ratio is shown in Figure 4-11. Specimens P-UB-1 and P-UB-2 were able to reach higher values than specimen P-UB-3. The latter specimen performed poorly because it developed a yield load similar to the other U-beam specimens but at a much larger yield displacement. Specimen P-COR-1 showed good performance up until failure. It was able to dissipate similar amounts of plastic energy as specimens P-UB-1 and P-UB-2; however, it accumulated far less displacements than the former due to its less ductile nature.

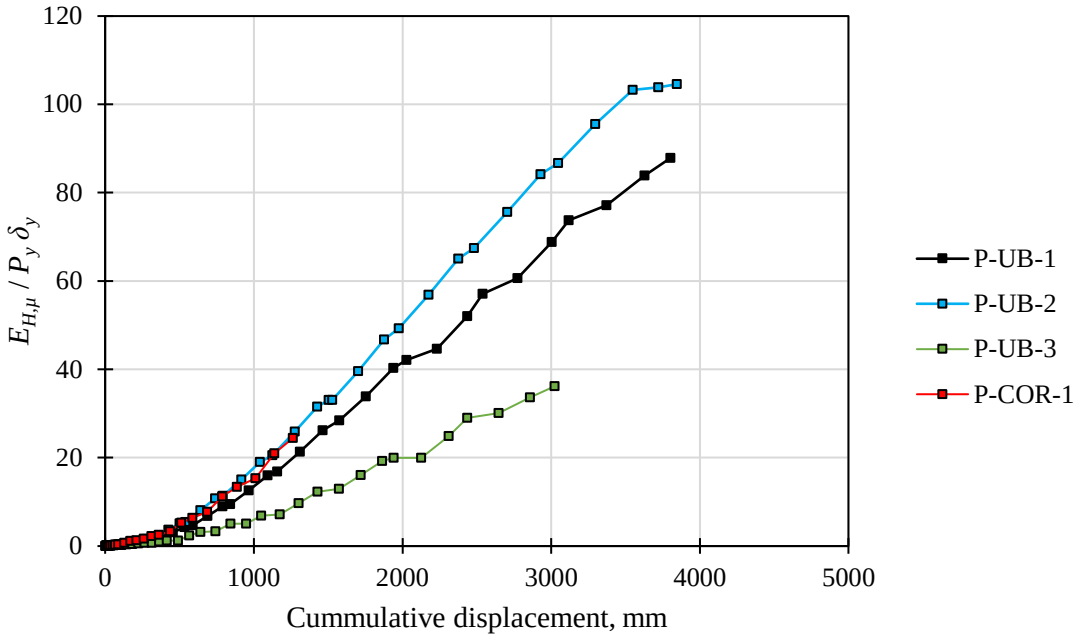

Figure 4-11. Cumulative ductility ratio.

4.4.4 Equivalent viscous damping

The equivalent viscous damping ratio, ζ_{eq}, can be obtained by equating the measured energy dissipated per cycle (E_D) under an experimental load cycle with that of an equivalent viscously damped one-degree-of-freedom oscillator, as follows [67]:

$$\zeta_{eq} = \frac{1}{4\pi}\frac{E_D}{E_{S0}} \tag{4-3}$$

where E_D is the measured energy dissipated per cycle, and E_{S0} is the straining energy stored in an elastic mass-spring oscillator.

The equivalent viscous damping ratios are plotted against the ductility ratios in Figure 4-12a. Before yielding, i.e. for ductility ratios below 1, the specimens dissipated small amounts of hysteretic energy, equivalent to damping ratios between 5% and 10%. It is recalled that this was also observed for the cast-in-place specimens studied in Chapter 3.

Damping ratios increased as the deformation increased, as expected. The maximum damping ratios reached values close to 25%. After yielding, damping ratios for all specimens increased similarly up to approximately 20%, at around μ = 3.5. After that, specimen P-UB-3 dropped off significantly due to its premature and abrupt failure. Specimen P-COR-1 behaved similarly to the U-beam specimens but only reached a ductility ratio close to 3.6.

In Figure 4-12b, the equivalent viscous damping is plotted against the normalized effective stiffness. In this graph, each point represents a feasible damping ratio for a given effective stiffness. Similarly to the cast-in-place specimens studied in Chapter 3, the damping ratios vary approximately linearly and inversely proportional to the effective stiffness, i.e., the effective stiffness decreases as the specimens undergo larger deformations.

As a reference, the cast-in-place (CIP) values from Chapter 3 are also shown in the graph. It is clear that all the specimens behave similarly. Thus, an equivalent viscous damping model is proposed, namely:

$$\zeta_{eq} = -a\frac{k_{eff}}{K_{i,ex}} + b \tag{4-4}$$

where $k_{eff}/K_{i,ex}$ is the effective stiffness normalized with respect to the initial stiffness of the specimen, and a and b are constant values obtained by linear regression analysis, to be 0.32 and 0.28, respectively. The model is shown in Figure 4-13. It will also be compared to the equivalent viscous damping model developed for the innovative precast beam-column connections studied in Chapter 6.

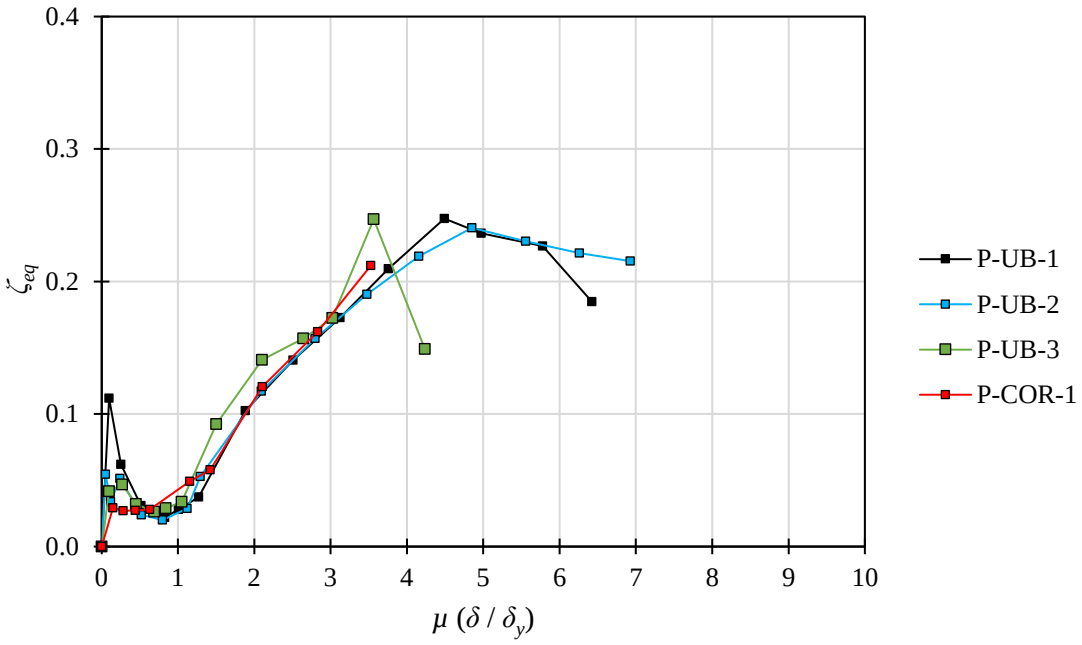

a) Equivalent viscous damping with ductility ratios

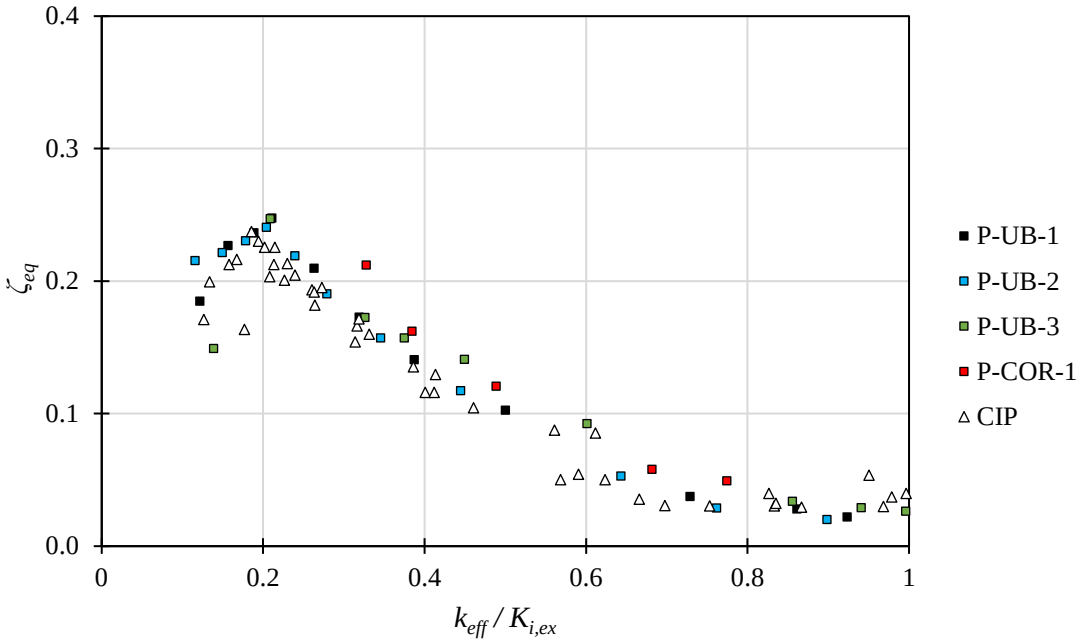

b) Equivalent viscous damping with normalized effective stiffness

Figure 4-12. Equivalent viscous damping.

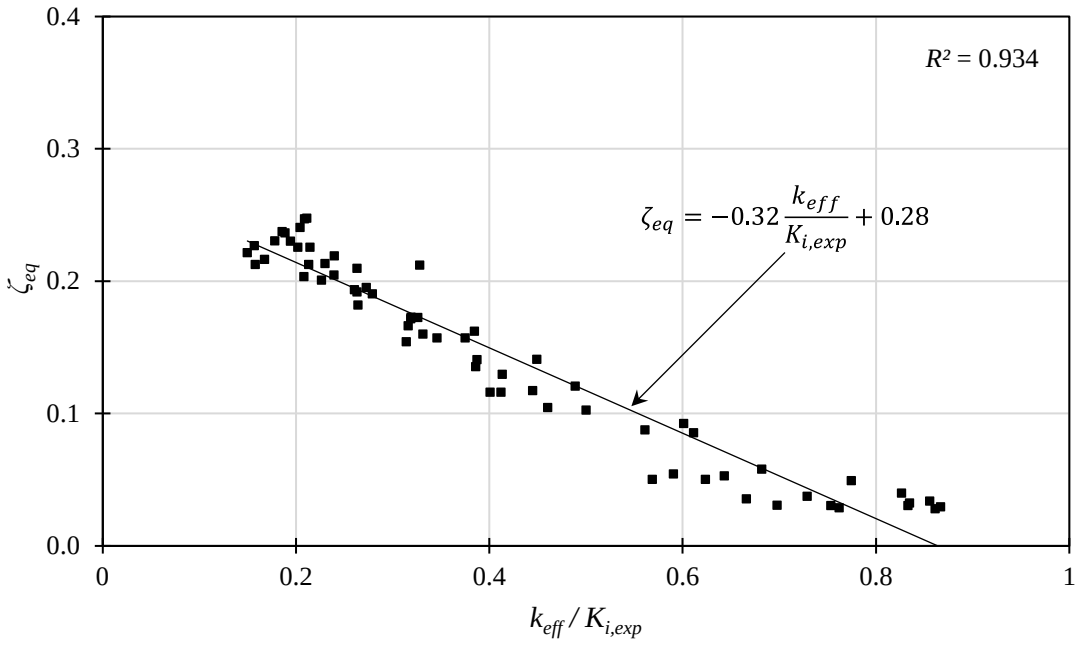

Figure 4-13. Equivalent viscous damping model.

4.5 Conclusions

Four full-scale exterior precast beam-column connections with longitudinal reinforcement ratios of 0.0069 and transverse reinforcement spacinhg of 300,150 and 75 mm were subjected to reversible incremental cyclic loading applied quasi-statically. Three of the specimens were representative of the precast U-beam system, while the fourth specimen was representative of the welded corbel system.

Based on the results of this experimental program, the following conclusions are offered:

1. Hysteresis loops were broad and remained stable throughout most of the tests, except for specimen P-UB-3. The hysteresis loops of the U-beam specimens displayed some pinching behavior, especially at higher drifts. It must be said that the selected longitudinal reinforcement ratios were significantly less than what is commonly used in practice. Experiments with higher reinforcement ratios should be studied.
2. Damage on the joints was minimal.
3. The theoretical ultimate flexural strengths were achieved in all cases, and the load-carrying capacity remained reasonably stable even in the final stages of the tests. The

load at crack initiation was precisely predicted. The overstrength developed by the U-beam specimens was, on average, 1.04. Specimen P-COR-1 developed an average overstrength of 1.28.

4. All precast specimens, except for P-UB-3, dissipated close to 40% of their idealized energy-dissipating capacity, that is, the ratio of the hysteresis loop area to the area of the idealized parallelogram with elastic-perfectly plastic behavior.
5. After a ductility ratio of 3, equivalent viscous damping ratios were above 20% in all cases, with a maximum of 25% developed by specimens P-UB-1 and P-UB-3.

Some key structural characteristics of the tested precast specimens were obtained experimentally and discussed in this chapter. They will be used to assess their cyclic behavior compared to the proposed innovative precast beam-column connections in the following chapters.

5

Experimental Program on Innovative Precast Reinforced Concrete Beam-Column Connections

5.1 Introduction

Precast construction can be classified into two general groups: emulative and non-emulative. Emulative construction uses connections that are designed and detailed to reproduce the behavior of conventional cast-in-place reinforced concrete structures in terms of strength, stiffness, and energy dissipation capacity [10]. Emulative construction is common in practice, and generally does not require special considerations other than those prescribed in codes.

Precast non-emulative construction, however, is not considered in codes (e.g. [40]). In general, emulative precast concrete structures with high ductility, i.e., structures equivalent to special moment frames in [52,78], are not permitted by codes like [40]. This and other restrictions and requirements, as described in Chapter 2, have been present in the MCBC [40] for decades, mostly due to the belief that precast structures are less ductile and have less stable inelastic behavior [4]. The lack of experimental investigations and the poor performance of poorly designed or constructed precast buildings in past seismic events have also contributed to implementing such restrictions and requirements.

The upcoming 2023 MCBC, to be published at the end of this year, is set to adapt the approach of ACI 318-19 [52], mainly that high ductility moment-resisting frames constructed with precast concrete and that do not satisfy certain requirements of the standard, can be used if they satisfy ACI 374.1 [18]. Therefore, it is important to start exploring the use of non-emulative precast systems and assessing their advantages and disadvantages for the precast industry.

The experimental program, described in this chapter, had the objective of showing the behavior of proposed innovative low-damage precast beam-column connections that do not emulate cast-in-place concrete behavior. Rather, all the inelastic behavior is concentrated on steel hysteretic dampers and, therefore, would avoid structural damage to the precast elements (columns ands beams) while being easily replaced if they were damaged during a seismic event.

Three beam-column sub-assemblies were tested. The first consisted of a beam-column connection equipped with a hysteretic damper, made of a steel W-beam, that would dissipate energy through shear deformation of the web. This device is referred to herein as an I-damper. The second is a slightly modified version of the first that addressed some of the complications observed in the first test. Although the second specimen had stable behavior up to a drift ratio of 0.015 rad, it failed abruptly due to capacity design issues. The last specimen took up the concept of energy dissipation through shear deformation of the I-damper. The device was intentionally weakened using a smaller W-beam and making its support more flexible so that the I-damper could deform freely. Additionally, a rotational hinge was made so that the beam could rotate freely and concentrate the inelastic behavior on the device. At small displacements, shear deformation was observed, but at larger displacements, the support of the I-damper exhibited large deformations and was the main mechanism of energy dissipation, which was not the objective.

The experimental program included a fourth beam-column specimen which is described in Chapter 6. The three tests described here did not render the desired results; however, they set the basis for the fourth specimen, which included a slit damper and addressed most of the shortcomings of the first three proposals. The experimental program was then expanded with cyclic tests carried out on eight isolated slit dampers (Chapter 7).

5.2 Experimental Program

The experimental program consisted of three precast beam-column connections equipped with steel hysteretic dampers subjected to cyclic loading applied quasi-statically. The program was based on ACI 374.1 [18] and is described below.

5.2.1 Test specimens

5.2.1.1 Specimen P-ID-1

Specimen P-ID-1, shown in Figure 5-1, is an exterior beam-column connection that represented half the span of the beam (L_b = 2500 mm) and half the height of the column above and below the joint (L_c = 2700 mm) of a moment-resisting frame. Cross sections of the beam and column were, respectively, 300 x 450 mm and 450 x 450 mm. The precast elements were fabricated as individual pieces and connected without needing cast-in-place concrete. The beam was completely separated from the column and connected with welded components. Therefore, the system is non-emulative of cast-in-place concrete behavior.

A steel box was assembled at the end of the beam to facilitate all the necessary connections. Four #8 rebars were welded to the top plate of the steel box and another four to the bottom plate (see Figure 5-2 and Figure 5-3). This gave continuity to the longitudinal reinforcement of the beam to develop its flexural strength since an adequate development length could not be given within the joint or the beam itself. The first stirrup of the beam was located 50 mm from the steel box.

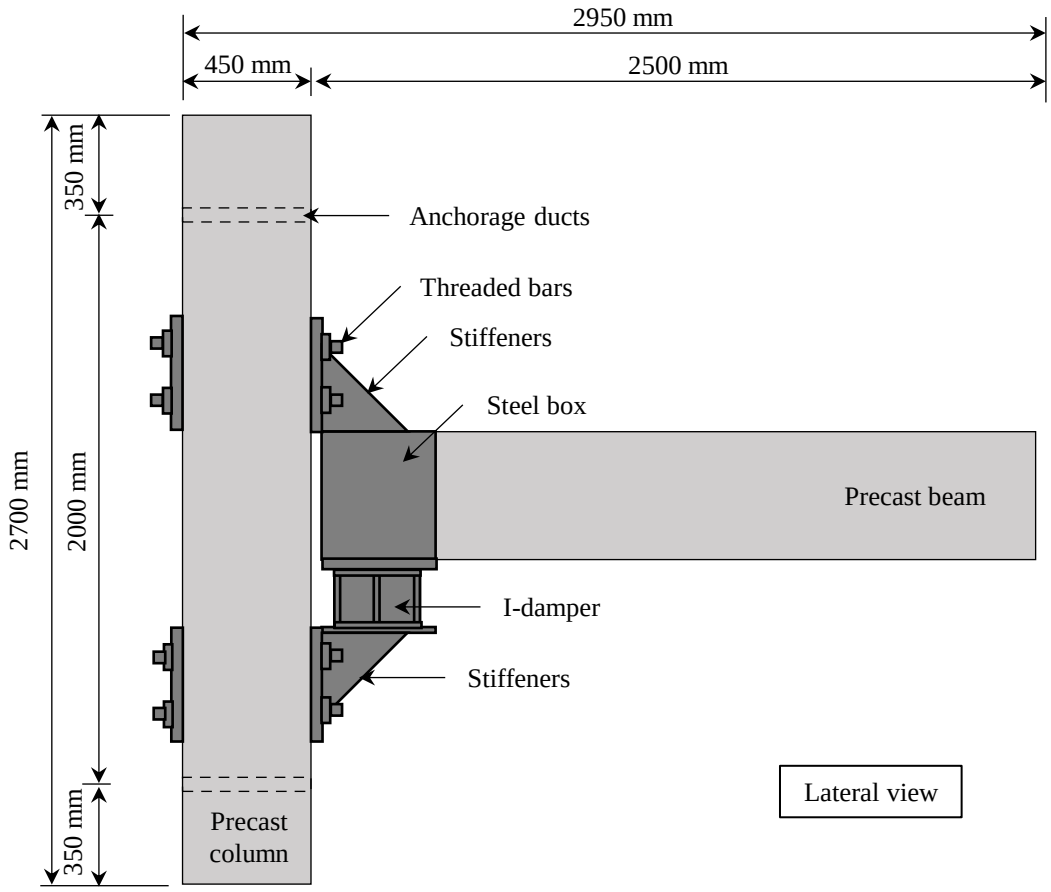

Figure 5-1. Specimen P-ID-1.

The column had two sets of plates, above and below the beam, fastened with six treaded bars. This type of connection is commonly known as a “dumbbell” in Mexico. A grout pad was poured between the plates and the precast column (see Figure 5-3) so that the compressive stresses were distributed uniformly on the column. Two stiffeners were welded to the top dumbbell and the top of the steel box of the beam. These stiffeners were designed to resist the total shear at the column interface. All the different components of the connection are shown in Figure 5-4.

The I-damper was assembled independently with two plates welded to the flanges and stiffeners welded on the I-beam’s web to avoid out-of-plane deformations in that region. The assembled I-damper is shown in Figure 5-5. Once the I-damper was placed below the beam,

two stiffeners were welded to the damper's support plate and the bottom dumbbell connection. A photograph of the connection is shown in Figure 5-6.

Figure 5-2. Steel box and welded longitudinal reinforcement of the beam.

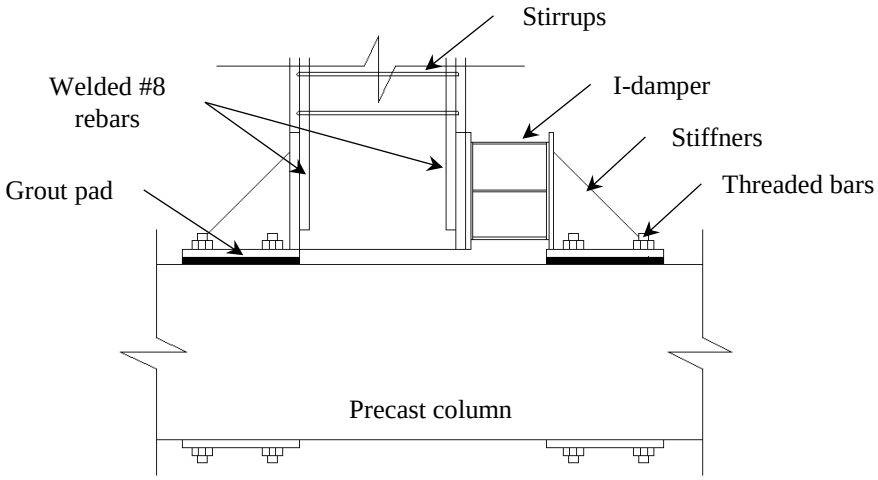

Figure 5-3. Connection details.

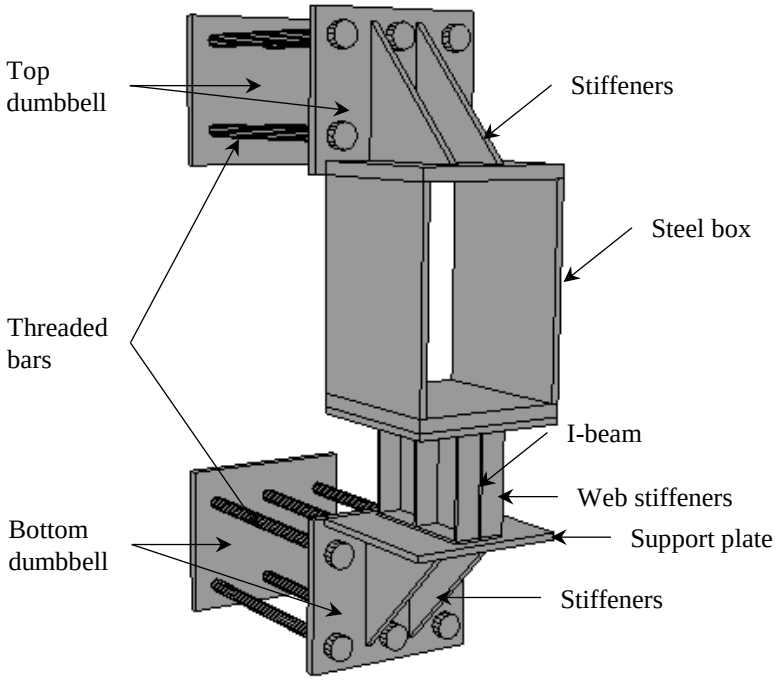

Figure 5-4. Details of the connection and the I-damper.

Figure 5-5. I-damper of specimen P-ID-1.

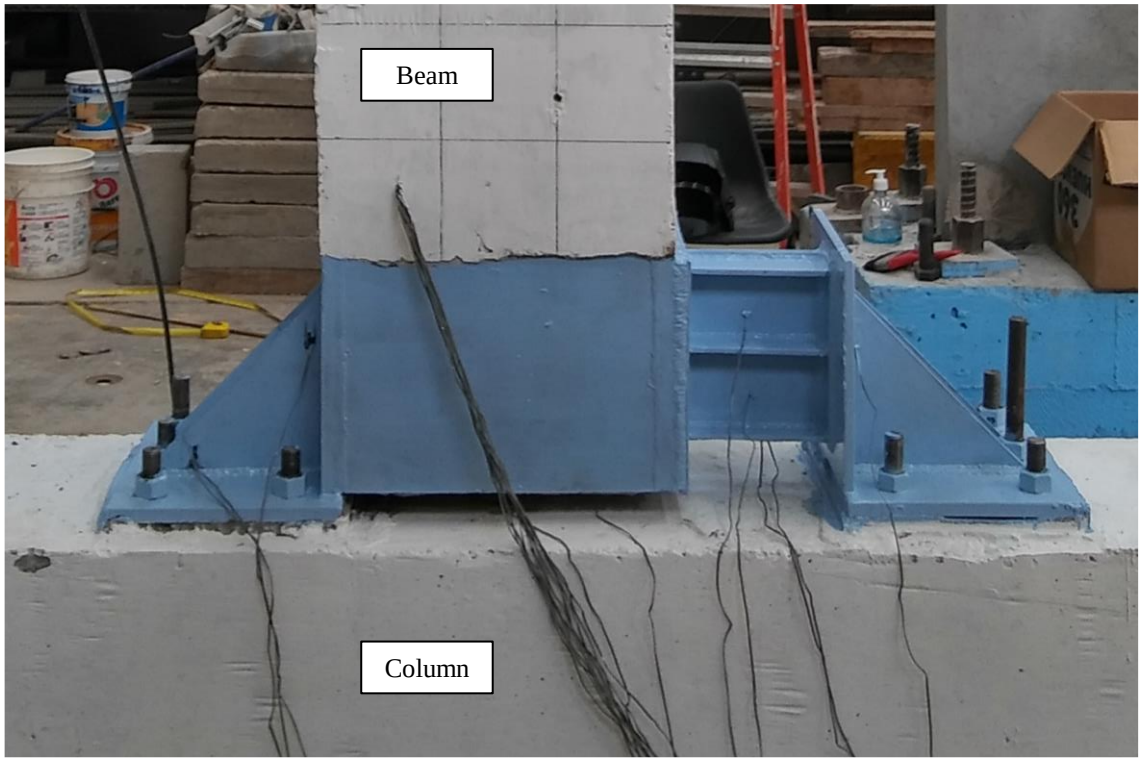

Figure 5-6. Connection of the beam and I-damper to the column of specimen P-ID-1.

5.2.1.2 Specimen P-ID-1M

Specimen P-ID-1M, shown in Figure 5-7, is the same as specimen P-ID-1 except for the fact that the bottom stiffeners which were intentionally weakened to make the support plate more flexible and allow the I-damper to deform in shear. This was done because the welds on the top flange of the I-damper were slowly failing due to the tension forces generated at the beam-damper interface due to the rotation of the beam. Consequently, the test was paused to cut the stiffener plates so that they were more flexible. The cut plates are shown in Figure 5-8.

During the tests, the beam of specimen P-ID-1M failed abruptly at a drift ratio of 0.015. Therefore, a revised version of the beam was constructed for a third test which is described in the following section.

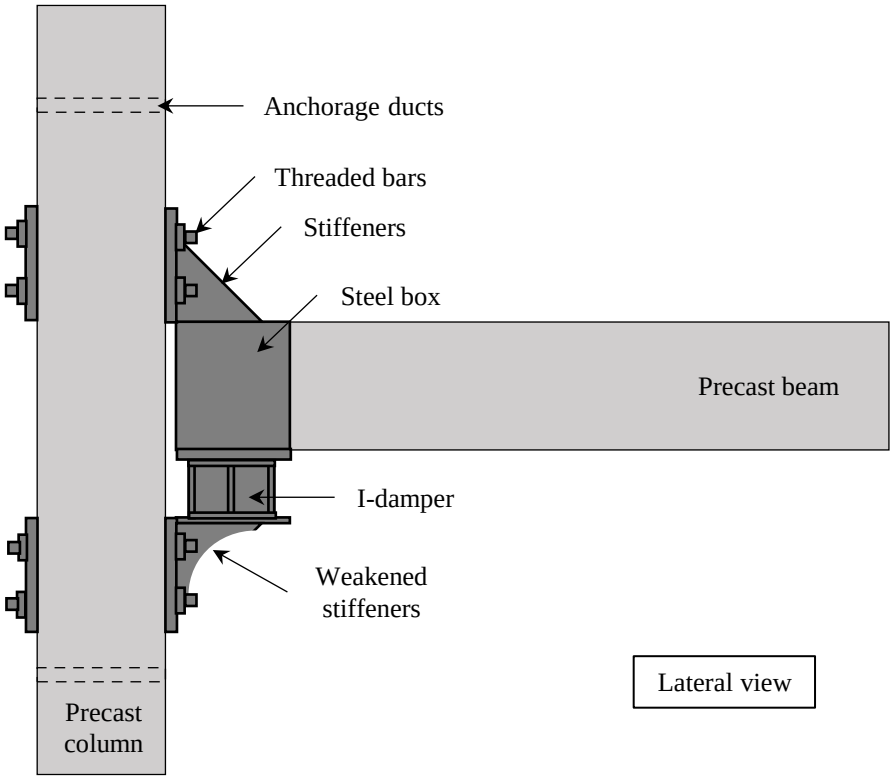

Figure 5-7. Specimen P-ID-1M.

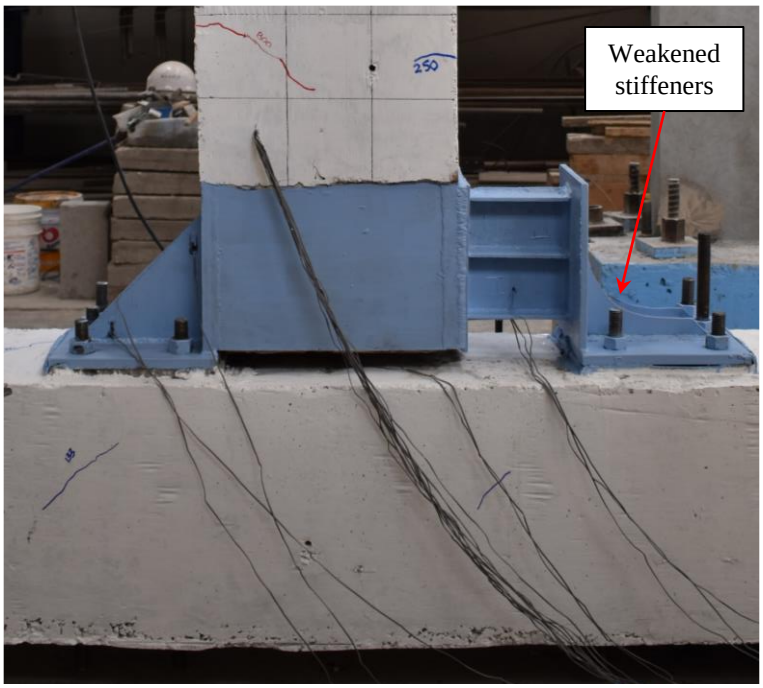

Figure 5-8. Connection of specimen P-ID-1M with weakened stiffeners.

5.2.1.3 Specimen P-ID-2

Specimen P-ID-2, shown in Figure 5-9, was a revised version of the I-damper system. First, the I-damper was made smaller than the previous specimens to ensure its yield before the beam developed its flexural strength.

Second, both sets of stiffeners were eliminated. At the top, the stiffeners were replaced by a rotational hinge that allowed the beam to rotate freely without introducing complex stress states on the beam and the top dumbbell. The rotational hinge was designed to resist the total shear. At the bottom, a horizontal plate without stiffeners, was placed with the intention of transferring moment-induced forces but allowing flexibility at the same time.

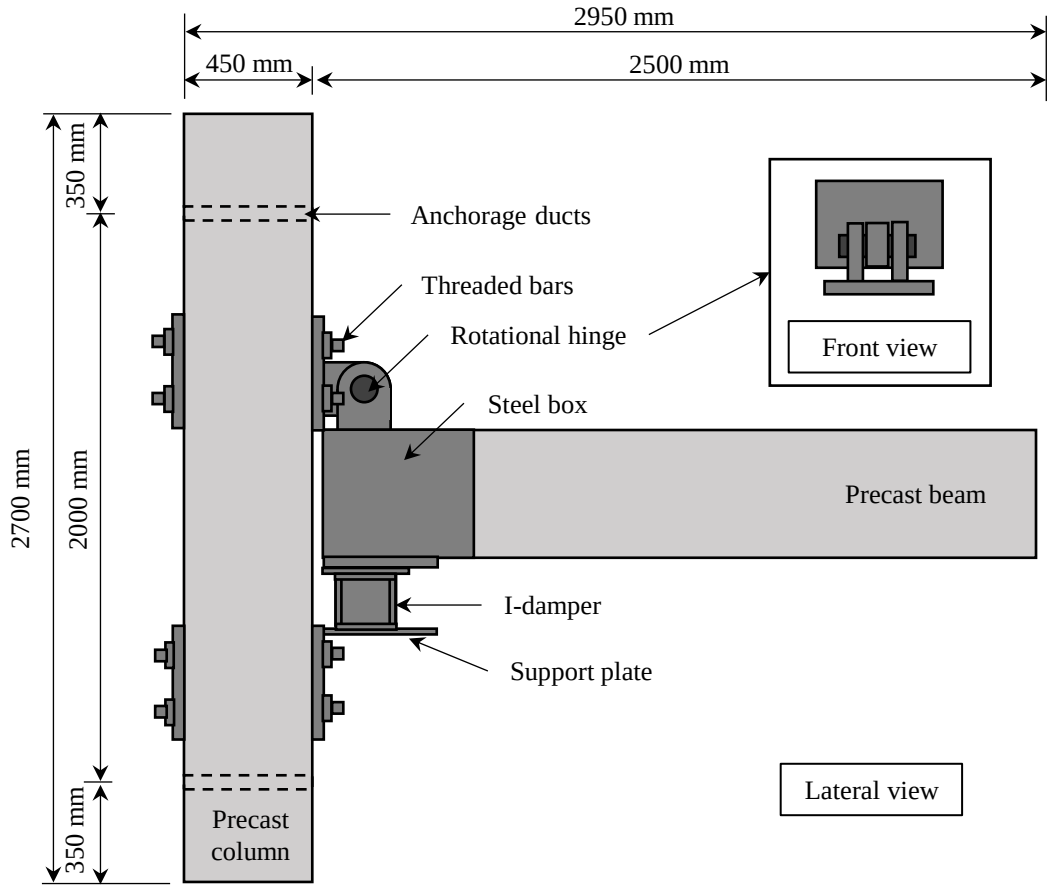

Figure 5-9. Specimen P-ID-2.

The steel box was enlarged to cover approximately 1.5 times the depth of the beam towards the free end of the beam. Also, the welds of the #8 rebars inside the beam were not extended

up to where the steel box ended, i.e. the steel-concrete interface, to not intentionally create a fragile plane at the interface since welding re-crystallizes the steel and decreases its strength and ductility [42,43]. A photograph of the connection of specimen P-ID-2 is shown in Figure 5-10.

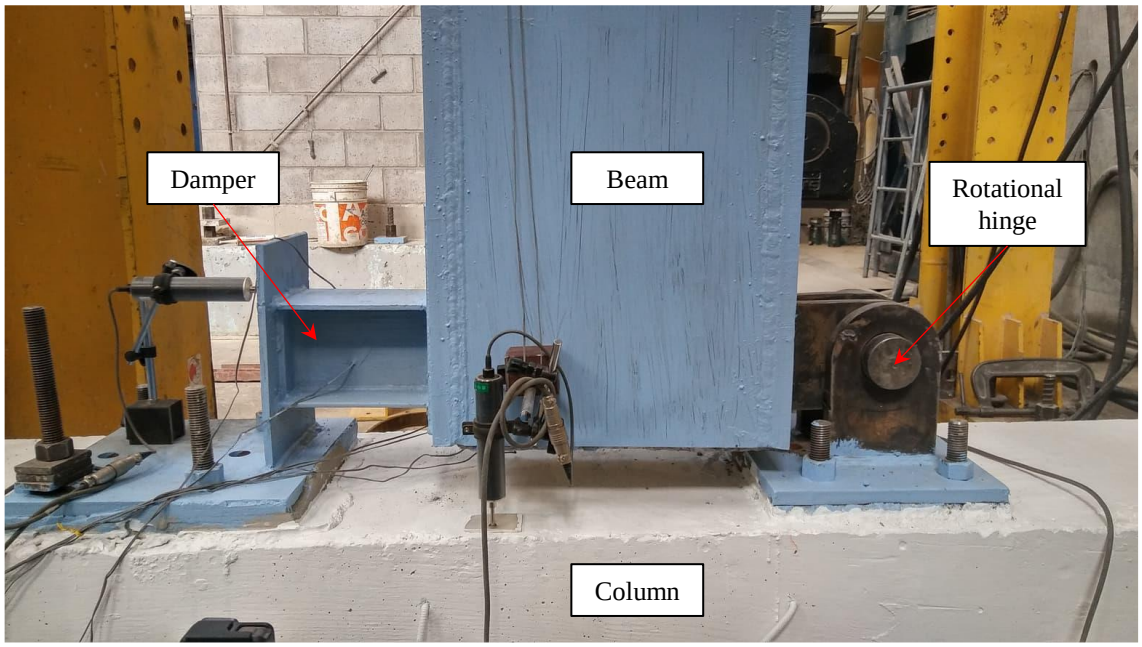

Figure 5-10. I-damper and rotational hinge of Specimen P-ID-2.

5.2.2 Test setup

The three specimens were exterior beam-column connections that represented half the span of the beam and half the height of the column above and below the joint of a moment-resisting frame. It was assumed that the specimen could be isolated this way because the points of zero moment, or inflection points, due to lateral loading, are localized at mid-height of the columns and mid-span of the beams. The columns were connected to the reaction slab at both ends using post-tensioned steel bars, which provided limited rotational restraint simulating a pinned support (see Figure 5-11). Similar configurations can be found in [61,63,79]. The specimen was subjected to a quasi-static cyclic loading protocol applied at the end of the beam with a 1000 kN hydraulic actuator with a ±200 mm stroke. The push direction of the actuator was set as positive and the pull direction as negative. Positive loading was performed first for each cycle. A photograph of the actual test setup is shown in Figure 5-12.

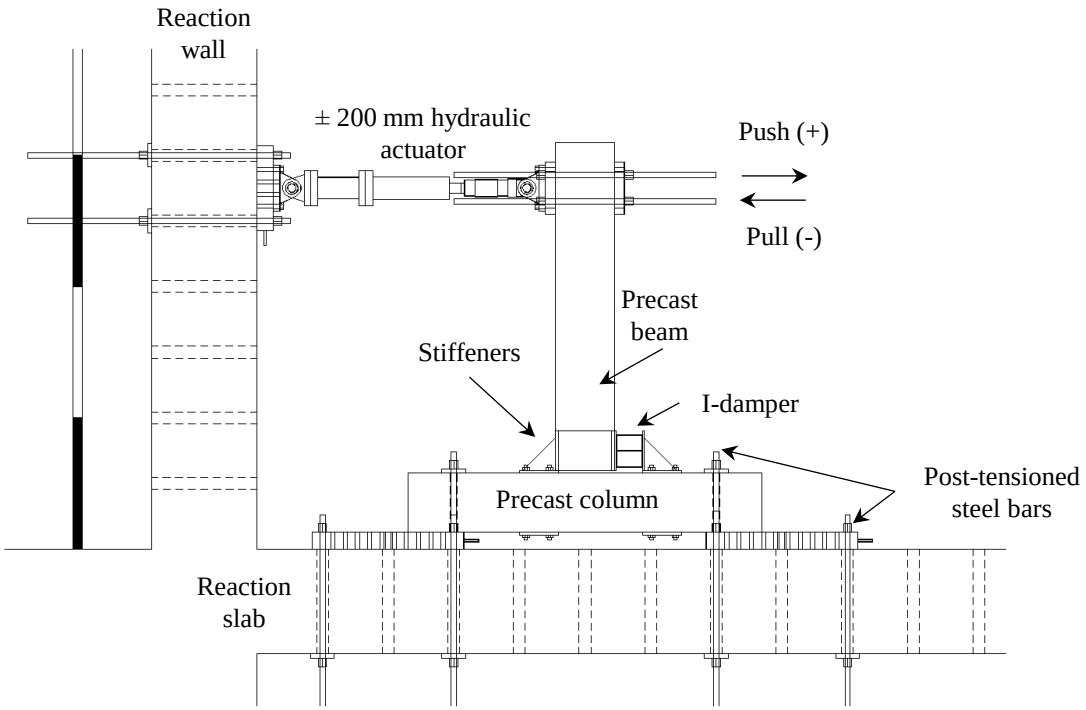

Figure 5-11. Test setup.

a) Northside b) Southside

Figure 5-12. Actual test setup.

5.2.3 Loading protocol

ACI 374.1 [18] defines the minimal experimental evidence necessary for the use, in regions with high seismic risk, of special moment frames constructed using precast concrete and that do not satisfy sections 18.9.2.1 (precast special moment frames with ductile connections) or 18.9.2.2 (special moment frames with strong connections) of ACI 318-19 [52]. Thus, the loading protocol was based on the recommendations of ACI 374.1 [18]. The protocol consisted of three cycles for each target displacement. The initial drift ratio was within the elastic range, followed by increments of no less than 1.25 and no more than 1.5 times the immediately preceding target displacement. The loading protocol is shown in Figure 5-13.

The proposed loading protocol satisfies the minimum requirements of ACI 374.1 [18], which is a minimum target displacement equivalent to a drift ratio of 0.035 rad. Certainly, loading can and must be continued beyond this objective to not only comply with the acceptance criteria of the document but also to study the failure modes of the test specimens. Unfortunately, none of the studied specimens of this chapter were able to reach a drift ratio of 0.035 rad. The premature failure of the specimens is described in the following sections.

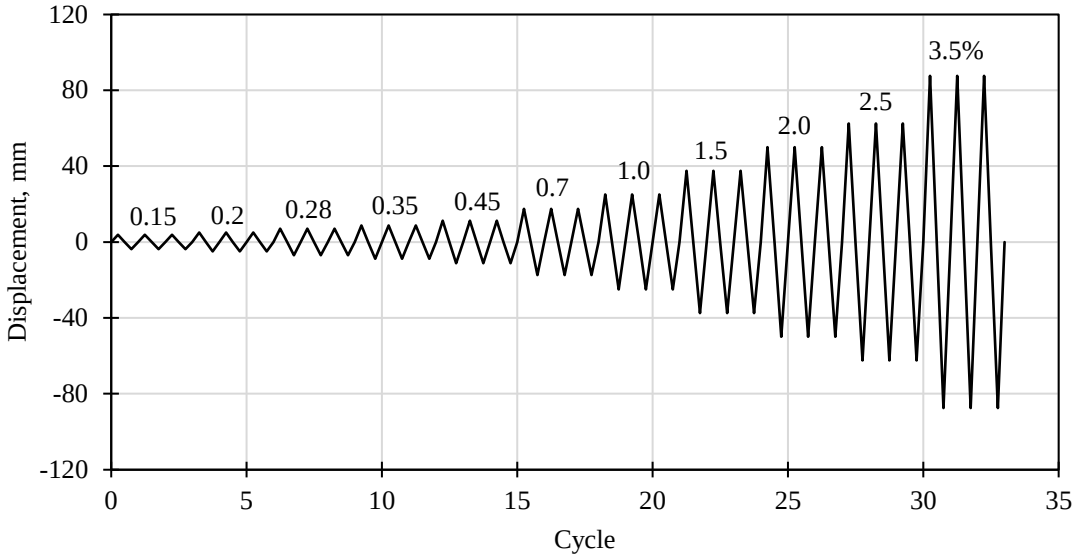

Figure 5-13. Loading protocol.

5.2.4 Instrumentation

5.2.4.1 Specimen P-ID-1

Local displacements were assessed with linear variable differential transducers (LVDTs). As shown in Figure 5-14, two horizontal LVDTs (H1) were placed to measure horizontal beam displacements at actuator height. Vertical displacements of the beam were measured with a vertical LVDT (V3) close to the beam-damper interface.

Diagonal LVDTs (D1 and D2) and vertical LVDTs (V1 and V2) were placed on the beam above the steel box to asses shear deformation in the region. Another two diagonal LVDTs (D3 and D4) were placed on the joint for the same purpose (see Figure 5-14). A photograph of the instrumentation with LVDTs is shown in Figure 5-15.

Reinforcement and structural steel strains were assessed with strain gauges (SGs). Eight SGs (SG-L1 through SG-L-8) were placed on the longitudinal reinforcement of the beam, and two SGs (SG-T1 and SG-T2) on the transverse reinforcement, as shown in Figure 5-16. Another 10 SGs were placed on different components of the connection and damper (see Figure 5-17). Four of them were placed on the damper (SG-D1 through SG-D4); three on stiffeners (SG-D5, SG-D9, and SG-D10); and the remaining three were placed on the steel box (SG-D6 through SG-D8).

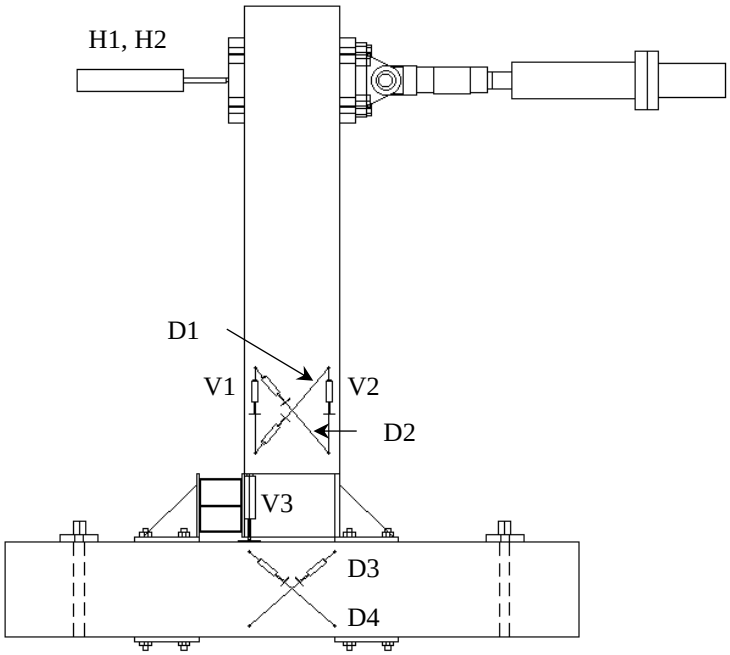

Figure 5-14. Instrumentation with LVDTs (specimen P-ID-1).

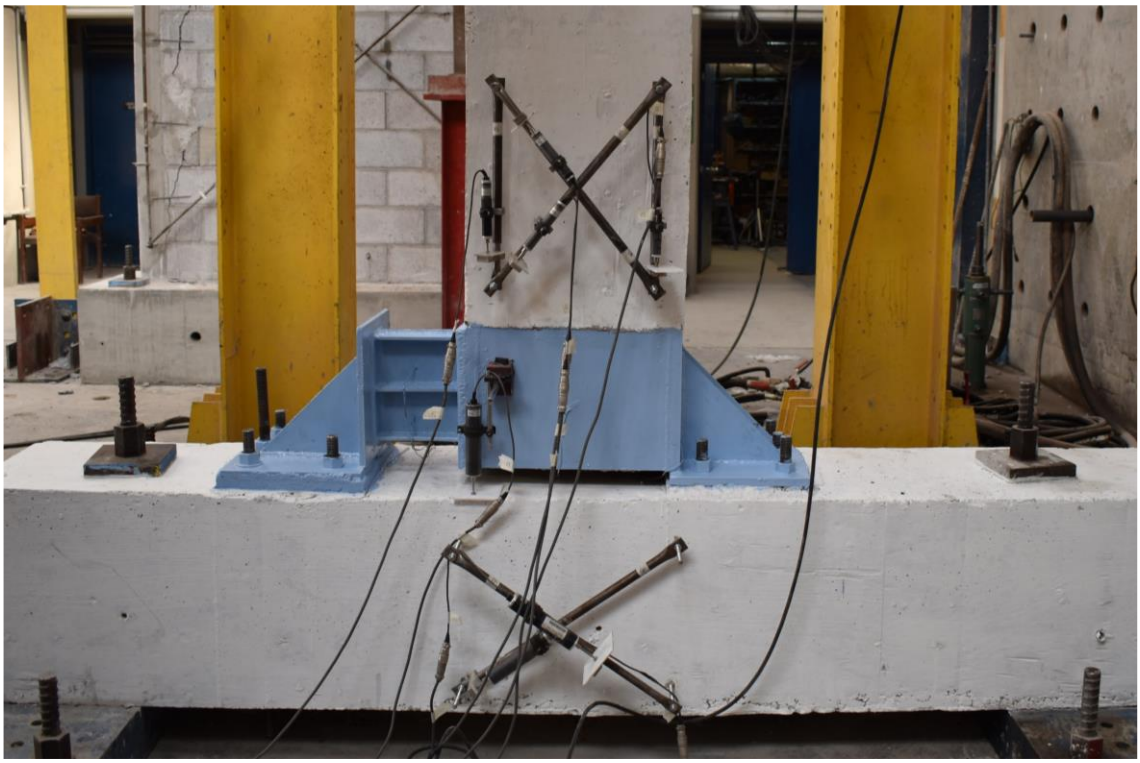

Figure 5-15. Photograph of the instrumentation of specimen P-ID-1.

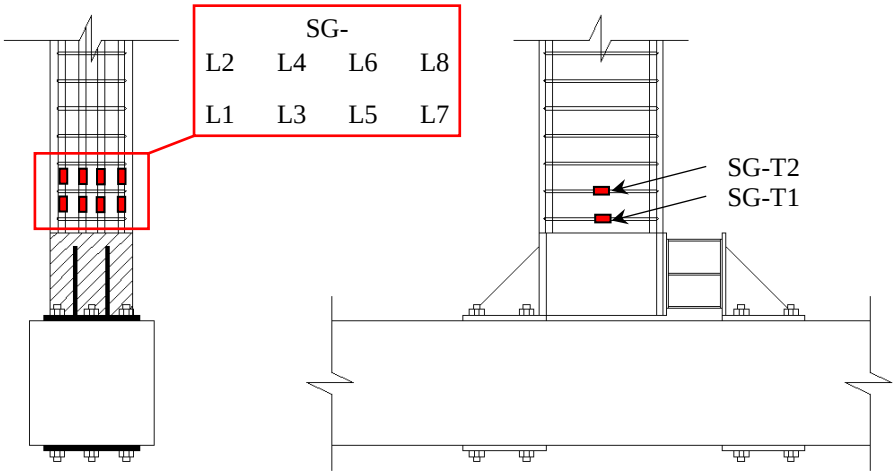

Figure 5-16. Instrumentation with SGs on reinforcing steel (specimen P-ID-1).

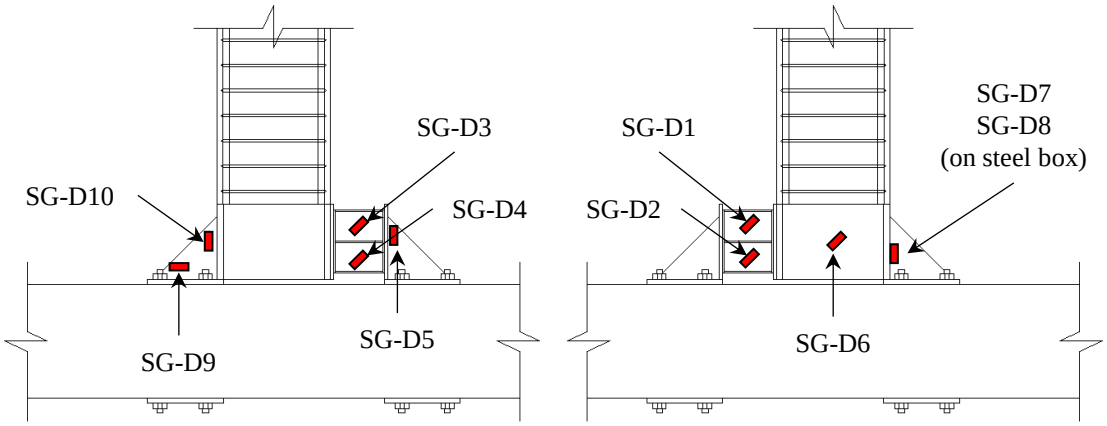

a) Northside b) Southside

Figure 5-17. Instrumentation with SGs structural steel (specimen P-ID-1).

5.2.4.2 Specimen P-ID-1M

The instrumentation of specimen P-ID-1M with LVDTs was the same as specimen P-ID-1. The SGs inside the beam were the same used in the first test. External SGs were basically the same as those shown in Figure 5-17, except between the first test and the second, two SGs (SG-D1 and SG-D5) were lost while the modifications of P-ID-1 were being made.

5.2.4.3 Specimen P-ID-2

The precast beam of specimen P-ID-1M failed beyond repair during the test, so it could not be reused for specimen P-ID-3. Thus, a new precast beam was fabricated, but due to limited resources, this beam could not be instrumented with SGs. Additionally, the external SGs on the connection components were lost. Specimen P-ID-2, therefore, only had the same external instrumentation with LVDTs as the previous tests.

5.3 Results

5.3.1 Failure modes and observed damage

Specimen P-ID-1 was not tested up to failure. The maximum applied drift was approximately 0.75%. Only minor flexural cracks appeared at that stage, as shown in Figure 5-18. Most cracks appeared while positive loads were applied, represented by red lines in Figure 5-18.

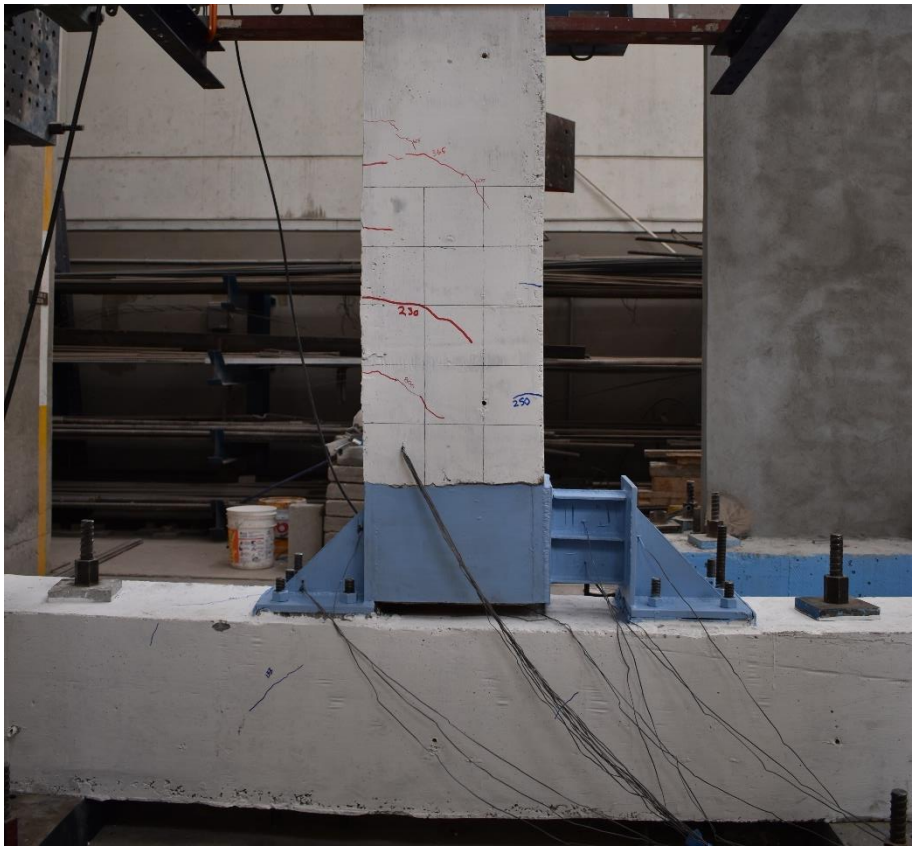

Figure 5-18. Cracking on specimen P-ID-1.

Loading of specimen P-ID-1 was terminated prematurely because the weld that connected the I-damper's flange to the steel box presented a local failure, shown in Figure 5-19. This failure started as a small crack that slowly extended as the target displacements at the beam's tip increased in the pull direction. Eventually, the flange of the I-damper was separated from the beam, as shown in Figure 5-20. The test was paused at that point, and the modifications described above were carried out for the next test.

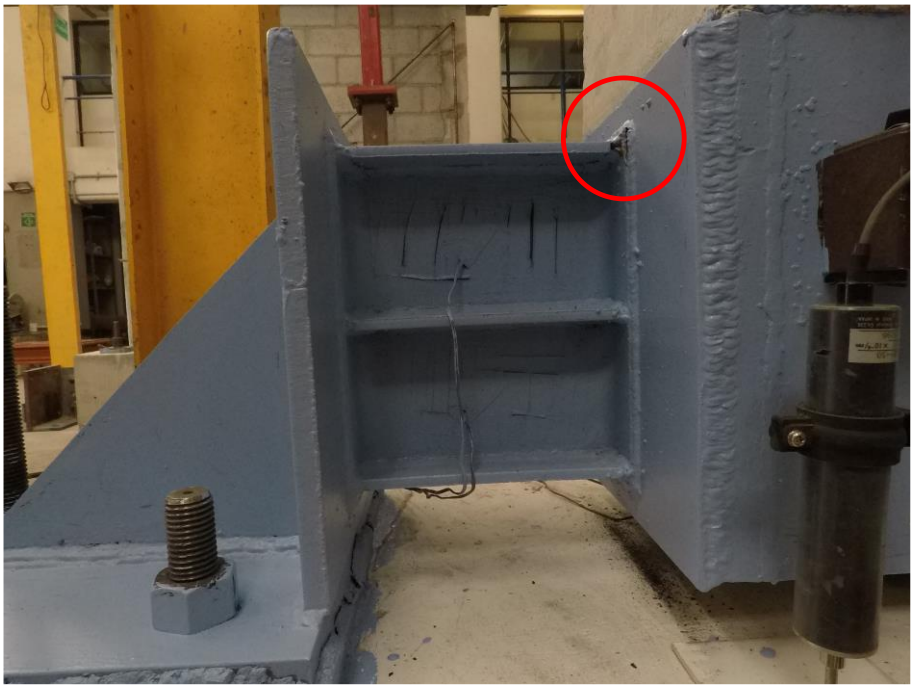

Figure 5-19. Weld failure at beam-damper interface due to tension forces.

Specimen P-ID-1M was similar to P-ID-1 but with more flexible stiffeners below the I-damper's support plate (see Figure 5-8). The specimen displayed a stable cyclic behavior up to 1.5% drift. An abrupt failure due to rebar fracture occurred at approximately 1.8% drift (push direction) while applying the first cycle with a target drift of 2%. The precast beam's top four #8 rebars fractured almost simultaneously at the concrete-steel box interface, as shown in Figure 5-21. Before this, shear deformation of the I-damper could be observed (see Figure 5-22). Failure of the specimen was mainly attributed to capacity design issues. A simple analysis was made to verify this statement as follows.

Figure 5-20. Weld failure at beam-damper interface.

Figure 5-21. Simultaneous fracture of beam rebars of specimen P-ID-1M.

The maximum load that can be applied at the beam's tip can be obtained with the following equation:

$$Q_y = \frac{P_y h_{Id}}{L_{Id}} \quad (5\text{-}1)$$

where the P_y is the load necessary to yield the I-damper in shear, h_{Id} is the distance from the top of the beam to the center height of the I-damper, and L_{id} is the distance from the point of load application at the beam's tip to the center of the I-damper. The maximum load that the beam can resist, at the cross-section where the fracture occurred (at the precast beam-steel box interface), is obtained as follows:

$$Q_b = \frac{M_n}{L_{bc}} \quad (5\text{-}1)$$

where M_n is the nominal flexural strength of the concrete beam, and L_{bc} is the distance from the point of load application to where the steel box starts.

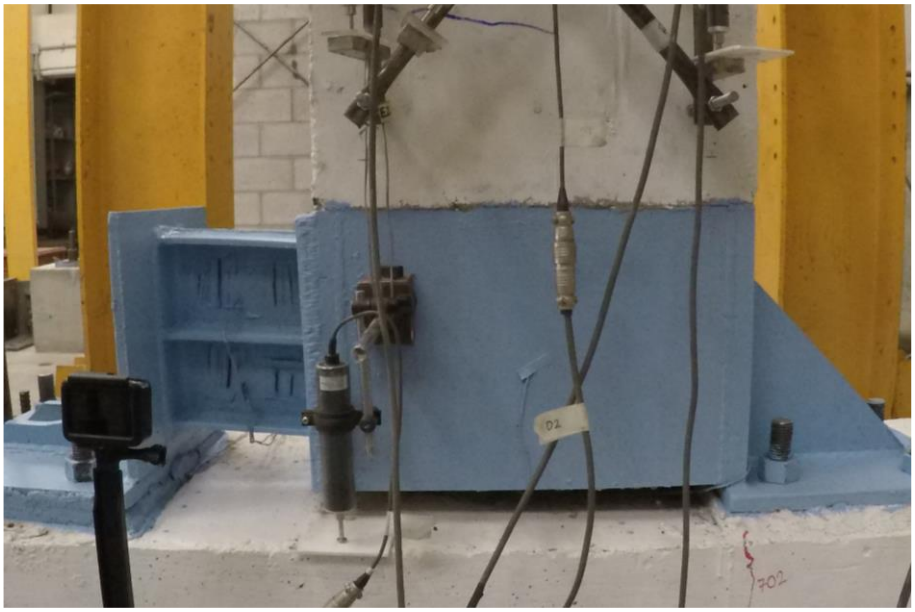

Figure 5-22. Damper deformation before failure of the beam (specimen P-ID-1M).

The ratio Q_b / Q_y, assuming 1.1f_y for the I-beam [80] and that the longitudinal rebars develop 1.25f_y [59], is approximately 1.34, which is already a low safety factor. However, it has been seen that welded rebars normally cannot develop a yield stress equal to 1.25f_y [43]. Therefore, if a nominal value of f_y is assumed, the ratio Q_b / Q_y is actually around 1.1. This analysis does not take into account the possible contribution of the I-damper's stiffeners to its strength, nor consider the limited rotation that the beam can exhibit due to the support plate and its stiffeners. Considering the above, the beam's strength to the system's strength ratio might as well be much less than 1.1; which explains the premature failure of specimen P-ID-1M.

For specimen P-ID-2, a new precast beam was fabricated and equipped with a smaller I-damper. The stiffeners were removed so that the support plate of the I-damper was more flexible, allowing the damper to deform in shear and avoiding large tension forces on the flanges. A perfect rotational hinge was connected to the top of the beam and the top dumbbell to allow the beam to rotate freely and concentrate the inelastic behavior on the device. At small displacements, shear deformation was observed, as shown in Figure 5-23.

Figure 5-23. Damper deformation at 0.01 drift (specimen P-ID-2).

At larger displacements, the support plate of the I-damper exhibited large deformations in flexure and was the main mechanism of energy dissipation, which was not the objective. Figure 5-24 and Figure 5-25 show the deformed state of specimen P-ID-2 at 0.025 and -0.025

rad, respectively. Additionally, large tension forces on the welds of the flanges of the I-damper were still a problem in this test. Localized failure of the welds was also observed close to the bottom of the beam (see Figures 5-24 and 5-25).

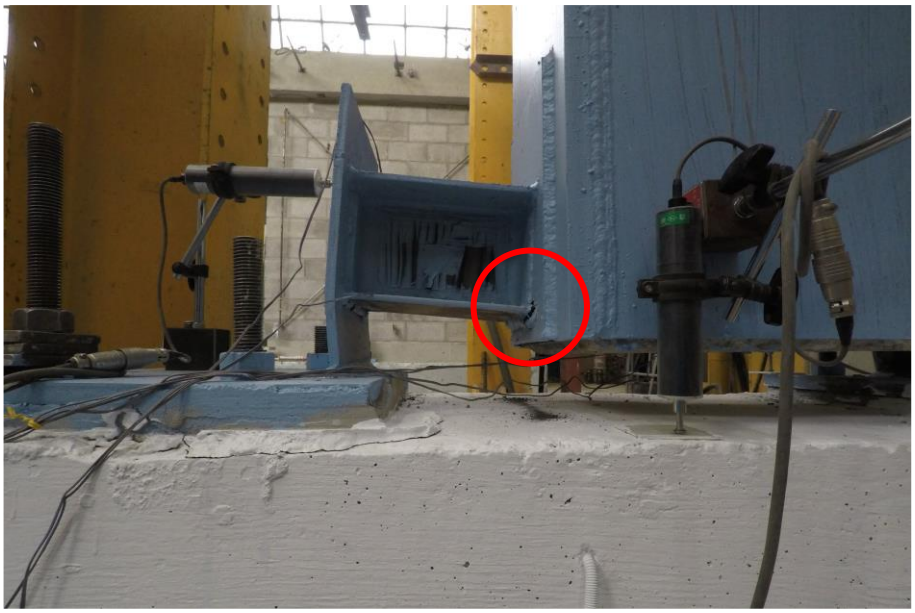

Figure 5-24. Damper deformation at 0.025 drift (specimen P-ID-2).

Figure 5-25. Damper deformation at -0.025 drift (specimen P-ID-2).

5.3.2 Hysteresis curves

Hysteresis curves of the three specimens are shown in Figure 5-26. The moment-rotation curve of specimen P-ID-1 is shown in Figure 5-26a. No significant observations can be made from this curve; except that the test was interrupted prematurely, so the predicted strength was not reached. In contrast, specimen P-ID-1M (Figure 5-26b) showed stable and symmetrical hysteresis loops. Specimen P-ID-2 showed relatively stable hysteresis loops before a target drift of 0.025 rad. Results for specimens P-ID-1M and P-ID-2 are summarized in Table 5-1. The yield load (P_y), initial stiffness ($K_{i,ex}$), and yield drift (θ_y) were obtained from the idealized bilinear curves of the backbone curves shown in Figure 5-26 with the methodology proposed in ASCE 41-17 [81].

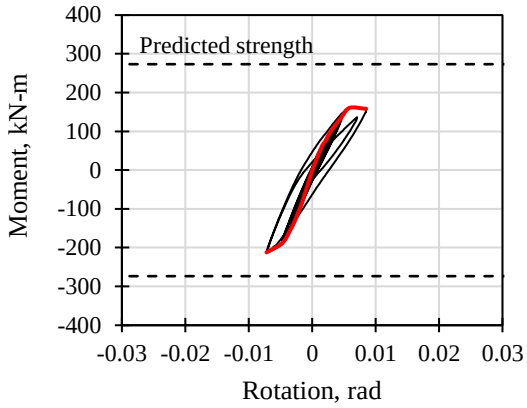

a) P-ID-1

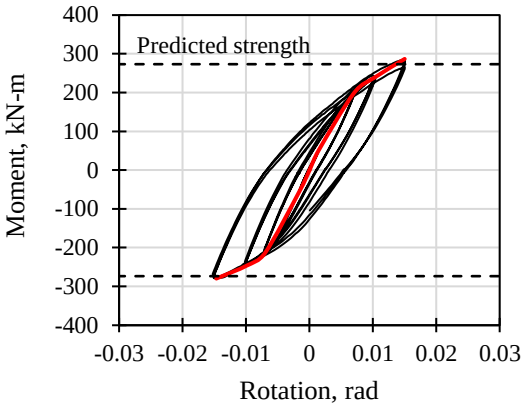

b) P-ID-M1

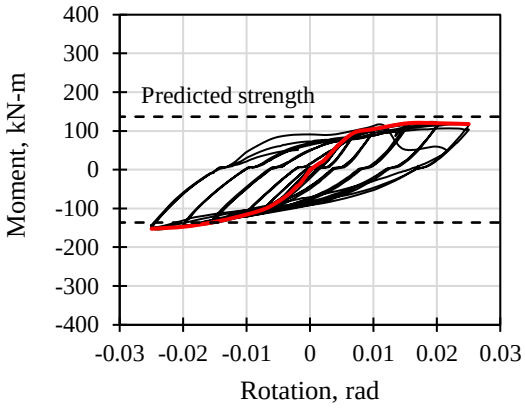

c) P-ID-2

Figure 5-26. Moment-rotation curves of the tested specimens.

Yield loads and initial stiffnesses were reasonably symmetrical. Ductility ratios were relatively small, especially for specimen P-ID-1M. P-ID-2 displayed adequate deformation capacity due to it yielding at a small drift. This, however, was mainly due to the bending of the support plate than to the shear deformation of the I-damper.

Table 5-1. Summary of test results.

Specimen	Direction	P_y (kN)	$K_{i,ex}$ (kN-mm)	θ_y (%)	θ_u (%)	μ
P-ID-1M	(+)	91.4	5.4	0.7	1.5	2.2
	(-)	101.9	5.7	0.7	1.5	2.0
P-ID-2	(+)	44.5	3.3	0.5	2.4	4.5
	(-)	50.0	4.2	0.5	2.5	5.2

5.3.3 Strain of reinforcing steel

Strains of the reinforcing steel of specimen P-SD-1 are shown in Figure 5-27. As can be seen, the reinforcing steel did not yield. Strains were slightly above 1000μ, close to half of the expected yield strain ($\varepsilon_y \approx 2000\mu$).

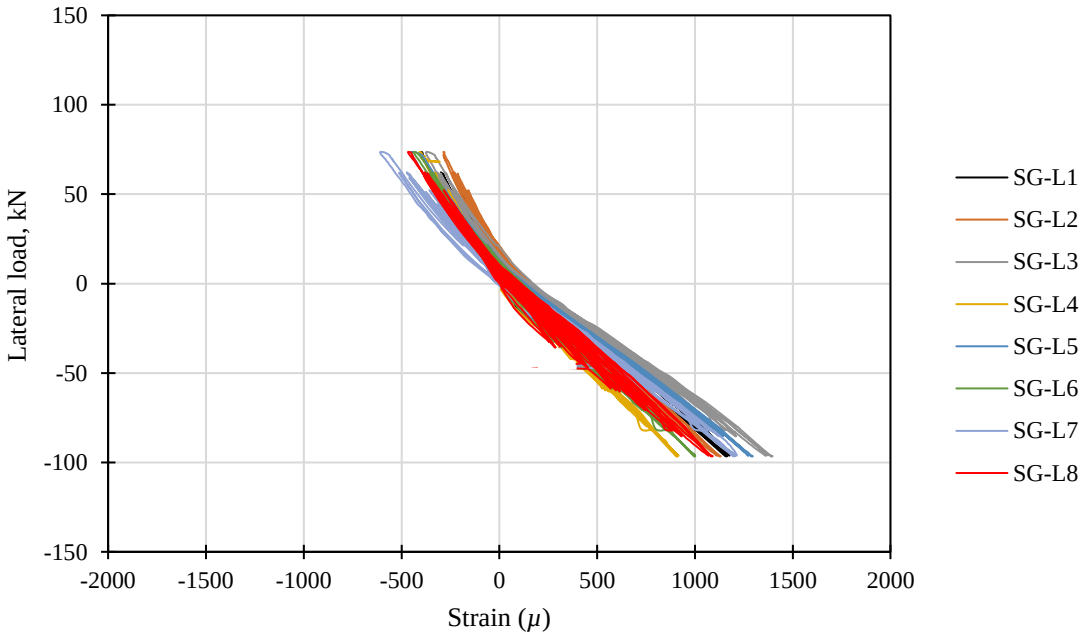

Figure 5-27. Strains of reinforcing steel (P-SD-1).

Strains of the reinforcing steel of specimen P-SD-1M are shown in Figure 5-28. In this case, no visible yield was displayed. Maximum strain values were close to 1500μ, which is 75% of the expected yield strain. This suggests that the longitudinal reinforcement of the beam (top four #8 rebars) fractured before yielding, that is, at a stress equal to $0.75f_y$. The effects of welding the longitudinal rebars should be examined carefully, and proper capacity design concepts should be applied.

As mentioned, specimen P-ID-2 was not instrumented with strain gauges.

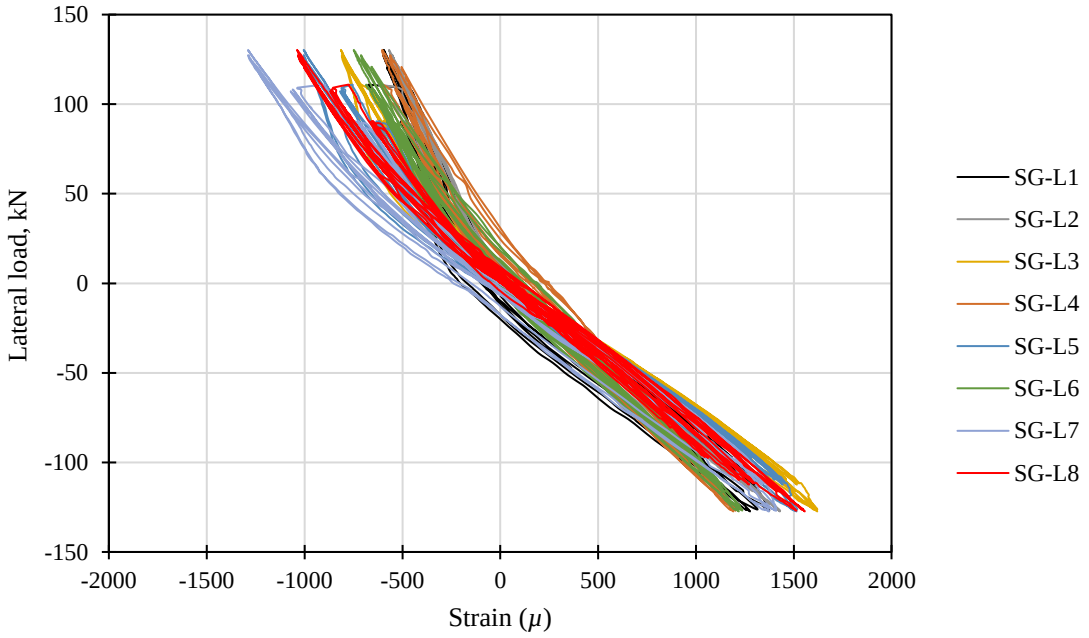

Figure 5-28. Strains of reinforcing steel (P-SD-1M).

5.3.4 Ductility and energy dissipation

The energy dissipating capacity of specimens P-ID-1M and P-ID-2 was evaluated with the relative energy dissipation, which is the ratio between the area of the hysteresis loop in question and the area of an idealized parallelogram with elastic-perfectly plastic behavior defined by the initial stiffness during the first cycle of the test and the maximum load during the cycle for which the energy dissipation is calculated:

$$\beta_i = \frac{A_h}{(P_1 + P_2)(\theta_1' + \theta_2')} \tag{5-3}$$

where A_h is the area of the hysteretic loop, P_1 and P_2 are the maximum loads, and θ'_1 and θ'_2 are the inelastic drift ratios in both directions.

The relative energy dissipation ratios are plotted in Figure 5-29. According to ACI 374.1 [18], β_i should to be above 12.5% at a drift of 0.035 rad. Neither P-ID-1M nor P-ID-2 could be taken to that threshold; however, the 12.5% limit is shown in Figure 5-29 as a reference.

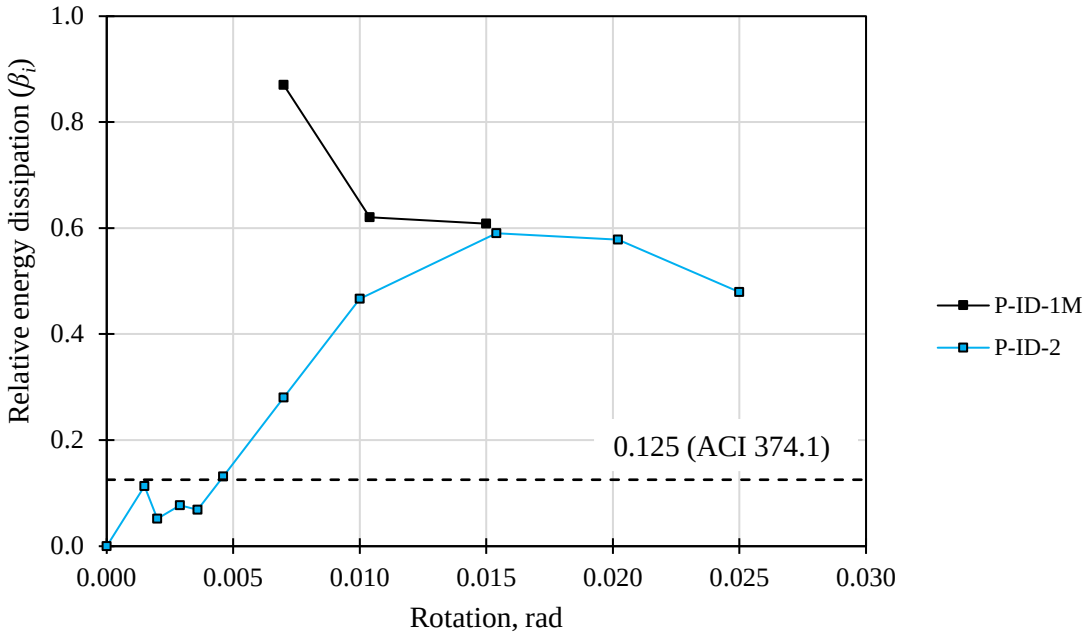

Figure 5-29. Relative energy dissipation ratio.

Specimen P-ID-1M dissipated significant amounts of energy in the earlier stages of the test at drifts below 0.007 rad. Data below this drift is not shown in the graph because it is beyond the unit, i.e., when the area of the hysteresis loop is the same as the area of its idealized energy dissipating capacity. For example, the third cycle at a drift of 0.007 rad is shown in Figure 5-30. The idealized parallelogram is shown with a continuous blue line. At this stage, the specimen is essentially within the elastic range; however, since there is hysteresis, possibly due to the opening and closing of small cracks or other mechanisms, the area of the hysteresis loop is approximately 85% of the area of the parallelogram. At smaller drifts, β_i was significantly larger than the unit for specimen P-ID-1M.

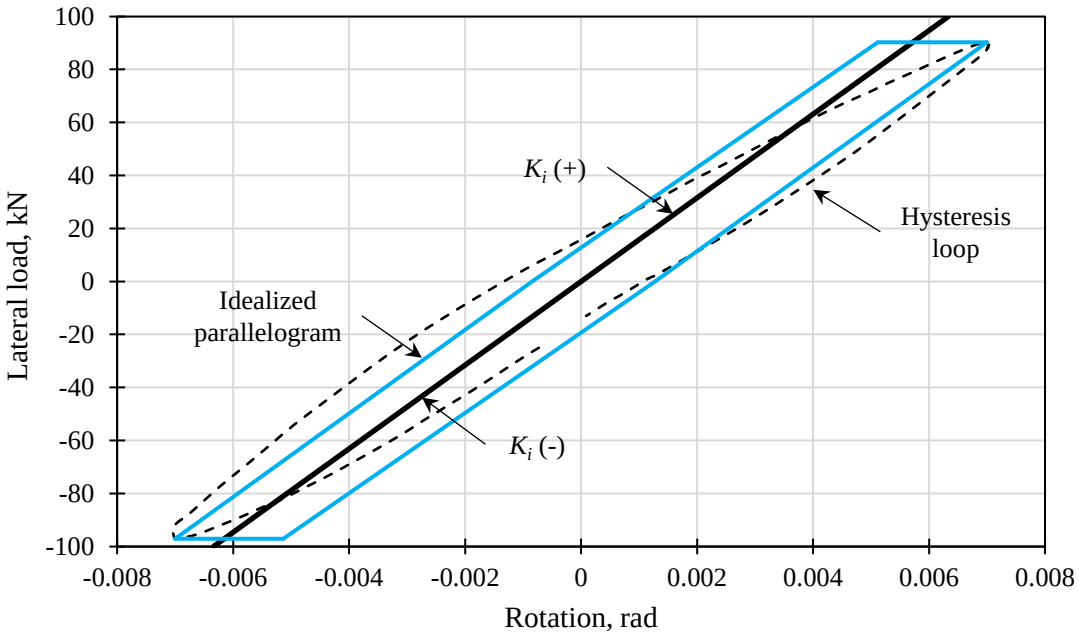

Figure 5-30. Comparison of the hysteresis loop and the idealized parallelogram (P-ID-1M).

The performance of the tested specimens was also evaluated with the cumulative ductility ratio, defined by Teran et al. [66] as

$$NE_{H\mu} = \frac{E_{H\mu}}{P_y \delta_y} \tag{5-4}$$

where $E_{H\mu}$ is the accumulated plastic energy, and P_y y δ_y are the load and the displacement at yield, respectively. The cumulative ductility ratio is plotted against the cumulative displacements in Figure 5-31. Between the two evaluated specimens, P-ID-2 displayed an apparent superior performance to the cast-in-place and precast connections studied in Chapters 3 and 4, respectively, because it dissipated more hysteretic energy for significantly smaller cumulative displacements. However, it must be mentioned that the results of P-ID-2 were not representative of the actual expected behavior of the proposed I-damper system.

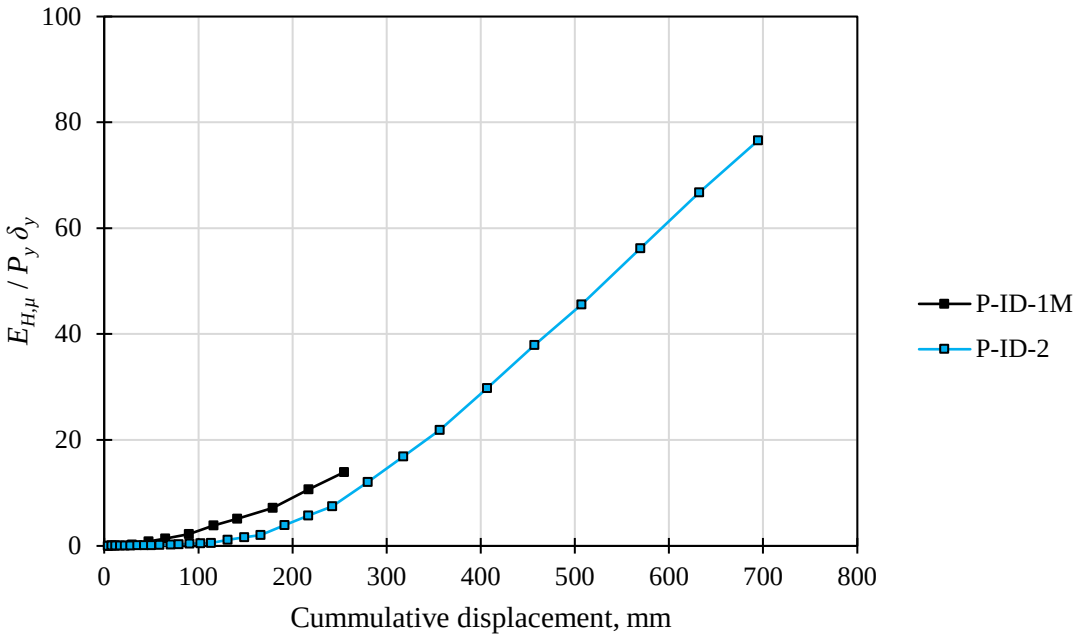

Figure 5-31. Cumulative ductility ratio.

5.3.5 Equivalent viscous damping

The equivalent viscous damping ratio, ζ_{eq}, according to Chopra [67], can be obtained as:

$$\zeta_{eq} = \frac{1}{4\pi}\frac{E_D}{E_{S0}} \tag{5-5}$$

where E_D is the measured energy dissipated per cycle, and E_{S0} is the straining energy.

Damping ratios are plotted against the ductility ratios in Figure 5-32a. Before yielding (μ<1), the specimens could dissipate small amounts of hysteretic energy, equivalent to damping ratios below 10%. This was also observed for the cast-in-place and precast specimens studied in Chapters 3 and 4, respectively. After yielding, values of 17 and 27% were reached, for specimens P-ID-2 and P-ID-1M, respectively.

In Figure 5-32b, damping ratios are plotted against the normalized effective stiffness. In this figure, each point represents a feasible damping ratio for a given effective stiffness. There is no clear similarity between both specimens. Damping ratios appeared to vary approximately linearly and inversely proportional to the effective stiffness, as observed in previous chapters.

However, as mentioned before, the results do not represent the expected energy dissipation mechanism, since dissipation was not produced by the I-damper working properly in shear.

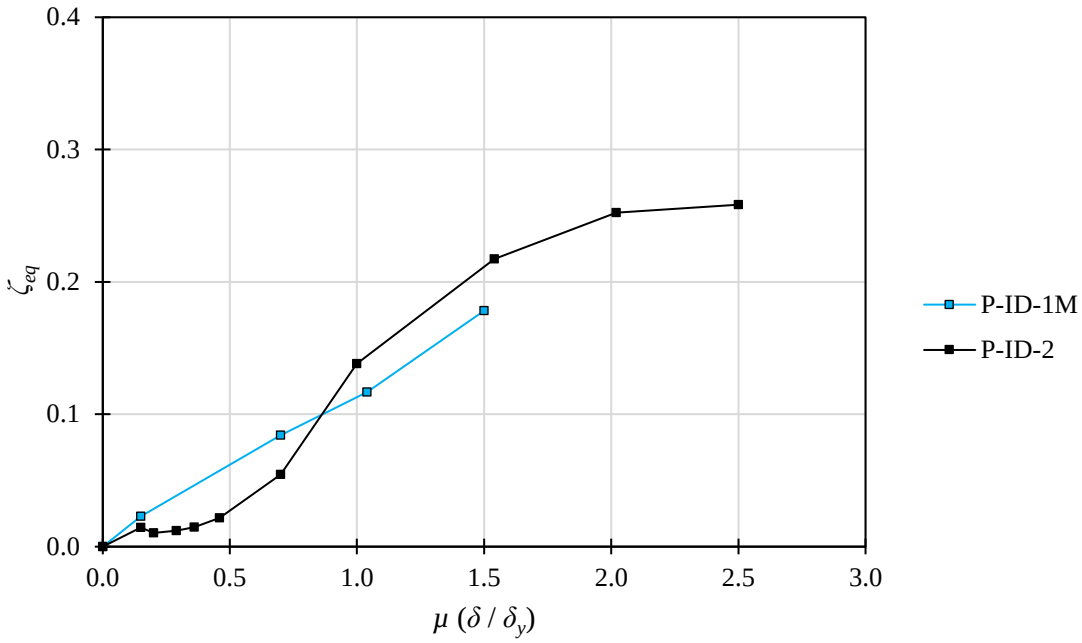

a) Equivalent viscous damping with ductility ratios

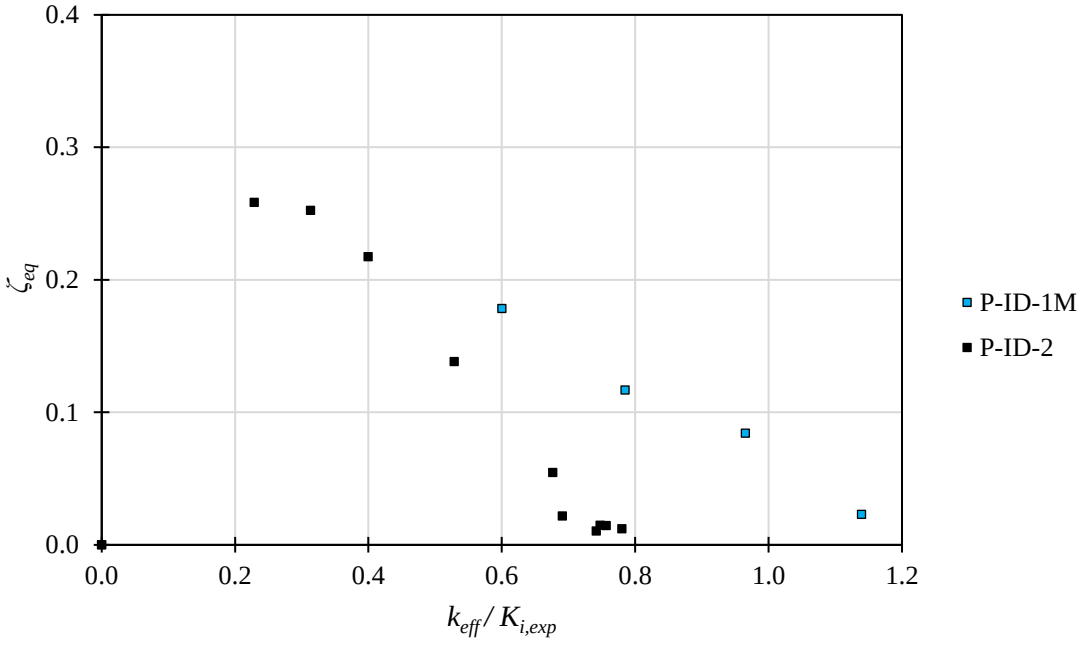

b) Equivalent viscous damping with normalized effective stiffness

Figure 5-32. Equivalent viscous damping.

5.4 Conclusions

In this chapter, innovative low-damage precast beam-column connections were proposed. Three beam-column sub-assemblies were tested. The first consisted of a beam-column connection equipped with a hysteretic damper, made of a steel W-beam (named I-damper), that dissipates energy through shear deformation of the web. The second was a slightly modified version of the first that addressed some of the difficulties observed during the first test. Although the second specimen had stable behavior, it failed abruptly due to capacity design issues. The last specimen took up the concept of shear deformation of the I-damper. The device was intentionally weakened using a smaller W-beam, and its support was made more flexible so that the I-damper could deform freely. Additionally, at the top of the beam, a rotational hinge was assembled so that the beam could rotate freely and, therefore, concentrate the inelastic behavior on the device. At small displacements, shear deformation was observed, but at larger displacements, the support of the I-damper exhibited large deformations and was the primary mechanism of energy dissipation.

Based on the experimental results, and with the objective of developing a more efficient system, the following conclusions are offered:

1. Energy dissipation through shear deformation is more challenging to control than flexural deformation. It would be preferable to make slots on the I-damper's web so that the smaller and more slender strips that are left yield in flexure and not in shear.
2. The vertical arrangement of the I-damper affects its inherent performance because the rotation of the beam introduces not only horizontal displacements in the shear direction of the damper but also vertical displacements that cause tension and compression. During the tests, it was observed that the welds on the flanges of the I-damper failed due to the large tension forces in that region. On the other hand, compression forces may cause local buckling of the web. Therefore, even an over-designed welded connection of the damper to the beam or its support plate would not be enough to extract the best performance of the damper. Instead, the horizontal placement of the damper should be considered.

3. In retrospect, the proposed I-damper system does not allow a swift replacement of the device in case of damage. A revised proposal should consider easier access and less precise tolerances.

Although the three tests described in this chapter did not render the desired results, they set the basis for a new prototype. A beam-column connection equipped with a slit damper is studied in Chapter 6 and addresses most of the shortcomings of the first three proposals presented in this chapter.

6

Experimental Tests of Precast Beam-Column Connections Equipped with Slit Dampers

6.1 Introduction

This chapter studies an innovative precast system consisting of a non-emulative low-damage precast beam-column connection equipped with a slit damper (SD), which is a passive energy dissipation device. Slit dampers have been extensively studied for their cost-effectiveness and ease of application. They exhibit stable hysteretic behavior and dissipate substantial amounts of energy under cyclic loading while keeping less ductile elements, such as the beams and columns, essentially elastic. Details on the behavior, analysis, and design of slit dampers are further discussed in Chapter 7.

The proposed system is conceptualized to minimize the damage to the concrete elements and to concentrate all the inelastic action on the dissipativedevice, which is placed below the beam and can be easily replaced in case of damage. The precast elements can be fabricated as individual pieces to be later connected on site, thus, minimizing cast-in-place concrete and excess use of formwork and significantly reducing assembly times. The connection between

the beam and the column can be achieved with welding or bolted techniques, as will be seen below.

The proposed system and the deformed shape of the SD are shown in Figure 6-1. As can be seen, the SD is installed between the beam's lower end and the column. On the other hand, an upper T-stub connection acts as a rotational hinge that allows the rotation of the beam. The rotation of the connection is resisted by the coupled moment due to the horizontal axial force developed at the top and bottom of the beam. According to Oh et al. [82], damage to the T-stub is avoided since the rotation points on the left and right sides of the frame stay at the top of the beam (see Figure 6-2). The rotational hinge is not easily accessible for replacement. Therefore, axial non-linear deformation of this component should be avoided with capacity design, and bending of the plate, due to the rotation of the beam, must be kept within the linear-elastic range to avoid fatigue. Additionally, a gap between the beam and the column should be sufficient so that the damper, or the beam, does not touch the column; but not too large to cause buckling of the rotational hinge in compression.

The SD is placed horizontally, and a vertical transfer plate is installed below the beam to transfer the axial force, *P*, to the damper. This configuration minimizes out-of-plane deformations. Some SDs, developed for steel beam-column connections, such as that proposed by Oh et al. [82], are oriented vertically. Unfortunately, this configuration can decrease the horizontal ductility capacity of the slit damper because the rotation of the beam induces not only horizontal displacements but also vertical displacements that cause tension and compression.

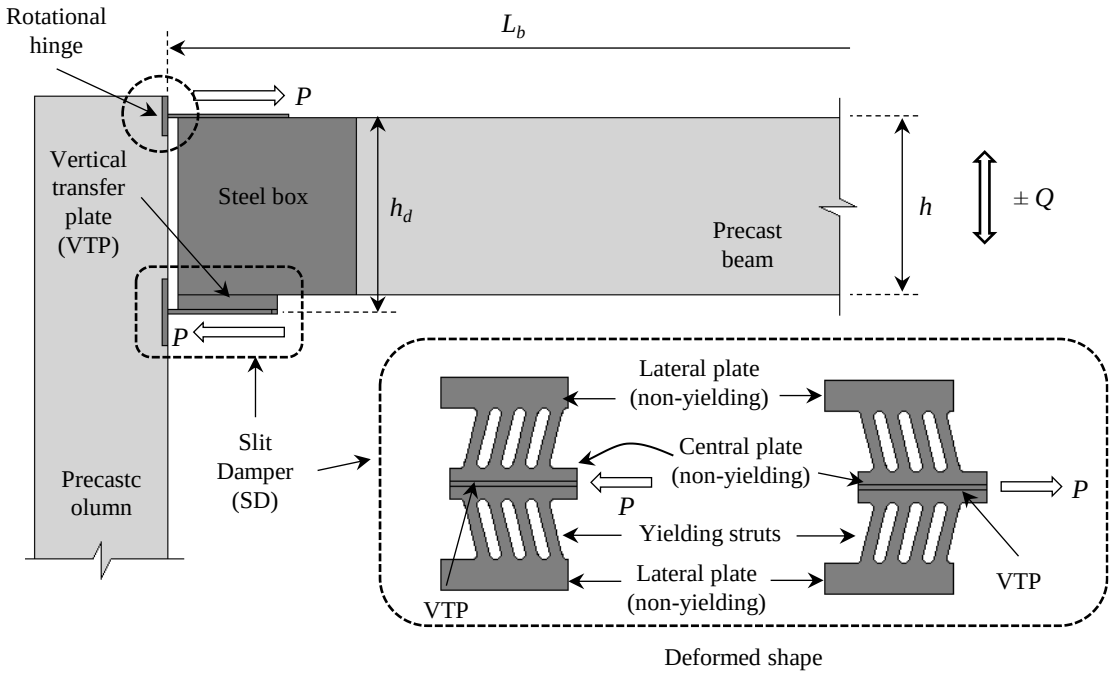

Figure 6-1. Proposed precast system.

The structural behavior of the proposed system was evaluated theoretically, followed by experimental verification. The experimental part of the program was carried out in the following order: first, a small-scale beam-column connection equipped with a slit damper with uniform struts was tested. Second, eight individual slit dampers were subjected to axial incremental and uniform cyclic loading. Two of these devices had non-uniform struts. Results of this stage of the program are presented in Chapter 7. Finally, two large-scale beam-column connections equipped with slit dampers with non-uniform struts were tested. A welded and a bolted connection of the SD to the beam were tested for these subassemblies. The results of the three beam-column connections are discussed in this chapter.

The results of the experimental tests are presented and discussed, emphasizing ductility and energy dissipation capacity. The specimens showed stable hysteretic behavior and adequate seismic performance. The welded large-scale subassembly developed a ductility ratio of 10, while the concrete elements remained undamaged up to a drift ratio of 0.035 rad. Repairability of the proposed system was also explored during the experimental study.

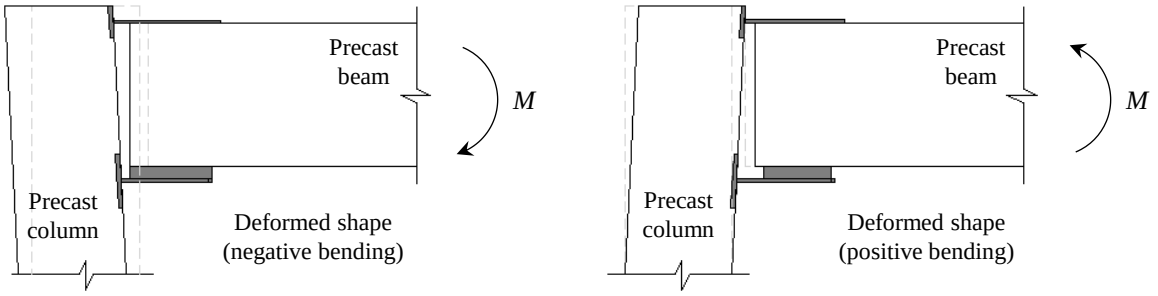

Figure 6-2. Deformed shape of the proposed precast system.

6.2 Design of Beam-Column connections equipped with slit dampers

The lateral stiffness of the beam-column connection can be evaluated with the elastic stiffness model shown in Figure 6-3. The total elastic flexural stiffness of the beam-column system, K_T, can be determined as the series sum of the flexural stiffness of the concrete beam, K_B, and the axial stiffness of the SD, K_{SD}, as

$$K_T = \left(\frac{1}{K_B} + \frac{1}{\beta K_{SD}}\right)^{-1} \tag{6-1}$$

where

$$K_B = \left(\frac{{L_{be}}^3}{3EI} + \frac{L_{be}}{A_w G}\right)^{-1} \tag{6-2}$$

and

$$K_{SD} = \left(\frac{1}{k_{SD}} + \frac{1}{k_{ce}} + \frac{2}{k_{le}}\right)^{-1} \tag{6-3}$$

In Equations (6-2) and (6-3), E is the modulus of elasticity of the material, I is the moment of inertia over the strong axis of the beam, A_w is the cross-sectional area of the beam's web on which the shear force acts, G is the shear modulus, $k_{ce,}$ and k_{le} are the elastic axial stiffnesses of the non-yielding plates of the SD (central and lateral plates, respectively, as

defined in Figure 6-1); and k_{SD} is the elastic stiffness provided by the struts of the SD, which can be determined with:

$$k_{SD} = n\left(\frac{1}{k_1} + \frac{1}{k_2}\right)^{-1} \tag{6-4}$$

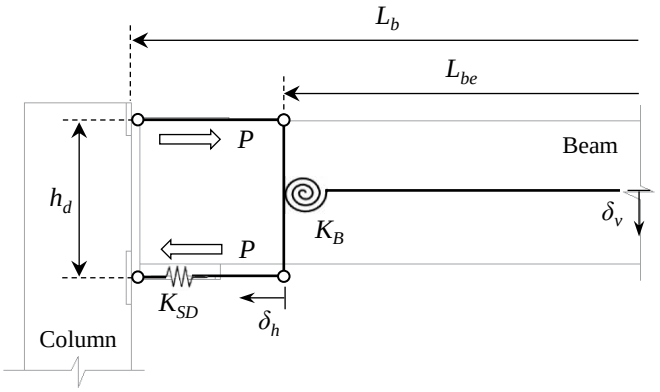

Figure 6-3. Elastic stiffness model of the beam-column system.

where n is the number of struts and k_1 and k_2 are an individual strut's flexural and shear stiffnesses.

More information on how to design SDs is presented in Chapter 7, where an effective length method is proposed for calculating the strength and stiffness of these devices.

For Eq. (6-1), the SD's contribution to the system's overall flexural stiffness must be determined by affecting K_{SD} by the factor β, which transforms the SDs axial stiffness into an equivalent flexural stiffness. From Figure 6-1, the load at mid-span, Q, can be related to the strength of the damper through the following relationship:

$$QL_{SD} = Ph_d \tag{6-5}$$

where L_{SD} is the distance from load application to the center of the. Also, from Figure 6-3,

$$P = K_{SD}\delta_h \tag{6-6}$$

and

$$\delta_h = \delta_v \frac{h_d}{L_{SD}} \tag{6-7}$$

Substituting Eq. (6-7) in (6-6), then the former in (6-5), and rearranging terms, the following relationship is obtained:

$$\frac{Q}{\delta_v} = K_{SD} \left(\frac{h_d}{L_{SD}}\right)^2 \tag{6-8}$$

where

$$\beta = \left(\frac{h_d}{L_{SD}}\right)^2 \tag{6-9}$$

At yield, assuming elastic-perfectly plastic behavior of the SD, the theoretical beam shear force, Q_y, and the moment at the column face, M_y, are

$$Q_y = \frac{P_y h_d}{L_{SD}} \tag{6-10}$$

$$M_y = Q_y L_b = \frac{P_y h_d L_b}{L_{SD}} \tag{6-11}$$

6.3 Specimen P-SD-0

6.3.1 Description of specimen P-SD-0

A prototype, P-SD-0, of the proposed precast system was fabricated to evaluate its viability. The reader should know that the concrete components (beam and column) were used in previous tests reported in Chapter 5. Both components presented virtually zero damage during these tests and were deemed appropriate for reuse. The test specimen was an exterior beam-column subassembly, representing the region from the mid-span of the beam to the

joint and half the column height below and above the joint. Cross sections of the beam and column were, respectively, 300 x 450 mm and 450 x 450 mm. The beam was 2500 mm long, and the column height was 2700 mm. Both components were connected with a rotational hinge welded to the top of the steel box and to a steel plate anchored to the column (dumbbell connection). Figure 6-4 shows a front and lateral view of the beam-column subassembly.

The mechanical properties of the materials were: 1) concrete with an average strength of 43 MPa and standard deviation of 2.97 MPa, measured from compressive tests (see Table 6-1); 2) steel bars with nominal yielding strength of 412 MPa; and 3) structural steel with a yield stress of 325 MPa and ultimate tensile strength of 478 MPa, measured from coupon tests. The maximum size of the coarse aggregate was 19 mm.

Table 6-1. Compressive test results.

Cylinder ID	Diameter (mm)	Height (mm)	Area (mm2)	Maximum load (kN)	f'_c (MPa)	Average f'_c (MPa)
CT-01	150	300	17671	670	37.9	43
CT-02				748	42.3	
CC-01				774	43.8	
CC-02				812	46.0	
CC-03				804	45.5	
CC-04				735	41.6	

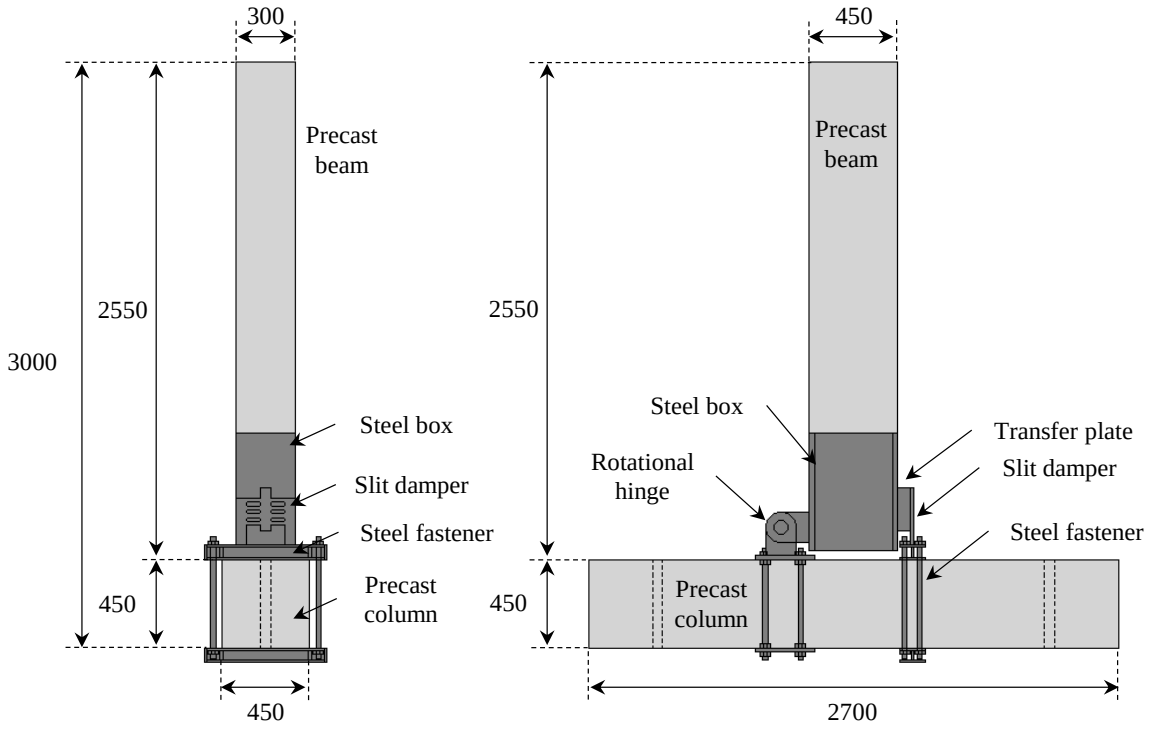

a) Front view b) Lateral view

Figure 6-4. Specimen P-SD-0.

The geometric characteristics of the SD used for specimen P-SD-0 are shown in Figure 6-5. It consisted of eight uniform struts with a total length (l) of 75 mm, a width (b) of 19 mm, and a uniform plate thickness (t) of 19 mm. The radius of the strut was equal to b / 2. No major manufacturing defects were observed after cutting the slits; however, the four outer struts were not properly rounded off as the rest, which led to the premature fracture during the test due to stress concentrations, as will be seen later. The two lateral elements were relatively flexible; therefore, their flexibility was considered in the design stage, which is explained upon later.

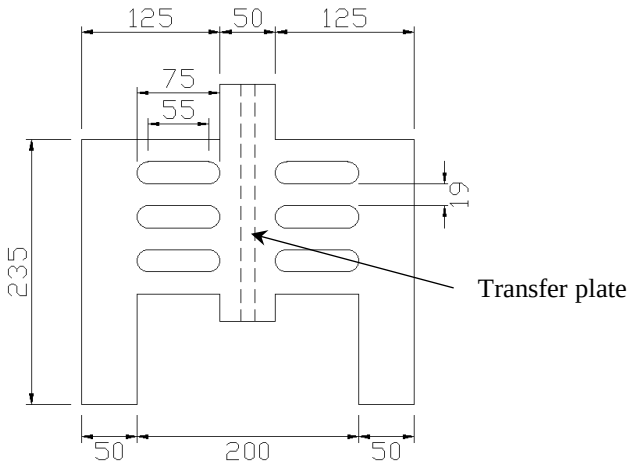

Figure 6-5. Slit damper for specimen P-SD-0, dimensions in mm.

6.3.2 Fabrication process

The beam and column steel reinforcement was detailed following the requirements of the Mexico City Building Code (MCBC) [40]. The beam longitudinal reinforcement was welded with E90XX electrodes to the top and bottom plates of the steel box, as shown in Figure 6-6. Once the steel box was assembled, it was placed within the formwork for later casting of the concrete. Twelve 50 mm diameter PVC pipes were placed vertically in the column formwork to pass threaded steel bars that could ensure a proper anchorage of the beam-column connection (see Figure 6-7). As mentioned, the concrete components were used in tests similar to the one described in this chapter. Multiple beam-column configurations were proposed and tested previously; however, only four of the top six PVC ducts were necessary for the connection proposed herein. The bottom six holes were not used for this test due to the unique configuration of specimen P-SD-0. Casting the concrete components was practical as the concrete could be poured into independent formworks, as shown in Figure 6-8.

Figure 6-6. Welding of reinforcing steel to the steel box.

The beam-column specimen was assembled inside the laboratory. The column was appropriately anchored to the reaction slab. After that, two steel plates were anchored to the column (see Figure 6-9a) with threaded steel bars passing through the four outer ducts of the column. Two steel plates with 72 mm diameter holes were welded to the column and another two to the beam (Figure 6-9b). Then, a 70 mm diameter pin was adjusted to complete the rotational hinge (Figure 6-9c).

Figure 6-7. PVC pipes in the column formwork.

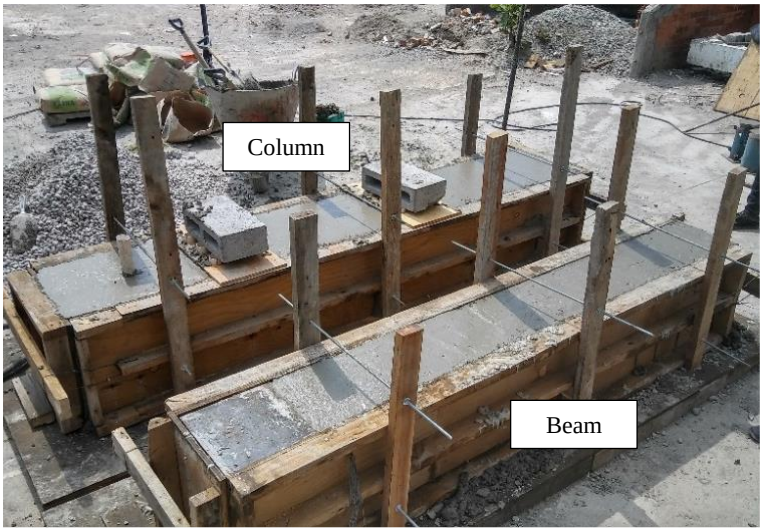

Figure 6-8. Casting of concrete.

a) Steel plate anchoring b) Welding of the hinge plates c) Pin adjustment

Figure 6-9. Rotational hinge assembly.

Once the beam was connected to the column through the rotational hinge (Figure 6-10a), a steel fastener was placed at the bottom of the beam that clamped the column, as shown in Figure 6-10b. This configuration was proposed for this test since the column was fabricated beforehand for other tests; however, the connection can also be achieved with another steel plate anchored to the column at the height of the damper. Although the latter would be the on-site approach, the former is still an accurate representation of the connection's behavior. Finally, the SD was welded to the beam through the vertical transfer plate and to the steel fastener at the bottom of the lateral elements of the SD.

a) Beam preparation and placement

b) Steel fastener and SD placement and welding

Figure 6-10. Beam-column assembly.

6.3.3 Design of the test specimen

The overall behavior of a beam-column subassembly equipped with an SD is governed primarily by the structural characteristics of the dissipation device; therefore, it is important to determine these characteristics as precisely as possible. To do that, the effective length method presented in Chapter 7 is used to determine the elastic stiffness and the strength of the proposed SD. Based on these results, the effective stiffness of the beam-column subassembly was obtained with Eq. (6-1), and the strength and moment at the column face were computed with Eqs. (6-5) and (6-11), respectively. The mechanical and geometric properties of the SD used for Specimen P-SD-0 are shown in Table 6-2. The lateral elements of the SD, shown in Figure 6-5, were deemed to be reasonably flexible, and their stiffness was taken into account in the determination of K_{SD} with Eq. (6-3); however, the central element was not included in the analysis due to it being restrained by the transfer plate located perpendicularly to the SD. This element added significant stiffness to the central element of the SD and therefore was deemed unnecessary to include. Depending on the size of the damper and the geometry of its different elements, the designer has the liberty to include the stiffness of each of its individual components if necessary. Finite element analysis (FEA) is also encouraged in some cases, as shown here.

FEA was carried out in ABAQUS [7] to determine the key structural characteristics of the SD, namely: the strength, the elastic stiffness, and the yield displacement. The model's deformed shape and stress state for an axial displacement of 15 mm (equal to 20% of the struts's total length) are shown in Figure 6-11. The capacity curve of the simulation is shown in Figure 6-12. The results obtained with the equations proposed in Chapter 7 are also shown for comparison. As can be seen, the structural characteristics of the SD could be precisely determined and would have been different if obtained with the traditional equations proposed in the literature [82,83], as will be seen in Chapter 7.

Table 6-2. Properties of the SD used for specimen P-SD-0.

Property	Definition	Value
f_{ye} (MPa)	Yield stress	325
E (MPa)	Young's modulus	200000
μ	Poisson's ratio	0.3
n	Number of struts	8
t (mm)	Strut thickness	19
b (mm)	Strut width	19
l (mm)	Strut total length	75
r (mm)	Strut radius	9.5
l_r (mm)	Effective length for strength	50.8
l_k (mm)	Effective length for elastic stiffness	76.7

With the general behavior of the SD determined, the key structural characteristics of the beam-column subassembly were obtained with the procedure mentioned above. To evaluate the flexural stiffness of the beam (K_B), an effective stiffness of $0.3EI$ was used, as recommended in [81]. The axial stiffness of the SD was transformed into an equivalent flexural stiffness with the factor β equal to 0.12 using Eq. (6-9). Through capacity design, it was ensured that the flexural strength of the precast beam was greater than the couple moment produced by the SD and, at the same time, less than the flexural strength of the precast column. Welded components were designed with a safety factor of at least 2.5. The most relevant results of the design are shown in Table 6-3.

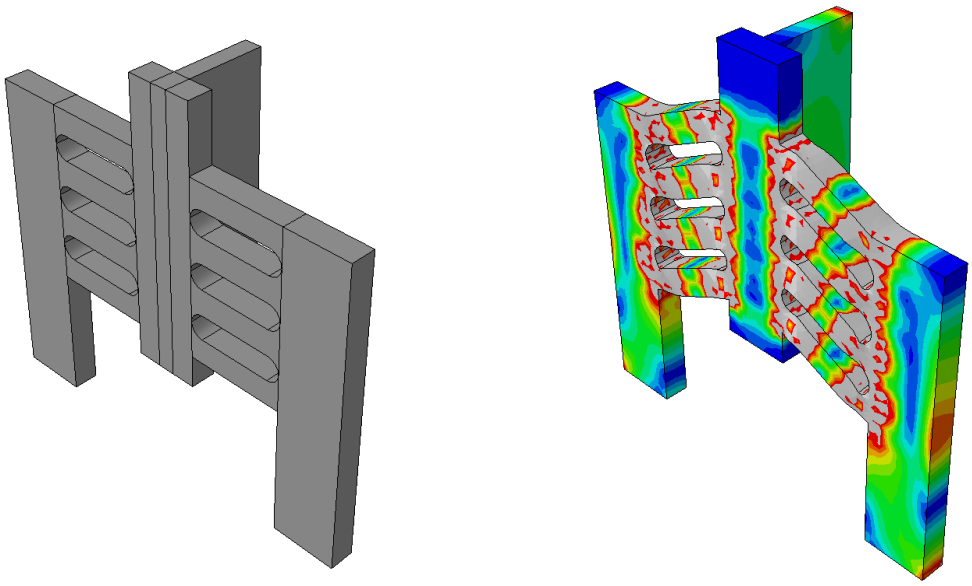

a) Model b) Deformed shape and stress state

Figure 6-11. Finite element model of the proposed SD.

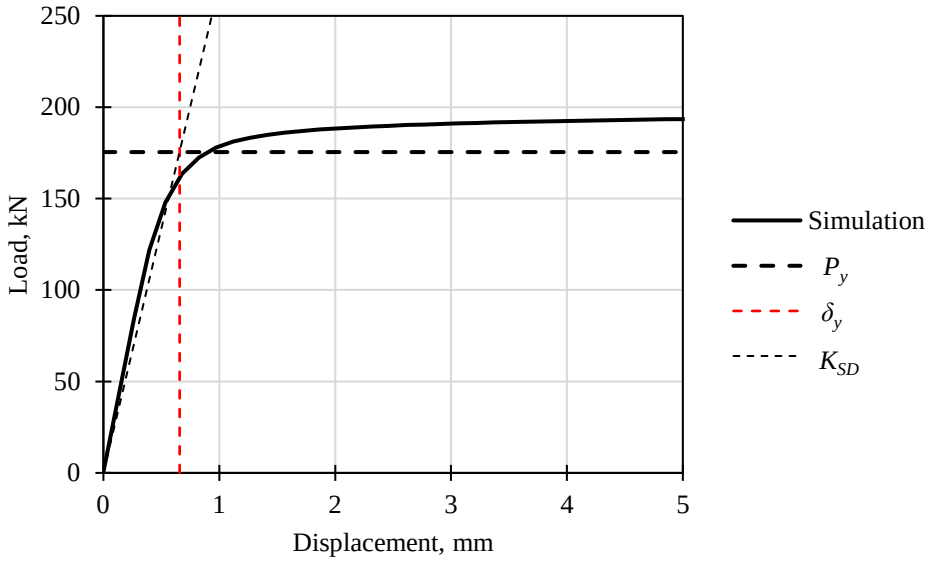

Figure 6-12. Theoretical capacity curve of the SD for specimen P-SD-0.

Table 6-3. Design summary.

Element /assembly	Structural characteristic	Value
Isolated SD	P_y (kN)	175.5
	K_{SD} (kN/mm)	267.2
	Δ_y (mm)	0.66
Beam-column (P-SD-0)	P_y (kN)	60.3
	M_y (kN-m)	121.2
	β	0.12
	K_B (kN/mm)	16.2
	K_T (kN/mm)	10.7
	Δ_y (mm)	5.64

The effective stiffness of specimen P-SD-0 can be predicted with the effective stiffness model proposed in Chapter 7, which is presented here for convenience:

$$k_{eff,n} = a{\theta_{SD}}^{-b} \tag{6-12}$$

where θ_{SD} is the strut drift ratio, and a and b are constant values obtained from linear regression analysis, to be 0.04 and 0.56, respectively. It is important to note that $k_{eff,n}$ is the normalized effective stiffness of the isolated damper and not of the beam-column system. Eq. (6-12) is plotted in Figure 6-13 (blue line). In this case, the effective stiffness of the damper is presented in terms of the beam lateral drift ratio obtained through the strut drift ratio with a geometric relationship. To obtain the effective stiffness of the overall system, first, the absolute effective stiffness of the SD must be obtained as follows:

$$k_{eff} = k_{eff,n}K_{SD} \tag{6-13}$$

where K_{SD} is the theoretical elastic stiffness of the SD and is obtained with Eq. (6-3). Then, similarly to Eq. (6-1), a total effective stiffness ($k_{T,eff}$) of the beam-column connection can be obtained as the series sum of the theoretical flexural stiffness of the beam (K_B) and the effective stiffness of the damper (k_{eff}), transformed into an equivalent flexural stiffness through the factor β:

$$k_{T,eff} = \left(\frac{1}{K_B} + \frac{1}{\beta k_{eff}}\right)^{-1} \quad (6\text{-}14)$$

Finally, $k_{T,eff}$ is normalized with respect to the theoretical stiffness of the beam-column subassembly, Eq. (6-1), as follows:

$$k_{T,eff,n} = \frac{k_{T,eff}}{K_T} \quad (6\text{-}15)$$

The elastic stiffness of the beam (K_B) can be used in Eq. (6-15) because it is assumed that the beam remains essentially elastic and without damage which, as will be seen below, is a reasonable assumption. Eq. (6-15) is also plotted in Figure 6-13 for different lateral drift ratios. If the effective stiffness is accurately determined, the contribution of the damper to the overall stiffness of the beam-column subassembly can clearly be seen. The drift ratios used for this prediction are the same target drift ratios from the loading protocol shown in section 6.4.4.2.

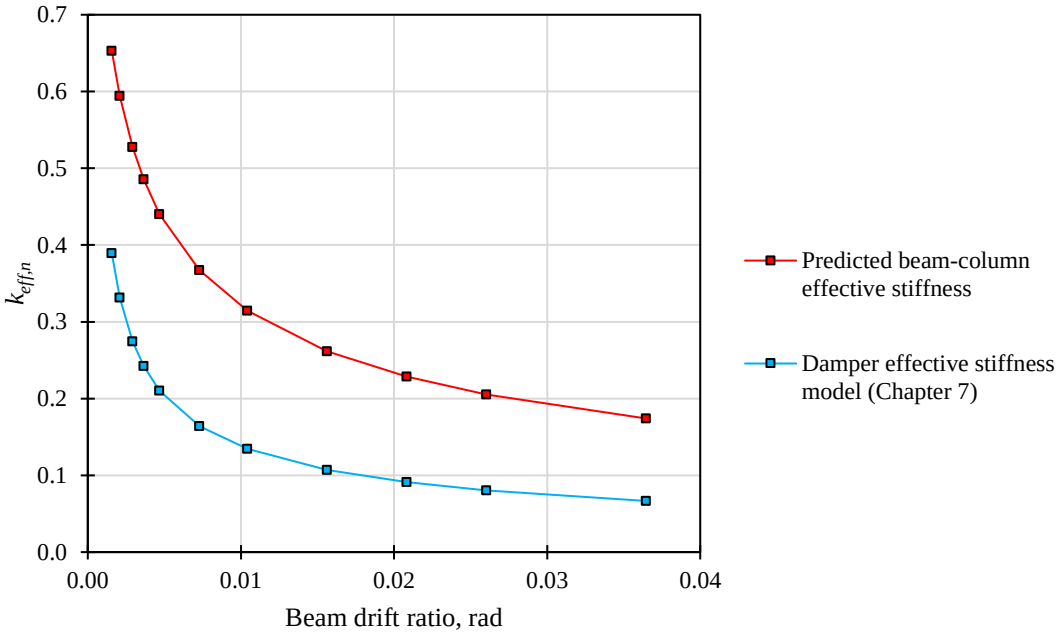

Figure 6-13. Predicted effective stiffness of specimen P-SD-0 at different drift ratios.

6.3.4 Experimental program

6.3.4.1 Test setup

The tested specimen represented an exterior beam-column connection of a moment-resisting frame. It was assumed that the specimen could be isolated this way because the points of zero moment, or inflection points, due to lateral loading, are localized at the mid-height of the columns and mid-span of the beams. Similar to previous studies [61–63], the column was connected to the reaction slab at both ends using post-tensioned steel bars, which provided limited rotational restraint simulating a pinned support (see Figure 6-14). The specimen was subjected to a quasi-static incremental cyclic loading protocol applied at the tip of the beam with a 1000 kN hydraulic actuator with a ±200 mm stroke connected to the reaction wall. The push direction of the actuator was set as positive and the pull direction as negative. Positive loading was performed first for each cycle.

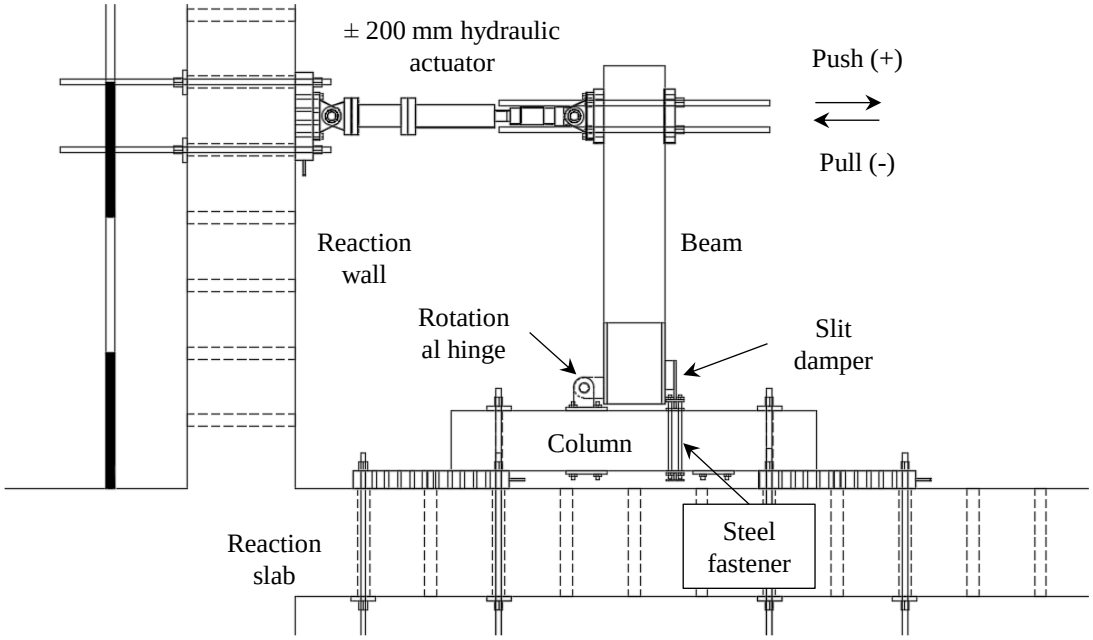

Figure 6-14. Test setup.

A picture of the experimental setup within the laboratory is shown in Figure 6-15. As can be seen, lateral bracing was placed just above mid-height of the beam to prevent out-of-plane displacements. This restriction did not generate undesired friction forces during the test since the beam remained within its working plane.

Figure 6-15. Actual test setup.

6.3.4.2 Loading protocol

The loading protocol was based on the requirements given in ACI 374.1 [18]. According to ACI 318-19 [52], special precast moment-resisting frames with jointed connections (non-emulative connections) that do not satisfy Sections 18.9.2.1 and 18.9.2.2 should satisfy ACI 374.1 [18]. The protocol consisted of three cycles for each target displacement. The initial drift ratio was within the elastic range, followed by increments of no less than 1.25 and no more than 1.5 times the immediately preceding target displacement. According to ACI 374.1 [18], increments should continue to reach a drift ratio of 0.035 rad at least. The loading protocol is shown in Figure 6-16.

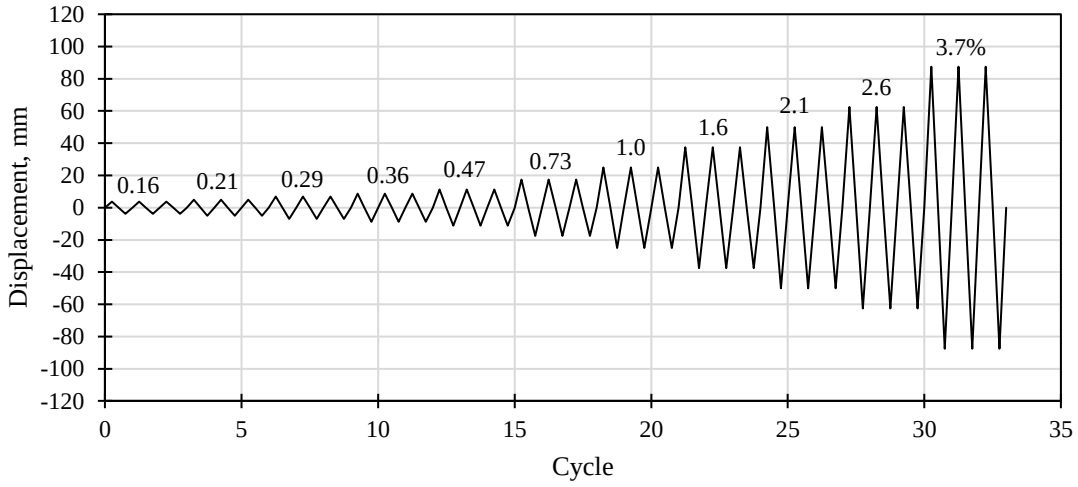

Figure 6-16. Loading protocol.

6.3.4.3 Instrumentation

Local displacements were assessed with three linear variable differential transducers (LVDTs). As shown in Figure 6-17a, one horizontal LVDT (H1) was placed to measure horizontal beam displacements at actuator height. Vertical displacements were measured with two vertical LVDTs (V1 and V2), one close to the rotational hinge (V2) and another closer to the SD (V1). The vertical LVDTs were used to check whether a simple geometric relationship between beam and damper displacements could be proposed and used confidently. Steel reinforcement strains were assessed with two strain gauges (SGs) placed on the top longitudinal reinforcement of the beam, as shown in Figure 6-17b. Two SGs were placed on transverse reinforcement but did not function properly.

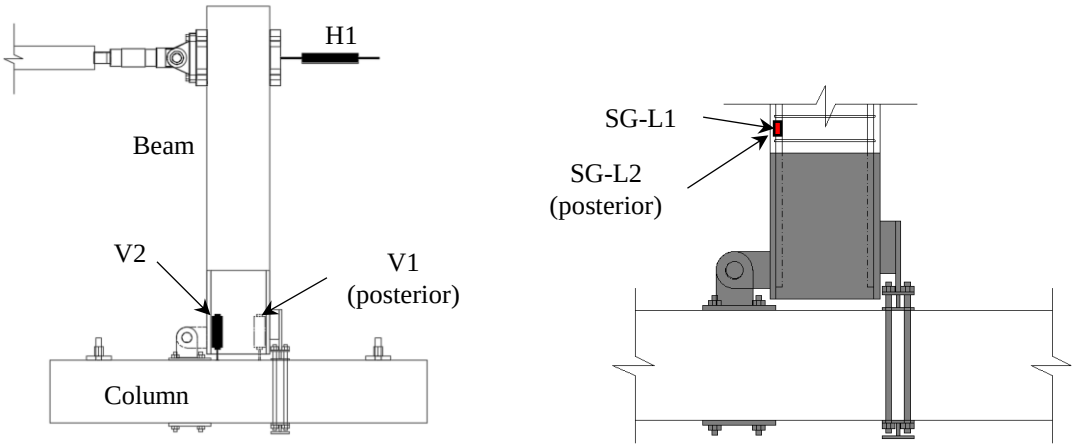

a) LVDTs b) SGs

Figure 6-17. Instrumentation.

6.3.5 Results

6.3.5.1 Failure mode

The deformed shape of the SD at different stages of the test, namely: a) ±1.6%; b) ±2.1%; and c) ±2.6% beam drift ratio, is shown in Figure 6-18. Each figure also shows the equivalent strut drift ratio values. The deformed shape of the damper at a 1.0% beam drift ratio was not evident; however, at a 1.6% beam drift ratio, the deformed shape was observable but with no apparent. At 2.1%, the struts were clearly in double curvature, as expected. At this level of deformation, minor cracks appeared at the struts' ends. At the first cycle of 2.6% beam drift ratio, cracks appeared on multiple struts, and one of them was completely fractured on the final cycle, after which the test was concluded. It is important to highlight that one of the outer struts, which was not properly rounded at the ends, was the strut to fracture completely. The larger section of the ends of the outer struts can lead to stress concentrations in those regions. The other struts had cracks at the ends, some extending vertically up to mid-height of the strut. The final state of the SD is shown in Figure 6-19, where the fractured strut is highlighted.

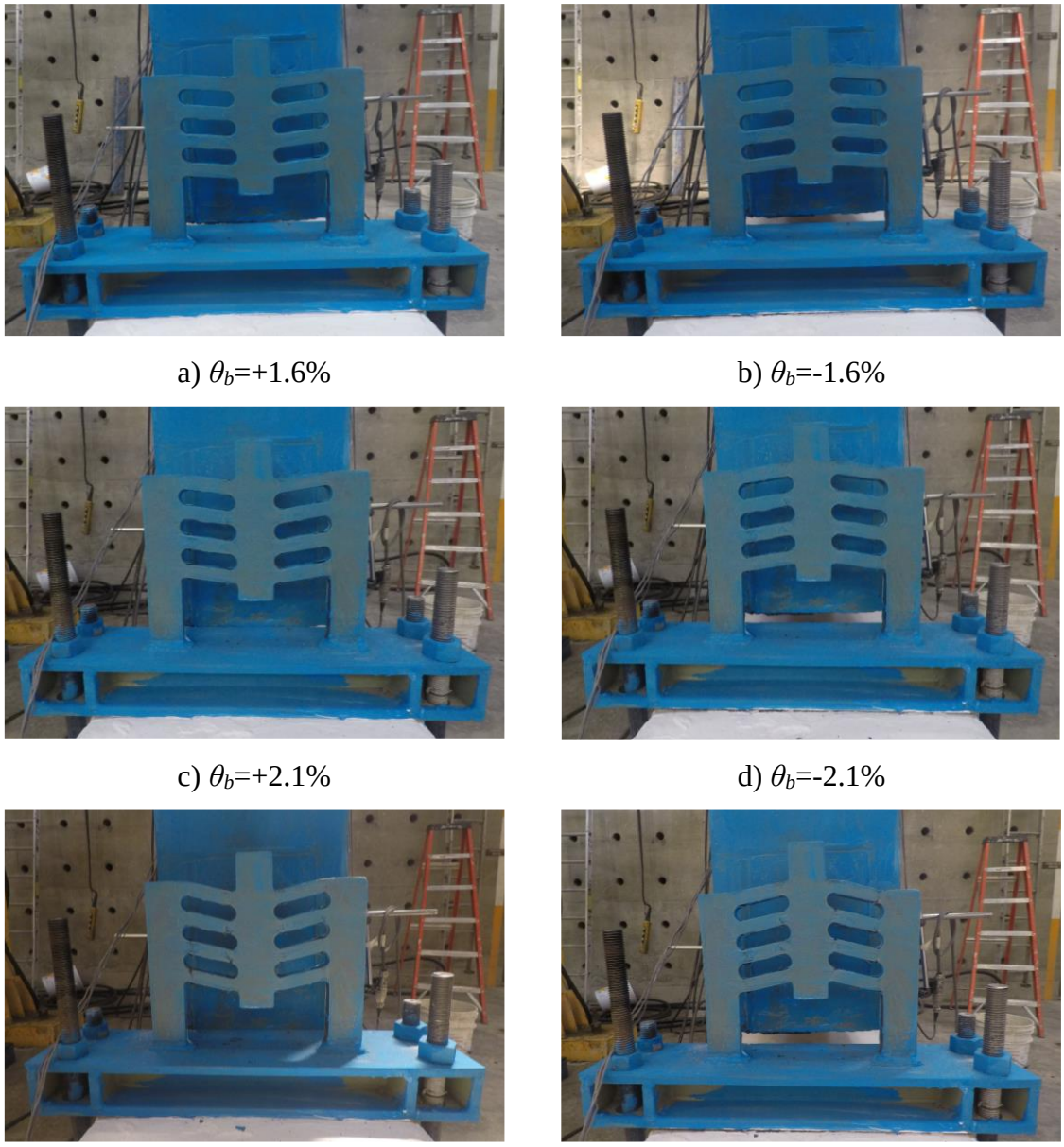

a) θ_b=+1.6% b) θ_b=-1.6%

c) θ_b=+2.1% d) θ_b=-2.1%

e) θ_b=+2.6% f) θ_b=-2.6%

Figure 6-18. Deformed shape of the SD at different stages of the test.

Figure 6-19. Final state of the SD after testing.

6.3.5.2 Hysteresis curves

The load-displacement curve of the tested specimen is shown in Figure 6-20, and the moment-rotation curve is shown in Figure 6-21. In the latter, the beam moments were obtained by multiplying the measured lateral load by the lever arm. The rotation was obtained as the ratio between the beam's horizontal displacement at actuator height and the vertical distance from mid-column depth to the actuator's center line.

The predicted strength in both response directions is also represented in these figures with black dashed lines. As can be seen, the test specimen presented wide, symmetrical, and stable hysteresis loops up to the first cycle at 0.026 rad. After that, load-carrying capacity slowly decreased in the second cycle at 0.026 rad due to the partial fracture of multiple struts. Finally, at the last cycle, applied partially, a total fracture of one of the struts was observed, and the test was concluded to not put personnel or equipment in danger. No significant stiffness degradation was observed; however, slippage close to zero load was observed, mainly attributed to size tolerance between the pin and the hole in the rotational hinge plates.

The backbone curve of the load-displacement curve is also shown with a red continuous line in Figure 6-20. The experimental structural characteristics such as yield displacement ($\delta_{y,ex}$), maximum displacement ($\delta_{max,ex}$), yield load ($P_{y,ex}$), ultimate load ($P_{u,ex}$), and initial stiffness ($K_{i,ex}$) were obtained with idealized bilinear curves determined with the methodology presented in ASCE 41-17 [81]. A summary of the test results is shown in Table 6-4.

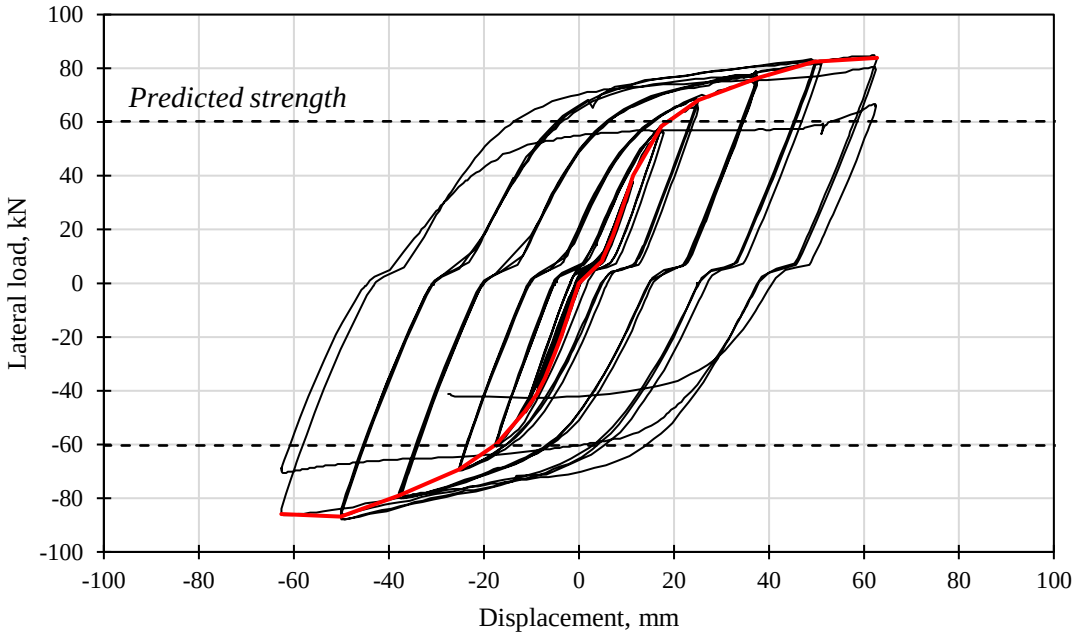

Figure 6-20. Load-displacement curve.

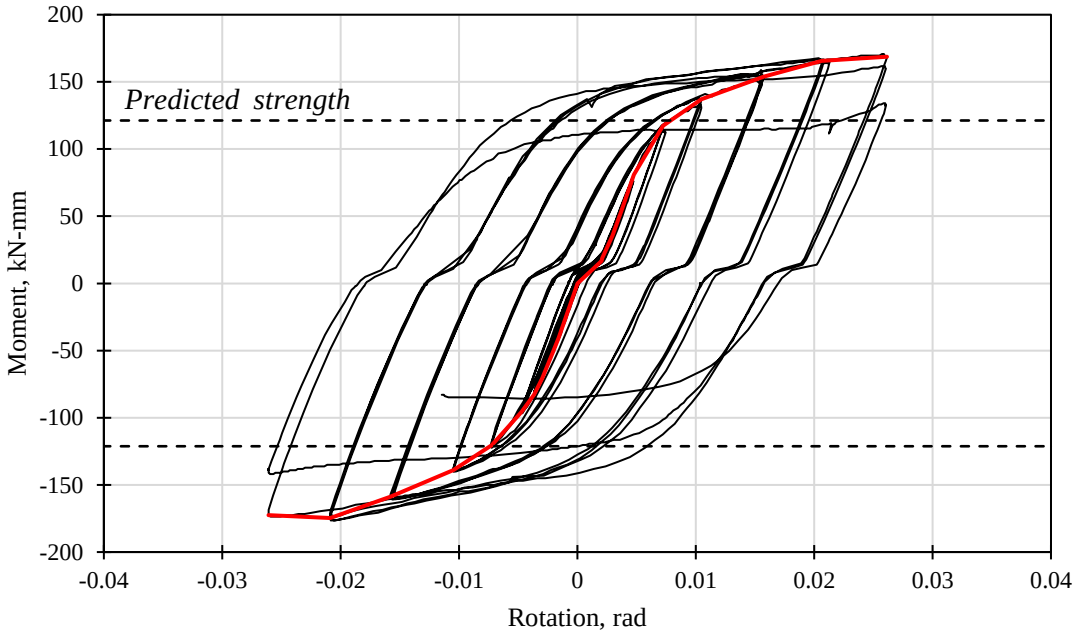

Figure 6-21. Moment-rotation curve.

A reasonably symmetrical response was observed from specimen P-SD-0. The experimental yield load and ultimate load were approximately 1.1 and 1.4 times the theoretical yield load, demonstrating that the proposed design method was appropriate for predicting the specimen's strength. The initial experimental stiffness, however, was 44% of the predicted elastic stiffness. Consequently, the yield displacement was significantly larger than the predicted value. This was mainly attributed to slippage and to the flexibility of the steel fastener, which was not factored in the analysis. Although minimal, the out-of-plane deformation of the SD could also have affected the specimen's stiffness. Unfortunately, the out-of-plane deformations were not measured during the test.

Table 6-4. Summary of test results.

Property	Direction		Average
	(+)	(-)	
$P_{y,ex}$ (kN)	67.4	65.7	66.5
$P_{y,ex}$ / $P_{y,c}$	1.1	1.1	1.1
$P_{u,ex}$ (kN)	83.9	86.8	85.3
$P_{u,ex}$ / $P_{y,c}$	1.4	1.4	1.4
$\delta_{y,ex}$ (mm)	14.74	13.40	14.07
$\delta_{max,ex}$ (mm)	59.66	62.64	61.15
$K_{i,ex}$ (kN/mm)	4.6	4.9	4.7
μ	4.0	4.7	4.4
α	0.08	0.08	0.08

The connection's yield displacement was, on average, at a drift ratio of 0.6%, equivalent to a strut drift ratio of 6.4%. The strut drift ratio at yield was expected to be approximately 2.6%. The larger yield displacement could be attributed to the flexibility of the steel fastener, which was not taken into account in the determination of the global elastic stiffness of the specimen. The global ductility ratio was (μ), on average, 4.4. Compared to the conventional cast-in-place and most precast connections, the global ductility ratio of specimen P-SD-0 was significantly less. It was only superior to the welded corbel specimen (P-COR-1), with a ductility ratio of 3.6, and specimen P-UB-3, which had a manufacturing defect and a ductility ratio of 4.1. Finally, the post-elastic stiffness ratio (α) was approximately 8% of the initial stiffness $K_{i,ex}$.

Although the load in the SD and the displacements at the center of the damper were not directly measured during the test, the hysteretic behavior of the damper as an isolated component could be reasonably estimated with geometric relationships. The relationship

between the beam's lateral displacements and the damper's vertical displacements is given by Eq. (6-7). The resultant curve is shown in Figure 6-22, and the key structural characteristics are shown in Table 6-5. The yield displacement was determined as 4.7 mm, equivalent to a strut drift ratio of 6.2%, and the maximum displacement of the damper was approximately 21.5 mm, equivalent to a strut drift ratio of 29% rad.

Certainly, most of the values in Table 6-5 can be obtained directly with reasonable precision from the properties of the beam-column subassembly presented in Table 6-4. Other parameters, namely, the average ductility ratio (μ) and the post-elastic stiffness factor (α), are the same. This observation validates that the ease of controlling the response of the overall system through the response of the SD is one of the most important properties of the proposed system. It also makes the proposed beam-column system more predictable than conventional cast-in-place or emulating precast beam-column connections. As long as appropriate capacity design concepts are applied, the response of the beam-column system will be governed by the response of the SD.

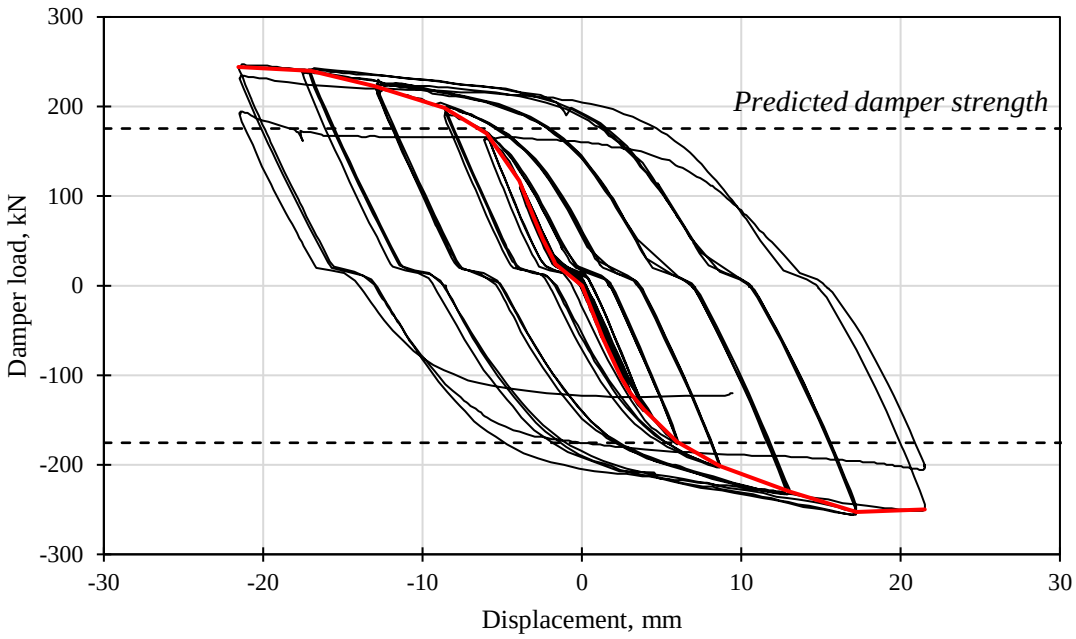

Figure 6-22. Damper load-displacement curve.

Table 6-5. Estimated structural characteristics of the isolated SD.

Property	Direction		Average
	(+)	(-)	
$P_{y,ex}$ (kN)	192.0	191.5	191.8
$P_{y,ex}$ / $P_{y,c}$	1.1	1.1	1.1
$P_{u,ex}$ (kN)	244.1	252.7	248.4
$P_{u,ex}$ / $P_{y,c}$	1.4	1.4	1.4
$\delta_{y,ex}$ (mm)	4.67	4.64	4.65
$\delta_{max,ex}$ (mm)	20.46	21.52	20.99
$K_{i,ex}$ (kN/mm)	41.1	41.3	41.2
μ	4.4	4.6	4.5
α	0.08	0.08	0.08

For illustration purposes, the estimated damper load is plotted against the strut drift ratio in Figure 6-23. These drift ratios were obtained as the ratios of the estimated vertical displacements at the center of the damper to the total length of the strut, in this case, 75 mm. The maximum drift ratios are approximately 29%, showing unexpected superior deformation capacity. According to the experimental results discussed in Chapter 7, slit dampers with uniform struts, like the one used for specimen P-SD-0, exhibit maximum strut drift ratios close to 20%.

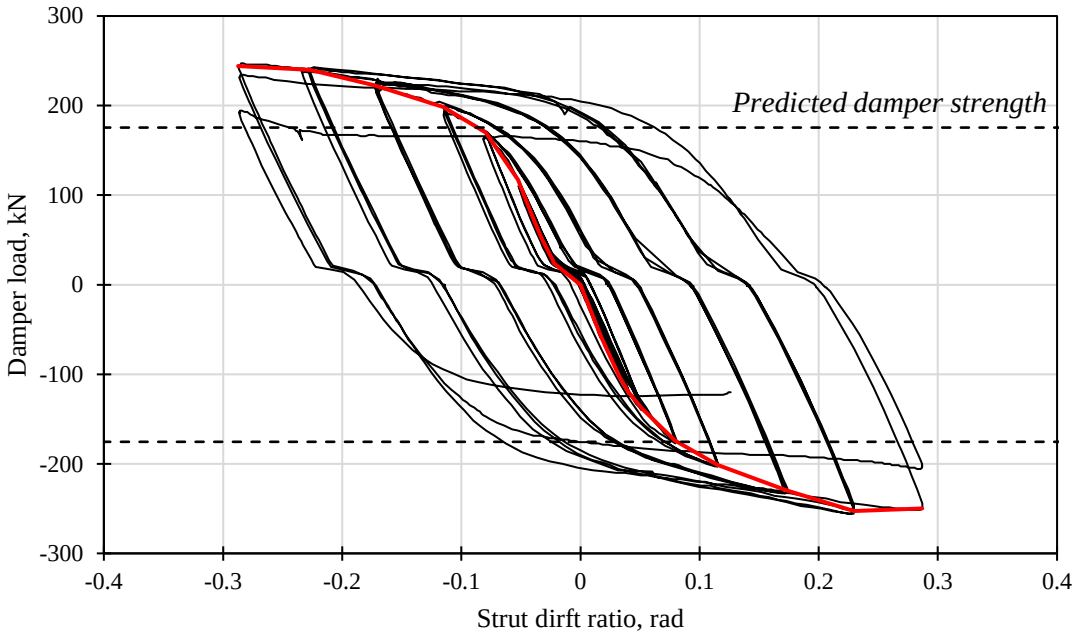

Figure 6-23. Damper load-strut drift ratio curve.

6.3.5.3 Strain of reinforcing steel

The measured strains of two longitudinal rebars of the precast beam are shown in Figure 6-24. The positive and negative values in the horizontal axis are related to the tensile and compressive strains, respectively. The results show an elastic behavior throughout the test. Maximum measured strains were approximately 900μ. For reference, rebar yielding is expected at around 2000μ. In contrast to specimen P-SD-1M (Chapter 5), appropriate capacity design was carried out on specimen P-SD-0, securing an elastic response from the precast beam.

The first two stirrups of the precast beam were also instrumented with SGs but they did not provide reliable measurements.

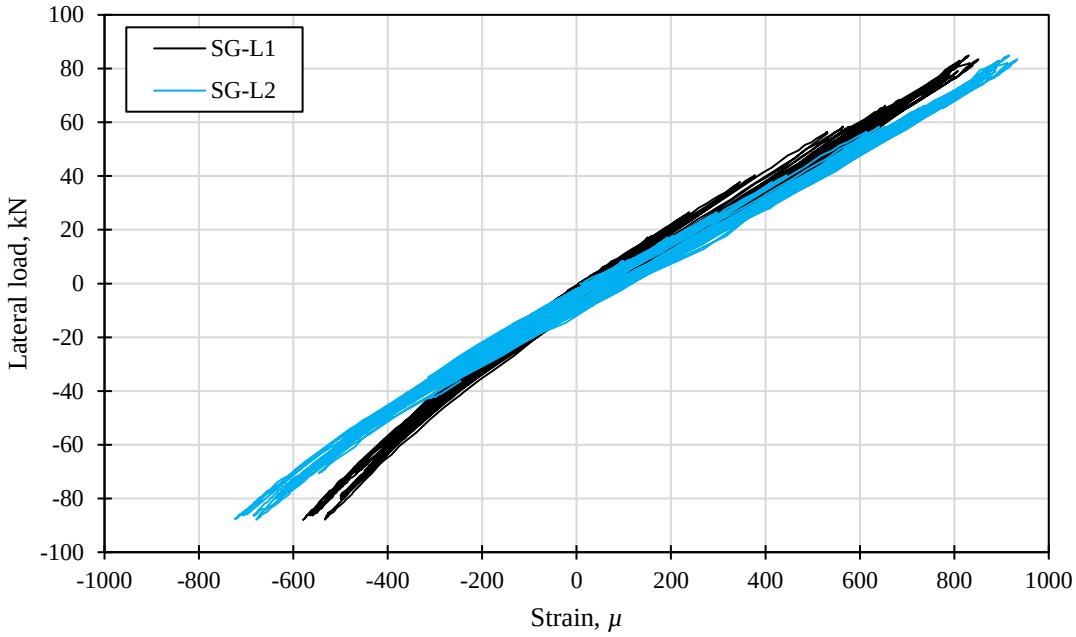

Figure 6-24. Longitudinal reinforcement strain.

6.3.5.4 Ductility and energy dissipation

The energy dissipation capacity of the specimen was evaluated with the same procedure described in Chapter 5. The relative energy dissipation ratios of specimen P-SD-0 are shown in Figure 6-25. In this case, energy dissipation never dropped below 12.5%; however, the test could only be taken to a drift of 0.026 rad. Therefore, the acceptance criteria of ACI 374.1

[18] were not fully met. Regardless, specimen P-SD-0 showed superior energy dissipation capacity, compared to the specimens describe in Chapters 3 and 4, with a maximum ratio of approximately 75%. As a comparison, the cast-in-place (Chapter 3) and precast (Chapter 4) specimens had maximum values of β_i close to 40%.

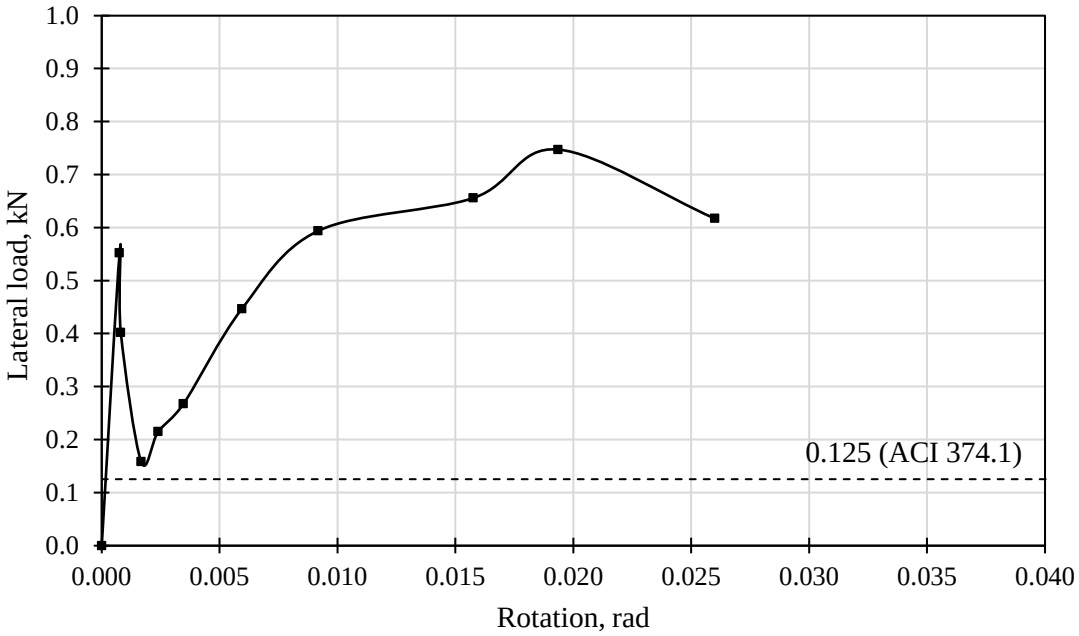

Figure 6-25. Relative energy dissipation ratio (P-SD-0).

To demonstrate how the relative energy dissipation ratio is obtained, Figure 6-25 shows the third cycle at a drift ratio of 0.02 rad (discontinuous black line) and its idealized parallelogram (continuous blue line) with an elastic-perfectly plastic behavior. The ratio β_i is obtained by dividing the area of the hysteresis loop by the area of the parallelogram. As can be seen, the experimental hysteresis loop occupies a large portion of the parallelogram, approximately 72% of the idealized area.

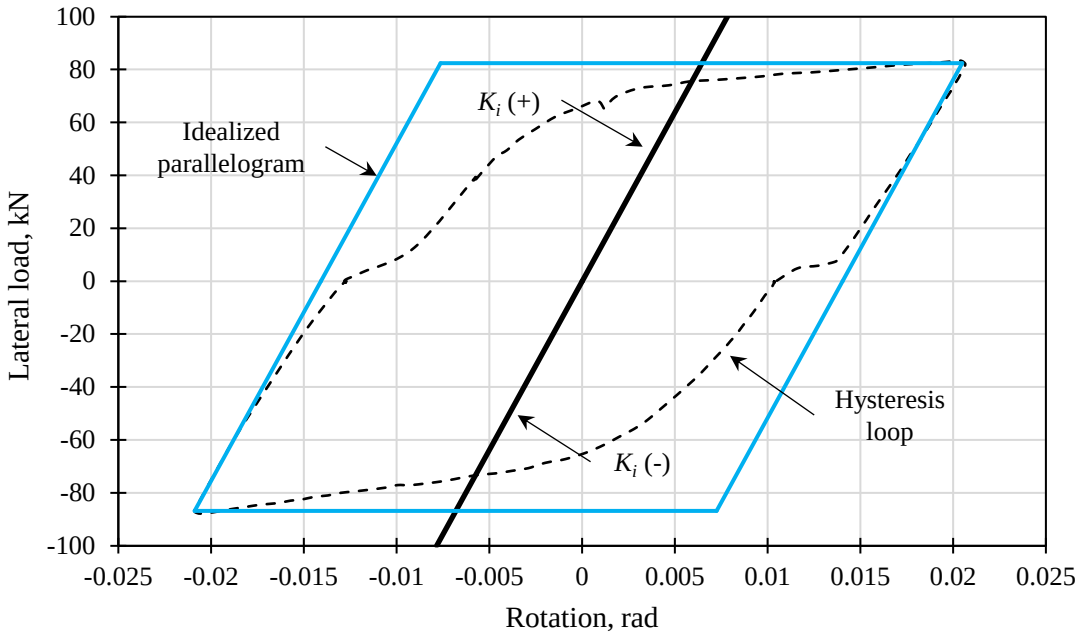

Figure 6-26. Relative energy dissipation at 2.0% drift.

The cumulative ductility ratio was also evaluated and plotted against the cumulative displacement in Figure 6-27. Specimen P-SD-0 showed acceptable behavior compared to the cast-in-place and precast specimens discussed in previous chapters. It dissipated similar amounts of hysteretic energy but for considerably smaller cumulative displacements and significantly smaller damage.

6.3.5.5 Effective stiffness

The experimental normalized effective stiffness, $k_{eff,n}$, at different stages of the test is shown in Figure 6-28. The effective stiffness, k_{eff}, defined as the slope of the peak-to-peak line connecting the maximum achieved displacement-load point in the positive and negative directions, was normalized by the theoretical stiffness (K_T). In Figure 6-28, the predicted beam-column normalized effective stiffness is also shown (red line). It can be seen that the experimental stiffness could be reasonably predicted with the method proposed in Section 6.3.3. The damper's response on its own is represented in blue and was determined with the effective stiffness model proposed later in Chapter 7. This clearly shows the damper's contribution to the beam-column system's overall response.

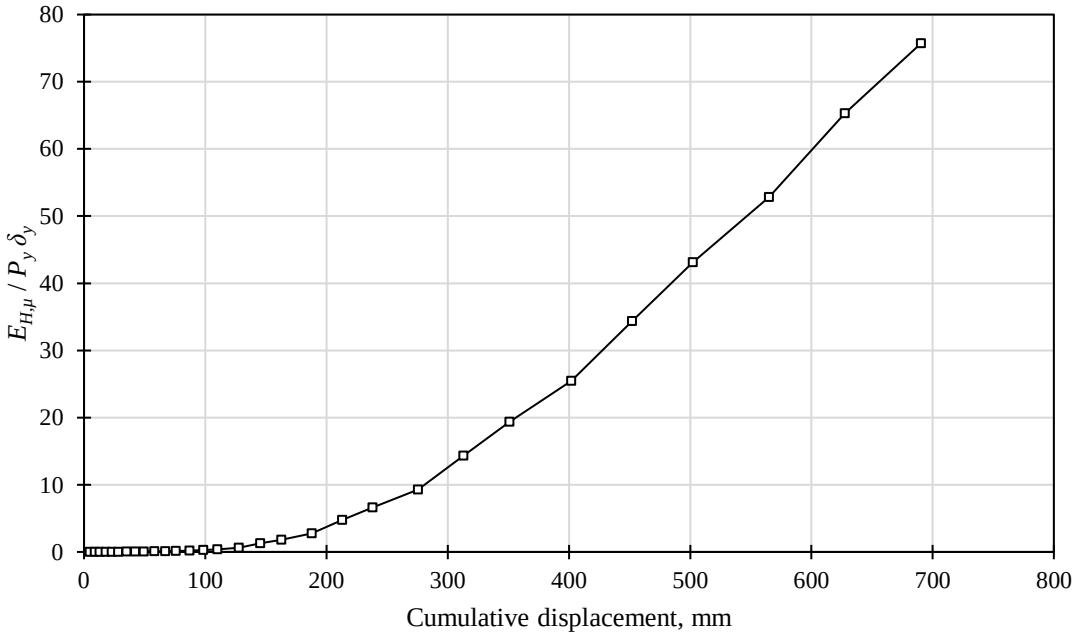

Figure 6-27. Cumulative ductility ratio for specimen P-SD-0.

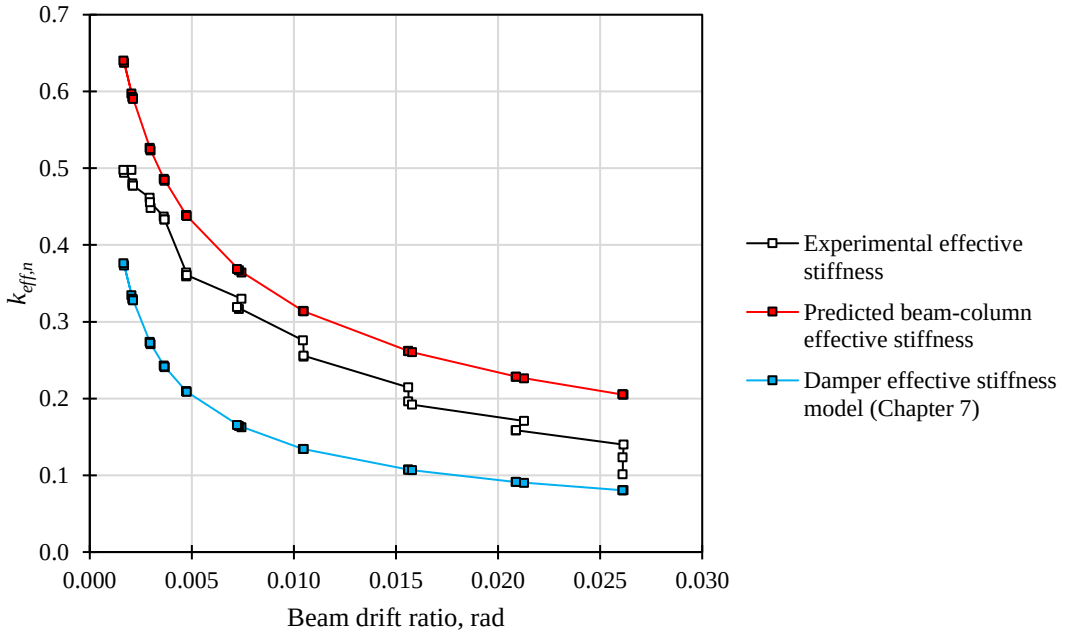

Figure 6-28. Effective stiffness for specimen P-SD-0.

6.3.5.6 Equivalent viscous damping

The equivalent viscous damping ratios are plotted in Figure 6-29 against the ductility ratios and the normalized effective stiffness. From Figure 6-29a, it can be seen that the damping increases as the deformation increases. Before yielding (μ = 1), it is seen that small amounts of hysteretic energy are dissipated, with values below 5%. After that, damping increases to values close to 40%.

In Figure 29b, the damping ratio is compared with the effective stiffness. As can be observed, the damping ratios vary approximately linearly and inversely proportional to the effective stiffness.

6.3.5.7 Observed damage

The observed damage in the precast beam and column existed from previous tests, where cracks developed were not significant. The concrete components were repainted before retesting to mark cracks during testing. However, no new cracks were formed in during testing of specimen P-SD-0.

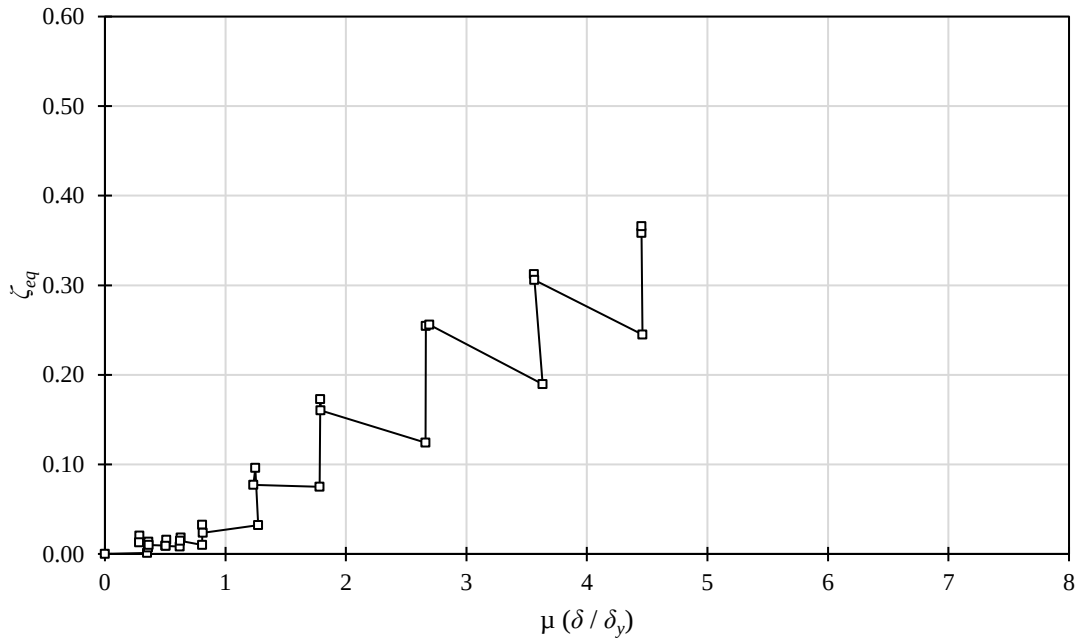

a) Equivalent viscous damping with ductility ratios

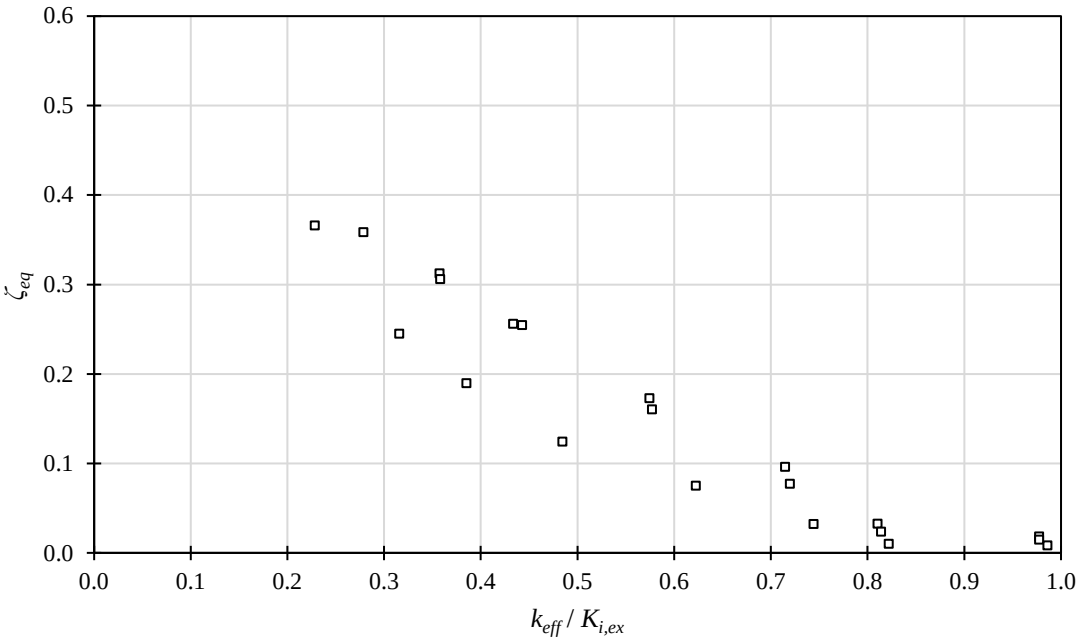

b) Equivalent viscous damping with normalized effective stiffness

Figure 6-29. Equivalent viscous damping.

6.4 Specimen P-SD-1 and P-SD-2R

6.4.1 Description of the tested specimens

Specimen P-SD-1 and P-SD-2R used the same precast beam and column, while the slit damper was welded to the column in P-SD-1 and bolted in P-SD-2R. They were at full-scale (1:1). The specimens were subjected to an incremental reversible cyclic loading protocol applied quasi-statically. The loading protocol was based on ACI 374.1 [18]. After testing P-SD-1, the damaged SD was replaced with the bolted one. The second specimen, named P-SD-2R, was retested with the same protocol. The general characteristics of both specimens are described below.

6.4.1.1 Precast beam and column

The proposed precast connection was non-emulative of cast-in-place concrete structures, that is, without cold or wet joints. The beam had a length of 5000 mm and a cross-section of 450 x 810 mm. The column had a length of 3300 mm and a cross-section of 600 x 600 mm. The geometry is shown in Figure 6-30, and the beam reinforcement is shown in Figure 6-31. There was a gap of 50 mm between the beam and the column. The connection between the beam and the column was achieved with welded components. A steel box at the end of the beam and three dumbbell connections embedded in the column were assembled to facilitate all the necessary connections. At the top of the beam, a steel plate was welded to the column and the top of the steel box. At the bottom of the beam, a vertical transfer plate was welded to the steel box and the SD. For specimen P-SD-1, the SD was welded to the column; while bolted for P-SD-2R. The column had four 75 mm PVC ducts to anchor the specimen to the reaction slab.

The main longitudinal reinforcement of the precast beam consisted of four #10 rebars at the top and bottom. All of them were welded to the steel box since continuity could not be provided through the joint or within the beam itself. In addition, the beam had two #4 rebars on its vertical faces as reinforcement for volumetric changes in accordance with NTC-C-2020 [41]. Transverse reinforcement consisted of #3 stirrups evenly spaced 150 mm apart. Beam reinforcement was consistent with low ductility detailing [41]. Details of the beam reinforcement are shown in Figure 6-31.

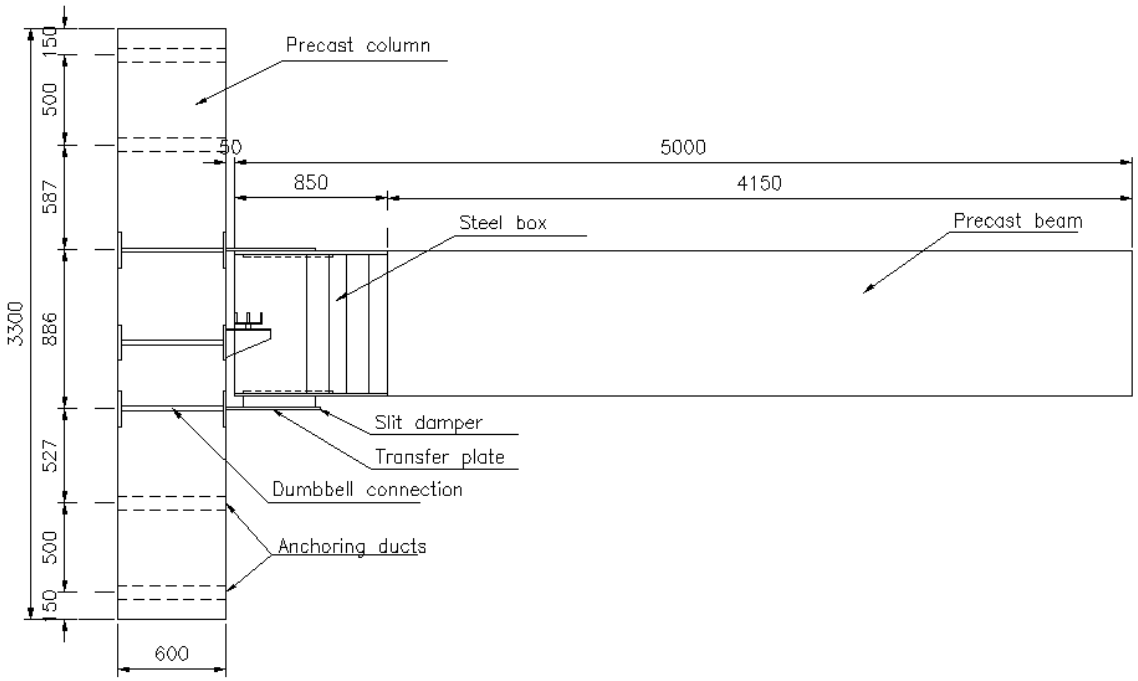

Figure 6-30. Geometry of specimen P-SD-1, dimensions in mm.

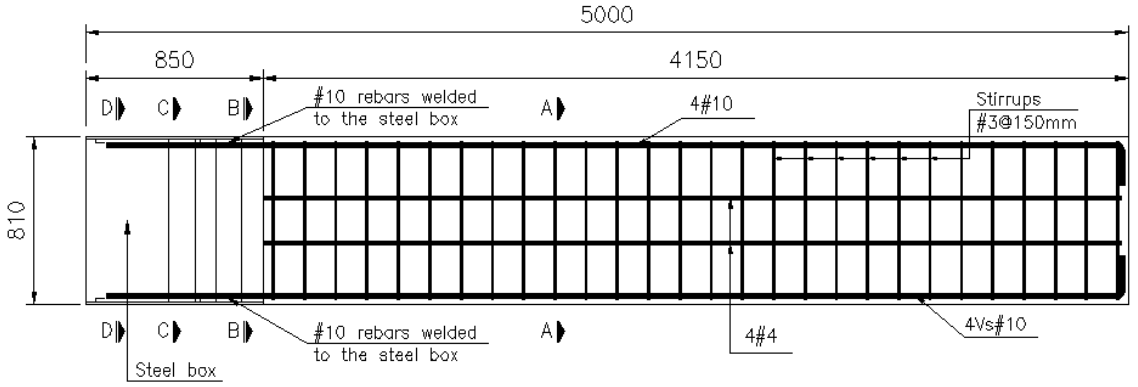

a) Beam reinforcement

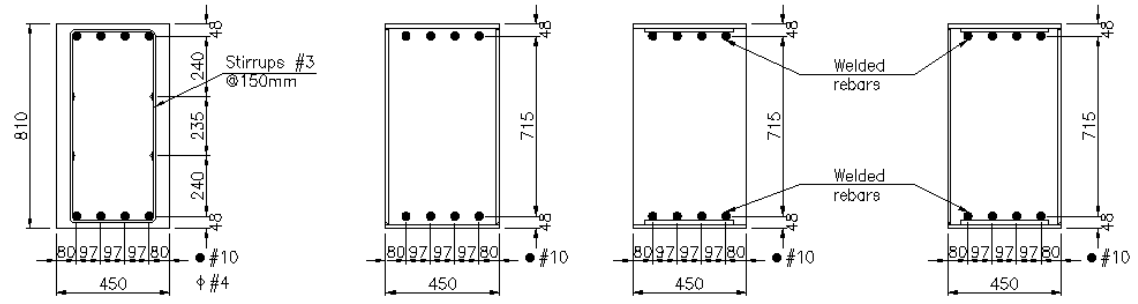

b) A-A c) B-B d) C-C e) D-D

Figure 6-31. Beam reinforcement, dimensions in mm.

At the end of the beam, where the connection was made, the concrete was confined by a steel box that spanned all four faces of the beam and extended toward the center of the beam for a length of approximately one depth of the beam. The superior and inferior plates of the steel box were continuous with a length of 850 mm. The side plates were discontinuous in order to use less steel and welding. The steel box before and after pouring of the concrete is shown in Figure 6-32. The continuity of the main longitudinal steel was achieved by welding the #10 rebars to the steel box at the top and bottom. A length of 300 mm free of welds was left inside the steel box, as shown in Figure 6-33. This was done so that the region where the weld ended, which would be less ductile, did not coincide with the interface between the concrete and the steel box.

a) Before concrete pouring b) After concrete pouring

Figure 6-32. Steel box.

In Figure 6-34, the geometry and reinforcement of the precast column are shown. The component had four 75 mm diameter ducts for anchoring it to the reaction floor in the laboratory. To achieve the connection with the beam, three “dumbbell” type connections were installed, consisting of two plates joined by four 25 mm diameter steel bars (see Figure6-34a and Figure 6-34b). It was decided to use three separate connections instead of a single piece to make the installation of the stirrups easier. The smaller dumbbells are also easier to maneuver for the precast plant workers. The longitudinal reinforcement of the column consisted of four #12, two #8, and four #6 rebars, and the transverse reinforcement consisted of three #3 stirrups spaced 150 mm apart (see Figure 6-34c and Figure 6-34d). A

20x20 mm chamfer was left on all edges of the precast column per common practice. The precast column, before and after the pouring of the concrete, is shown in Figure 6-35.

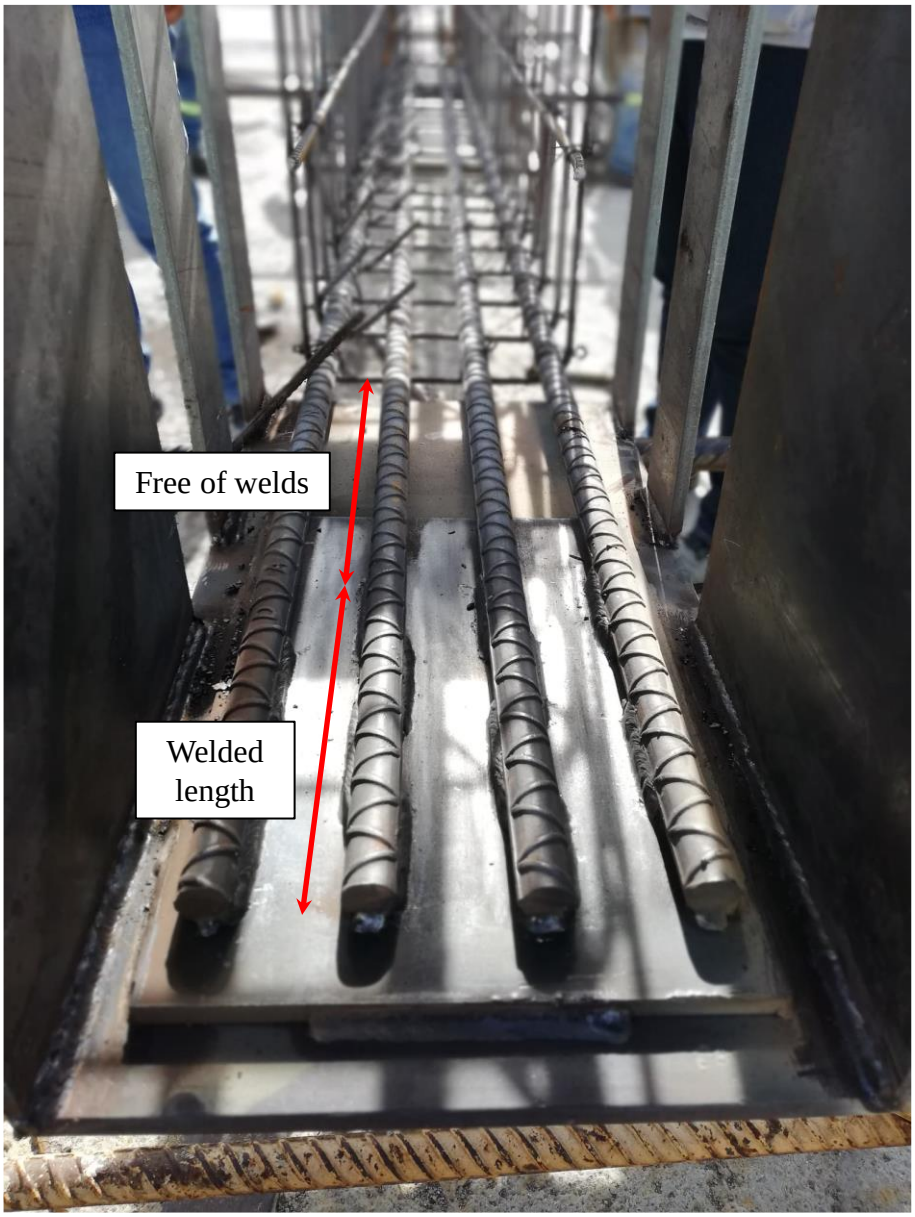

Figure 6-33. Welding of #10 rebars.

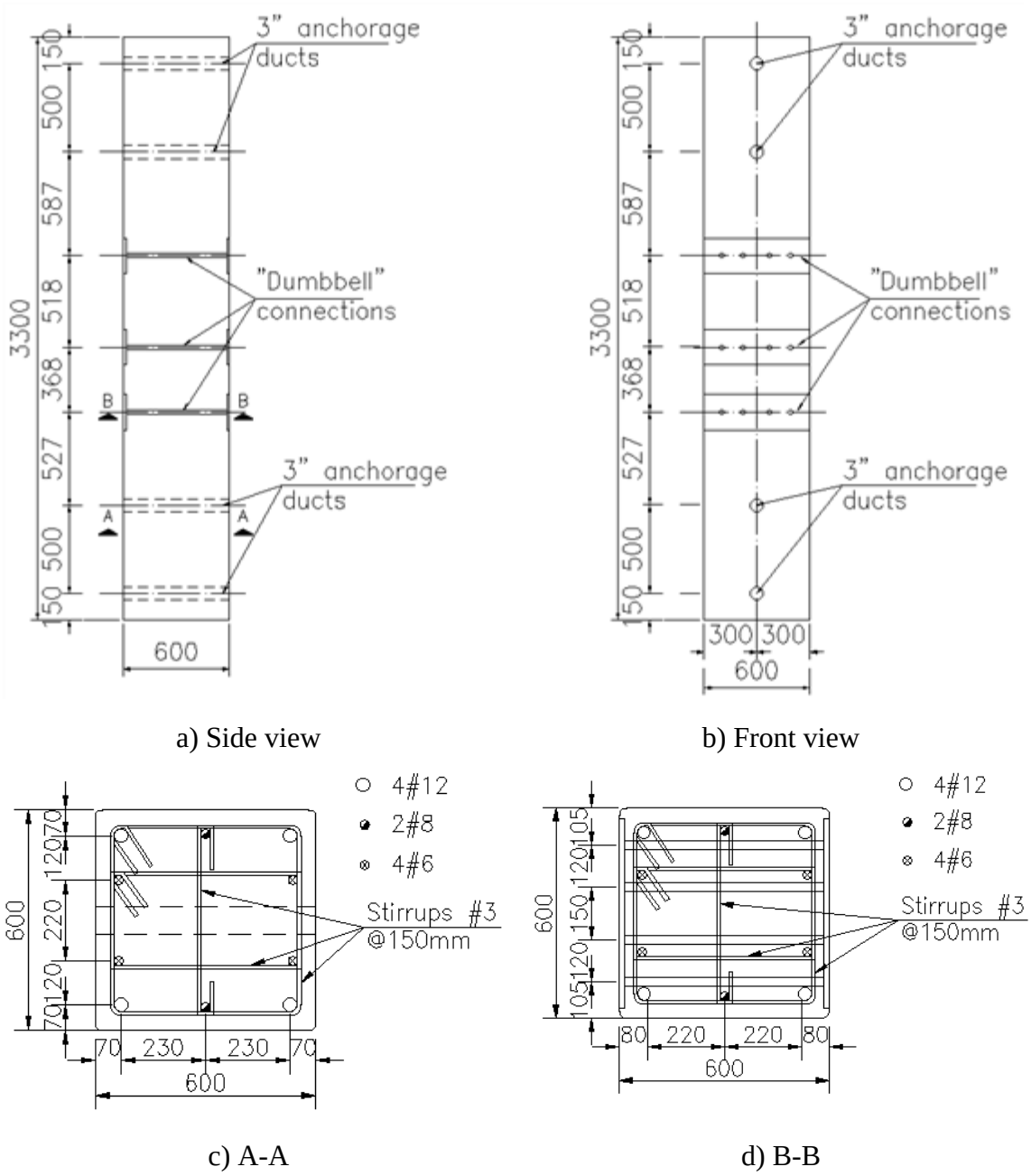

a) Side view

b) Front view

c) A-A

d) B-B

Figure 6-34. Geometry and reinforcement of the precast column.

a) Before pouring of concrete

b) After pouring of concrete

Figure 6-35. Precast column.

6.4.1.2 Slit damper

The two SDs used for specimens P-SD-1 and P-SD-2 were identical. They had 40 non-uniform struts with a width of 15.9 mm at the ends and 7.95 mm at the center, with a length of 110 mm. The dampers were made of structural steel with a nominal yield stress of 345 MPa. The geometry of the proposed SD is shown in Figure 6-36. In Figure 6-37, the bolted configuration for specimen P-SD-2R is shown. The dimensions of the damper are the same as in Figure 6-36. As mentioned, the same precast concrete components were used for both specimens.

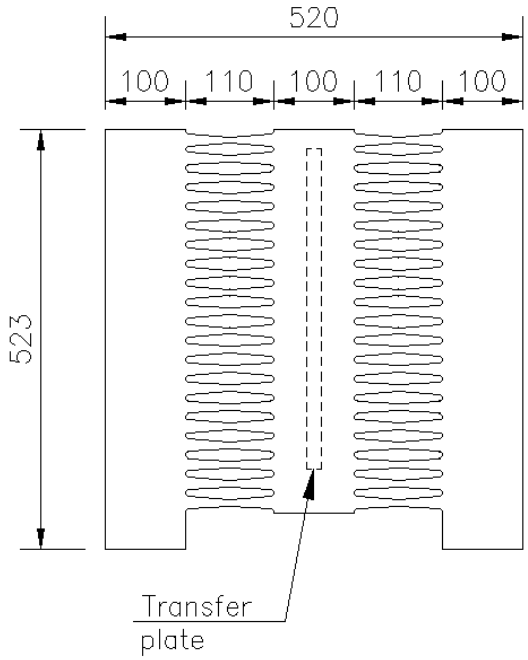

Figure 6-36. Slit damper used for specimen P-SD-1, dimensions in mm.

The damaged SD was removed once the first test was concluded, but two pieces of the first damper (the welded lateral elements) were left to make the replacement more practical. These pieces were later drilled to connect the damper to them with four connection plates, two on each side (see Figure 6-37). The SD was connected to the beam through a welded transfer plate. Certainly, bolts could also be used for the beam-damper connection. However, this was, at the time, a more practical and economical solution. A photograph of the bolted damper is shown in Figure 6-38.

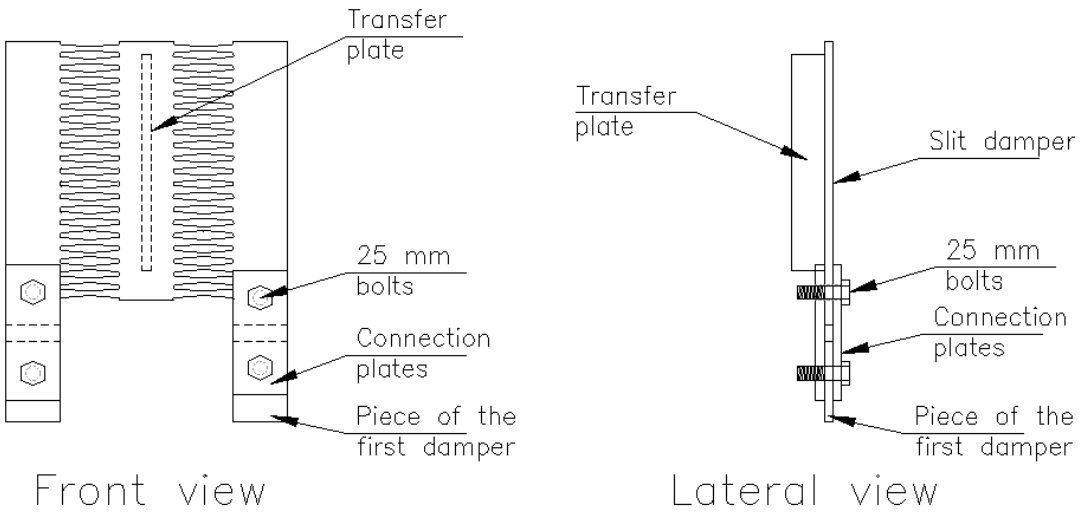

Figure 6-37. Slit damper used for specimen P-SD-2R.

Figure 6-38. Bolted configuration for specimen P-SD-2R.

6.4.1.3 Materials

The specified compressive strength of the concrete (f'_c) was 50 MPa. The reinforcing steel was specified to have a nominal yield stress of 412 MPa, and the structural steel a nominal yield stress of 345 MPa.

Compressive tests were performed on 100 mm-diameter concrete cylinders at different stages, namely before the testing of the specimens (at 63 hours and 28 days) and the day testing of specimen P-SD-1 started. The results are shown in Table 6-6. At 144 days of age, which was the time when specimen P-SD-1 was tested, the average compressive strength of the concrete was 70.8 MPa.

Table 6-6. Compressive test results.

Cylinder ID	Age	Diameter (mm)	Height (mm)	Area (mm2)	Maximum load (kN)	$f'c$ (MPa)	Average $f'c$ (MPa)
CL-1101	63 hours	100	200	7854	345	43.9	44.1
CL-1102	63 hours				349	44.4	
CL-1201	28 days				504	64.1	64.0
CL-1202	28 days				502	63.8	
CL-1301	144 days				560	71.3	70.8
CL-1302	144 days				553	70.4	

Tensile tests were also performed on reinforcing steel and structural steel coupons taken from the batches of materials used to fabricate the specimen. Three Grade 42 [60] rebars of 600 mm in length of each of the following diameters were tested: 9.5 mm (#3), 12.7 mm (#4), 19.0 mm (#6), 25.4 mm (#8), 31.8 mm (#10) and 38.1 mm (#12). The stress-strain curves are shown in Figure 6-39, where the deformation is reported over a length of 200 mm.

Table 6-7 shows a summary of the mechanical properties of the tested specimens. Average values of yield stress, f_{ye}, and tensile strength, f_{ue}, are shown. The ratios f_{ue} / f_{ye} and f_{ye} / f_{yn} are also shown, where f_{yn} is the nominal yield stress, which in this case is 412 MPa. According to the Mexican Standard NMX-B-506-CANACERO-2011 [60], the ratio f_{ue} / f_{ye} must not be less than 1.25. All of the tested rebars complied with this requirement. It can also be observed that, depending on the diameter of the bar, the actual yield stress can vary between 1.15 and 1.34 times the nominal yield stress. The average value of f_{ye} / f_{yn} is approximately 1.25; therefore, this value was used for design and modeling purposes. Considering $1.25f_y$ is also

consistent with the recommendations given in ACI 352R-02 [84], which accounts for strain hardening and other factors.

Three coupons were tested to assess the mechanical properties of the structural steel used for the beam steel box and the column dumbbells. The geometry of the coupons is shown in Figure 6-40. A picture of the tested coupons is shown in Figure 6-41.

The stress-strain curves of the structural steel specimens are shown in Figure 6-42. The reported deformation is over a length of 200 mm. However, slippage was noted between the specimens and the wedges of the testing machine; therefore, the deformations are not completely reliable. From these curves, it can be seen that specimen P2 had the lowest deformation capacity and presented the lowest tensile strength, mainly due to a manufacturing defect where the failure occurred (see Figure 6-43).

Table 6-8 shows the mechanical properties of the three tested steel specimens. Considering specimens P1 and P3, an average yield stress of 330 MPa and an average tensile strength of 451 MPa was obtained. It is clear that the manufacturing defect affected the behavior of specimen P2; however, the ratio f_{ue} / f_{ye} is consistent with that of the other specimens.

Similarly, three structural steel coupons, taken from the same material from which the two SDs were made, were tested with the same geometry shown in Figure 6-40. A photograph of the tested coupons is shown in Figure 6-44. The stress-strain curves of these coupons are shown in Figure 6-45. The reported deformation is over a length of 200 mm. The same problems with slippage were observed. Table 6-9 shows the mechanical properties of the tested coupons. An average yield stress of 342 MPa and average tensile strength of 461 MPa was obtained.

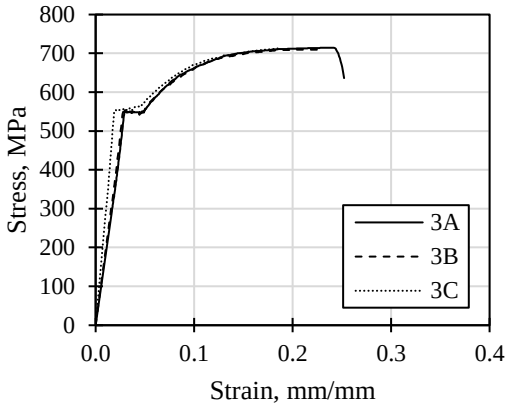

a) #3

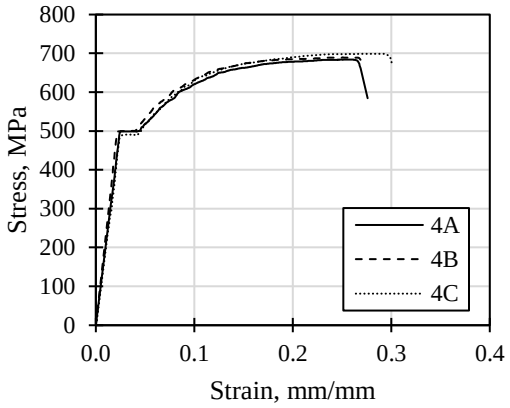

b) #4

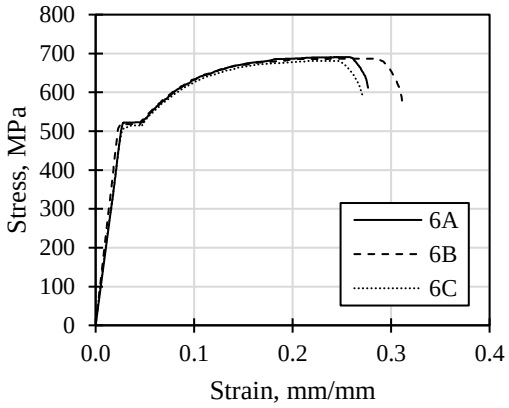

c) #6

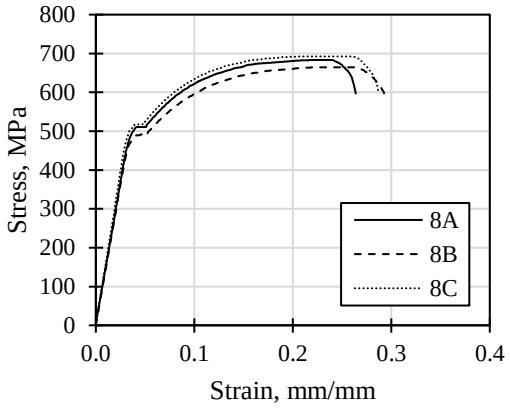

d) #8

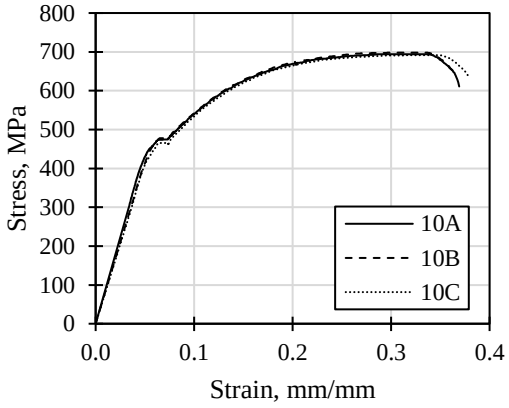

e) #10

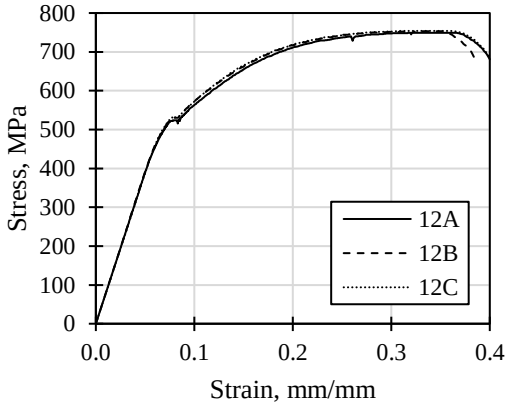

f) #12

Figure 6-39. Stress-strain curves of reinforcing steel coupons.

Table 6-7. Tensile test results of reinforcing steel coupons.

Rebar No.	f_{ye} (MPa)	f_{ue} (MPa)	f_{ue} / f_{ye}	f_{ye} / f_{yn}
3	551	712	1.29	1.34
4	496	690	1.39	1.20
6	518	681	1.31	1.26
8	507	680	1.34	1.23
10	473	682	1.44	1.15
12	529	743	1.41	1.28
Average	512	698	1.36	1.24

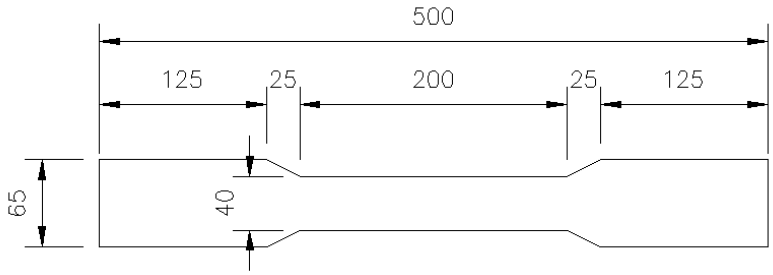

Figure 6-40. Geometry of structural steel coupons.

Figure 6-41. Structural steel coupons.

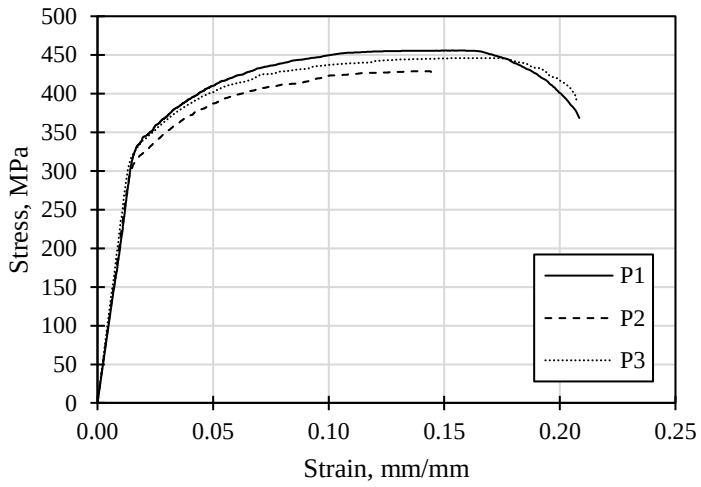

Figure 6-42. Tensile test results of structural steel coupons.

a) Manufacturing defect b) Fracture

Figure 6-43. Coupon C-2.

Table 6-8. Tensile test results of structural steel coupons.

Coupon	f_{ye} (MPa)	f_{ue} (MPa)	f_{ue} / f_{ye}
C-1	334	456	1.36
C-2	313	429	1.37
C-3	325	446	1.37
Average	324	444	1.37

a) Initial state b) Final state

Figure 6-44. Typical damper coupon.

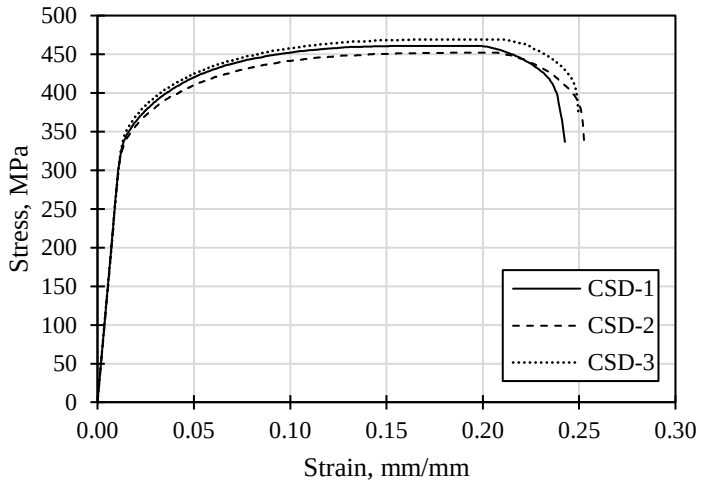

Figure 6-45. Tensile test results of damper coupons.

Table 6-9. Tensile test results of damper coupons.

Coupon	f_{ye} (MPa)	f_{ue} (MPa)	f_{ue} / f_{ye}
CSD-1	341	461	1.35
CSD-2	335	452	1.35
CSD-3	349	469	1.34
Average	342	461	1.35

6.4.2 Fabrication process

Documenting the fabrication process of the tested specimen, carried out in a precast plant, was fundamental in developing the proposed system to evaluate its viability. In general, the fabrication was straightforward, with a small learning curve since the personnel in charge of

the production of the steel and precast components are well-trained and normally execute similar tasks on a daily basis and in controlled environments. The general fabrication process is described below.

First, eight #10 rebars were welded to two 15.9 mm thick, 200 x 250 mm support plates (four rebars on each) that were previously welded to the larger plates that formed the top and the bottom of the steel box. The support plates were used to give an adequate cover to the steel reinforcement without using a thicker plate. These components were then aligned with the lateral plates and welded together to form the box (see Figure 6-46). At the same time, three dumbbells were assembled with four 25 mm diameter bars using plug welds (Figure 6-47).

Figure 6-46. Steel box assembly.

Figure 6-47. Dumbbell connection assembly.

The steel reinforcement of the column was assembled as per common practice (see reference [41]), introducing the dumbbells at the indicated heights of the column (see Figure 6-48). Meanwhile, the transverse reinforcement of the beam was also being assembled (see Figure 6-49). The assembled steel box and the welded rebars are shown in Figure 6-50.

Figure 6-48. Assembly of the column with the “dumbbell” type connections.

Figure 6-49. Beam assembly.

Figure 6-50. Steel box and welded rebars.

At this point, instrumentation could be carried out. Figure 6-51 shows a general view of the SGs located on longitudinal and transverse reinforcement of the beam. Eight SGs were placed on longitudinal rebars, and two were placed on the first pair of stirrups adjacent to the steel box. No SGs were installed in the precast column nor on structural steel components.

Preparation of the metallic formwork followed, as shown in Figure 6-52. Then casting of the beam (Figure 6-53) and column (Figure 6-54), and finally, concrete polishing (Figure 6-55). Figure 6-56 shows the finished precast components a week after extraction.

Figure 6-51. Strain gauges on longitudinal and transverse reinforcement.

a) Placement of formwork

b) Formwork securing

Figure 6-52. Preparation of metallic formwork.

Figure 6-53. Casting of the beam.

Figure 6-54. Casting of the column.

a) Beam b) Column

Figure 6-55. Concrete polishing.

a) Precast beam b) Precast column

Figure 6-56. Finished components.

6.4.3 Design of specimen P-SD-1

The design of P-SD-1 was similar to the design of P-SD-0 shown in section 6.3.3. The effective length method of Chapter 7 was used to determine the elastic stiffness, strength, and yield displacement of the proposed SD. These parameters were obtained with the mechanical and geometric properties shown in Table 6-10. The yield stress was obtained from coupon tests.

Table 6-10. Properties of the SDs used for specimens P-SD-1 and P-SD-2R.

Property	Definition	Value
f_{ye} (MPa)	Yield stress	342
E (MPa)	Young's modulus	200000
μ	Poisson's ratio	0.3
n	Number of struts	40
t (mm)	Strut thickness	15.9
b (mm)	Strut width	15.9
l (mm)	Strut total length	110
r (mm)	Strut radius	4.0
l_r (mm)	Effective length for strength	110
l_k (mm)	Effective length for elastic stiffness	132

A FEA was conducted in ABAQUS [7] to corroborate the calculated structural characteristics of the SD. The steel material was considered to have an elastic-perfectly plastic behavior with a yield stress of 342 MPa and a Poisson's ratio of 0.3. The SD was modeled using C3D10 (10-node quadratic tetrahedron) elements [7] with an approximate size of 5 mm. The model is shown in Figure 6-57. The capacity curve of this simulation is shown in Figure 6-58. The results obtained with the equations proposed in Chapter 7 are also shown for comparison. As can be seen, the structural characteristics of the SD could be precisely determined.

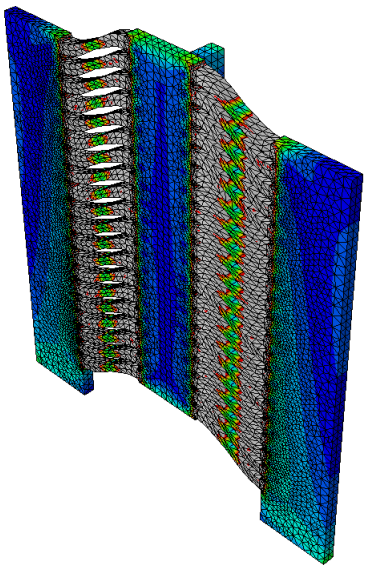

Figure 6-57. Finite element model of the proposed SD and deformed shape.

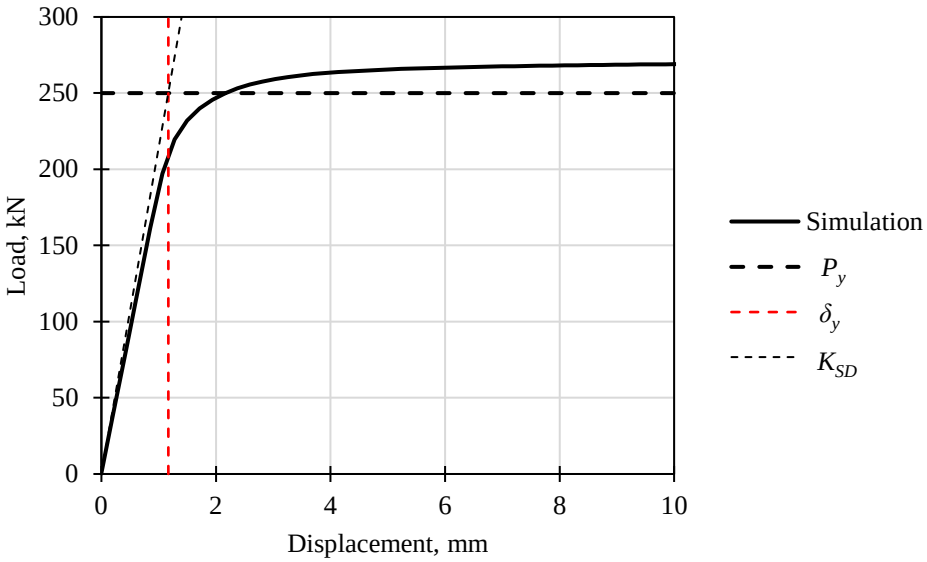

Figure 6-58. Theoretical capacity curve of the SD for specimen P-SD-1.

With the general behavior of the SD determined, the key structural characteristics of the beam-column subassembly were obtained with the procedure proposed in Section 6.2. The most relevant results of the design are shown in Table 6-11.

Table 6-11. Design summary of specimens P-SD-1 and P-SD2R.

Element / assembly	Structural characteristic	Value
Isolated SD	P_y (kN)	250.0
	K_{SD} (kN/mm)	214.2
	Δ_y (mm)	1.17
Beam-column (P-SD-1)	P_y (kN)	52.7
	M_y (kN-m)	234.6
	β	0.04
	K_B (kN/mm)	13.3
	K_T (kN/mm)	5.6
	Δ_y (mm)	9.50

The effective stiffness of the tested specimens was predicted with the same procedure shown in section 6.3.3. The predicted effective stiffness of P-SD-1 is shown in Figure 6-59, and the effective stiffness model of the isolated damper, governed by Eq. (6-12), is also shown for comparison. Assuming that the effective stiffness was accurately characterized, the contribution of the damper to the overall stiffness of the beam-column subassembly can clearly be seen. In this case, due to the geometry of the specimen, the flexural stiffness of the beam is greater than the equivalent flexural stiffness of the damper. The stiffness ratio K_B / βK_{SD}, which was 1.39, means that the contribution of the beam is less significant, and that is why the predicted effective stiffness is closer to the isolated effective stiffness model, which represents the contribution of the damper only. The drift ratios used for this prediction are the same target drift ratios from the loading protocol shown below.

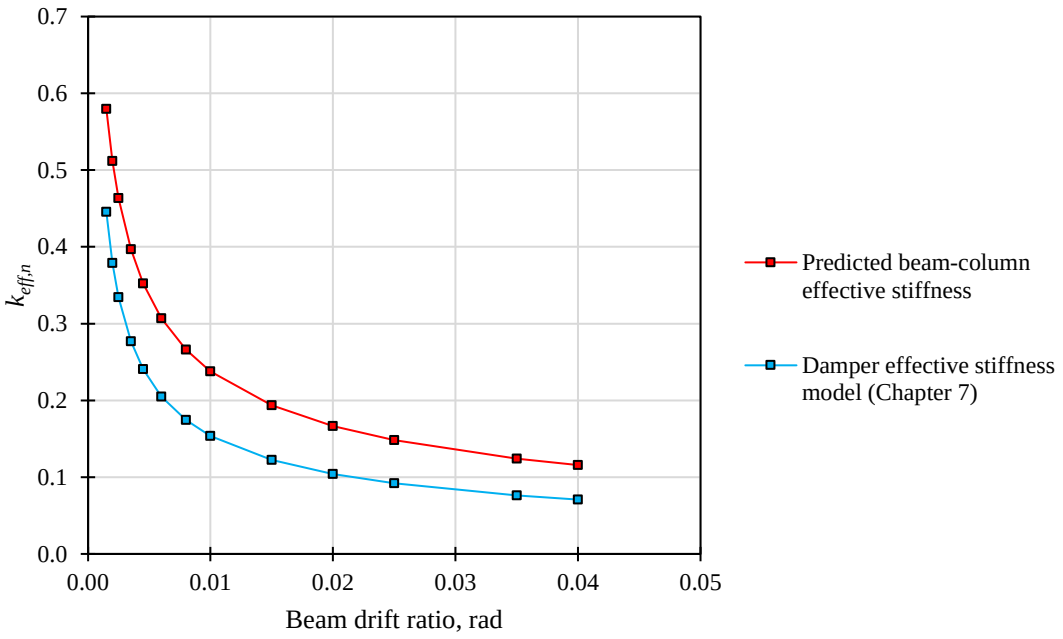

Figure 6-59. Predicted effective stiffness of specimen P-SD-1 at different drift ratios.

6.4.4 Experimental Program

6.4.4.1 Test setup

The test setup of specimens P-SD-1 and P-SD-2R was similar to that applied to specimen P-SD-0. The setup is shown in Figure 6-60. As can be seen, the beam was oriented vertically and the column horizontally. A displacement-controlled loading protocol was applied at the tip of the beam utilizing two 500 kN hydraulic actuators connected in series. The forces necessary to achieve said displacements were measured with two load cells installed in each actuator. The column was anchored to the reaction slab with four post-tensioned steel bars. The actuator was anchored to a 130 mm thick steel plate, and this was anchored to the reaction wall. No axial load was applied to the column. According to ACI 374.1 [18], applying an axial force to the column is unnecessary. Additionally, a metallic column was placed that functioned as a support for the instrumentation. The experimental arrangement is shown in plan in Figure 6-61.

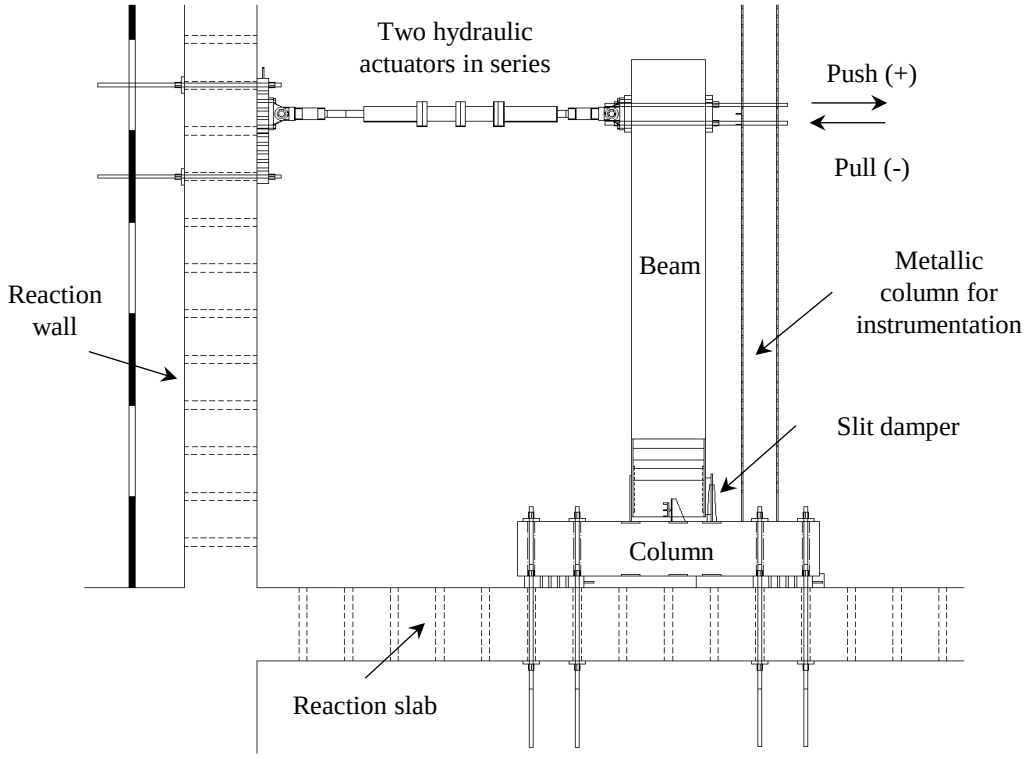

Figure 6-60. Test setup (elevation).

6.4.4.2 Loading protocol

A displacement-controlled loading protocol based on the recommendations of ACI 374.1 [18] was applied. The loading protocol is shown graphically in Figure 6-62.

6.4.4.3 Instrumentation

Linear variable displacement transducers (LVDTs) were used to measure local displacements. Horizontal LVDTs were used to measure horizontal displacements at different beam heights. Vertical LVDTs were used to measure relative rotations of the column and vertical displacements of the SD and the beam. Finally, diagonal LVDTs were used to measure shear deformations in the beam and joint.

In Figure 6-63, the vertical and horizontal LVDTs locations are shown. Four horizontal LVDTs were placed at different heights of the beam. Two of them (H1 and H2) were placed at the height of the load application, approximately 4750 mm from the center of the column; another at 2850 mm (H3); and the last one at 1900 mm (H4). An LVDT was placed at the

center of the damper (V1), and another two were placed 100 mm from the base of the beam towards the center (V2 and V3). Finally, five LVDTs were placed along the column to measure its relative rotations (V4 to V8).

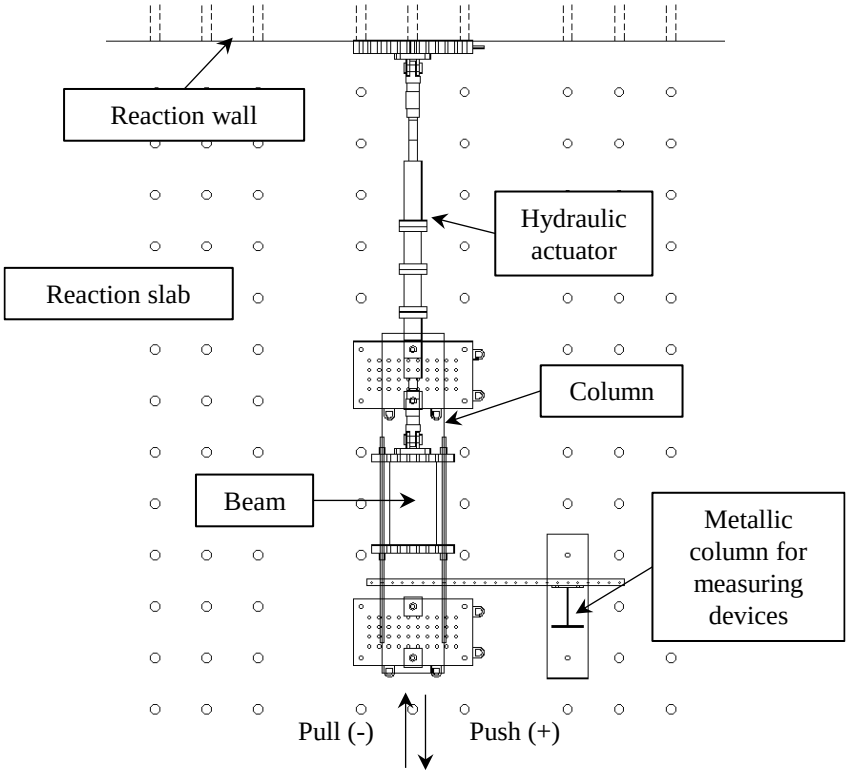

Figure 6-61. Test setup (plan).

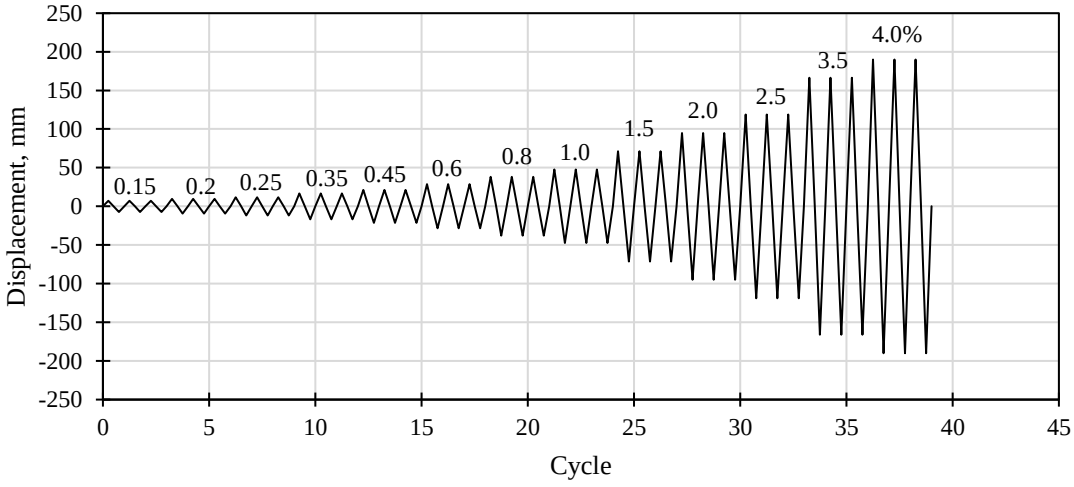

Figure 6-62. Loading protocol.

Two diagonal LVDTs were placed on the beam 100 mm from the steel box towards the free end of the beam (D1 and D2), and another two were centered in the joint region (D3 and D4). All diagonal LVDTs had a length of approximately 730 mm. Locations of the diagonal LVDTs are shown in Figure 6-64.

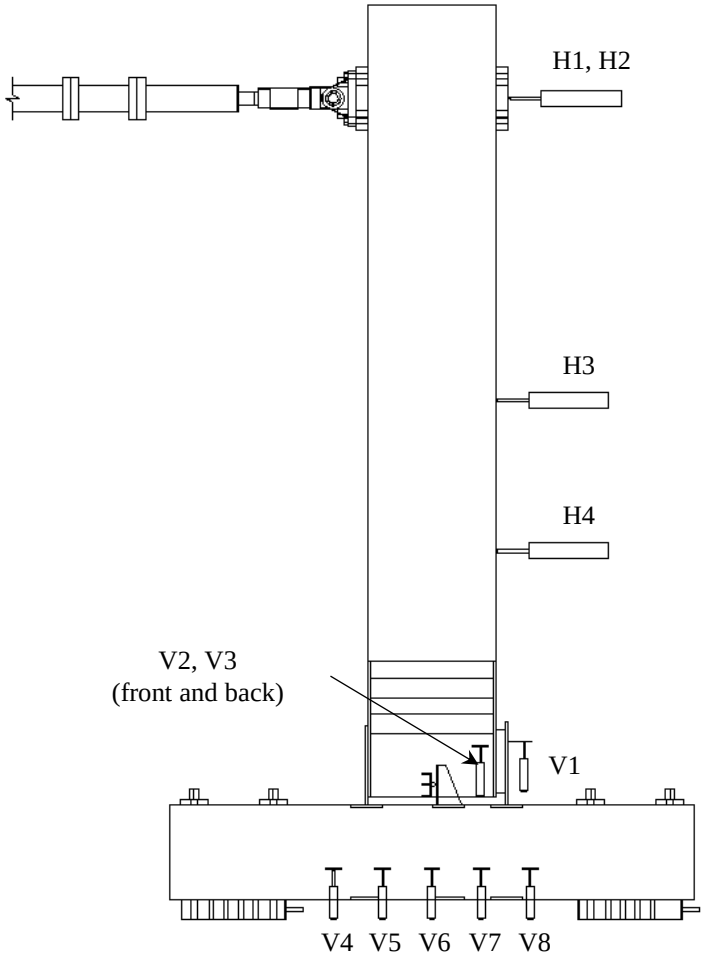

Figure 6-63. Horizontal and vertical LVDTs.

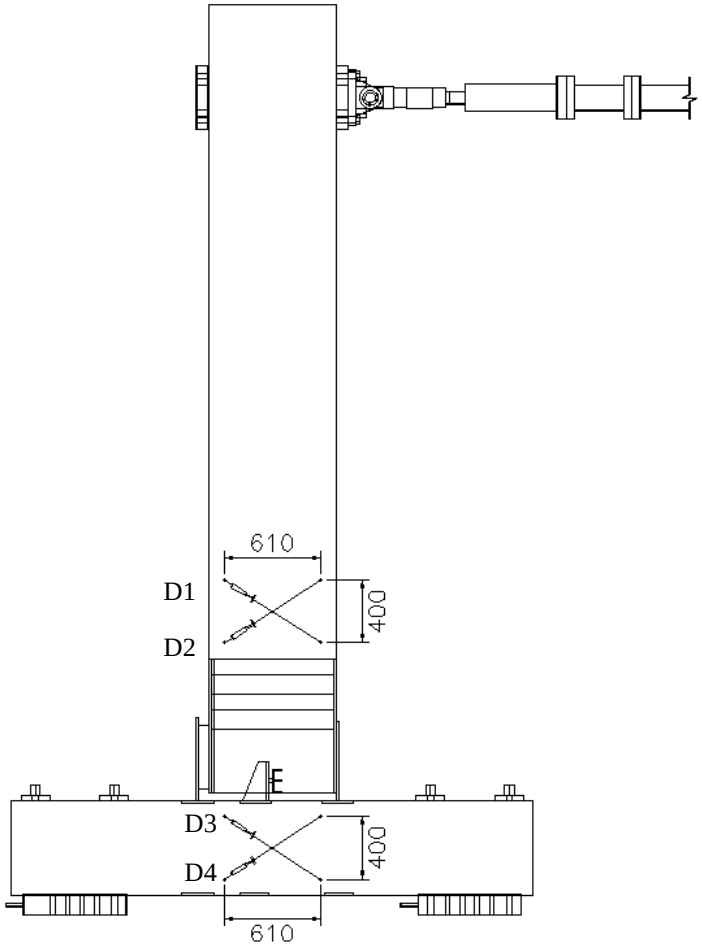

Figure 6-64. Diagonal LVDTs.

Strain gauges (SGs) were placed to measure strains of the longitudinal and transverse reinforcement of the beam. The specimen was instrumented with 10 SGs. Eight SGs were installed on longitudinal rebars (SG-L), and the other two were placed on transverse reinforcement (SG-T). Locations of the SGs are shown in Figure 6-65. Two of the longitudinal SGs were installed inside the steel box on the top rebars where there was no welding (SG-L1 and SG-L3). The other longitudinal SGs were outside the steel box. The two transverse SGs were placed in the first two stirrups at half the height of the beam (SG-T1 and SG-T2). The column was not instrumented with SGs.

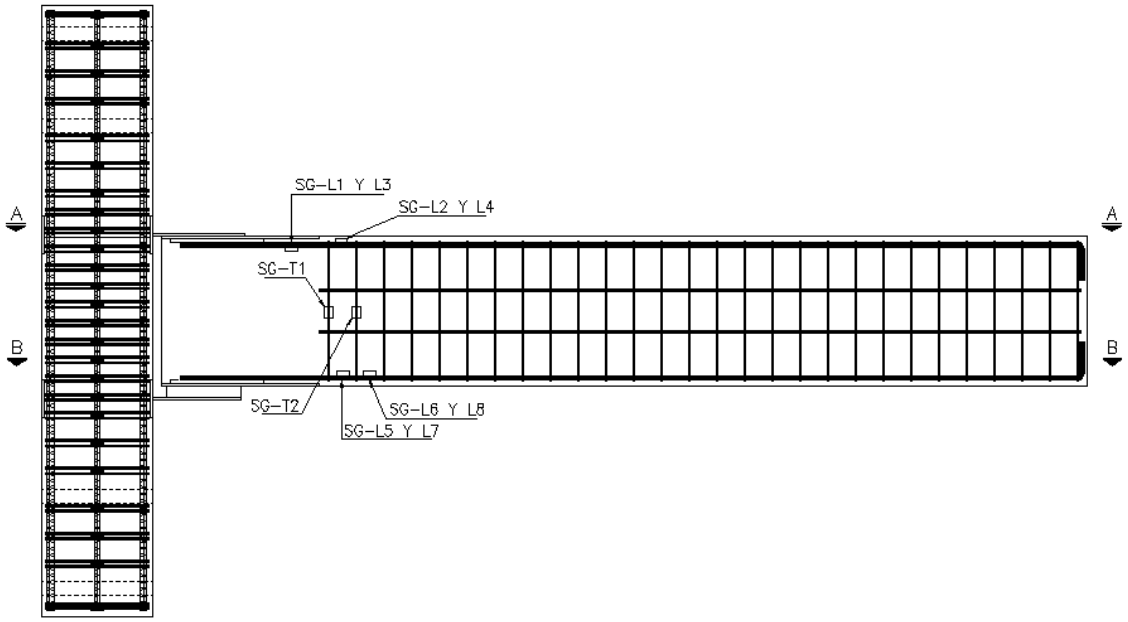

a) Location of SGs.

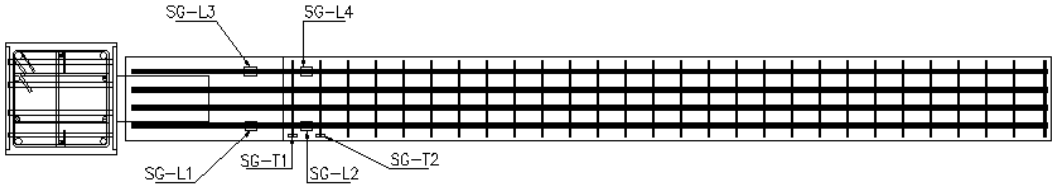

b) A-A

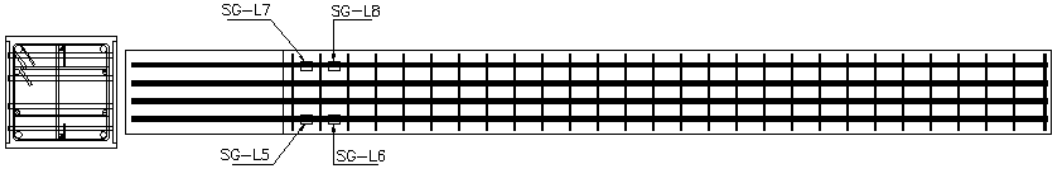

c) B-B

Figure 6-65. Strain gauge locations on reinforcing steel.

Finally, three strain gauges were placed on the damper of specimen P-SD-1, as shown in Figure 6-66. Specimen P-SD-2R's damper was not instrumented.

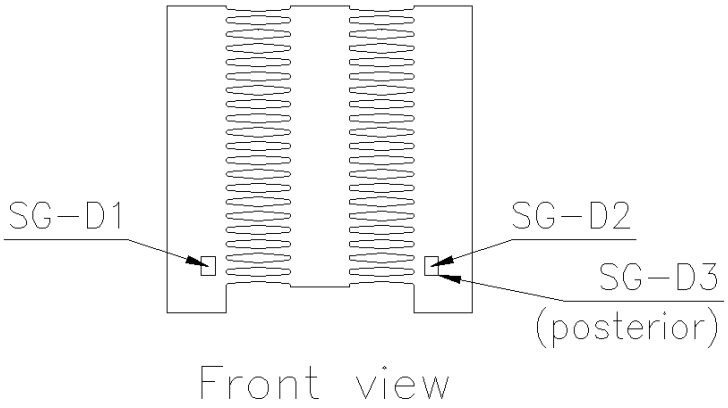

Figure 6-66. Strain gauge locations on SD (specimen P-SD-1).

6.4.5 Results

6.4.5.1 Beam vertical displacement and steel strain histories

Vertical displacements of the beam (close to the bottom) and the damper are shown in Figure 6-67. For specimen P-SD-1, maximum displacements at the center of the damper were approximately 35 mm (32% strut drift ratio), while for specimen P-SD-2R, maximum displacements were around 40 mm (36% strut drift ratio).

With Eq. (6-7), the vertical displacements at the center of the damper could be predicted through the lateral displacements at the beam's tip. Values using this simple geometric relationship, calculated using the lateral displacements measured with H1, are shown in Figure 6-68. Again it can be seen that the system's response can be easily predicted with precision, which also suggests that the beam rotates as a rigid body.

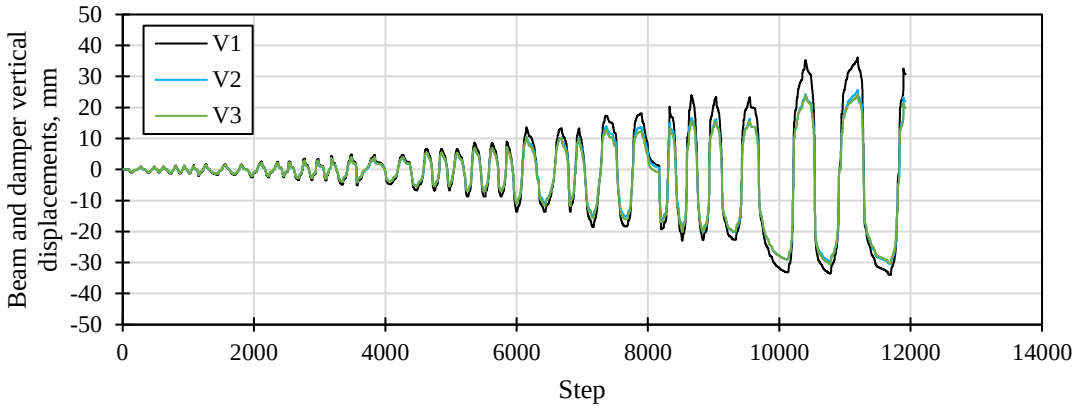

a) P-SD-1

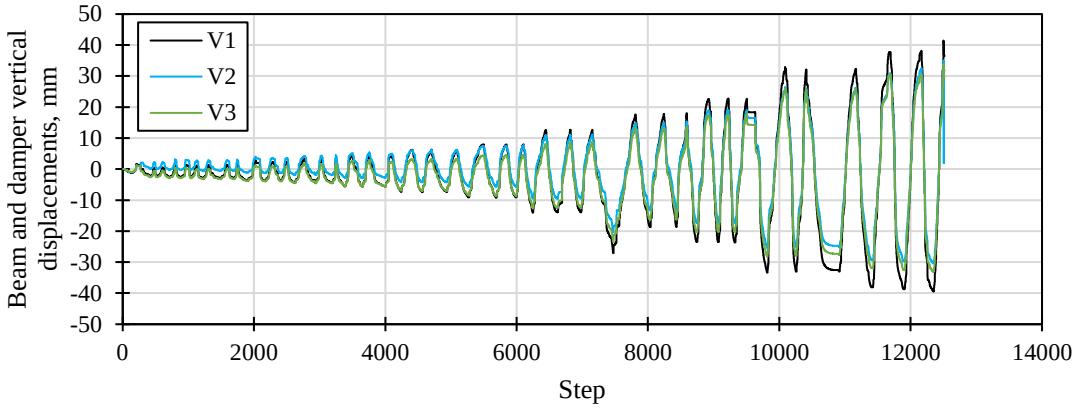

b) P-SD-2R

Figure 6-67. Beam and damper vertical displacements.

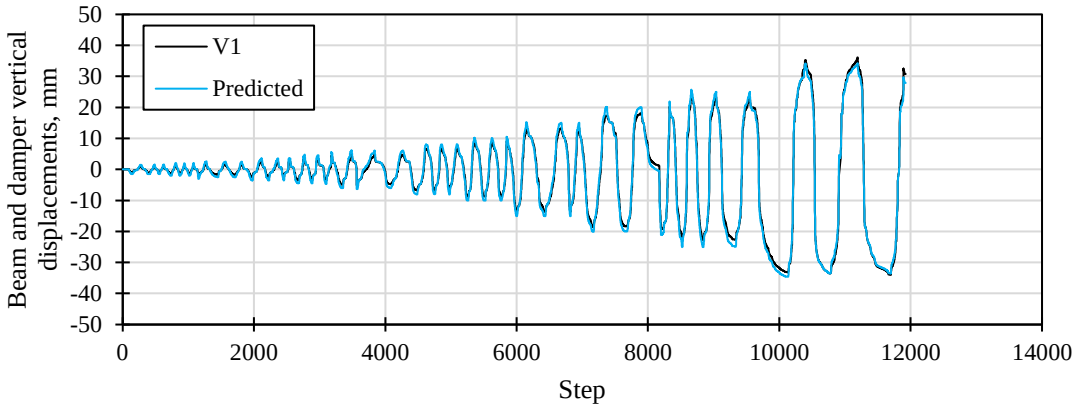

Figure 6-68. Estimated damper vertical displacements.

Strains on longitudinal reinforcements are shown in Figure 6-69. For reference, yielding is normally expected at 2000μ. Specimen P-SD-1 developed maximum strain values around 800μ, and P-SD-2R exhibited maximum strain values close to 600μ. These values are reasonable since the beam strength to damper strength ratio was greater than 2. Strains on transverse reinforcement were significantly lower, with values lower than 60μ, basically negligible (Figure 6-70).

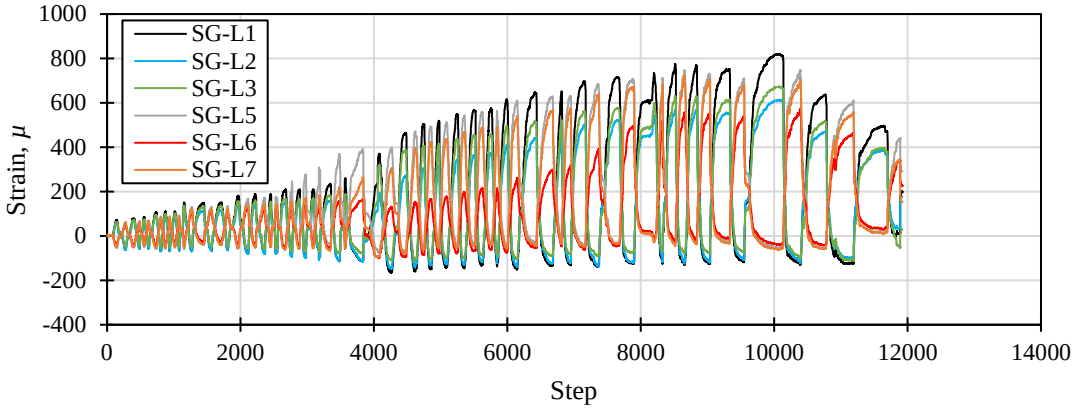

a) P-SD-1

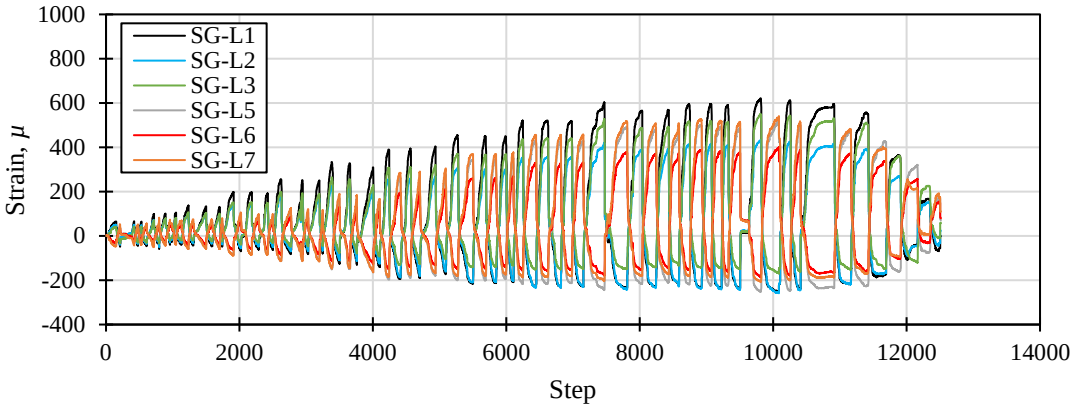

b) P-SD-2R

Figure 6-69. Longitudinal reinforcement strain history.

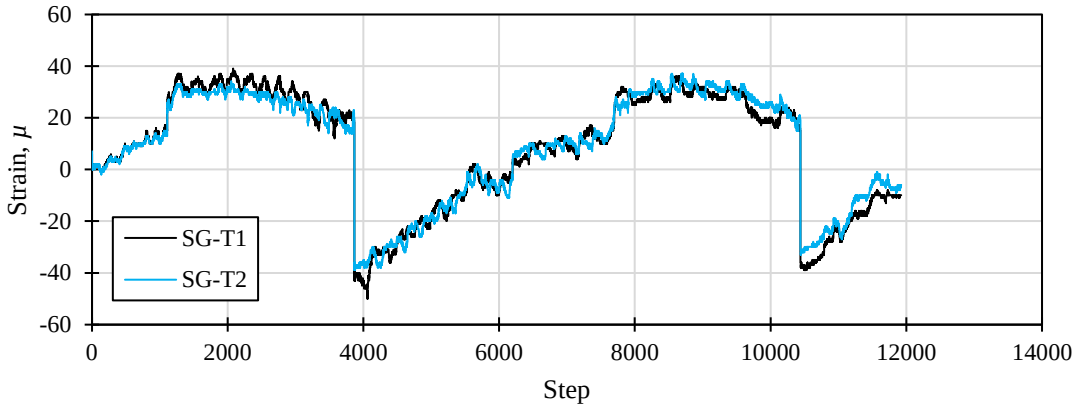

a) P-SD-1

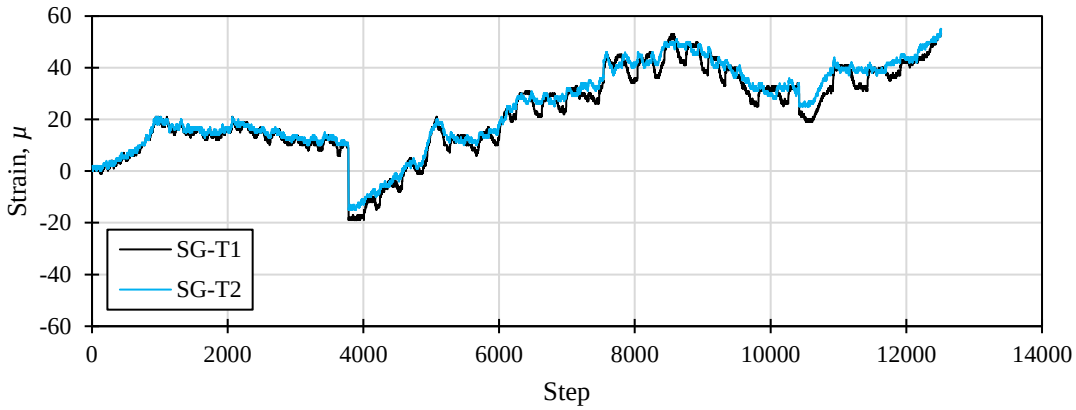

b) P-SD-2R

Figure 6-70. Transverse reinforcement strain history.

Strains on specimen P-SD-1's damper were significantly high in the final stages of the test (see Figure 6-71). Yielding of the damper (aproximately 2000μ) was reached around displacements equivalent to rotations of 0.02 rad.

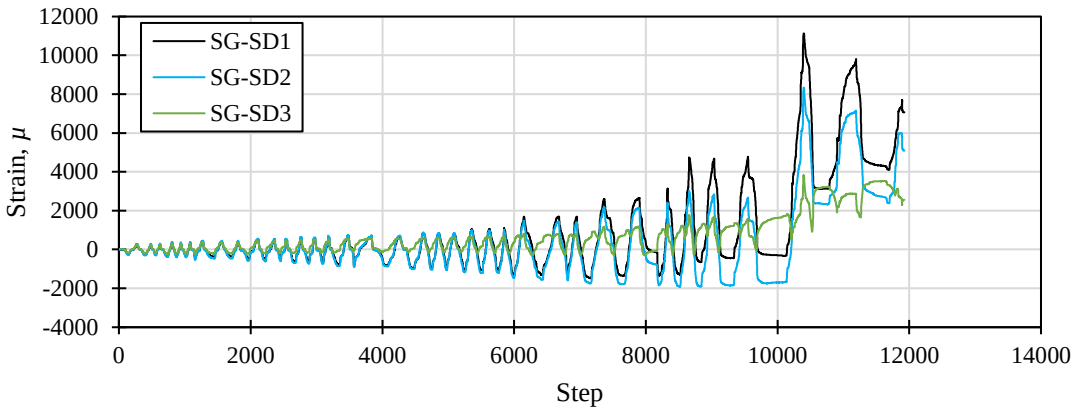

Figure 6-71. Damper strain history (P-SD-1).

6.4.5.2 Failure modes

The deformed shape of specimen P-SD-1's SD at the final cycle of the test is shown in Figure 6-72. At this stage, most struts had fractured at the ends, indicating stress concentrations in those regions. In the push direction (Figure 6-72a), most struts were observed to be in double curvature, as expected. Minor flexural cracks also appeared close to the ends of the struts. Struts gradually fractured, one by one, until completing the last cycle at a drift ratio of 0.035 rad. Therefore, the strength of the damper was lost gradually and not abruptly. In the pull direction (Figure 6-72b), the typical S-shape associated with double curvature was not clearly observed on most struts. Many of them appeared to be almost entirely in tension. This was also observed in the tests discussed later in Chapter 7.

Similar failure modes were observed in specimen P-SD-2R (Figure 6-73). Struts in double curvature were observed in the push direction (Figure 6-73a), and in the pull direction (Figure 6-73b) the struts appeared mostly in tension. Most struts had fractured by the end of the third cycle at a drift ratio of 0.035 rad.

a) θ_b = 3.5% b) θ_b = -3.5%

Figure 6-72. Deformed shape of the SD (P-SD-1).

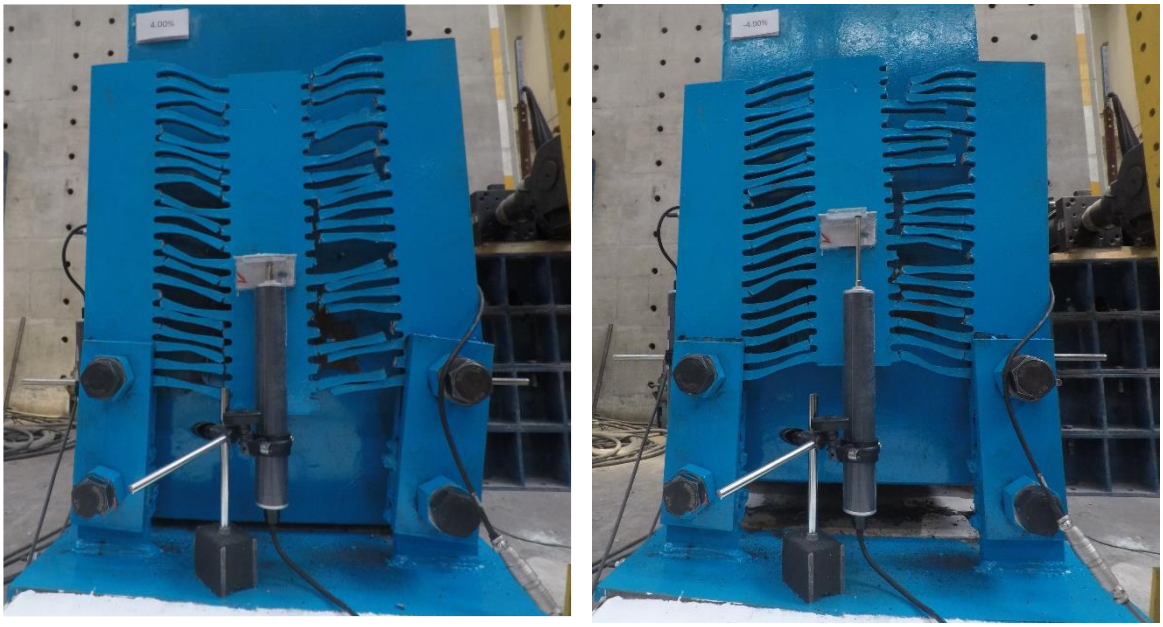

a) θ_b = 4.0% b) θ_b = -4.0%

Figure 6-73. Deformed shape of the SD (P-SD-2R).

6.4.5.3 Hysteresis curves

Hysteresis curves are shown in this section. The global behavior of the specimens, governed by the displacements measured by the LVDTs H1 and H2 and by the forces necessary to achieve these displacements, could be considered unacceptable if the minimum requirements of section 9 of ACI 374.1 [18] are not met in both response directions, these are:

1. The test specimen must reach the nominal lateral resistance, P_n, before the experimental drift has exceeded the maximum drift ratio allowed by the International Building Code (or IBC) [85]. For the purposes of the test described in this chapter, which was carried out in Mexico, the experimental drift ratio when P_n is reached, was compared with the maximum drift ratio allowed by the Complementary Technical Standards for Earthquake Design and Comments (NTC-S-2020) [50]. Both specimens complied with this requirement.
2. For cycles at the level of drift at which validation is sought, but not less than 0.035 drift, the characteristics of the third full cycle shall comply with the following: a) the peak force for one direction of load shall not be less than $0.75P_u$, for the same direction of load; b) the relative energy dissipation ratio must not be less than 0.125; and c) the secant stiffness from a drift ratio of -0.0035 to a drift ratio of +0.0035 shall not be less than 0.05 times the initial stiffness specified in ACI 374.1 section 7.3 [18]. Specimen P-SD-1 did not comply with the first of the three requirements described above for a drift ratio of 0.035 rad.

The load-displacement curves, representing the global behavior of the specimens, are shown in Figure 6-74. The equivalent moment-rotation curves are shown in Figure 6-75. Different behaviors were observed from both specimens.

For specimen P-SD-1, the following observations are made:

1. Wide, stable, and symmetrical hysteresis loops up to a drift ratio of 0.025 rad.
2. The load-carrying capacity of the specimen gradually decreased during the final three cycles at a drift ratio of 0.035 rad.
3. Predicted yield loads ($P_{y,c}$) using the equivalent length method proposed in Chapter 7 were similar to the experimental yield loads.

4. Yielding of the specimen occurred at relatively low drifts, approximately 0.003 rad.

For specimen P-SD-2R, the following observations are made:

1. Significant slippage occurred close to zero load due to the tolerances provided to the bolted components.
2. The specimen presented stable hysteresis loops up to a drift ratio of 0.035 rad, after which its load-carrying capacity gradually decreased during the final three cycles at a drift ratio of 0.04 rad.
3. Predicted yield loads ($P_{y,c}$) were similar to the experimental yield loads.
4. Yielding occurred at drift ratios significantly higher than the predicted values.

The envelopes of the hysteresis curves are also shown in Figure 6-74 (red line). They were determined using the largest load value for each cycle applied at each target drift. Load and deformation parameters were obtained from the idealized bilinear curves from the envelopes using the methodology suggested in ASCE 41-17 [81], as indicated in Figure 6-76. A summary of the test results is shown in Table 6-12.

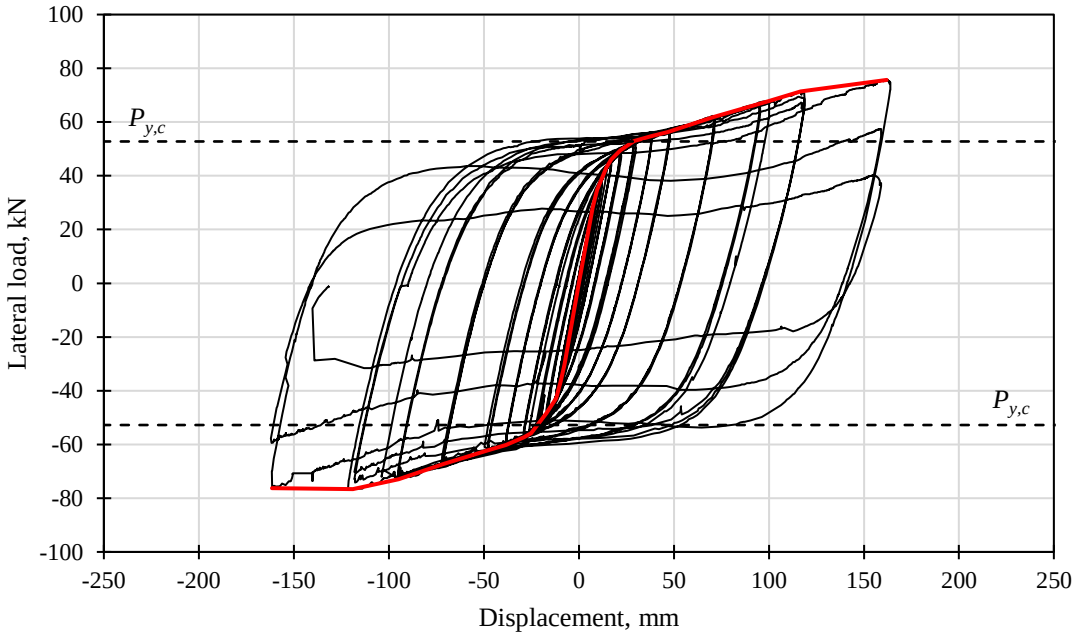

a) P-SD-1

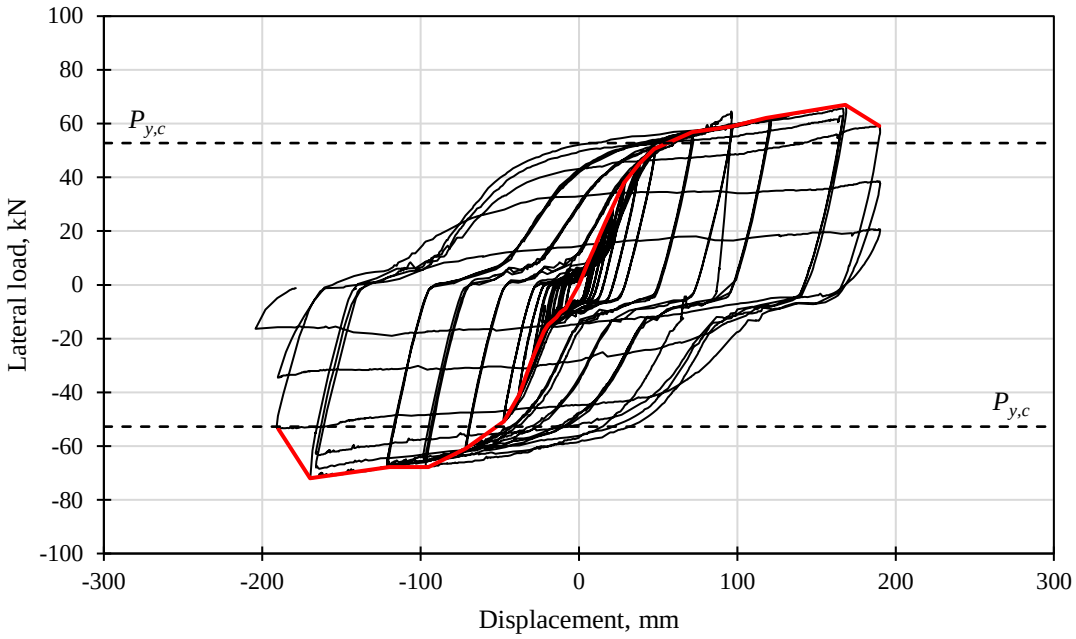

b) P-SD-2R

Figure 6-74. Load-displacement curves.

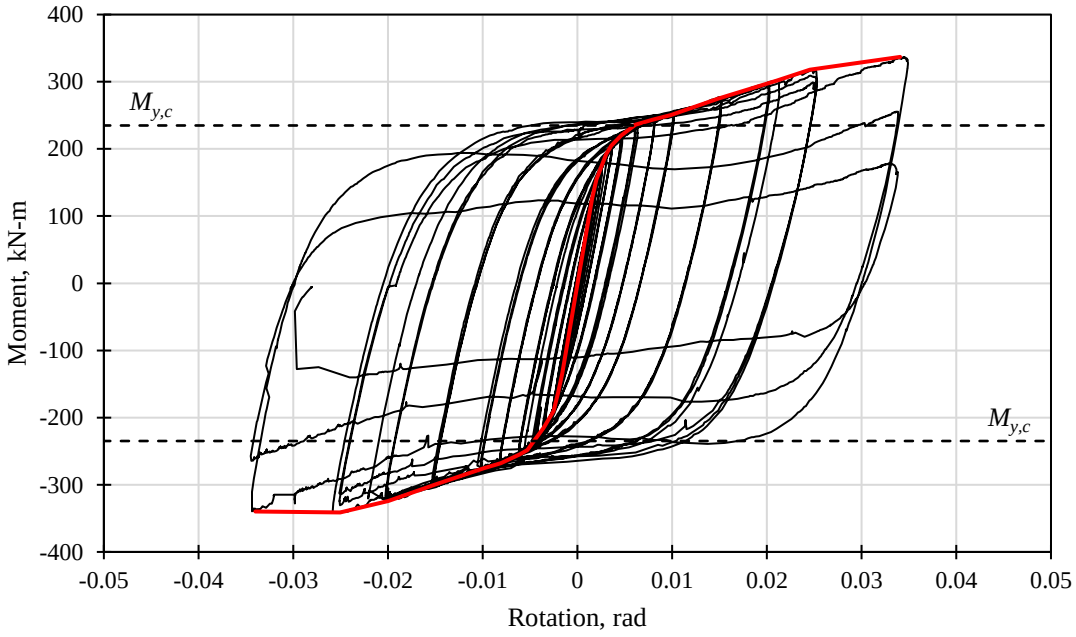

a) P-SD-1

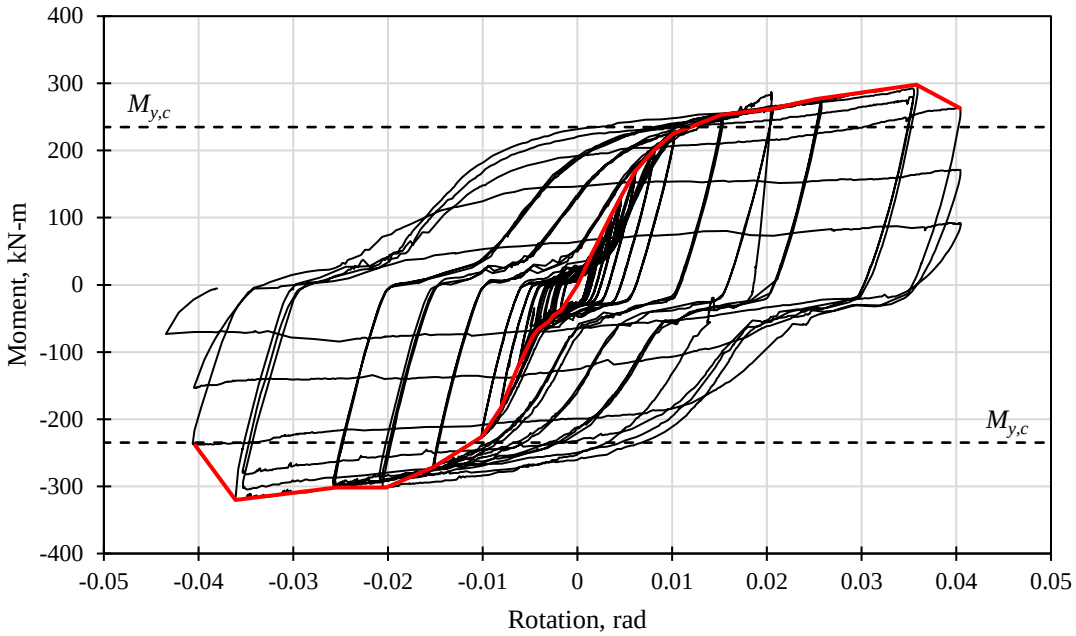

b) P-SD-2R

Figure 6-75. Moment-rotation curves.

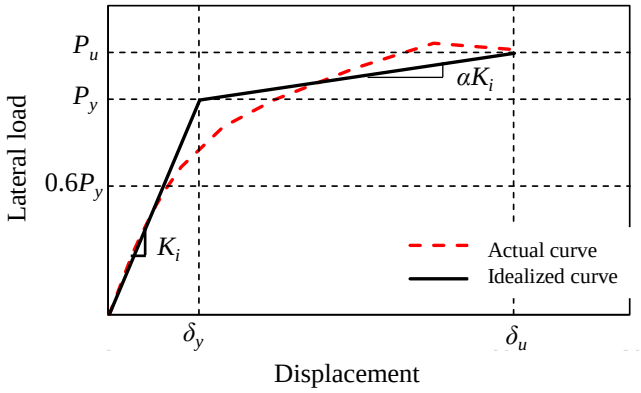

Figure 6-76. Idealized bilinear curve [81].

Table 6-12. Summary of test results.

Specimen	Property	Direction		Average
		(+)	(-)	
P-SD-1	$P_{y,ex}$ (kN)	52.2	60.9	56.6
	$P_{y,ex}$ / $P_{y,c}$	1.0	1.2	1.1
	$P_{u,ex}$ (kN)	75.7	76.3	76.0
	$P_{u,ex}$ / $P_{y,c}$	1.4	1.4	1.4
	$\delta_{y,ex}$ (mm)	13.44	15.27	14.36
	$\delta_{max,ex}$ (mm)	161.90	161.51	161.71
	$K_{i,ex}$ (kN/mm)	3.9	4.0	3.9
	μ	12.0	10.6	11.3
	α	0.04	0.03	0.03
P-SD-2R	$P_{y,ex}$ (kN)	62.1	56.0	59.0
	$P_{y,ex}$ / $P_{y,c}$	1.2	1.1	1.1
	$P_{u,ex}$ (kN)	67.0	62.5	64.8
	$P_{u,ex}$ / $P_{y,c}$	1.3	1.2	1.2
	$\delta_{y,ex}$ (mm)	44.44	38.44	41.44
	$\delta_{max,ex}$ (mm)	182.77	189.77	186.27
	$K_{i,ex}$ (kN/mm)	1.4	1.5	1.4
	μ	4.1	4.9	4.5
	α	0.03	0.03	0.03

From Table 6-12, the following observations can be made regarding specimen P-SD-1:

1. The experimental yield loads ($P_{y,ex}$) in both directions were, on average, 1.1 times the predicted yield load ($P_{y,c}$). Ultimate loads were 1.4 times $P_{y,c}$.

2. On average, the experimental yield displacements were 1.5 times the predicted yield displacement ($\delta_{y,c}$). The measured yield drift was 0.003 rad, compared to a predicted value of 0.002 rad.
3. The initial experimental stiffness ($K_{i,ex}$) was equal to $0.7K_{i,c}$, being $K_{i,c}$ the theoretical stiffness.
4. The average global ductility ratio was 11.3, which was the highest obtained experimentally in this research project, either cast-in-place or precast connections. Also, the obtained ductility ratio is consistent with those shown later in Chapter 7. The superiority of specimen P-SD-1 should be highlighted, considering that it had larger longitudinal reinforcement ratios -generally associated with lower ductilities- and less ductile detailing for shear than, for example, specimen CIP-3 which had the second highest ductility ratio (8.1) and had low longitudinal reinforcement ratios and small stirrup spacings (75 mm). However, specimen CIP-3 had significant damage at similar drift ratios, while specimen P-SD-1 had virtually zero damage, as will be seen later.
5. The post-elastic stiffness was approximately 3% of the initial experimental stiffness.

The experimental structural characteristics of the proposed beam-column system were generally in good agreement with the predicted values using the methodology described in Section 6.2 in combination with the effective length method proposed later in Chapter 7, thus corroborating their accuracy and the predictability of the system's response.

Regarding specimen P-SD-2R, the following observations are made:

1. As with specimen P-SD-1, the experimental yield loads in both directions were, on average, 1.1 times the predicted yield load. Ultimate loads were lower in this case, mainly due to the specimen's more flexible nature, which did not allow the damper to develop its full strength. This suggests that the stiffness of the bolted plates should be taken into account in the design process or should be designed to be significantly stiffer.
2. The experimental yield displacements were significantly higher, on average, 4.3 times the predicted yield displacement, attributed to its more flexible nature and the slippage presented during the tests.

3. The initial experimental stiffness was equal to $0.25K_{i,c}$, for the above reasons.
4. The average global ductility ratio was 4.5, one of the lowest of all the specimens studied here and in previous chapters.
5. The post-elastic stiffness was approximately 3% of the initial experimental stiffness, as was for specimen P-SD-1.

The response of specimen P-SD-2R was far less predictable due to the tolerances provided to the bolted components. In contrast, the welded connections of specimen P-SD-1 ensured a predictable cyclic response of the system.

The vertical displacements at the center of the damper (measured with LVDT V1) are shown in Figure 6-77. The predicted values, in discontinuous red lines, were obtained with Eq. (6-7) using the measured lateral displacements at the beam's tip. The predicted values are in good agreement with the measured values, which suggests that the beam rotates as a rigid body mainly.

Vertical displacements at the base of the beam were also assessed with two LVDTs (V2 and V3) to have redundancy in the experimental results. The displacements are shown in Figure 6-78. Between the two LVDTs, the measured vertical displacements were similar. They were also slightly smaller than those measured at the damper level (Figure 6-77), thus corroborating the accuracy of the results.

Finally, the damper load-strut drift ratio curves are shown in Figure 6-79. The loads were estimated with a geometric relationship through the loads measured at the beam's tip. The strut drift ratios were obtained with the displacements measured at the center of the damper divided by the total length of the strut. Strut drift ratios for specimen P-SD-1 were just above 0.3 rad, which was expected. From the tests described later in Chapter 7, it was determined that the maximum drift ratio that a strut can develop is approximately 30% of the strut's length.

In contrast, for specimen P-SD-2R, maximum drift ratios were around 0.35 rad. This was mainly attributed to the slippage presented during the test and not to the deformation capacity of the struts, as LVDT V1 measured the absolute vertical displacements at the damper level.

In retrospect, another LVDT measuring the vertical displacements of the bolted connection would have been necessary to obtain the relative displacement of the damper.

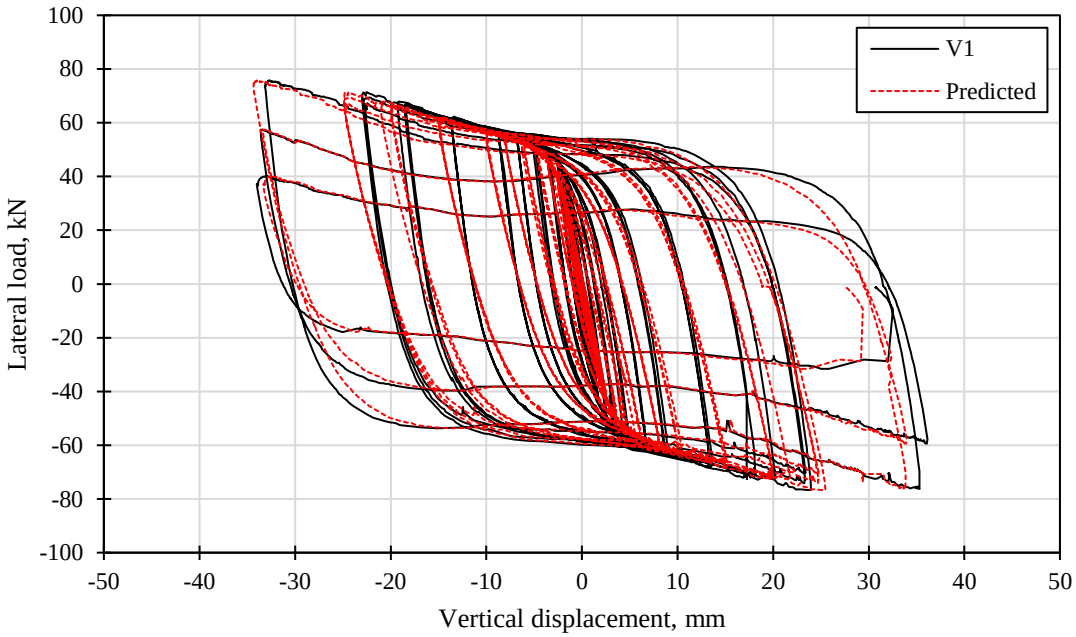

a) P-SD-1

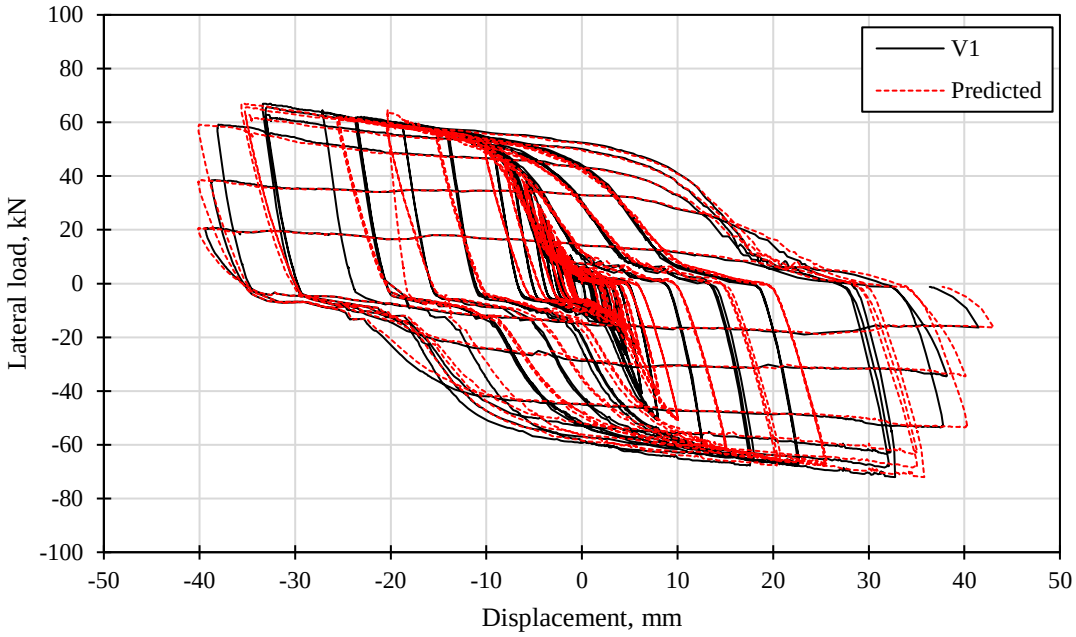

b) P-SD-2R

Figure 6-77. Damper vertical displacement (V1).

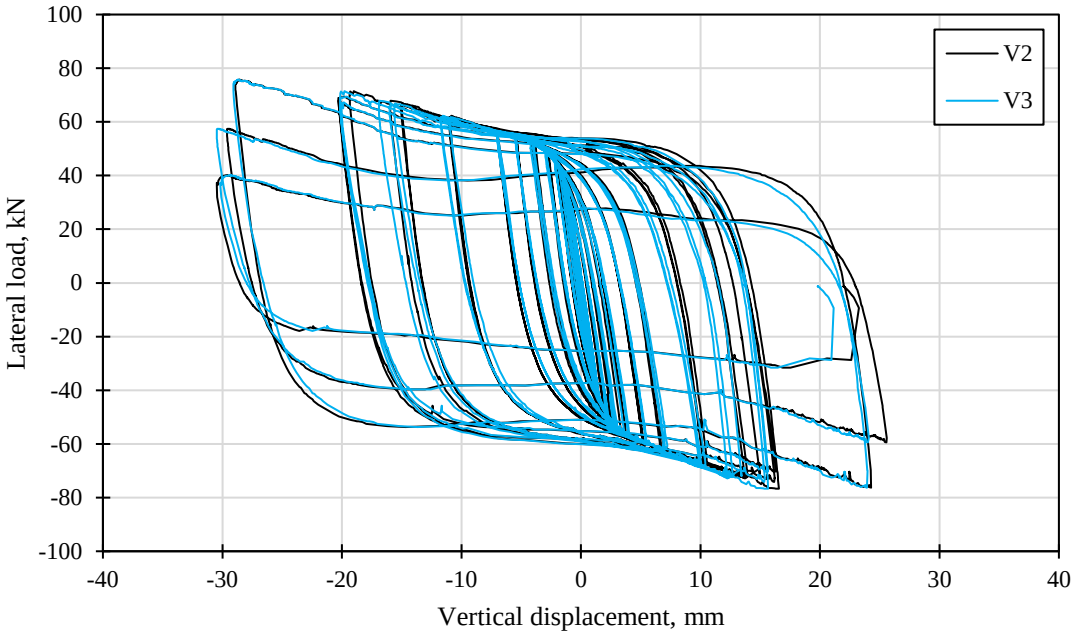

a) P-SD-1

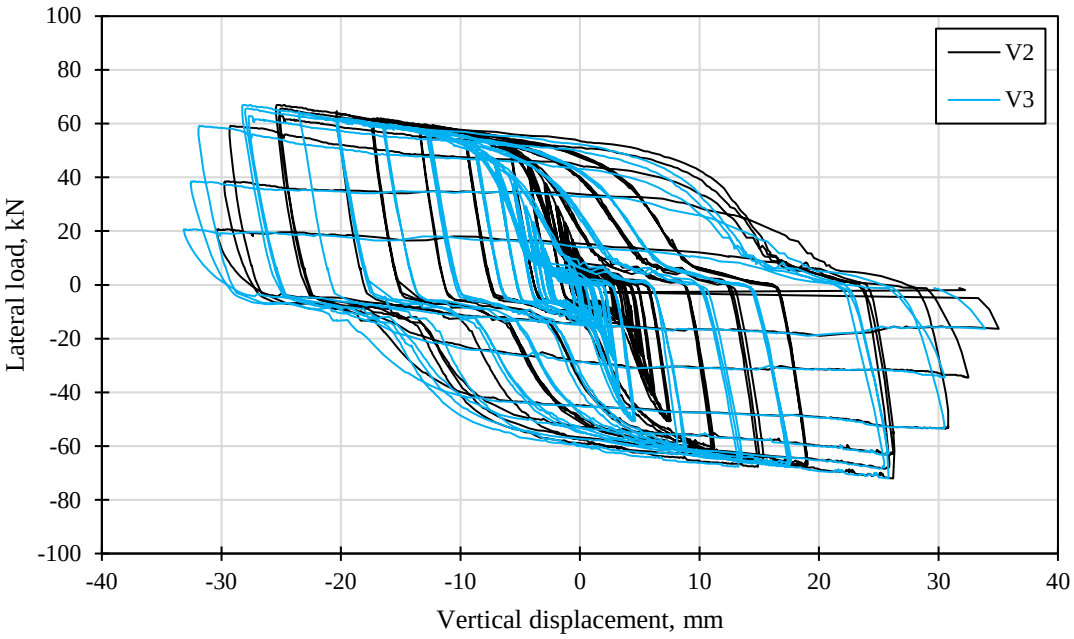

b) P-SD-2R

Figure 6-78. Beam vertical displacements (V2 and V3).

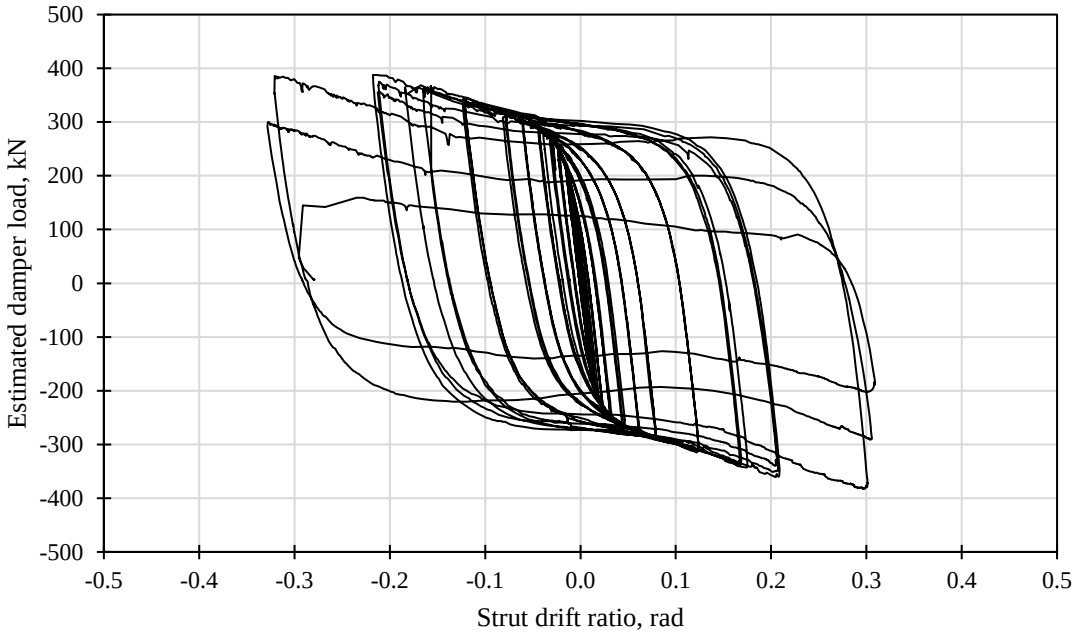

a) P-SD-1

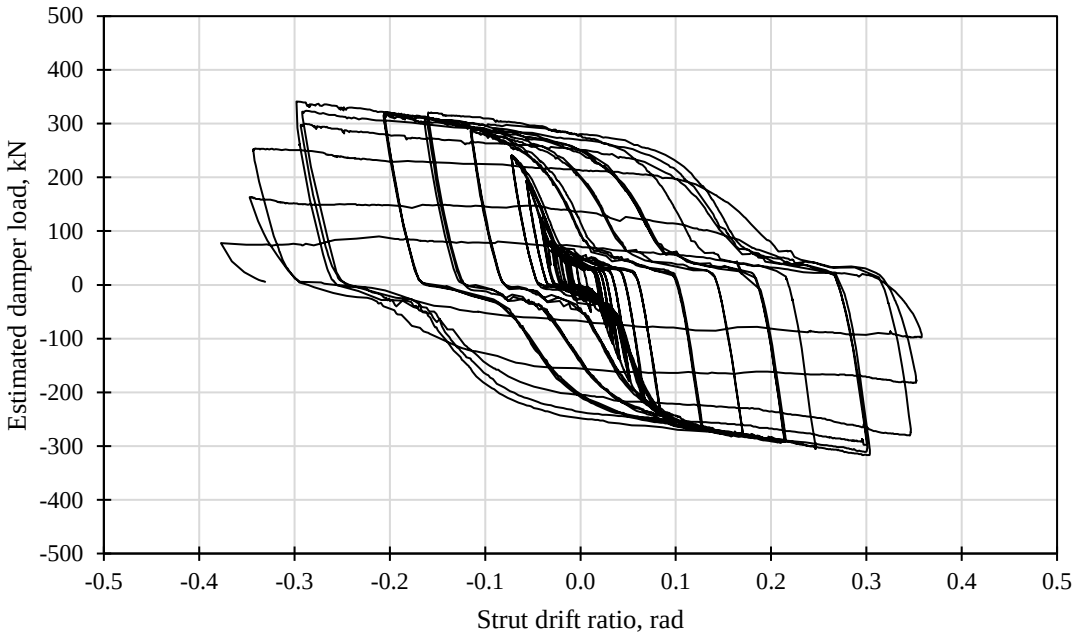

b) P-SD-2R

Figure 6-79. Damper load-strut drift ratio.

6.4.5.4 Strain of reinforcing and structural steel

The measured strains of the top and bottom longitudinal rebars of the precast beam are shown in Figure 6-80. The positive and negative values in the horizontal axis are related to the tensile and compressive strains, respectively. Maximum measured strains were around 800μ, significantly below the expected yield strain (approximately 2000μ). On the other hand, no flexural cracks were developed in the instrumented region or anywhere else; therefore, it can be assumed with confidence that the response of the beam was essentially elastic.

The measured strains of the transverse reinforcement are shown in Figure 6-81. They were significantly lower than those measured from the longitudinal rebars, with values lower than 60μ, which was basically negligible.

The strains developed on the damper are shown in Figure 6-82. Only the strains of specimen P-SD-1 are shown as P-SD-2R was not instrumented with SGs. Only the results of SGs SG-D2 and SG-D3 are shown. Their average value is also shown to assess the strains developed in the damper accurately. Strains were considerably high in the final stages of the test. From the average values, a maximum strain of approximately 6000μ was observed on the first cycle at a drift ratio of 0.035 rad, that is, before the damper had lost significant load-carrying capacity.

It is possible that the measured strains were not completely accurate. The SGs were placed on the lateral elements of the damper in a region close to the ends of the struts (see Figure 6-66). Out-of-plane deformations and strain penetration towards the outskirts of the struts may have affected the results. In retrospect, the SGs should have been placed at the center of the damper's lateral elements, at both faces and closer to the welded connections at the bottom in order to assess the axial strains accurately. Future tests should consider that.

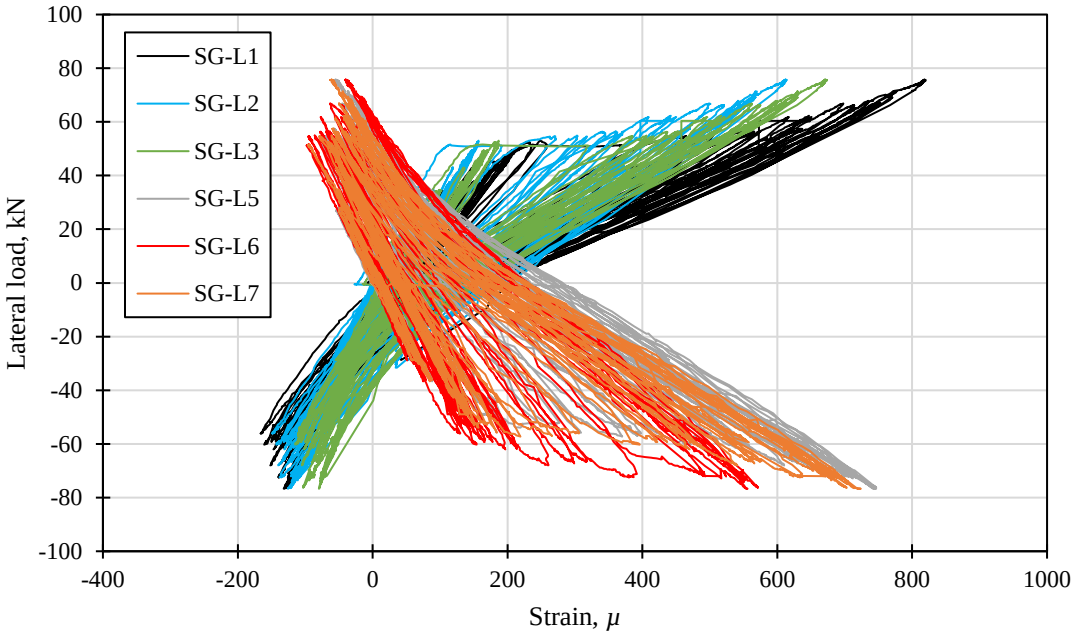

a) P-SD-1

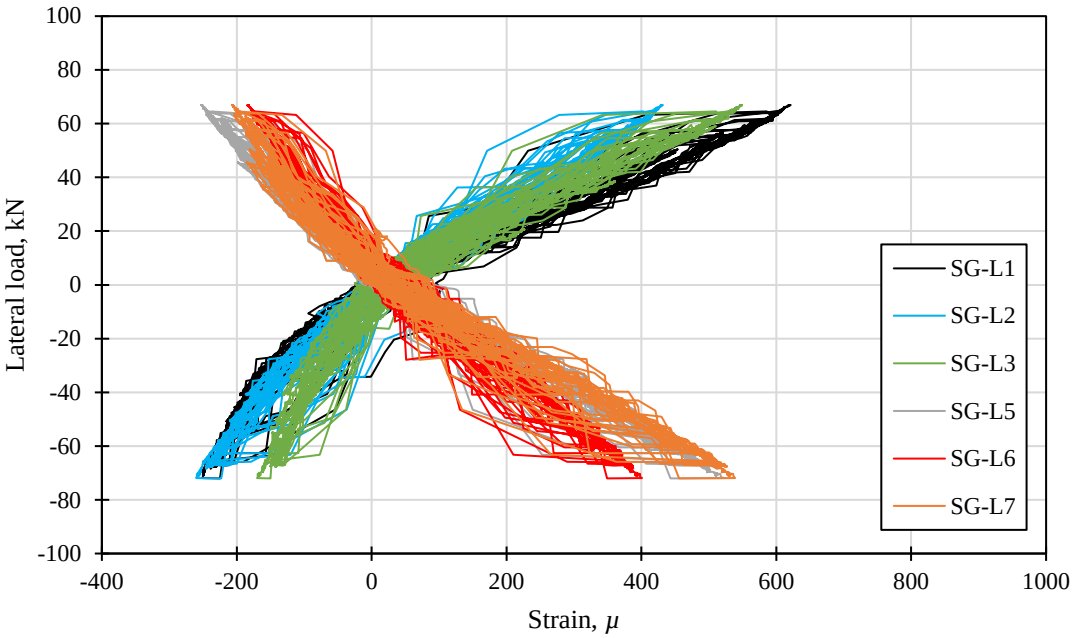

b) P-SD-2R

Figure 6-80. Longitudinal reinforcement strain.

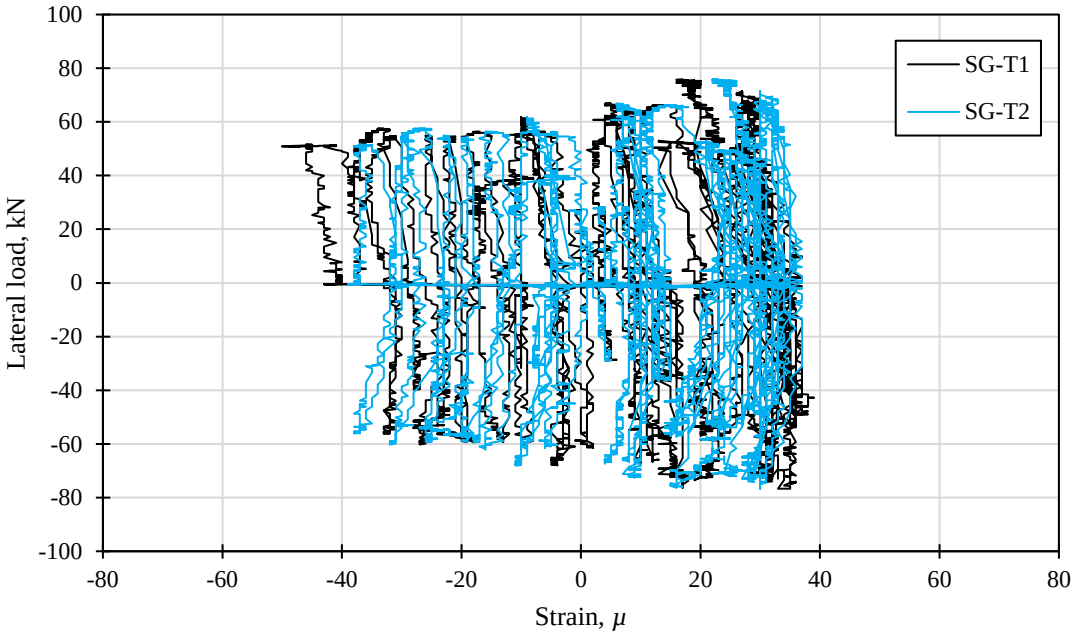

a) P-SD-1

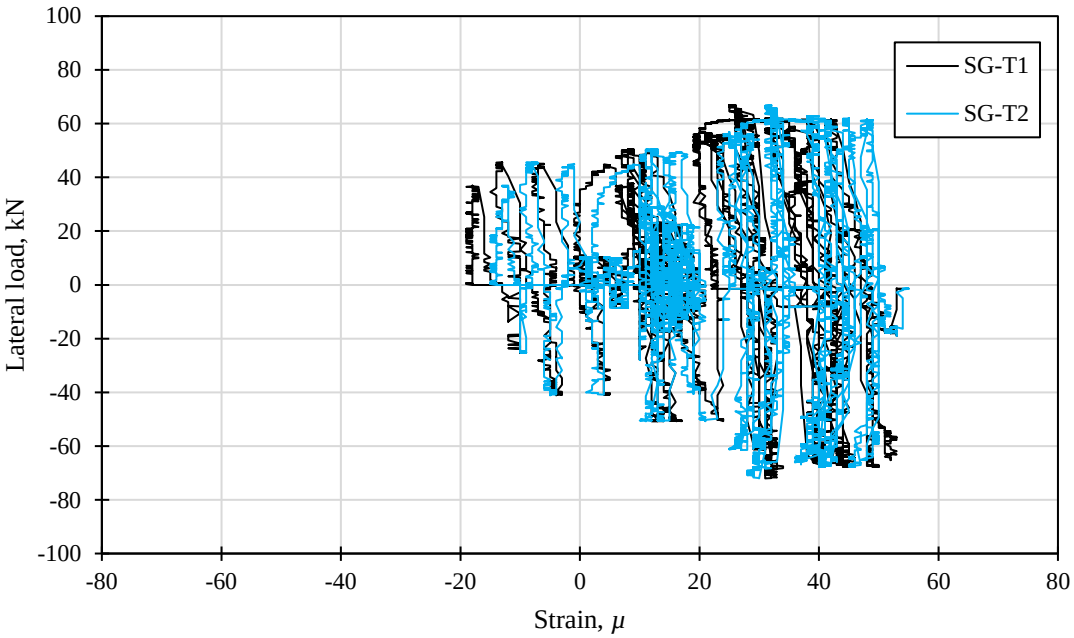

b) P-SD-2R

Figure 6-81. Transverse reinforcement strain.

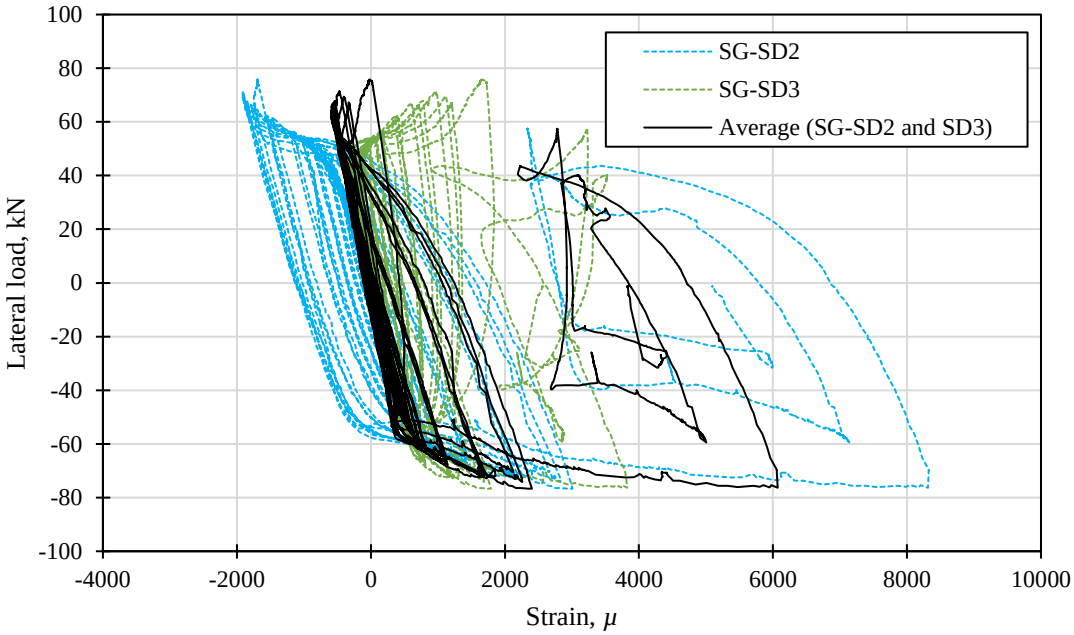

Figure 6-82. Damper strain (P-SD-1).

6.4.5.5 Ductility and energy dissipation

As with the prototype P-SD-0, the energy dissipation capacity of specimens P-SD-1 and P-SD-2R was evaluated with the relative energy dissipation ratio (β_i) and the cumulative ductility ratio ($NE_{H\mu}$).

The relative energy dissipation ratios for both specimens are shown in Figure 6-83. Both specimens have a similar capacity to dissipate energy, with their ratios at 0.035 rad or above not being less than 12.5% as required from ACI 374.1 [18]. Between drift ratios of 0.01 and 0.02 rad, energy dissipation was consistently high at 75%.

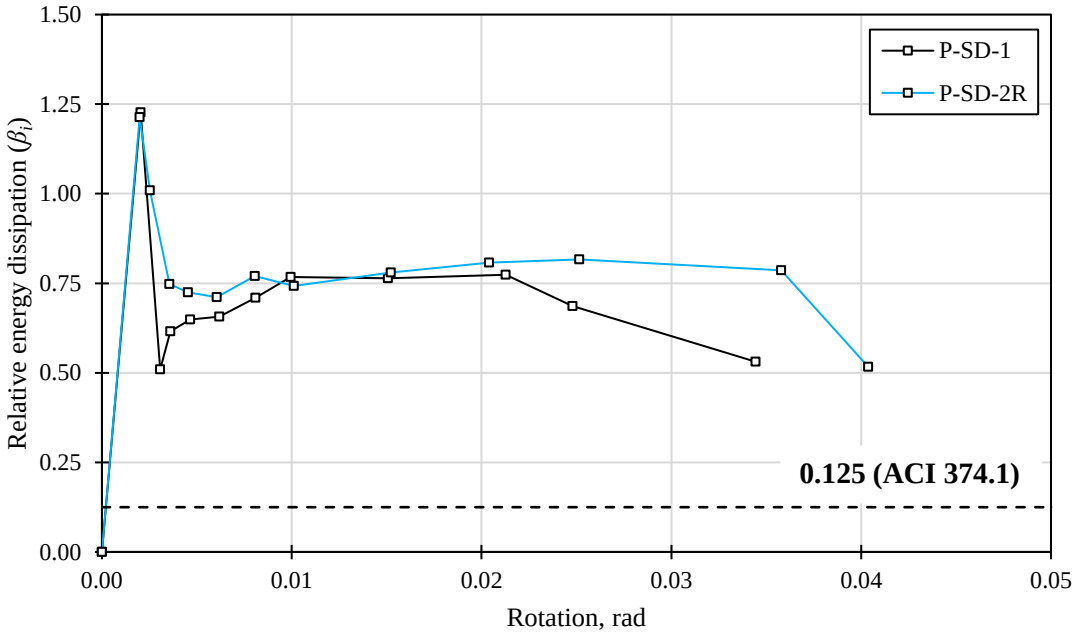

Figure 6-83. Relative energy dissipation ratio.

The relative dissipation ratio alone does not provide enough information to assess structural performance [66]. Therefore, the performance of the tested specimens was also assessed with the cumulative ductility ratio.

The cumulative dissipated energy per cycle is shown in Figure 6-84a. Both specimens dissipated similar amounts of energy by the end of the tests, which was also observed in the relative energy dissipation ratios in Figure 6-83. However, the cumulative ductility ratios of both specimens are significantly different for the same amounts of cumulative displacements (see Figure 6-84b). This is primarily due to specimen P-SD-2R having a larger yield displacement, almost three times that of specimen P-SD-1, even when correcting for slippage, while having similar yield loads. These comparisons demonstrate the advantages of the welded specimen (P-SD-1), namely a highly predictable and stable cyclic response capable of dissipating more plastic energy with respect to its strength and stiffness. The bolted specimen (P-SD-2R) can be improved with a more stable configuration and smaller tolerances for the bolts to avoid slippage. However, smaller tolerances can make it difficult to assemble the structure on site, especially in precast construction where usually large components are used. Tightening the bolts more may be a more viable solution to avoid

slippage; however, measures must be taken so that the plates that connect the damper to the column do not rotate as observed during the tests.

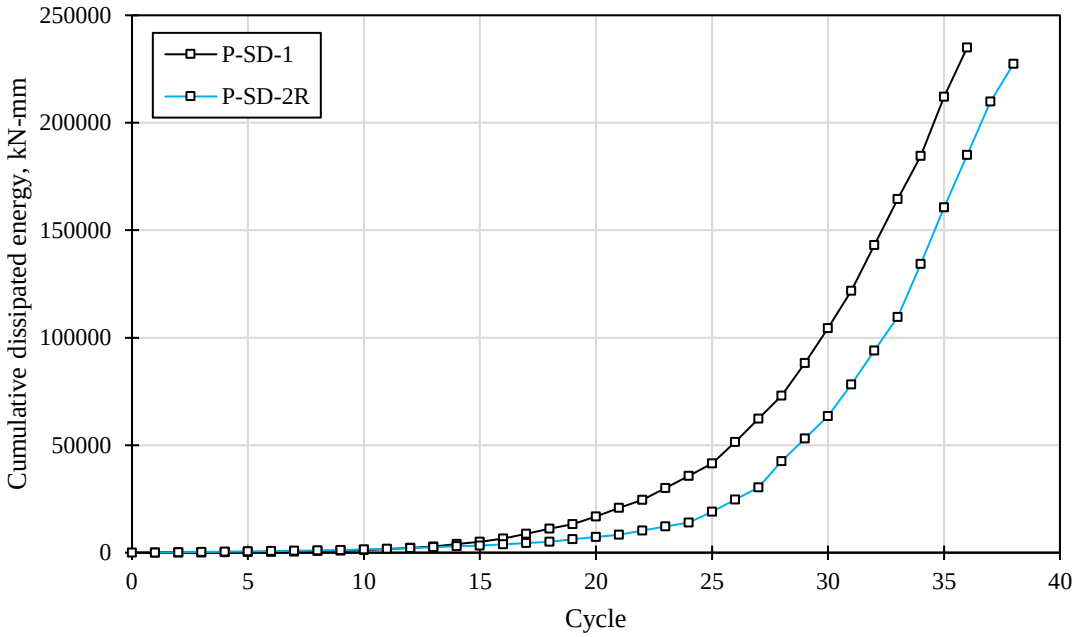

a) Cumulative dissipated energy per cycle

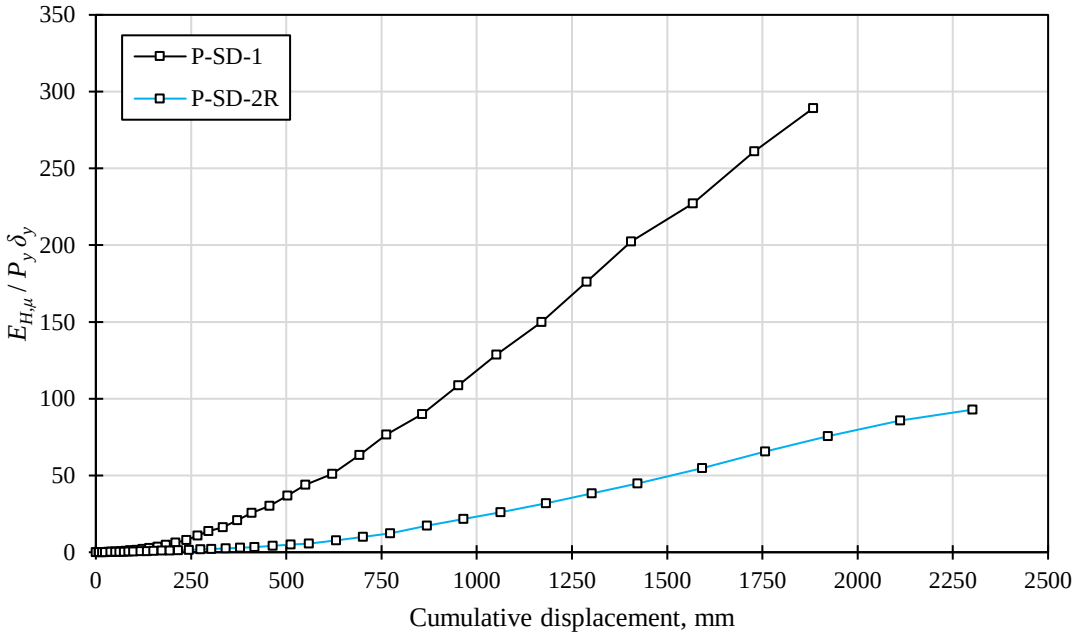

b) Cumulative ductility ratio

Figure 6-84. Cumulative dissipated energy.

6.4.5.6 Effective stiffness

For the third cycle at 0.035 drift ratio, the secant stiffness from a drift ratio of -0.0035 to a drift ratio of +0.0035 should not be less than 0.05 times the initial stiffness, K_i [18]. If the stiffness is very small at drift ratios close to zero, the structure may be exposed to large displacements due to small lateral force changes after an earthquake. Figure 6-85 shows an example of an unacceptable hysteresis loop form where the stiffness around zero drift ratio is unacceptably small for positive, but not for negative, loading [18]. The comparison of the initial stiffness and the stiffness at 0.035 is shown in Table 6-13. Both specimens, in both directions of response, meet the requirements of ACI 374.1 [18].

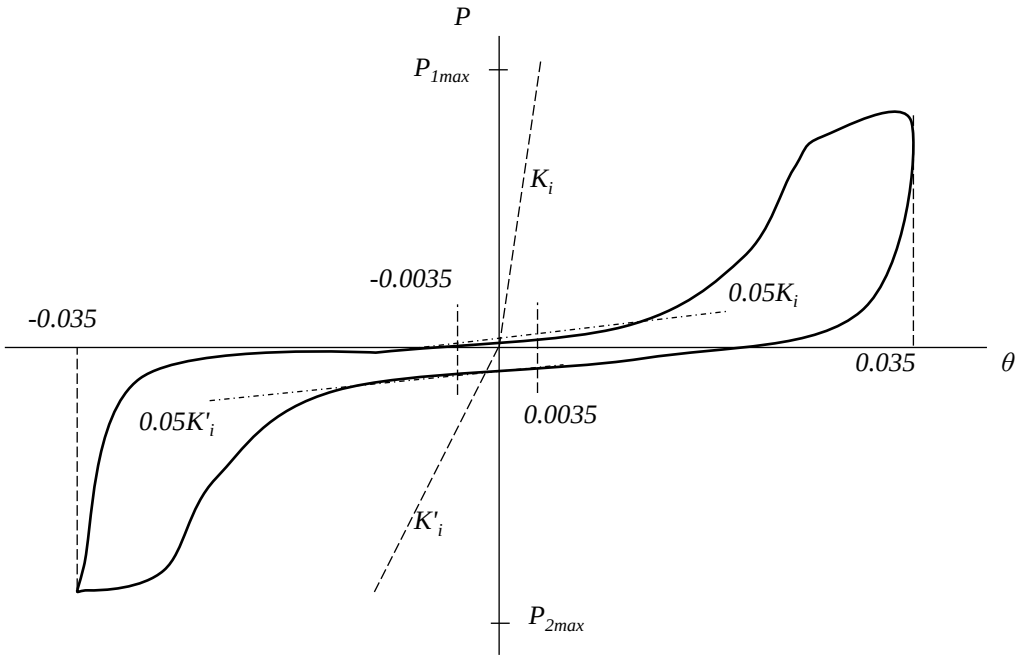

Figure 6-85. Unacceptable hysteretic behavior according to ACI 374.1 [18].

Table 6-13. Comparison of initial stiffness and stiffness at 3.5% drift ratio.

Specimen	Direction	$0.05K_{i,ex}$	$K_{0.035}$	Acceptance criteria $K_{0.035} > 0.05K_{i,ex}$
P-SD-1	(+)	0.19	0.25	Ok
	(-)	0.20	0.20	Ok
P-SD-2	(+)	0.07	0.15	Ok
	(-)	0.07	0.11	Ok

To expand on the study of the proposed system's stiffness, the experimental normalized effective stiffness, $k_{eff,n}$, at different stages of the test is shown in Figure 6-86. The specimens' predicted normalized effective stiffness is also shown (red lines). For specimen P-SD-1 (Figure 6-86a), it can be seen that the experimental response could be reasonably predicted. Regarding specimen P-SD-2R, for drift ratios less than 0.01 rad, normalized effective stiffness values are significantly lower than the predicted ones due to the slippage of the specimen. After that, values were reasonably similar to the prediction and, at the end of the test, values were closer to the isolated damper response (in blue).

6.4.5.7 Equivalent viscous damping

The equivalent viscous damping ratios, as defined by Chopra [67], are shown in Figure 6-87. In Figure 6-87a, the damping ratios are plotted against the global ductility ratios. As expected, damping increases as the deformation increases. Up to a ductility ratio of 5, damping ratios were similar between both specimens. After that, damping ratios of specimen P-SD-1 stabilized around 40% up to a ductility of 12. The maximum ductility ratio of specimen P-SD-2R was significantly lower than P-SD-1 due to the excesive slippage of the bolted components near zero load.

In Figure 6-87b, the equivalent viscous damping ratios are plotted against the normalized effective stiffness. In this graph, each point represents a feasible damping ratio for a given effective stiffness. Damping ratios vary approximately linearly and inversely proportional to the effective stiffness. Thus, similar to the cast-in-place and precast specimen studied in previous chapters, the proposed equivalent viscous damping model was used. The central trend is presented in the figure.

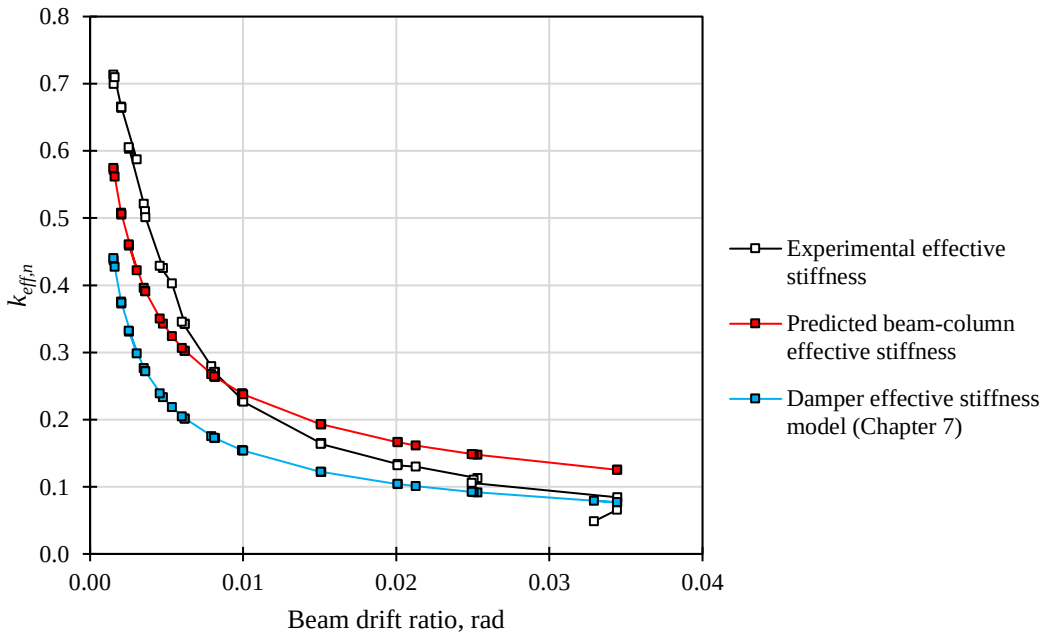

a) P-SD-1

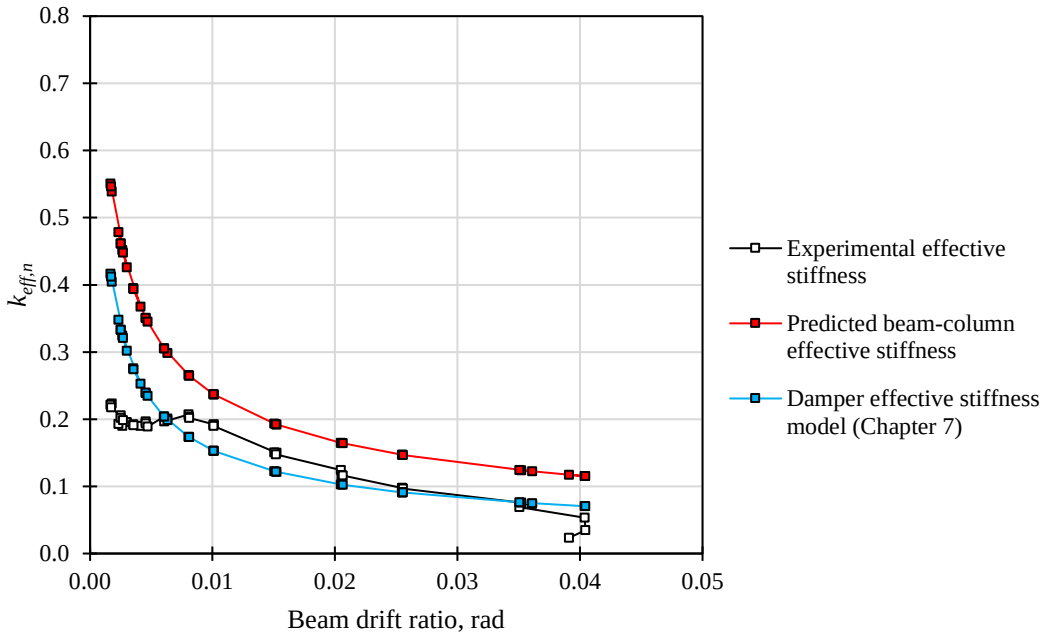

b) P-SD-2R

Figure 6-86. Effective stiffness.

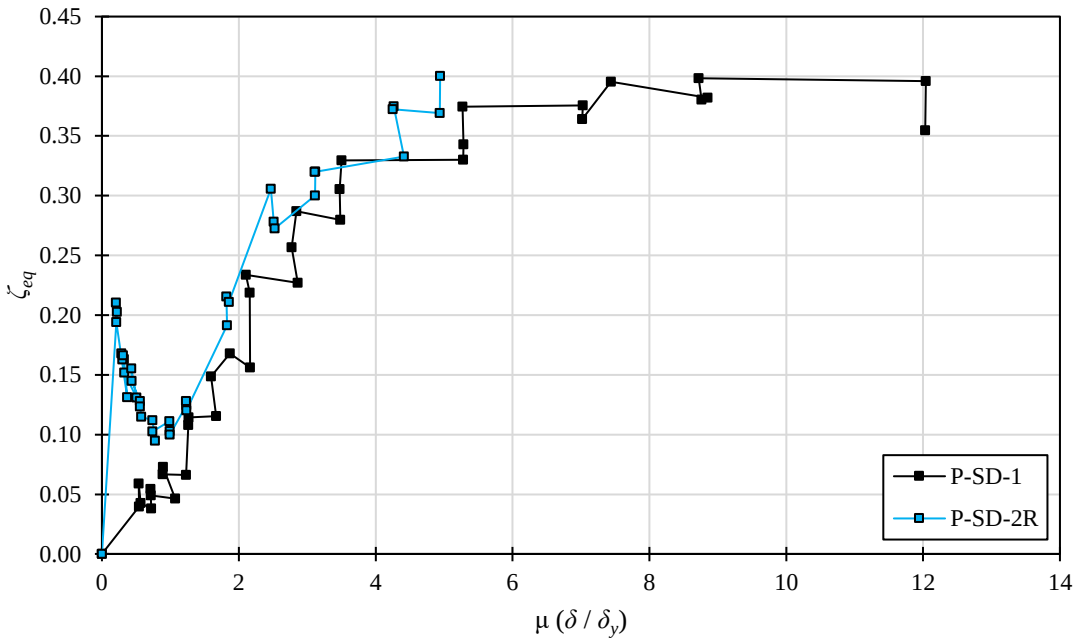

a) Equivalent viscous damping with ductility ratios

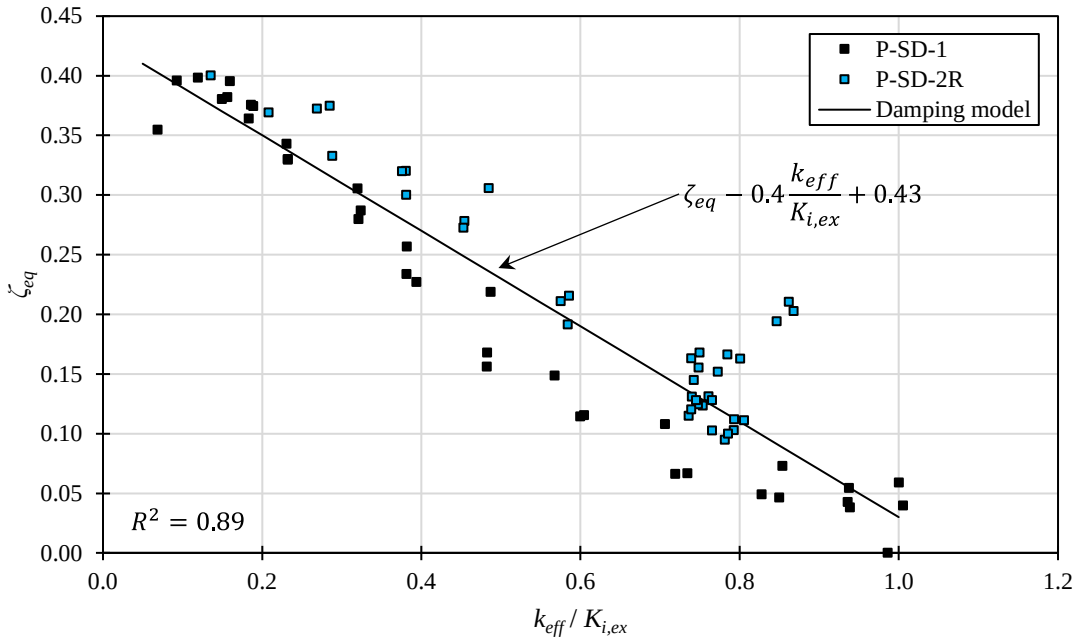

b) Equivalent viscous damping with normalized effective stiffness

Figure 6-87. Equivalent viscous damping.

6.4.5.8 Observed damage

Figure 6-88 shows the observed damage on specimen P-SD-1. At the top of the beam, as can be seen from Figure 6-88a and Figure 6-88b, the rotational hinge remained undamaged during the test. No significant damage was observed in the concrete, with only one vertical crack appearing parallel to the steel bars of the top dumbbell (Figure 6-88b), which also coincides with the axial force being transferred from the rotational hinge to the dumbbell. This crack appeared when the beam was pushed, i.e., when the rotational hinge and the dumbbell were in tension. The maximum force in the damper was estimated to be 363 kN. The four steel bars that formed the dumbbell could have had a combined strength as low as (4) (507 mm^2) (250 MPa) = 507 kN, giving them a safety factor of approximately 1.4. A larger safety factor could be given; however, the crack had a width of 0.1 mm even in the latter stages of the test, and the force transferred from the rotational hinge would not be enough to elongate the steel bars more than 0.5 mm.

Similarly, at the bottom of the beam, a vertical crack appeared on both sides of the column under the damper. These were hairline cracks similar to the one described above. Additionally, two cracks formed adjacent to the top dumbbell plate, one at the back at a lateral drift ratio of 0.35% (Figure 6-88c), and one at the front at a drift ratio of 0.8% (Figure 6-88d). By the end of the test, both cracks (at peak displacement) had a width of 2.8 mm; however, this was cover concrete affected by stress concentrations when the damper was in tension and had no structural consequences.

No new cracks were formed during the second test (specimen P-SD-2R), nor did the existing cracks increase in width or length.

a) Beam top (front)

b) Beam top (back)

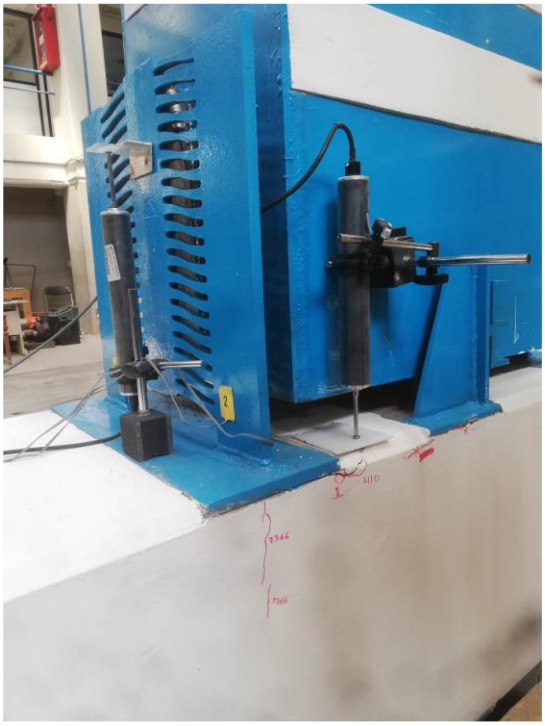

c) Beam bottom (front)

d) Beam bottom (back)

Figure 6-88. Observed damage on specimen P-SD-1.

6.5 Discussion

Some key structural parameters of the conventional cast-in-place and precast beam-column specimens studied in previous chapters are difficult to compare to the proposed non-emulative system equipped with a slit damper due to their very different characteristics. However, there are relative parameters that can be compared and are relevant to seismic design and seismic performance. Some of them are discussed here, comparing the response of the conventional systems (eight specimens in total) with the response of specimens P-SD-1 and P-SD-2R.

The cumulative ductility ratio of the studied specimens is shown in Figure 6-89. For the same cumulative displacements, specimen P-SD-1 could dissipate significantly more plastic energy, relative to $P_y\ \delta_y$, than the other specimens. On the other hand, although the response of specimen P-SD-2R was severely affected by the slippage presented during the tests, it could dissipate more plastic energy than the cast-in-place (CIP) and precast (PC) specimens.

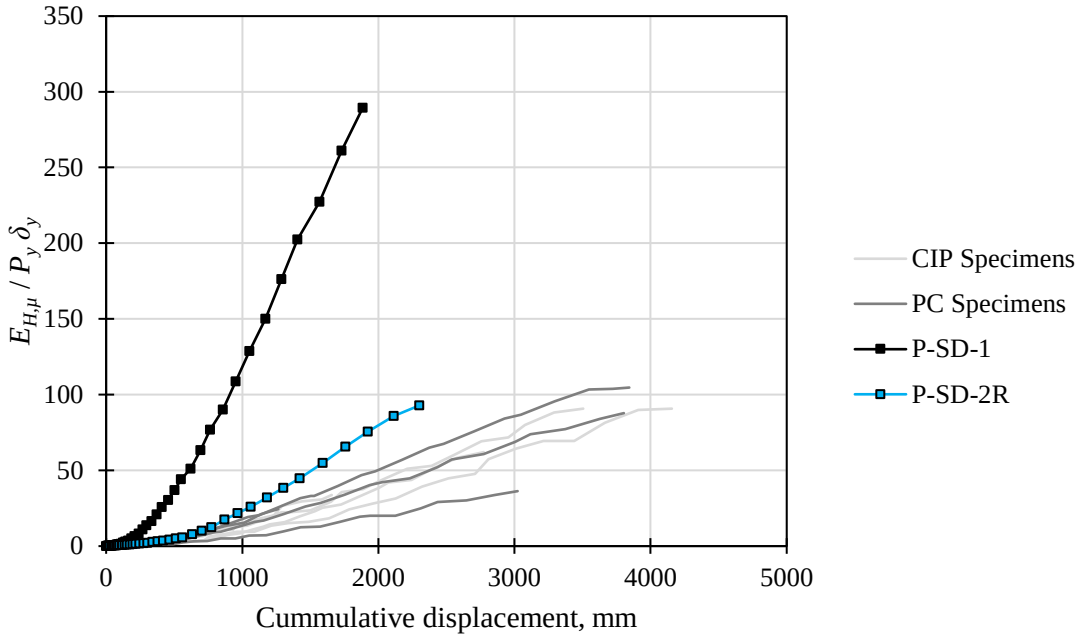

Figure 6-89. Cumulative ductility ratios of all tested specimens.

The equivalent viscous damping ratios (ζ_{eq}) are plotted against the global ductility ratios ($\mu = \delta / \delta_y$) in Figure 6-90. In all cases, damping ratios increase as the deformation increase. All

specimens showed some energy dissipation capacity before yielding ($\mu < 1$), with damping ratios of 10% or less. Only specimen P-SD-2R exhibited ratios around 20% before yielding, probably due to the friction forces between the bolted connections. Maximum damping ratios were approximately 40% for specimens P-SD-1 and P-SD-2R and close to 25% for the precast specimens.

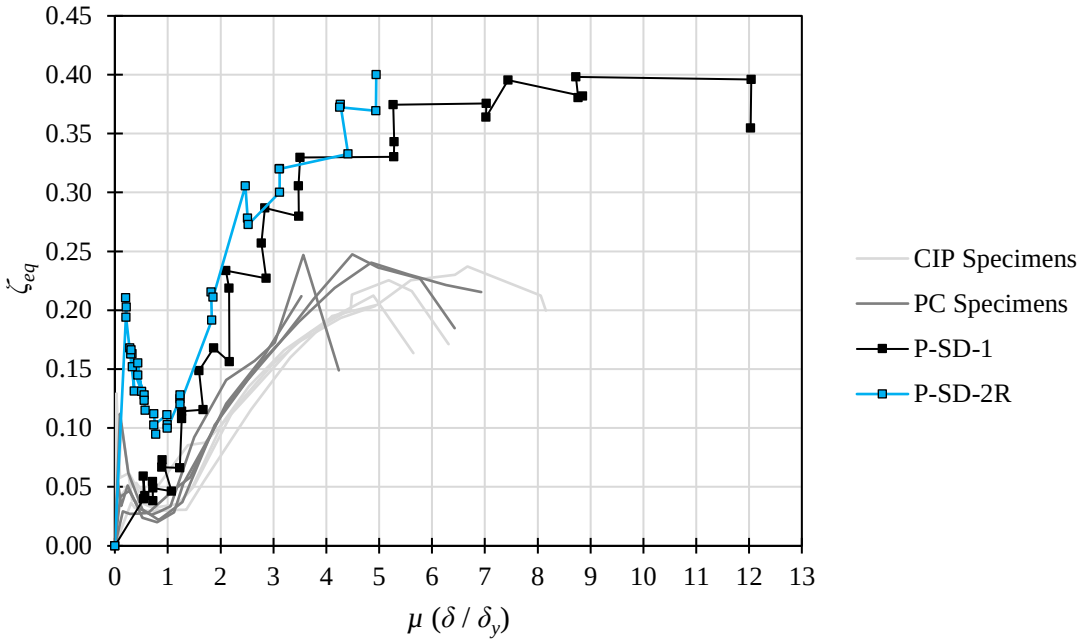

Figure 6-90. Equivalent viscous damping ratios of all tested specimens.

6.6 Conclusions

In this chapter, one small-scale and two full-scale exterior non-emulative precast beam-column connections with low ductility detailing were subjected to reversible incremental cyclic loading applied quasi-statically.

Based on the experimental results, the following conclusions are offered:

1. The precast elements of the proposed beam-column system can be fabricated as individual pieces to be later connected on-site. The beam and the column can be connected with welding or bolted techniques or a combination of these.

2. The repairability of the proposed system was also explored during the experimental study as the damaged damper of specimen P-SD-1 was replaced, and the precast components were reused for specimen P-SD-2R.
3. Damage on specimens P-SD-1 and P-SD-2R was minimal. No cracks were developed on the precast beam. Vertical cracks with widths no larger than 0.1 mm appeared below the top plates of both dumbbell connections. Near the damper, two cracks formed adjacent to the top plate of the dumbbell. Both cracks, at peak displacement, had a width of 2.8 mm by the end of the test; however, this was cover concrete affected by stress concentrations when the damper was in tension and had no structural consequences.
4. The energy-dissipating and deformation capacities of specimen P-SD-1 were superior to that of the conventional specimens in all respects. Specimens P-SD-1 and P-SD-2R complied with the acceptance criteria ACI 374.1 [18] except for the drop in strength below 75% of the peak measured load at a drift ratio of 0.035 rad. Even with low-ductility detailing, specimen P-SD-1's deformation and energy-dissipating capacities were superior to the rest while developing no damage on the beam and close to zero damage on the column and joint region.
5. Along with the low-damage characteristics, another of the most important features of the proposed system is the predictability of its response. Structural parameters used for seismic design, such as the stiffness, and the strength and displacement at yield, are accurately determined. Since there is a gap between the beam and the column, moment-curvature relationships cannot be determined. However, moment-rotation relationships can be obtained and depend almost entirely on the structural characteristics of the slit damper and the inter-story drifts of the frame.

7

Cyclic Behavior of a Slit Damper Proposed for Precast Concrete Beam-Colum Connections

7.1 Introduction

After large damages observed in recent earthquakes around the world, the use of energy dissipation devices has become more common. Passive control systems are becoming an attractive alternative for structural control due to their efficiency in mitigating seismic risk. There are various types of passive energy dissipation devices, such as metallic hysteretic or yielding dampers [86], viscous dampers [87,88], viscoelastic dampers [87] and friction dampers [88]. One of the main advantages of passive control systems is that they do not require an external power source; therefore, reliability associated with power supply and computer control during a seismic event is eliminated [83]. Additionally, if necessary, damaged devices can be replaced with minimal time and cost; hence interruption to occupancy is minimized, which is an ever-increasing concern for stakeholders.

Passive control systems can dissipate seismic energy through several mechanisms. One of the most popular mechanisms for energy dissipation is through the yielding of metallic materials. Metallic hysteretic dampers are one of the most effective and economical

mechanisms for the dissipation of seismic energy, which is achieved through the inelastic deformation of the metallic material [89]. Many metallic dampers have been proposed, such as the added damping and stiffness (ADAS) device [89] and its triangular alternative (TADAS) [90,91]; the honeycomb damper [92]; the buckling-restrained brace [93]; the pipe-based damper [94]; the ductile steel damper-brace [95]; and the slit damper (SD), which by itself has several variations [82,83,96–104] and is this study's main focus. Most of the existing devices are designed to be incorporated into the bracing system of structural frames; however, some have been developed to be installed in the connections. For example, Javidan et al. [105] proposed a steel hysteretic damper for retrofiting pinned precast frames, which can significantly reduce displacement demands and prevent the global collapse of the structure while being easily replaced if needed. Other proposed devices installed between the beams and columns can be found in references [106–108].

Steel SDs can dissipate energy through flexural and shear deformations of the struts, which are made from a steel plate. Sometimes they are also made from a standard wide-flange section with slits cut from the web, such as the I-shape damper proposed by Lor et al. [109]. Certainly, the yielding deformation of the device has to be set low to activate the energy dissipation as early as possible, while the yielding -displacement of the primary structure (i.e., the frame elements) is set relatively large to delay structural damage.

Though there are studies on SDs, and the design of such devices is somehow simple, some concerns have arisen over the years that must be considered. For example, Chan and Albermani [83] noted that their slit dampers presented, on average, 30% of the calculated stiffness obtained from simplified elastic stiffness models. Therefore, a stiffness coefficient, *c*, calibrated from experiments was necessary when evaluating the damper stiffness analytically. Another concern is the possible loss of energy dissipation capacity due to the fracture of one or multiple struts if large deformation demands are expected. Naeem and Kim [97] developed an interesting variant of the slit damper with two stages of energy dissipation. Their multi-slit damper (MSD) consisted of one-story-high steel plates with weak and strong struts connected in series with two different stiffnesses and yield strengths. The MSD dissipated energy through the yielding of the weak portion under low-to-medium earthquake ground motions, while the strong SD remained elastic. For severe ground motions, both weak

and strong dampers acted together to dissipate considerable seismic energy; however, near the fracture point of the weak portion, further displacement was prevented by a stopper, and the force was transferred entirely to the strong part of the damper. A follow-up experimental investigation by Javidan et al. [110] studied the application of the MSD for retrofitting school structures by testing three full-scale reinforced concrete frames: one bare frame and two frames equipped with the MSD.

Another key feature that affects the SD's performance is the stress concentrations at the struts' ends. Cracking or fracturing at these zones can compromise the fatigue capacity of the damper. Consequently, some researchers have searched for improved geometries to distribute the non-linear strains better, and several alternatives have been developed. Lee et al. [96] developed an SD with non-uniform struts, which distributes yielding over the length of the struts and improves ductility and low-cycle fatigue performance significantly. More recently, Kiani et al. [111] proposed a multi-objective shape optimization algorithm to further enhance the cyclic performance of SDs with non-uniform struts. Bae et al. [112] developed an hourglass-shaped SD with multiple preselected segments, where plastic hinges occur almost simultaneously, providing the damper with increased ductility and improved hysteretic behavior.

Some SDs, developed for steel beam-column connections, such as that proposed by Oh et al. [82], are oriented vertically. Unfortunately, this can decrease the horizontal ductility capacity of the slit damper because the rotation of the beam induces not only horizontal displacements but also vertical displacements that cause tension and compression. This issue was later addressed in a study by Park and Oh [98]. They proposed a T-stub SD, which was oriented horizontally and installed below the bottom flange of the beam, transferring the axial force to the damper. Similarly, the SD proposed in this study is conceptualized to be placed horizontally, and a transfer plate is installed below the beam to transfer the axial force to the damper. This configuration restricts out-of-plane deformations.

Slit dampers are economical and reliable options for steel beam-column connections [97]. In general, they present stable hysteretic behavior and dissipate substantial amounts of energy under cyclic loading while maintaining less ductile elements essentially elastic [82]. The SD proposed in this study is conceptualized to be installed horizontally, and a transfer plate is

placed below the beam to transfer the axial force to the damper. This installation scheme minimizes out-of-plane deformations of the damper. Also, the symmetrical placement of the struts allows versatility for increasing or decreasing the strength and stiffness of the damper with ease, as well as using different-sized struts as needed.

The SD proposed in this investigation is aimed at protecting precast concrete structures built in seismic zones, although it certainly can be used in other structural systems. It is designed to concentrate most of the plastic deformation on itself. Consequently, reliable data for design purposes, such as accurate ductile capacity, is needed. Unfortunately, reported ductility ratios in the literature, for SDs, are sometimes ambiguous due to the different methods and criteria used to determine both idealized bilinear curves from experimental data and the structural characteristics. Along with the different approaches, ductility ratios can vary due to the geometry of the damper and the experimental setup. Therefore, it is crucial to determine reliable ductility ratios based on physical principles for the actual damper proposed in this study. For this, the structural behavior of the proposed SD was evaluated theoretically, followed by experimental verification. A total of eight SDs were tested under cyclic loading to study their seismic performance. Results and discussions are presented, emphasizing ductility and energy dissipation capacity. The results show stable hysteretic behavior and adequate seismic performance. Effective lengths for calculating the SD's strength and elastic stiffness are also proposed based on finite element analyses. Using these effective lengths renders more reliable results than traditional approaches proposed in the literature. Finally, comparisons between experimental results and numerical predictions are offered.

7.2 Design of Slit Dampers

7.2.1 Uniform slit dampers

The proposed SD connection detail and its deformed shape are shown in Figure 7-1. The SD is installed between the beam's lower end and the column, and the upper T-stub connection acts as a rotational hinge that allows the rotation of the beam. The rotation of the connection is resisted by the coupled moment due to the horizontal axial force developed at the top and bottom of the beam. According to Oh et al. [82], damage to the T-stub is avoided since the rotation points on the left and right sides of the frame stay at the top of the beam. Axial non-linear deformation of the rotational hinge should be avoided with capacity design, and

bending of the plate, due to the rotation of the beam, must be kept within the linear-elastic range to avoid fatigue. Moreover, a vertical transfer plate is installed at the bottom of the beam to effectively transfer the axial load, *P*, from the beam to the damper. The lateral elements of the damper are resistant in the axial direction to the struts' flexure and shear behavior and transfer the axial load *P* to the column as shear. The separation between the beam and the column should be sufficient so that the damper, or the beam, does not hit the column; but is not large enough to cause buckling of the rotational hinge in compression.

The connection between the SD and the precast concrete is facilitated by assembling a steel box at the end of the beam. The column must also be prepared with the corresponding components for appropriate connection. It is also important to note that the proposed SD cannot resist the shear force acting on the beam due to the gravity loads. At the time of writing this chapter, a shear connection is being conceptualized. A proposal for this connection is shown in Figure 7-2 and consists of two steel corbels connected to the column where the beam will be supported through shear tabs and stiffeners. This connection is being developed to resist the total shear and to help guarantee the rotation of the beam without introducing complex stress states. Connection details between the steel components and the precast concrete are out of the scope of this study but will certainly be addressed in future investigations.

The proposed SD is manufactured from a single steel plate with elongated slits that are rounded at the ends to reduce stress concentrations in those areas. The steel strips on the device, which provide the system with energy-dissipating capacity, are referred to herein as struts. A typical configuration of the proposed damper and its geometric properties are shown in Figure 7-3. The struts of the damper can be idealized with straight lines as defined by Oh et al. [82], with a constant cross-sectional width, *b*, and an effective length, l_e.

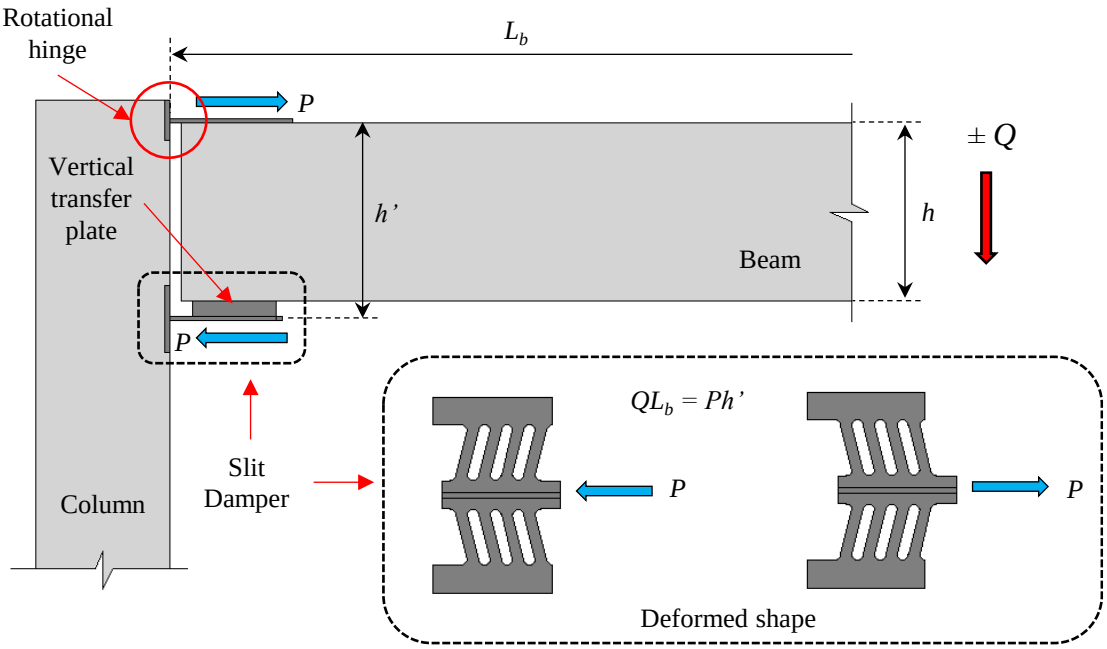

Figure 7-1. Proposed SD connection detail and deformed shape.

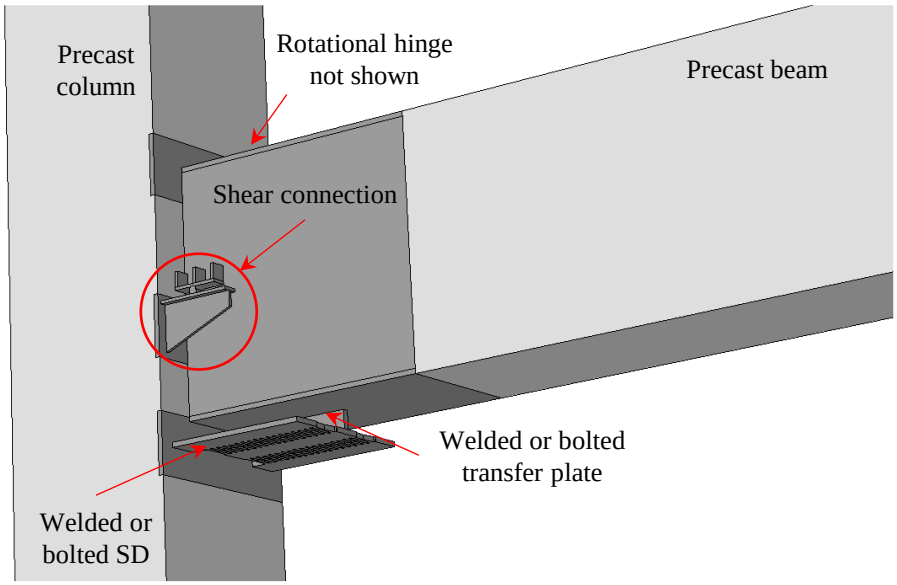

Figure 7-2. Isometric view of the beam-column connection equipped with the SD.

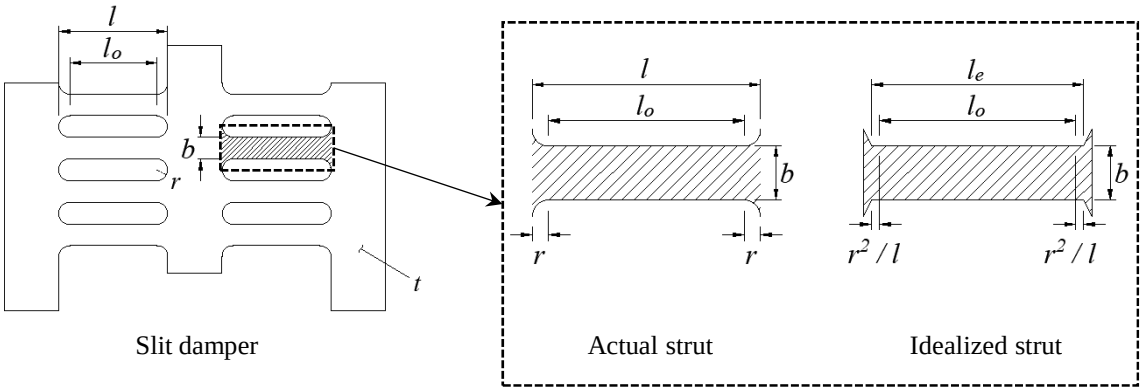

Figure 7-3. Geometric properties of the proposed SD and strut idealization.

When an SD is subjected to a horizontal in-plane force, bending moment and shear force occur simultaneously in the struts. In cases where the aspect ratio of the strut, defined as the width-to-effective length ratio (b / l_e), is relatively small, the behavior of the damper is governed primarily by flexure. Under small relative displacements between the center and lateral portions of the damper, the struts behave as partially fixed-ended beams, deforming in double curvature. Under larger displacements, the bending moment can cause the extreme fibers to reach yielding stress, forming plastic hinges at both ends of the strut, with a rotation θ_p. The struts can be simplified into the equivalent beam model with fixed ends, as shown in Figure 7-4a. The bending moment increases linearly from mid-span to the ends of the struts, as shown in Figure 7-4b. For rectangular prismatic sections, the full plastic moment of the strut, M_p, is given by

$$M_p = \frac{f_y t b^2}{4} \tag{7-1}$$

where f_y is the material yielding stress, and t and b are the struts' cross-sectional thickness and width, respectively.

Assuming elastic-perfectly plastic behavior, the yielding load, P_y, can be determined based on a plastic mechanism analysis when plastic hinges are formed at both ends of the struts [83], as

$$P_y = \frac{nf_y tb^2}{2l_e} \tag{7-2}$$

where n is the number of struts, and l_e is the effective length (see Figure 7-3) given by the following equation [82]:

$$l_e = l_o + \frac{2r^2}{l} \tag{7-3}$$

where r is the radius and l is the total length of the strut, both shown in Figure 7-3. Eq. (7-3) gives the effective length in which the strength of the strut is developed. In summary, the yielding load, P_y, can be obtained analytically with the following equation:

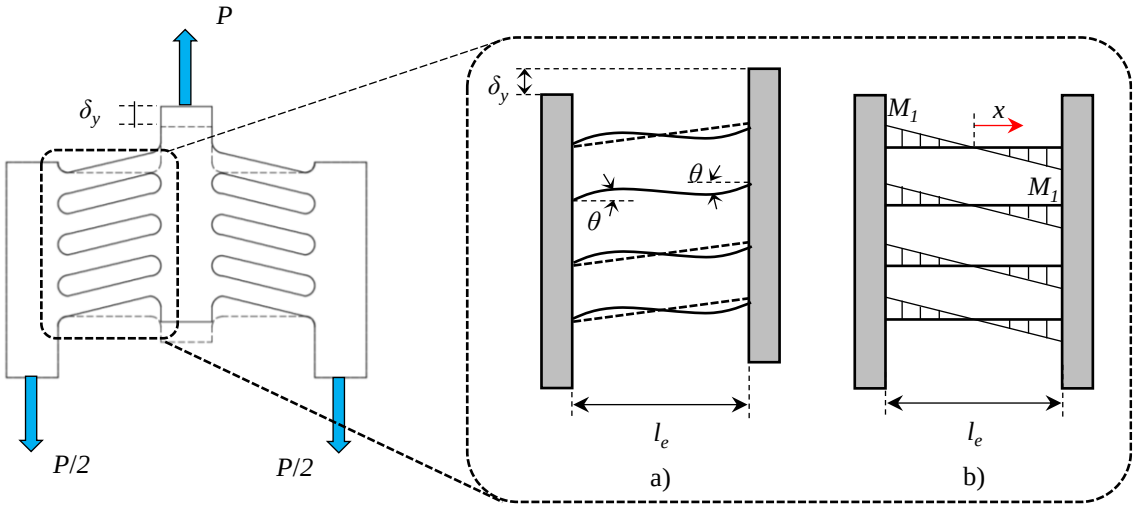

Figure 7-4. Equivalent beam model: a) deformed shape of the SD; b) bending moment in the SD.

$$P_y = min\left\{\frac{nf_y tb^2}{2l_e}\ ;\ \frac{n2f_y tb}{3\sqrt{3}}\right\} \tag{7-4}$$

where the first term represents the yielding strength of the SD due to the bending moment, while the second term refers to the yielding under shear force.

Assuming the damper is controlled by flexure, the elastic stiffness of the SD provided by the struts and the yielding displacement can be calculated, respectively, as:

$$k_{SD} = c\frac{nEtb^3}{l_e^3} \tag{7-5}$$

$$\delta_y = \frac{1}{c}\,\frac{f_y l_e^2}{2Eb} \tag{7-6}$$

where *c* is a stiffness coefficient calibrated from experiments, and *E* is the material's modulus of elasticity. From their experimental research, Chan and Albermani [83] found that the stiffness coefficient could be as low as 0.25, with an average value of 0.30 obtained from nine specimens. The loss in stiffness can be attributed to multiple factors, such as the experimental configuration or the accuracy of the effective length (l_e) used to compute a strut's strength and elastic stiffness.

It is worth mentioning that the deformation of the struts has two components, shear and bending. Due to their geometry, the shear deformation is expected to be small and, therefore, negligible. More details are given in Section 7.3, where the contribution of the shear deformation to the total deformation is shown.

7.2.2 Non-uniform slit dampers

When the struts of a slit damper are fully restrained, the shear force is distributed uniformly, while the moment has a linear distribution, as seen in Figure 7-4b. Thus, the acting moment on any individual strut at a length *x* from mid-span is as follows:

$$M_x = \frac{2M_1 x}{l_e} = Px \tag{7-7}$$

where M_1 is the maximum bending moment at the ends of the strut (as shown in Figure 7-4b), l_e is defined in Figure 7-3, and *P* is the axial load acting on the damper. Therefore, the struts can be designed so that plastic hinges are distributed throughout the entire length of the strut simultaneously, assuming that all the cross-sections reach the plastic bending

moment, M_p. Thus, the plastic bending moment at a given location x can be obtained with Eq. (7-8), and the optimized cross-sectional width along the length of the strut can be evaluated with Eq. (7-9), which is obtained by making Eq. (7-7) equal to Eq. (7-8).

$$M_{p,x} = \frac{f_y t_x b_x^2}{4} \tag{7-8}$$

$$b_x = \sqrt{\frac{4Px}{f_y t_x}} \tag{7-9}$$

where t_x and b_x are, respectively, the struts' cross-sectional thickness and width at location x.

In this study, the thickness of the damper is assumed to be uniform; therefore, t_x can be substituted by t, as will be done henceforth. This assumption results in a parabolic shape of the strut [96]. Eq. (7-9) assumes that the strut is only subjected to bending moment. However, shear stress also acts in the strut; therefore, it must have a minimum width to avoid brittle failure before the formation of plastic hinges due to the bending moment. The minimum width, b_o, of the strut is obtained as follows :

$$b_o = \frac{2\sqrt{3}P}{f_y t} \tag{7-10}$$

An optimal minimum width (b_o) that can ensure adequate strength larger than M_p, can be assumed as $0.5b_1$, being b_1 the width at the end of the struts, but not less than that calculated with Eq. (7-10), as suggested by Lee et al. [96]. Finally, the elastic stiffness (k_{SD}) and the yield displacement (δ_y) can be obtained with Eqs. (7-11) and (7-12), respectively.

$$k_{SD} = c\,\frac{E}{24\int_0^{h/2}(x^2/b_x^3 t)dx} \tag{7-11}$$

$$\delta_y = \frac{1}{c}\,\frac{2f_y t b_1^2}{6l_e}\,\frac{24\int_0^{h/2}(x^2/b_x^3 t)dx}{E} \tag{7-12}$$

More information on non-uniform slit dampers can be found elsewhere [96,111].

7.3 Theoretical vs. Numerical Properties

A finite element analysis (FEA) was conducted in ABAQUS [7] to obtain the capacity curve of a 6-strut SD. The steel material was considered to have an elastic-perfectly plastic with a yield stress of 345 MPa and a Poisson's ratio of 0.3, as was assumed in the hypotheses in Section 7.2. The SD was modeled using C3D10 (10-node quadratic tetrahedron) elements [7] with an approximate size of 5 mm. The capacity curve obtained from this analysis is shown in a Figure 7-5a and compared with the theoretical results (dashed lines) obtained with Eqs. (7-2) to (7-6). The applied loads are normalized by the yielding load obtained numerically. As can be seen, the theoretical results differ significantly from the FEA model, which implies that one or the other lacks precision. Therefore, a multi-stage parametric study was conducted to investigate the accuracy of the calculations. In particular, the effective length (l_e) used to calculate an SD's strength and elastic stiffness was varied. The analysis stages consisted of studying: 1) uniform struts without rounded ends, 2) uniform struts with rounded ends and lateral elements (see Figure 7-6), and 3) non-uniform struts with rounded ends and lateral elements. All models were made in ABAQUS [7].

Stage 1 showed that as a strut's aspect ratio (b / l) increases, the error between the theoretical and the numerical stiffnesses increases and can be as high as 10% for an aspect ratio of 0.2. However, if the theoretical analysis also considers the shear stiffness, the error is below 2% regardless of the aspect ratio. Using the total length of the strut was found to be accurate in computing the elastic stiffness; however, not for the strut's strength.

The typical model for Stage 2 is shown in Figure 7-6. All models were rounded at the ends with a radius equal to b / 2. The error between theoretical and numerical results was larger in this stage than in Stage 1. It was observed that the stresses penetrated some length into the lateral elements. Therefore, it can be assumed that the stiffness is developed over an effective length larger than the length of the strut (l), say l_k, as shown in Figure 7-7. Additionally, the study showed the struts' strength was underestimated by 13%, on average. Although the plastic hinges are concentrated at the struts' ends, these develop over a region called here l_p. The strength, however, can be approximately calculated considering a length smaller than l,

say l_r, representing the average length between the regions where the plastic hinges develop (see Figure 7-7).

From the results of the parametric analysis, the following three steps are proposed for calculating the stiffness, strength, and yielding stress of SDs:

Step 1: calculate the elastic stiffness of the SD as the series sum of the flexural (k_1) and shear (k_2) stiffnesses:

$$k_{SD} = n\left(\frac{1}{k_1} + \frac{1}{k_2}\right)^{-1} \tag{7-13}$$

being

$$k_1 = \frac{Etb^3}{l_k^3} \tag{7-14}$$

$$k_2 = \frac{AG}{l_k} \tag{7-15}$$

where A is the cross-sectional area, G is the shear modulus, and l_k is given by Eq. (7-16):

$$l_k = 0.93b + 1.01l_e \tag{7-16}$$

Eq. (7-16) was obtained from the Stage 2 results of the parametric study shown in Figure 7-8. In the figure, l_k was normalized by l_e. The horizontal axis shows the strut's aspect ratio b / l_e. It is noted that the effective length (l_k) is approximately equal to l_e plus a strut width (b).

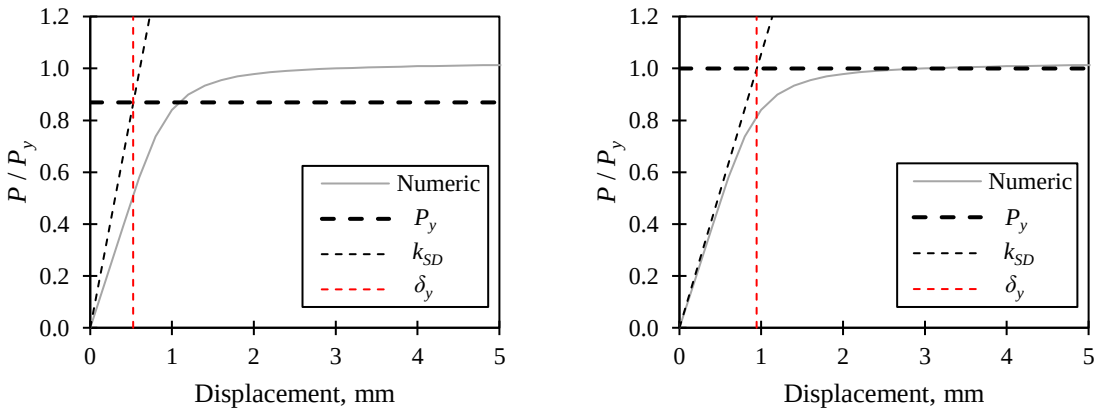

a) Comparison using the traditional method

b) Comparison using the proposed effective length method

Figure 7-5. Results comparisons using the traditional and proposed methods.

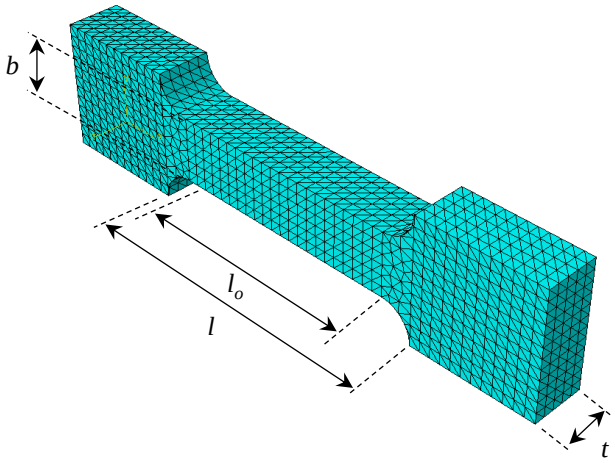

Figure 7-6. Typical model for Stage 2 of the parametric analysis.

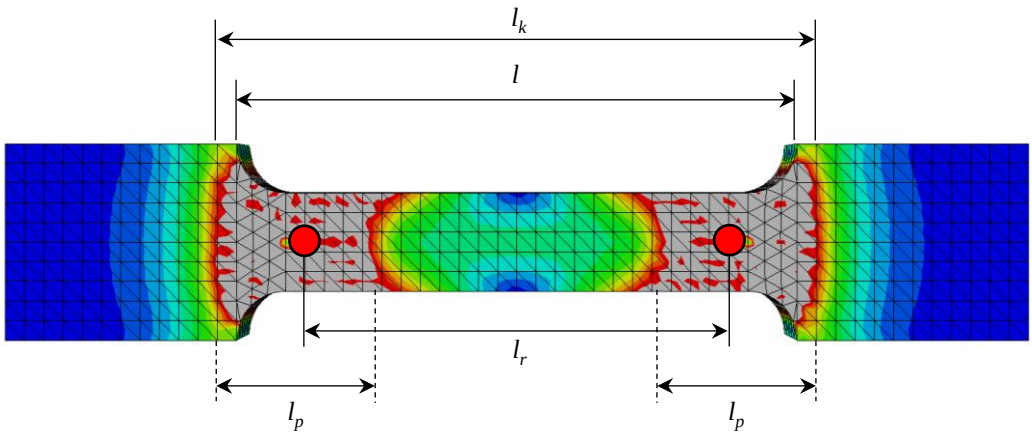

Figure 7-7. Proposed effective lengths.

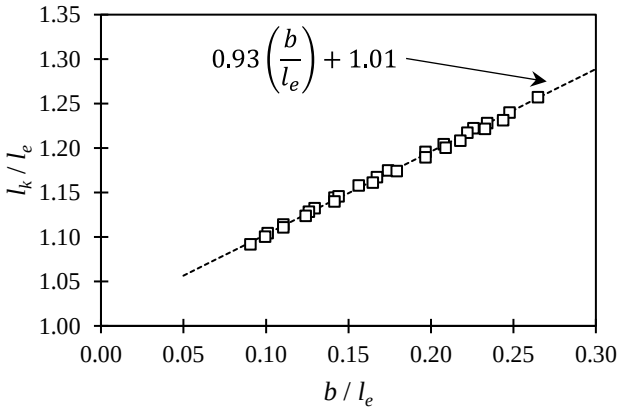

Figure 7-8. Variation of the effective length (l_k) as a function of the aspect ratio (b / l_e).

Step 2: compute the strength of the SD with the following equation:

$$P_y = n\frac{f_y t b^2}{2l_r} \tag{7-17}$$

where l_r can be estimated as $0.87l_e$.

Step 3: compute the yield displacement as:

$$\delta_y = \frac{P_y}{k_{SD}} \tag{7-18}$$

The results, using Eqs. (7-13) to (7-18), are compared to the numerical results in Figure 7-5b. As can be seen, the theoretical results are now in good agreement with the capacity curve. There is still a difference with the initial slope of the curve. The difference can be attributed to various factors, such as the rotation and axial deformation of the lateral and central plates of the SD. The latter issue is addressed below. It must be noted, however, that the proposed method should be limited to uniform SDs with a radius of b / 2, a width-to-thickness ratio (b / t) of 1.0, and an aspect ratio (b / l_e) between 0.10 and 0.25.

Eq. (7-13) assumes that only the struts provide axial stiffness to the damper. This would be true if the central and lateral elements of the SD had infinite stiffness. However, in the actual devices studied here, evaluating the effects of the lateral and central elements on the global stiffness is essential; while neglecting the shear deformation of the vertical transfer plate because it is small and capacity design dependent. Figure 7-9 shows an elastic stiffness model of the damper. It is seen that the total stiffness is the series sum of each component's stiffness. Thus, the total elastic stiffness, KSD, is given by the following equation:

$$K_{SD} = \left(\frac{1}{k_{SD}} + \frac{1}{k_{ce}} + \frac{2}{k_{le}}\right)^{-1} \tag{7-19}$$

where k_{ce} and k_{le} are the axial elastic stiffnesses of the central and lateral elements of the SD, respectively. Therefore, if the total elastic stiffness is to be used, the yielding displacement of the damper can be obtained as follows:

$$\Delta_y = \frac{P_y}{K_{SD}} \tag{7-20}$$

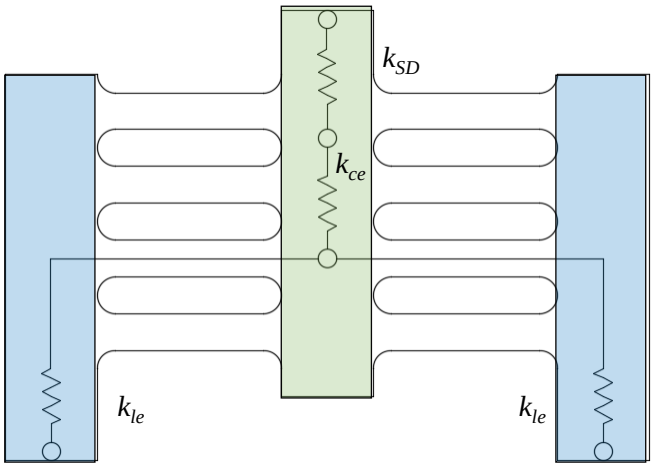

Figure 7-9. Elastic stiffness model of a typical SD.

Stage 3 of the parametric study focused on non-uniform SDs. The design of SDs with non-uniform struts can be simplified with an approach similar to that proposed above using Eqs. (7-13) to (7-15) and Eqs. (7-17) and (7-19) as long as the struts have a width-to-thickness ratio (b / t) of 1.0, an aspect ratio (b / l) between 0.10 and 0.2, and rounded-off edges with a radius equal to b / 4. In this case, the effective lengths l_k and l_r can be estimated as 1.2l and l, respectively. Given that non-uniform struts can have many configurations (see reference [96]), the method proposed here should be limited to struts that vary linearly from a width b at the ends to a width b / 2 at the center of the strut but not less than the width given by Eq. (7-10).

Not all of the blue and green shaded areas shown in Figure 7-9 exhibit a constant axial force. However, using the entire height of these elements simplifies the problem. It is on the conservative side while still being a rational parameter to compare with the stiffness of the struts, which ultimately should govern the global design. Actual devices implemented on frame buildings would have the central element constrained by the vertical transfer plate and, therefore, would be essentially undeformable. In contrast, the lateral elements (shaded in blue), as the damper increases in size, less of their height would be stressed.

In some cases, shear deformation of the struts and axial deformation of the other elements could be negligible. For example, shear deformation becomes more relevant as the aspect ratio (b / l_e) increases to values higher than 0.2. In the case of the SDs studied here and

described in Section 4.1, the shear deformation represents between 4 and 6%, while the axial deformation of the vertical elements represents between 7 and 14%. Together, they can accumulate a difference between 10 and 20%. Therefore, using Eq. (7-20) is considered better for calculating the yield displacement as it minimizes errors.

7.4 Experimental Program

The main objectives of the experimental program described below were to verify the theoretical evaluation of the proposed device's structural properties and to study its cyclic and fatigue performance.

7.4.1 Test specimens

A total of eight specimens, similar to that shown in Figure 7-3, were tested under cyclic loading. Five specimens were subjected to incremental cyclic loading, while the remaining three were subjected to constant-amplitude cyclic loading. The test specimens ID and their geometric and mechanical properties are shown in Table 7-1, where $P_{y,c}$ is the calculated yielding load, $\delta_{y,c}$ is the calculated yield displacement, and $K_{SD,c}$ is the calculated elastic stiffness. The test type applied to each specimen is also shown in the last column. Three specimen configurations were evaluated, with IDs preceded by: SD1, SD2, and SD3-NU, in Table 7-1, where NU stands for non-uniform struts. Figure 7-10 shows the geometric properties of the three configurations. It is significant to mention that the last part of the specimen ID is composed of I (incremental test) or C (constant amplitude test) and a consecutive number. Since the proposed damper is aimed at precast structures built in seismic zones, ductility and energy dissipation capacity were the main features studied in this investigation; thus, having more than one specimen for each configuration was paramount to obtaining reliable data for design purposes.

In Figure 7-10, it is seen that the ends of the struts for all specimens were rounded off. A radius equal to b / 2 was used for the uniform specimens, and a radius of b / 4 was used for the non-uniform specimens since the width of the slots at the ends is approximately half the width at the center. Additionally, coupon tests of the used steel gave an average tensile yielding stress of 354 MPa and an ultimate tensile stress of 530 MPa.

Table 7-1. Test specimens.

Specimen ID	Test type	n	t (mm)	b (mm)	b / l_e	$P_{y,c}$ (kN)	$K_{SD,c}$ (kN-mm)	$\delta_{y,c}$ (mm)
SD1-I1	Incremental	8	12.7	12.7	0.14	37.8	35.3	1.07
SD1-I2	Incremental							
SD1-C3	Constant amplitude							
SD2-I1	Incremental	8	12.7	12.7	0.17	45.5	55.0	0.83
SD2-I2	Incremental							
SD2-C3	Constant amplitude							
SD3-NU-I1	Incremental	8	12.7	12.3	0.14*	30.9	29.5	1.05
SD3-NU-C2	Constant amplitude							

*For NU specimens, the aspect ratio b/l is used.

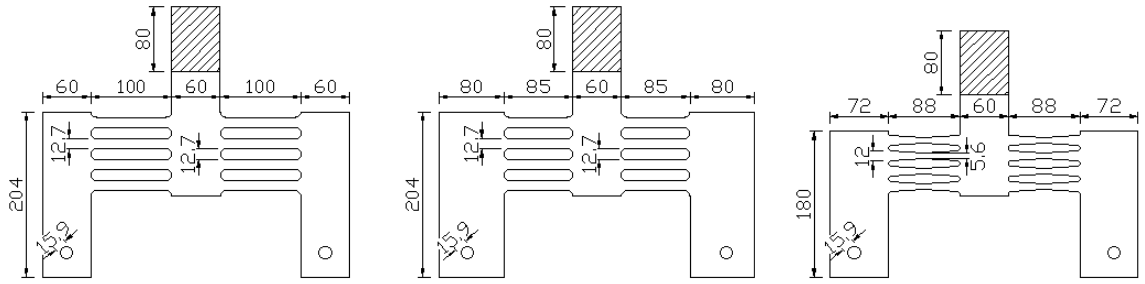

a) SD1 b) SD2 c) SD3-NU

Figure 7-10. Dimensions of tested specimens, in mm.

7.4.2 Test setup

To evaluate the performance of the proposed dampers, quasi-static cyclic tests were conducted using a 250 kN capacity universal testing machine. The test setup is shown inFigure 7-11. Each damper had two 15.9 mm diameter holes drilled at the bottom of the lateral vertical plates to connect a steel fastener (see Figure 7-12). The lower wedge grip of the universal machine clamped the fastener. The top wedge grip clamped approximately 80 mm of the center vertical plate of the damper (see shaded areas in Figure 7-10). Loads were measured with a 220 kN load cell installed above the top wedge grip. Displacements were measured with a linear variable differential transformer (LVDT) installed inside the testing machine.

It is possible that the proposed test setup could cause the buckling of the struts and out-of-plane deformations of the device, which, in consequence, could affect the cyclic response of the device. This phenomenon was avoided by defining a strut geometry so that the lateral-torsional strength was greater than the yielding strength. On the other hand, it is recalled that the lateral-torsional buckling modification factor, C_b, is relatively high in doubly symmetric sections with equal end moments of opposite sign (i.e., in elements working in double curvature). The ratio between the two mentioned limit states (lateral-torsional buckling to yielding strength) was 2.3 for the most unfavorable case of the studied specimens. As a consequence, no out-of-plane deformations were expected nor observed during the tests.

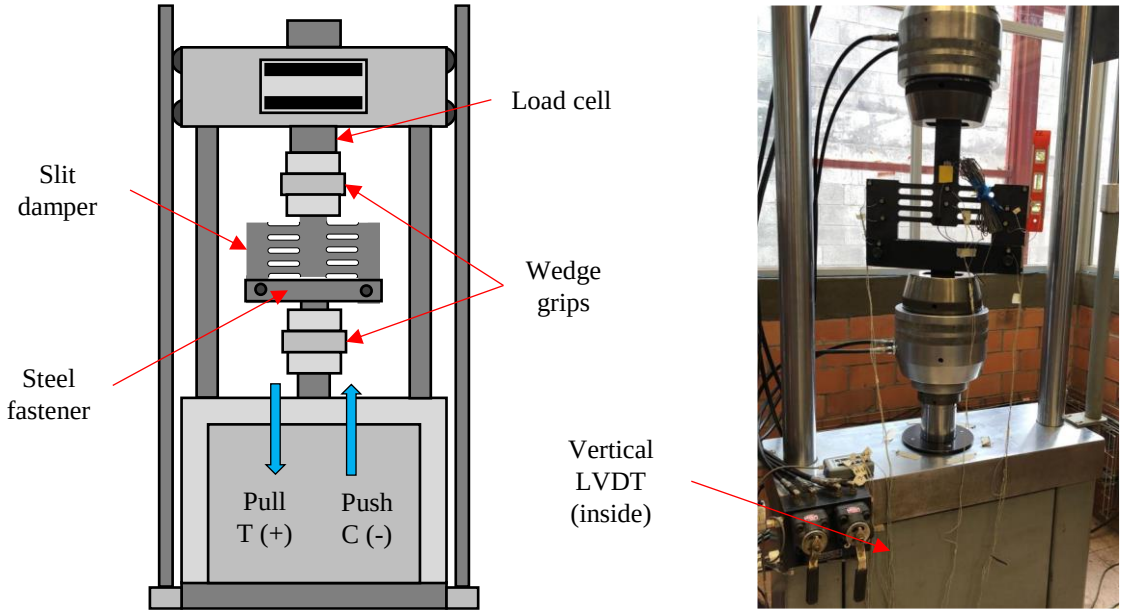

a) Test setup b) Photograph of the test setup

Figure 7-11. Test setup.

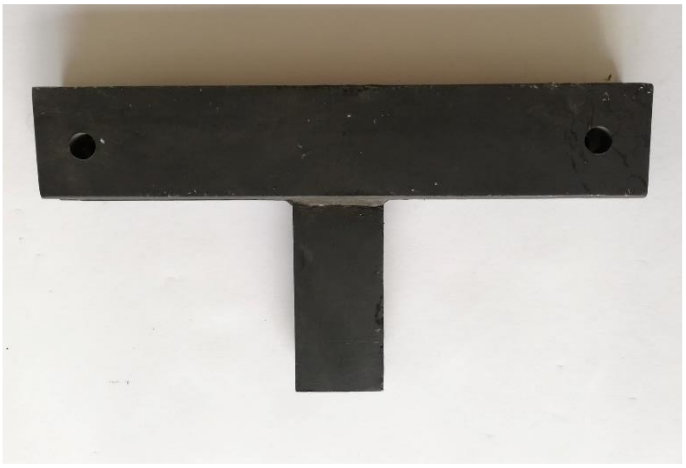

Figure 7-12. Steel fastener.

7.4.3 Loading protocols

7.4.3.1 Incremental cyclic tests

A displacement-controlled loading protocol with incremental amplitudes was applied quasi-statically. Since the struts of the three types of SDs had different aspect ratios, a loading protocol based on the strut drift ratio was proposed. In this way, the displacements at the center of the three damper types are different, but the struts' relative deformations are the same. The strut drift ratio was defined as the ratio between the displacement at the center of the damper and the total length of the strut, namely: δ / l. The loading protocol consisted of two cycles per displacement objective. The ratio between one displacement objective and the subsequent increment was between 1.4 and 1.5, up to a 15% strut drift ratio, as recommended by [96]. Afterward, the increments were fixed at a 2.5% strut drift ratio until failure was reached. Failure was considered to occur when the maximum registered load dropped by 20%. The typical loading protocol is shown in Figure 7-13. The applied load was considered positive when the damper was in tension, while it was considered negative when the damper was in compression. Tension was applied first on each cycle.

For design purposes, the inter-story drift ratio can be expressed in terms of the displacement at the center of the damper (δ) or as a function of the strut drift ratio (θ_{SD}) as follows:

$$\theta = \frac{\delta_{col}}{H_{col}} = \frac{\delta}{(H_{col} - h')} = \frac{\theta_{SD} l}{(H_{col} - h')} \tag{7-21}$$

where δ_{col} is the lateral displacement of the column or frame, H_{col} is the story height, h' is the center-to-center distance between the rotational hinge and the damper (see Figure 7-1), and l is the total length of the damper's struts.

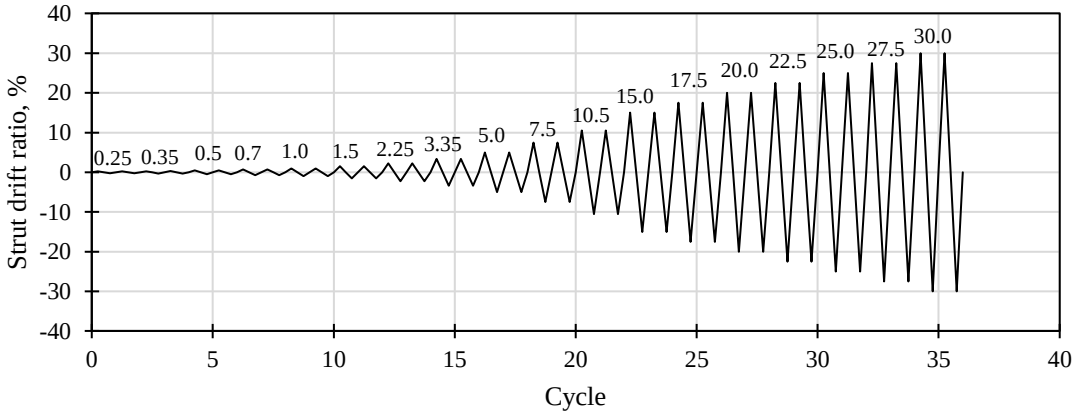

Figure 7-13. Incremental cyclic loading protocol.

7.4.3.2 Constant-amplitude tests

A uniform ductility-based cyclic loading protocol was proposed to assess fatigue under such conditions. It is illustrated in Figure 7-14. Note that two cycles at a ductility ratio of μ = 1 and two cycles at μ = 2 were used first before applying cycles at a ductility of μ = 4. The constant ductility amplitude of 4 was applied until failure of the specimen was reached. Specimens were considered to have failed when the maximum applied load had dropped 20%. The ductility ratio was defined as the ratio between the imposed displacement during testing and the yielding displacement based on the experimental results obtained from the incremental cyclic tests.

The inter-story drift ratio can be set in terms of the ductility ratio, in this case, 4, as shown in Eq. (7-22). Assuming that the yield displacement is approximately 3% of the length l -which is appropriate, as shown in the results and discussions section- the inter-story drift will typically be around 0.5%. This relatively small drift ratio makes the damper prone to fatigue and, therefore, essential to study.

$$\theta = \frac{\mu\delta_y}{(H_{col} - h')} = \frac{4\delta_y}{(H_{col} - h')} \tag{7-22}$$

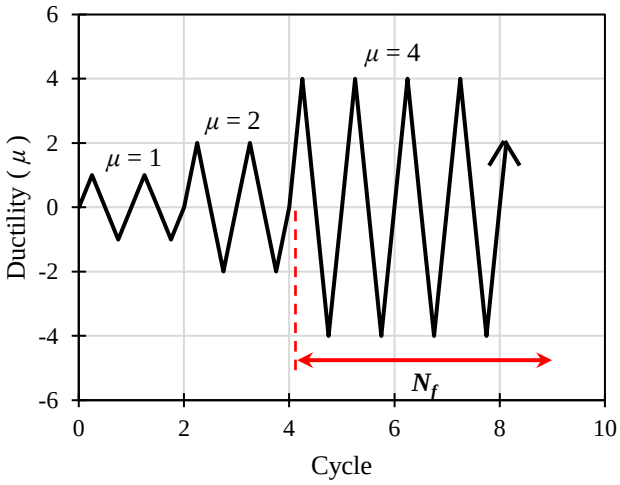

Figure 7-14. Loading protocol for the constant-amplitude tests.

7.5 Tests Results and Discussion

7.5.1 Incremental cyclic tests

7.5.1.1 Load-deformation curves

Load-deformation curves from the incremental cyclic tests are shown in Figure 7-15. The measured loads were normalized with respect to the calculated yielding load (see Table 7-1) to make a rational comparison between specimens. Contrary to the results of Figure 7-5b in it is noted that the maximum strength is significantly larger than the calculated yielding strength ($P_{y,c}$). This is attributed to two effects: strain hardening of steel and geometric nonlinearity. These effects are further evaluated below. On the other hand, displacements in the horizontal axis are presented in terms of strut drift ratios. The complete cycle after failure is shown for illustration purposes. In most cases, multiple struts had fractured after reaching the failure criteria, and the load-carrying capacity was quickly lost. SD1 specimens lost significant load-carrying capacity after the first cycle at a strut drift ratio of 0.2, while SD2 specimens only completed the first cycle at the same drift ratio. The measured load of Specimen SD3-NU-I1 slightly fell below 80% of the maximum registered load on the second cycle at a strut drift ratio of 0.3 rad.

The SD1 and SD2 specimens, with uniform struts, showed stable behavior up to a drift ratio of 0.175 without an abrupt loss of strength. At a drift ratio of 0.2, these specimens lost strength on the first loading cycle and significantly lost more strength on the second cycle. The specimen with non-uniform struts, SD3-NU-I1, presented a stable but asymmetrical hysteretic behavior with greater deformation capacity than the uniform counterparts. Also, from Figure 7-15f, it is clear that specimen SD3-NU-I1 had no abrupt loss of strength close to failure.

7.5.1.2 Failure modes

At strut drift ratios below 0.1 rad, struts of the SD1 and SD2 specimens were deformed in double curvature in tension and compression. However, the same cannot be said for higher drift ratios. Figure 7-16a and Figure 7-16b show the deformed shapes of specimen SD1-I1 at strut drift ratios of ±0.02 rad, respectively. While the damper was in tension, each strut appeared almost entirely in tension, contributing to its flexural strength, and no longer under double curvature bending, which can explain the asymmetry of the hysteresis curves. On the other hand, while the damper was in compression, the struts were reasonably still in double curvature, even with wide cracks appearing at their ends. This phenomenon can mainly be attributed to the boundary conditions that do not behave the same in tension or compression. As the tests were displacement-controlled, a symmetrical behavior would still be expected with axial tension in the struts when the damper was in compression. However, at large deformations, while the damper was in compression, the lateral elements tended to rotate, which contributed to the apparent loss of strength in the hysteresis curves, being more evident in specimen SD3-NU-I1.

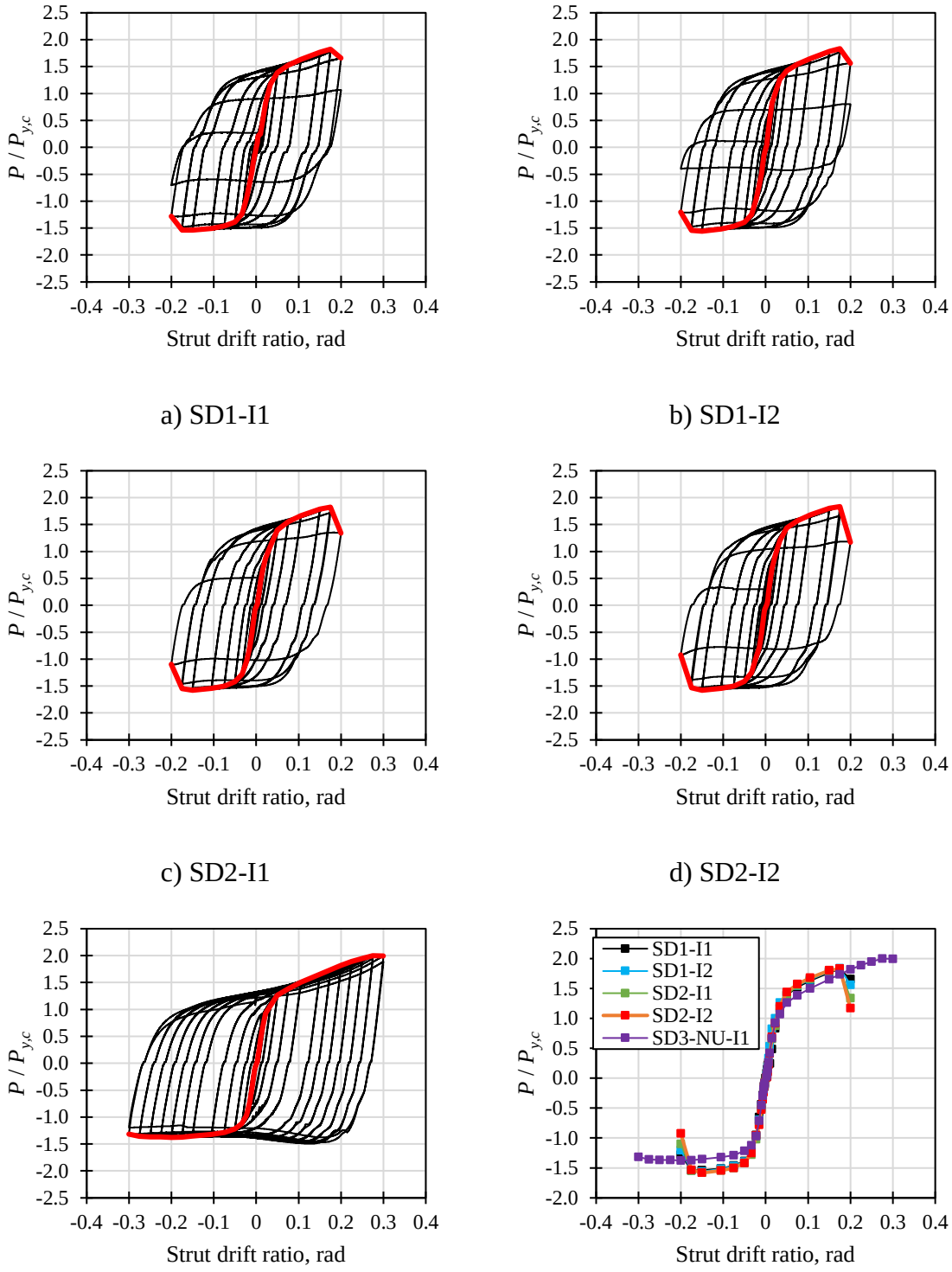

a) SD1-I1

b) SD1-I2

c) SD2-I1

d) SD2-I2

e) SD3-NU-I1

f) Envelopes

Figure 7-15. Load-deformation curves.

After reaching the failure criteria, a cycle at 0.225 rad was attempted for specimen SD1-I1. At this stage, the specimen lost multiple struts on the right side of the damper nearly at the same time (see Figure 7-16c). A photograph of the state of the damper after testing is shown in Figure 7-16d. In general, specimens SD1-I2, SD2-I1, and SD2-I2 behaved similarly and presented comparable failure modes. To ratify this, Figure 7-17 shows the state of specimen SD2-I2 before and after testing.

a) θSD = 0.02 rad

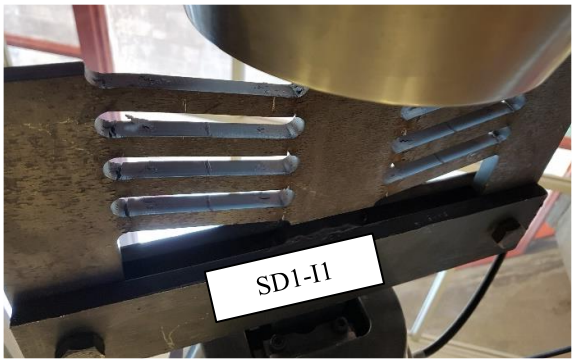

b) θSD = -0.02 rad

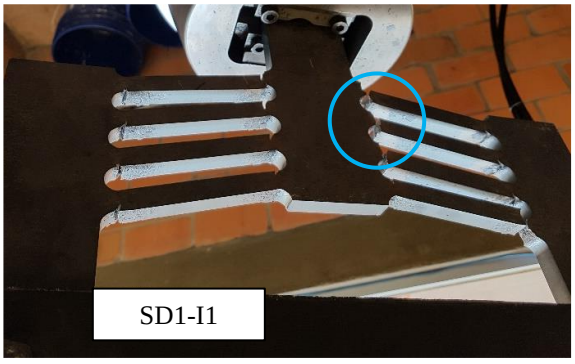

c) θSD = 0.0225 rad

d) Final state

Figure 7-16. Failure modes of SD1-I1.

Specimen SD3-NU-I1 behaved differently from the specimens with uniform struts. In this case, the struts were deformed in double curvature while the damper was in tension and compression even at large drift ratios. Additionally, only one strut was fractured during the test, as seen in Figure 7-18. As mentioned before, this did not imply an abrupt loss of strength, unlike the other tested specimens. Figure 7-18 also shows manufacturing defects on one of the struts. Although multiple struts had similar defects, the most damaged strut during the manufacturing process was the one that fractured close to failure. The rest presented minor

flexural cracking at the ends, as shown in Figure 7-19. The difference between manufacturing defects and minor flexural cracks developed during the test is clearly seen.

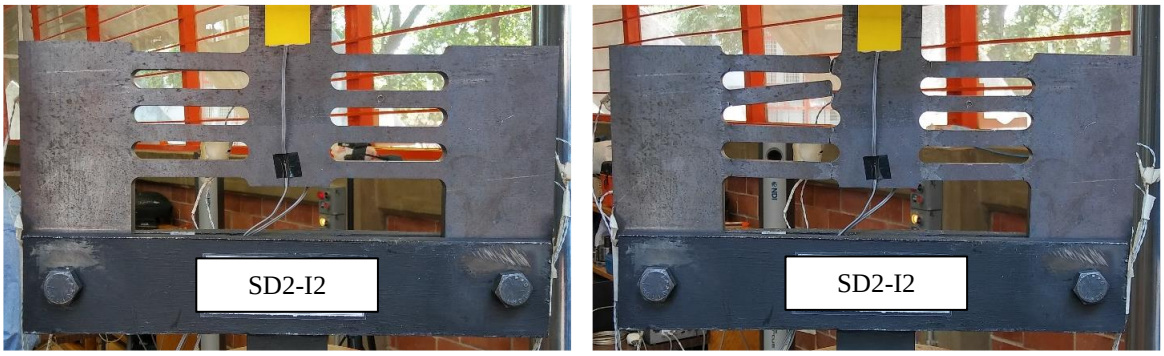

Figure 7-17. Specimen SD2-I2 before and after testing.

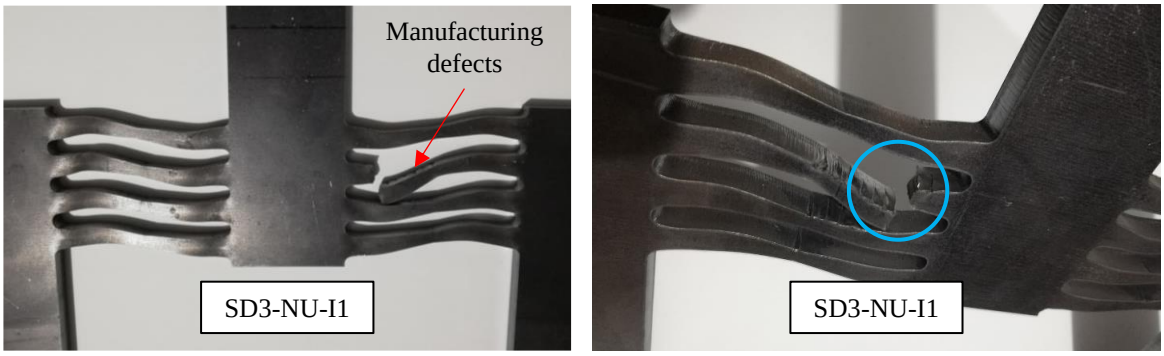

Figure 7-18. Specimen SD3-NU-I1 after testing.

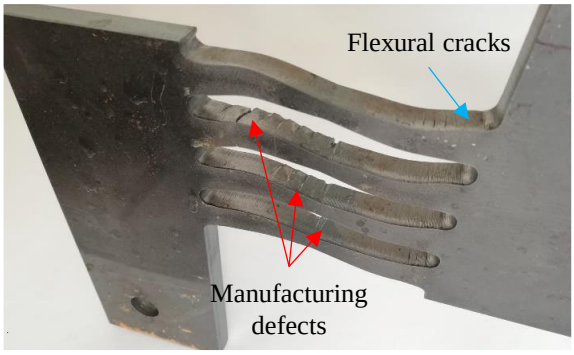

Figure 7-19. Difference between manufacturing defects and minor flexural cracks.

7.5.1.3 Load and deformation capacity

Load and deformation parameters were obtained from idealized bilinear curves based on the envelopes shown in Figure 7-15. The idealized bilinear curves were obtained using the equivalent energy method described in ASCE 41-17 [81]. Figure 7-20 shows the concept and definition of the idealized bilinear curve and its structural characteristics. Table 7-2 shows a summary of the test results. Results were deemed reasonably dissimilar in tension (+) and compression (-); therefore, they are presented separately.

Experimental yielding drift ratios ($\theta_{y,ex}$) were, on average, 3% of the strut's total length (l), which is significantly higher than the theoretical yielding displacements. Initial experimental stiffnesses ($K_{i,ex}$) are approximately 50% of the theoretical stiffnesses shown in Table 7-2. Stiffness loss can be mainly attributed to the pinned condition of the tested dampers, which permitted rotation of the lateral elements of the damper. Therefore, in actual applications, preferably, the damper should be reasonably pinned at the ends of the lateral elements to estimate the yielding displacement as $0.03l$.

The initial experimental stiffnesses of SD3-NU-I1 are similar to those presented by the SD1 specimens, which have similar global geometric characteristics. This suggests that the stiffnesses of uniform and non-uniform struts are similar if they have similar aspect ratios, which can be attributed to the uniform struts having less material, compared to the non-uniform struts, being stressed during the test. Specimens with uniform struts presented average ultimate ductility ratios (μ) of 6.4, while specimen SD3-NU-I1 reached an average ductility ratio of 10.6. Finally, the post-elastic stiffness coefficients, α, for specimens with uniform struts were, on average, 0.02 and 0.01 in tension and compression, respectively. For the specimen with non-uniform struts, these values were, respectively, 0.05 and 0.01.

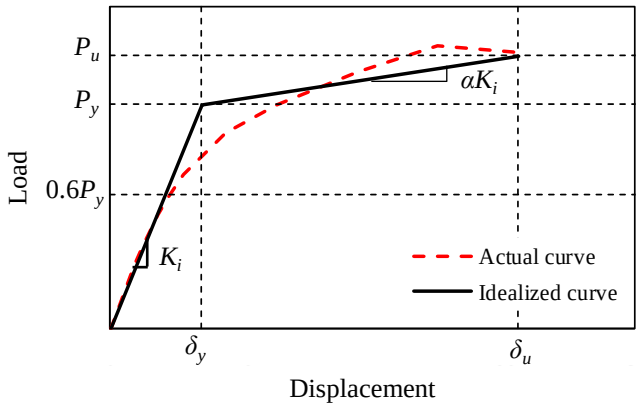

Figure 7-20. Idealized bilinear curve and its structural characteristics.

Table 7-2. Summary of test results.

Specimen	Direction	$P_{y,ex}$ (kN)	$P_{y,ex}$ / $P_{y,c}$	$P_{u,ex}$ (kN)	$P_{u,ex}$ / $P_{y,c}$	$K_{i,ex}$ (kN-mm)	$\theta_{y,ex}$ (%)	$\theta_{u,ex}$ (%)	μ	α
SD1-I1	(+)	55.6	1.5	68.9	1.8	16.7	3.33	19.60	5.9	0.04
	(-)	51.7	1.4	58.2	1.5	17.3	2.99	20.00	6.7	0.02
SD1-I2	(+)	56.9	1.5	69.4	1.8	19.5	2.91	20.00	6.9	0.02
	(-)	53.8	1.4	59.0	1.6	16.7	3.23	20.00	6.2	0.01
SD2-I1	(+)	67.9	1.5	83.0	1.8	26.1	3.06	19.32	6.5	0.02
	(-)	65.2	1.4	72.0	1.6	27.6	2.78	19.32	7.2	0.01
SD2-I2	(+)	70.6	1.6	83.4	1.8	24.1	3.44	19.31	5.8	0.01
	(-)	64.4	1.4	72.0	1.6	25.5	2.97	19.32	6.5	0.01
SD3-NU-I1	(+)	40.5	1.3	61.8	2.0	16.9	2.73	30.00	11.0	0.05
	(-)	39.9	1.3	42.6	1.4	15.4	2.95	30.00	10.2	0.01

7.5.1.4 Ductility and energy dissipation

As stated by Teran-Gilmore [66], the cumulative ductility ratio, i.e., the ratio of cumulative plastic displacement to the yielding displacement of the structure, can be calculated as follows:

$$NE_{H\mu} = \frac{E_{H\mu}}{P_y \delta_y} \tag{7-23}$$

where $E_{H,\mu}$ is the cumulative plastic energy. The cumulative hysteretic energy is shown in Figure 7-21a, while the cumulative ductility ratio, i.e., the normalized values, is shown in

Figure 7-22b. Both values are plotted against the cumulative displacement. As observed by Teran-Gilmore [66], $E_{H\mu}$ by itself does not provide enough information to assess structural performance as the energy demand of a system with high lateral strength that undergoes one plastic incursion can be larger than that of a system with low lateral strength that undergoes several cycles. From Figure 7-21b, it can be seen that, when normalizing the values to their structural characteristics, the specimen with non-uniform struts (SD3-NU-I1) dissipates more plastic energy for the same level of cumulative displacements. Also, because it can accumulate more plastic displacements, around two times more, the cumulative ductility ratio was 3.5 times higher than its uniform counterparts, i.e., the SD1 and SD2 types. This clearly shows the benefit of using an SD with non-uniform struts designed to achieve similar strengths. The cumulative ductility ratio and the cycle number at failure for each specimen are shown in Table 7-3. The superior cyclic performance of specimen SD3-NU-I1 is evident, having a similar aspect ratio as specimen SD1-I1 but having withstood more cycles at larger deformations, thus presenting higher energy dissipation capacity.

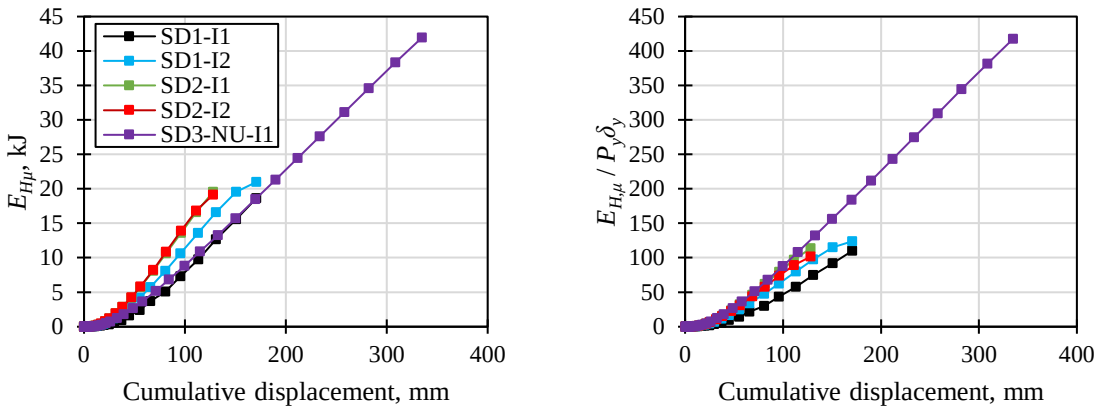

a) Cumulative hysteretic energy b) Cumulative ductility ratio

Figure 7-21. Energy dissipation capacity of tested specimens.

Table 7-3. Cumulative ductility ratios of the incremental cyclic tests.

Specimen	b / l_e	$E_{H,\mu}$ (kN-mm)	$N_{EH,\mu}$	Cycle at failure
SD1-I1	0.14	18603	110	28
SD1-I2		20994	124	28
SD2-I1	0.17	18740	113	27
SD2-I2		19153	101	27
SD3-NU-I1	0.14*	41940	418	36

*For NU specimens, the aspect ratio b/l is used.

7.5.1.5 Effective stiffness

The normalized effective stiffness, $K_{eff,n}$, at each applied cycle is shown in Figure 7-22a. The effective stiffness, K_{eff}, defined as the slope of the peak-to-peak line connecting the maximum achieved displacement-load point in the positive and negative directions, was normalized by the theoretical stiffness ($K_{SD,c}$). In general, all specimens exhibited similar behavior throughout the tests. This suggests that specimens with non-uniform struts possess a similar effective stiffness to their uniform counterparts due to the latter having more material that is not used or effectively stressed. Note that specimen SD3-NU-I1 reached higher drift ratios without an abrupt loss of effective stiffness. For drift ratios close to zero, some effective stiffness values were lower than the initial experimental stiffness ($K_{i,ex}$). This is mainly attributed to slippage in the pull direction, which took a large portion of the target displacement for small cycles and resulted in a smaller slope of the peak-to-peak line.

With the collected data, an effective stiffness model (see Figure 7-22b) was developed to have a practical method for calculating the effective stiffness of an SD at a given displacement. The following equation governs the trendline shown in Figure 7-22b:

$$k_{eff,n} = a\theta_{SD}{}^{-b} \tag{7-24}$$

where $k_{eff,n}$ is the normalized effective stiffness, θ_{SD} is the strut drift ratio of the SD, and a and b are constant values obtained by linear regression analysis, to be 0.04 and 0.56, respectively. The coefficient of determination for the accuracy of Eq. (7-24) is R^2 = 0.745, which may be considered appropriate as it means that 25.5% of the variance in effective stiffness is not accounted for in the model. For drifts smaller than 0.005, $k_{eff,n}$ can be taken as

1.0 for simplification sakes; however, it is recognized that small stiffness values at very small displacements can be developed in real-world applications. Therefore, studying the damper's behavior when located on an actual precast concrete beam-column connection or frame system is essential.

The following procedure can be used to calculate the effective stiffness of any damper. First, the yielding displacement (δ_y) can be approximated as $0.03l$, based on the experimental evidence shown in Table 7-2. Then, the expected yielding load (P_{ye}) can be taken as $1.5P_y$ or $1.3P_y$ for uniform or non-uniform SDs, respectively. Thus, the elastic stiffness can be approximated as $K_{SD} = P_{ye} / \delta_y$. Finally, K_{SD} is multiplied by the normalized effective stiffness obtained from Eq. (7-24) to obtain the effective stiffness at any given strut drift ratio.

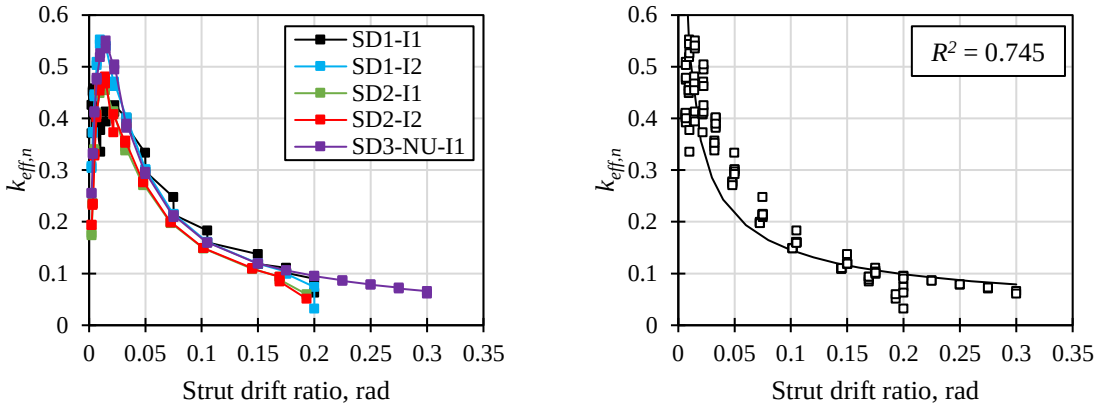

a) Normalized effective stiffness b) Normalized effective stiffness model

Figure 7-22. Effective stiffness.

7.5.1.6 Equivalent viscous damping

Plots of the equivalent viscous damping ratios, calculated in this study, are shown in Figure 7-23. They are plotted with the ductility ratios (Figure 7-23a) or the normalized effective stiffness (Figure 7-23b). From Figure 7-23a, it can be seen that the damping increases as the deformation increases. However, after a ductility ratio of 5, the damping ratio stabilizes at around 45%. Before yielding (μ=1), the devices can dissipate small amounts of hysteretic energy, equivalent to damping ratios of up to 10% within the elastic range.

In Figure 7-23b, each point represents a feasible damping ratio for a given effective stiffness. As can be observed, damping ratios vary approximately linearly and inversely proportional to the effective stiffness. Thus, an equivalent damping model was developed. The following equation is proposed:

$$\zeta_{eq} = -c\frac{k_{eff}}{K_{i,ex}} + d \tag{7-25}$$

where $K_{i,ex}$ is the initial experimental stiffness and can be replaced by K_{SD} as explained above, and c and d are constant values obtained by linear regression analysis, to be 1.0 and 0.5, respectively. The proposed device can provide equivalent damping ratios up to 45%; however, for small displacements (i.e., the first three pairs of cycles), the effective stiffness is low (see Figure 7-22a). As a consequence, damping ratios at these displacements are close to zero, as shown in the shaded area in Figure 7-23b. It is significant to mention that these values were not considered for the equivalent damping model of Eq. (7-25). The equivalent damping model proposed by Chan and Albermani [83] is also shown for comparison. The difference between the models highlights the importance of the damper geometry and the experiment configuration when defining its properties and overall behavior.

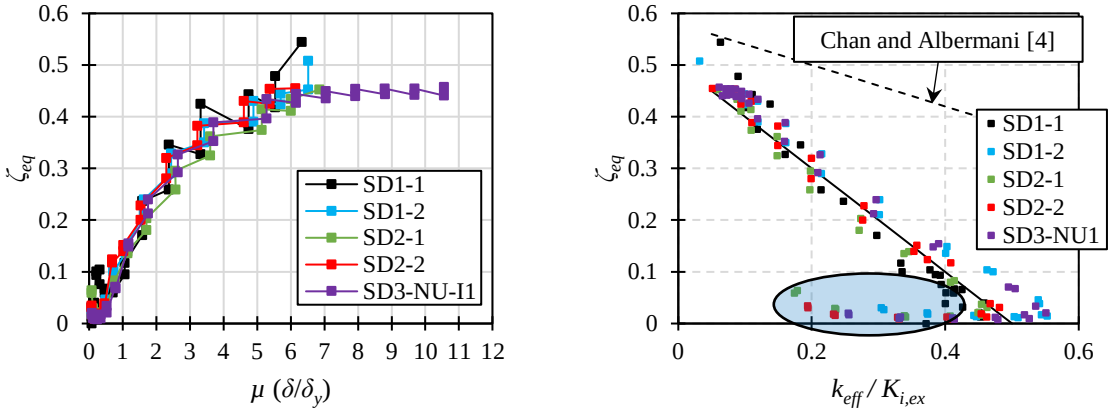

a) Equivalent viscous damping with ductility ratios

b) Equivalent viscous damping with normalized effective stiffness

Figure 7-23. Equivalent viscous damping.

7.5.2 Constant amplitude tests

7.5.2.1 Ductility and energy dissipation

Three specimens were tested using the uniform ductility-based cyclic loading protocol shown in Figure 7-14. The resultant load-ductility curves are shown in Figure 7-24a-c, and a comparison between them is shown in Figure 7-24d. It is recalled that cycles were repeated until failure for a ductility of 4.0. The cycle number at failure, $N_{f,4}$, is also shown in Figure 7-24. Specimen SD3-NU-C2 showed superior fatigue performance. Great advantages are observed when compared to its uniform counterpart (SD1-C3). First, the number of cycles, applied to specimen SD3-NU-C2 at ductility of 4.0 was 66, i.e., 6.6 times larger than those applied to specimen SD1-C3. Second, while the fatigue performance was improved, damage to the damper was significantly delayed. In fact, damage was uniformly distributed along the strut length instead of being concentrated at the ends, as observed for specimens SD1-C3 and SD2-C3. Indeed, the ductility demand was the same for all specimens; however, the ductility demand to capacity ratio (DCR) -defined as the ratio between the maximum ductility achieved from the incremental cyclic tests and the target ductility (in this case 4) - were approximately 1.6 for the uniform specimens and 2.6 for specimen SD3-NU-C2. Although the DCRs were not precisely the same, the objective was to compare the fatigue performance of specimens SD1-C3 and SD3-NU-C2, which were designed with similar aspect ratios and strengths under similar ductility demands. This comparison displays that the non-uniform SD has a significantly larger residual fatigue capacity than the uniform counterpart. Certainly, more tests and comparisons under similar DCRs should be of interest for future studies.

The deformed shape of SD3-NU-C2 during the last applied cycle (cycle 66) is shown in Figure 7-25. Similar to specimen SD3-NU-I1, before cycle 62, only one strut had fractured. It is observed in Figure 7-24c that, contrary to specimens SD1-C3 (Figure 7-24a) and SD2-C3 (Figure 7-24b), the load-carrying capacity reduced slowly, while specimens SD1-C3 and SD2-C3 lost strength quickly after a strut was lost.

The cumulative ductility ratios and the cycle at which failure was reached during the tests are shown in Table 7-4. The aspect ratios of the struts are also shown for comparison purposes. As seen from the two uniform dampers (SD1-C3 and SD2-C3), the higher the aspect ratio, the smaller the cumulative ductility ratio is achieved. This may suggest that more

robust dampers have less energy dissipation capacity; however, the sample size is too small to confirm this. On the other hand, specimen SD3-NU-C2 presented a cumulative ductility ratio six times greater than its uniform counterpart SD1-C3.

The state of specimen SD3-NU-C2 after testing is shown in Figure 7-26. Some minor flexural cracks developed during the tests are indicated with blue arrows. On the other hand, a red arrow points to a series of manufacturing defects. As also observed in specimen SD3-NU-I1 (from the incremental cyclic tests), multiple struts presented similar defects; however, the most affected strut during the manufacturing process (indicated in a blue circle) was the only one to have completely fractured.

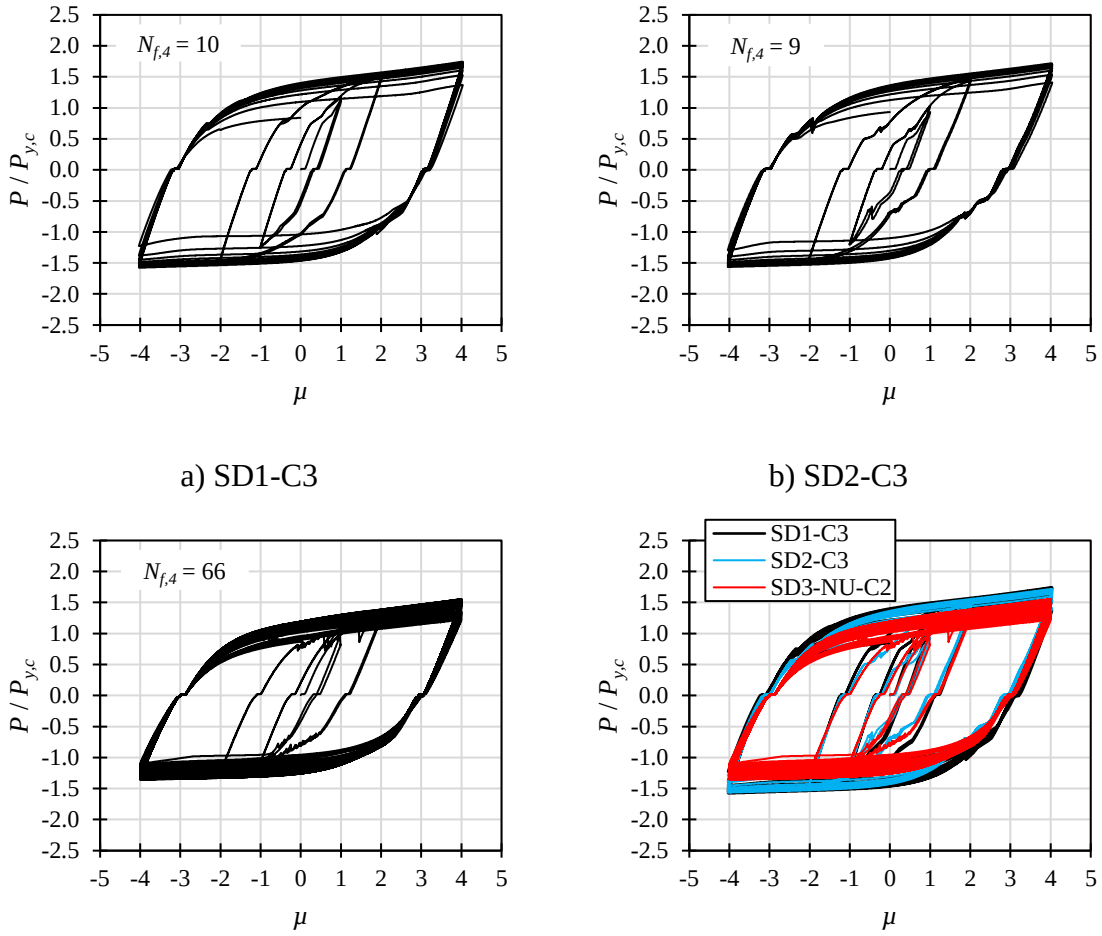

a) SD1-C3

b) SD2-C3

c) SD3-NU-C2

d) Comparison of the fatigue curves

Figure 7-24. Specimen load-ductility curves.

Table 7-4. Cumulative ductility ratios of the fatigue tests.

Specimen	b / l_e	$E_{H,\mu}$ (kN-mm)	$NE_{H,\mu}$	$N_{f,4}$
SD1-C3	0.14	20154	119	10
SD2-C3	0.17	17161	97	9
SD3-NU-C2	0.14*	71859	716	66

*For NU specimens, the aspect ratio b/l is used.

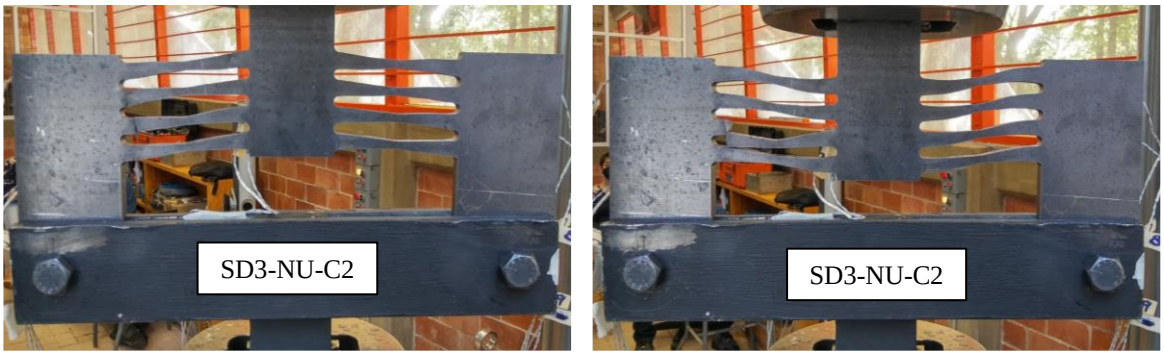

a) μ = +4 b) μ = -4

Figure 7-25. Failure modes of SD3-NU-C2.

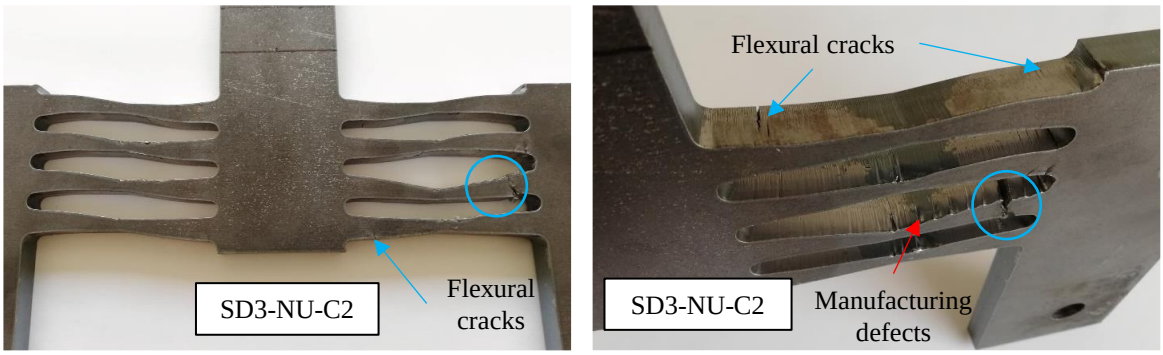

Figure 7-26. Specimen SD3-NU-C2 after testing.

7.6 Finite Element Analysis

Experimental results were validated with finite element analysis (FEA) using ABAQUS [7]. Three models were developed to simulate the cyclic behavior of the three studied damper types, namely: SD1, SD2, and SD3-NU.

7.6.1 Analysis method

The three studied dampers were modeled using C3D10 (10-node quadratic tetrahedron) elements with an approximate size of 5 mm. The models are shown in Figure 7-27. Cyclic loading was applied to the models at the top of the central, vertical element using the "Static, General" analysis method available in ABAQUS [7]. Geometric nonlinearity was taken into account. The loading protocol was the same as in Figure 7-13. For simplicity, the clamped region shown in Figure 7-10 and the steel fastener (Figure 7-12) were not included in the analyses.

The elastic-plastic behavior of the steel material was modeled using the combined non-linear isotropic and kinematic hardening model. All the material's mechanical properties are shown in Table 7-5, where v is the Poisson ratio, and the hardening parameters Q_∞, b, c, and γ were based on the values given by Yoshida et al. [113] and Madheswaran and Tesamariam [114]. In parentheses is the value of Q_∞ used specifically for the non-uniform model (SD3-NU), as recommended by Saeed et al. [91].

Table 7-5. Mechanical properties for FEA models.

Hardening parameters		Elastic properties		Plastic properties	
Q_∞, MPa	108 (80)	E, MPa	200000	σ_y, MPa	354
b	13.5	v	0.3		
c, MPa	5880				
γ	55				

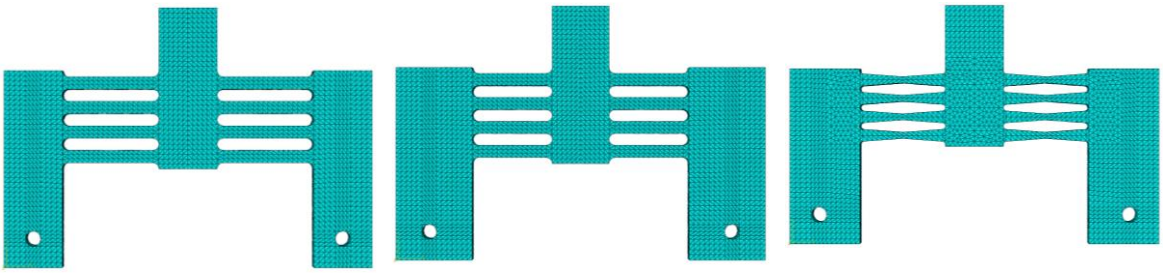

a) SD1 b) SD2 c) SD3-NU

Figure 7-27. Finite element models of the three types of studied SDs.

7.6.2 Comparisons with test results

Results of the FEA are compared with the experimental results in Figure 7-28. In general, it can be said that the cyclic behavior and strain hardening could be reasonably simulated with the mechanical properties proposed in Table 7-5. For specimens SD1 (Figure 7-28a) and SD2 (Figure 7-28b), the sudden loss of strength at a strut drift ratio of 0.2 rad could not be predicted with the current model; however, up to a drift ratio of 0.175 rad, the load-deformation relationship was in good agreement with the experimental results. Of course, in the experiments, sudden loss of strength was due to the fracture of struts, which was not considered in the numerical models. Additionally, the hysteretic response of specimen SD3-NU (Figure 7-28c) matched well with the numerical results. The asymmetric response of the damper was accurately represented with the proposed model.

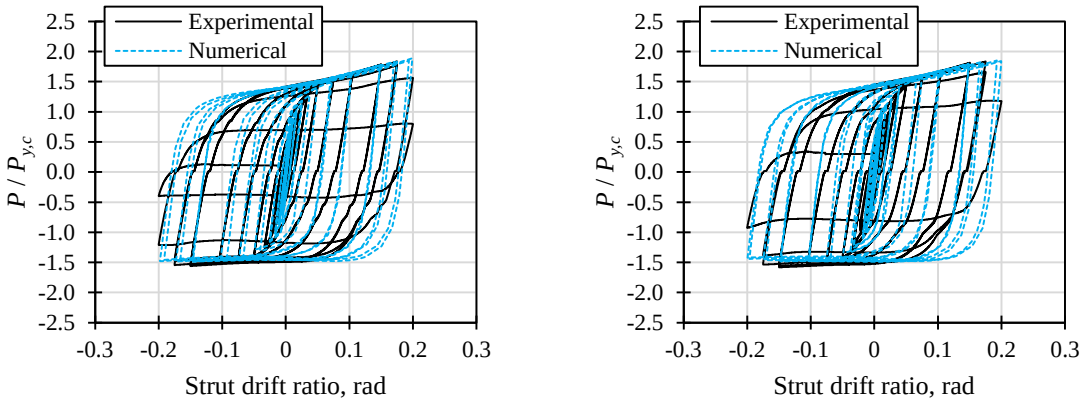

a) SD1

b) SD2

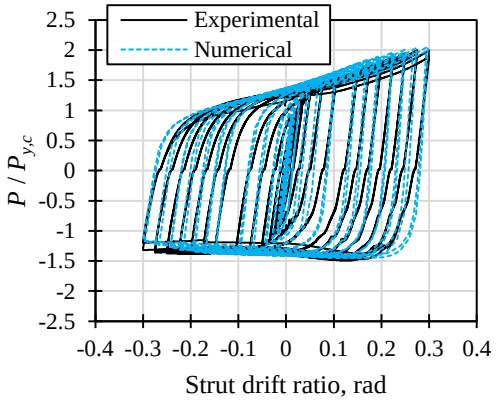

c) SD3-NU

Figure 7-28. Comparisons of experimental and numerical hysteresis curves.

Numerical and experimental backbone curves and the cumulative ductility ratio of specimen SD3-NU-I1 are shown in Figure 7-29a and Figure 7-29b, respectively. The backbone curves are in agreement in both loading directions (indicated with "+" and "-"). It is seen that the experimental results showed a lower elastic stiffness. Consequently, the experimental yielding displacement was around two times higher than what was expected from the numerical model. Yielding loads and maximum loads were accurately predicted. The numerical cumulative ductility ratio resulted slightly higher than the experimental results for the same cumulative displacements, primarily due to the higher elastic stiffness. Differences between numerical and experimental results can be mainly attributed to the boundary conditions and possible deformation of the testing machine during the experiment; however, the proposed analysis method is generally deemed a good benchmark.

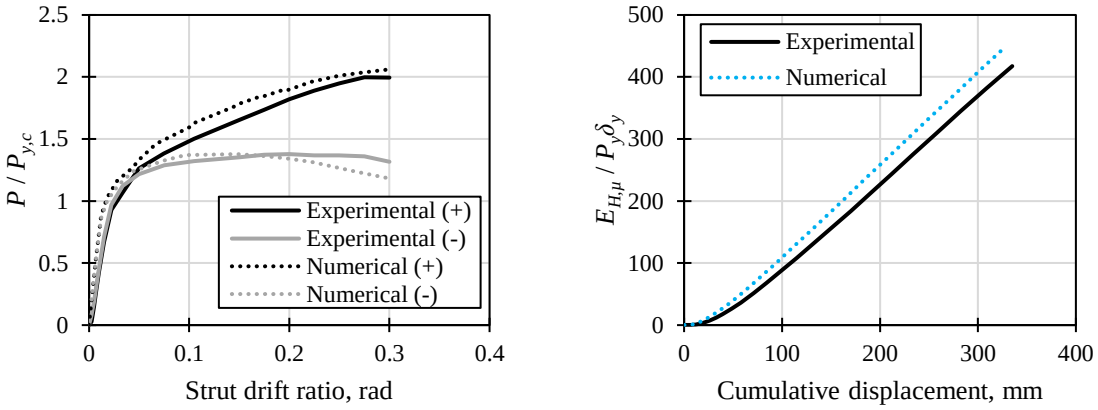

a) Backbone curves b) Cumulative dissipated energy

Figure 7-29. Comparisons of experimental and numerical results of SD3-NU-I1.

Stress distributions of models SD1 and SD2 are shown in Figure 7-30 and provide a good representation of the damage observed during the tests. Stresses were mainly concentrated at the ends of the struts and were beyond the yielding stress at a drift ratio of 0.2 rad. The yield stress was surpassed at small deformations due to strain hardening, which explains the material fatigue observed during the experimental tests and may explain the sub-estimation of the theoretical strength, P_y. For model SD3-NU, stresses were more distributed towards the center of the strut, as shown in Figure 7-31. This also agrees with the observed damage, where minor flexural cracks were uniformly distributed along the length of the struts. It is

also worth highlighting that the central and lateral elements of the dampers were not overstressed, thus verifying that the capacity design of the proposed damper's components is reliable.

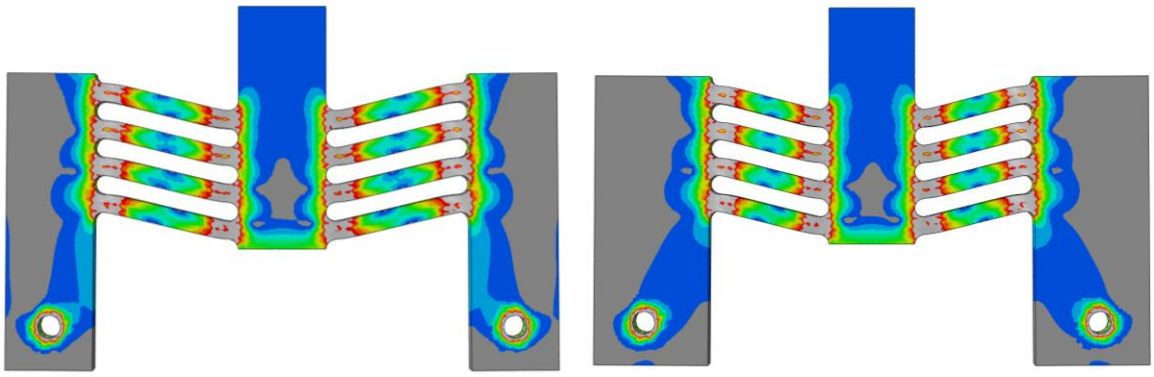

a) SD1 b) SD2

Figure 7-30. Stress distributions in models SD1 and SD2.

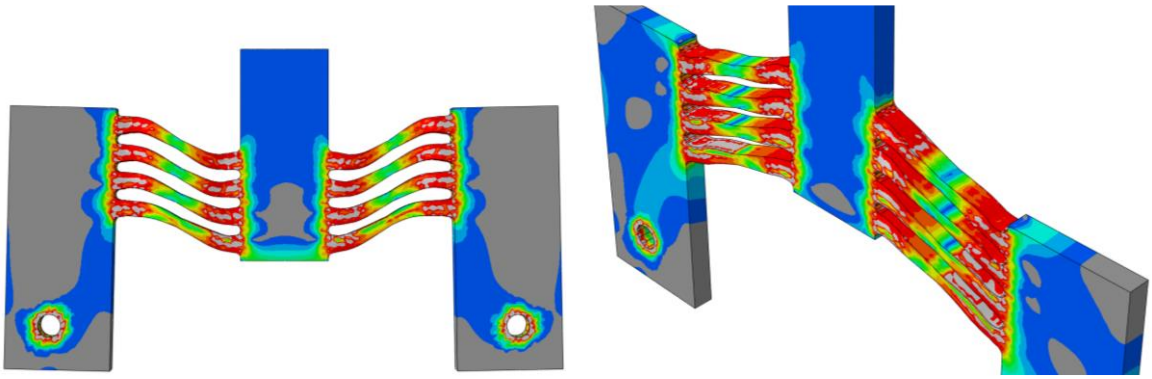

a) SD3-NU (compression) b) SD3-NU (tension)

Figure 7-31. Stress distributions in model SD3-NU.

In general, the results of the FEA show that using the combined isotropic and kinematic hardening model, the proposed mechanical properties available in the literature, and the C3D10 element, is appropriate and satisfactory for an adequate numerical simulation of the SDs cyclic response. Since the results are easily reproduced numerically, it can be said that the proposed device is reliable for practical applications. It is highlighted that a damage model could also be introduced into the current models to predict crack initiation; however,

that was considered time-consuming and certainly out of the scope for validation purposes. However, future studies may be focused on such analyses.

7.6.3 Effects of strain hardening and geometric nonlinearity

The experimental backbone curve of specimen SD3-NU-I1 is shown in Figure 7-32 and compared to the numerical results of multiple models made in ABAQUS [7] considering different conditions of the material behavior. The Complete Model is the same as shown in Figure 7-29a, which considers strain hardening and geometric nonlinearity. The Strain Hardening Model considers strain hardening due to cyclic loading. The Geometric NL Model considers the effects of nonlinearity due to large deformations. Finally, the Simple Model only considers an elastic-perfectly plastic behavior of steel. Only the response in the positive direction is shown.

The combined isotropic-kinematic hardening model used in ABAQUS [7] describes the cyclic transient elastic-plastic material behavior, which can include the following effects: the Bauschinger effect, cyclic hardening with plastic shakedown, ratcheting, and relaxation of the mean stress. In Figure 7-32, although the response in the negative direction is not shown, the Strain Hardening Model (blue dotted line) presented a symmetrical hysteretic response. On the other hand, the Geometric NL Model accurately captured the asymmetrical hysteretical response. In the positive direction, as shown in Figure 7-32, the load consistently increases after yielding as the deformation increases, while the response in the negative direction will plateau. The Simple Model represents the damper's response that can be accurately predicted with the proposed effective length method, which, as can be seen, does severely underestimate the maximum load developed in the device and, therefore, its energy dissipation capacity.

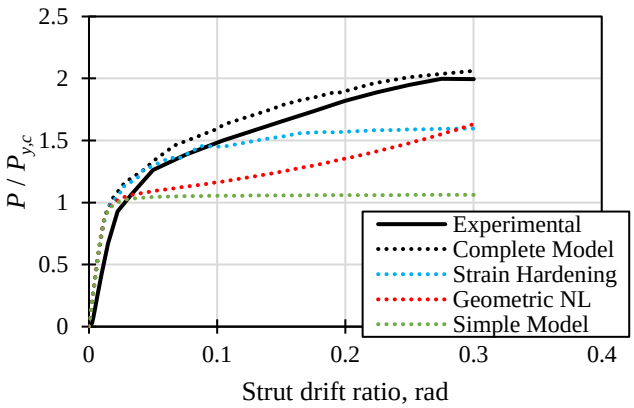

Figure 7-32. Response of specimen SD3-NU-I1 compared to numerical results obtained from multiple models under different conditions.

7.7 Conclusions

In this chapter, a slit damper proposed for, but not limited to, precast concrete beam-column connections was studied. The structural behavior of the damper was studied numerically and theoretically, followed by experimental verification. To evaluate the seismic performance of the damper, incremental and constant-amplitude cyclic tests were conducted on eight specimens with similar characteristics. Results were addressed with an emphasis on ductility and energy dissipation capacity. The experimental results were also validated with finite element analysis carried out in ABAQUS [7]. Based on the experimental and numerical results, the following conclusions are offered below:

1. The cyclic tests demonstrated stable hysteretic behavior for the proposed damper. The tested specimens dissipated significant amounts of energy. Specifically, the dampers with non-uniform struts exhibited superior deformation and energy dissipation capacities compared to their uniform counterparts. Maximum ductility ratios developed by the specimens with uniform struts were 6.4 on average, while that of those with non-uniform struts was 10.6. Additionally, from the incremental cyclic tests, the non-uniform specimen's cumulative ductility ratio was around 3.5 times higher than the uniform ones. The constant-amplitude tests showed an even larger difference, as the cumulative ductility ratio for the specimen with non-uniform struts was approximately six times greater than that of the specimens with uniform struts.

2. Due to strain hardening and geometric nonlinearity, the ultimate strength of the dampers was significantly larger than their respective yielding strength by an average factor of 1.8 and 1.6 in tension and compression, respectively, for the specimens with uniform struts. For the specimens with non-uniform struts, these values were 2.0 and 1.4.
3. For slit dampers with similar geometric characteristics to those studied in this paper, key structural characteristics can be obtained with simplified expressions for analysis and design purposes. Yielding displacements (δ_y) can be estimated as $0.03l$. Expected yielding loads (P_{ye}) for both uniform and non-uniform slit dampers can be obtained as $1.5P_y$ and $1.3P_y$, respectively, where P_y is the theoretical yielding load of the damper. Thus, the elastic stiffness can be calculated as $K_{SD} = P_{ye} / \delta_y$. Finally, the post-elastic stiffness coefficient (α) can be taken as 0.02 and 0.01 in tension and compression, respectively, for the SDs with uniform struts, while these values can be taken as 0.04 and 0.01 for SDs with non-uniform struts. Certainly, validation of these simplified expressions on larger dampers should be carried out.
4. Using non-uniform struts can significantly increase the proposed damper's deformation capacity and fatigue performance. For seismic zones where long-duration earthquakes are expected, such as the lakebed zone of Mexico City, non-uniform SDs can be the most efficient solution.
5. The hysteretic response of slit dampers, with uniform and non-uniform struts, obtained from the finite element analyses matched reasonably well with the test results. The stress distributions were in good agreement with the observed damage during the tests. The proposed cyclic hardening parameters could also accurately predict yielding and ultimate loads. As a consequence, it can be concluded that the performance of the studied device, which was proposed for precast concrete beam-column connections, is predictable and, therefore, reliable for practical applications.

It is significant to mention that, like other studies, this research investigation has some limitations, including testing a reduced number of specimens at an isolated level. Further investigations should include testing more specimens and measuring their experimental behavior when located on actual precast concrete beam-column connections and frame structures. Such investigations will certainly be conducted in the near future.

8

Numeric Modelling of Precast Beam-Column Connections Equipped with Slit Dampers

8.1 Introduction

The most efficient way to evaluate the performance of structural systems or sub-assemblies is through experimental testing. Unfortunately, full-scale testing of any structural system is complex, expensive, time-consuming, logistically challenging, error-prone, amongst others. Therefore, finite element analysis is a powerful and economical tool to reasonably predict the behavior of precast beam-column connections or other structural systems. Nevertheless, both experimental and numerical analyses must be complementary. In order to validate the results of a numerical model, it must be calibrated with experimental results. Once validated, parametric analyses can be conducted to simulate different conditions the structural system can be subjected to in real life.

This chapter presents the results of nonlinear finite element analyses conducted to simulate the behavior of precast beam-column connections equipped with slit dampers (SDs). The main objective was to develop reliable numerical models of the proposed beam-column system. The results from specimens P-SD-0 and P-SD-1, described in Chapter 6, were used

to calibrate the models. In the case of specimen P-SD-0, the load-displacement characteristics could be reasonably simulated. The load-displacement curve of specimen P-SD-1 could not be predicted using the same modeling techniques as for P-SD-0. However, an alternative method is offered for determining the structural characteristics of a beam-column system through a finite element model of the damper as an isolated component.

8.2 Specimen P-SD-0

8.2.1 Analysis method

Specimen P-SD-0 was analyzed with the finite element method (FEM) using ABAQUS [7]. The FEM model is shown in Figure 8-1. The precast concrete elements, connection components, and load plate are shown in Figure 8-1a. The steel reinforcement embedded in the concrete is shown in Figure 8-1b.

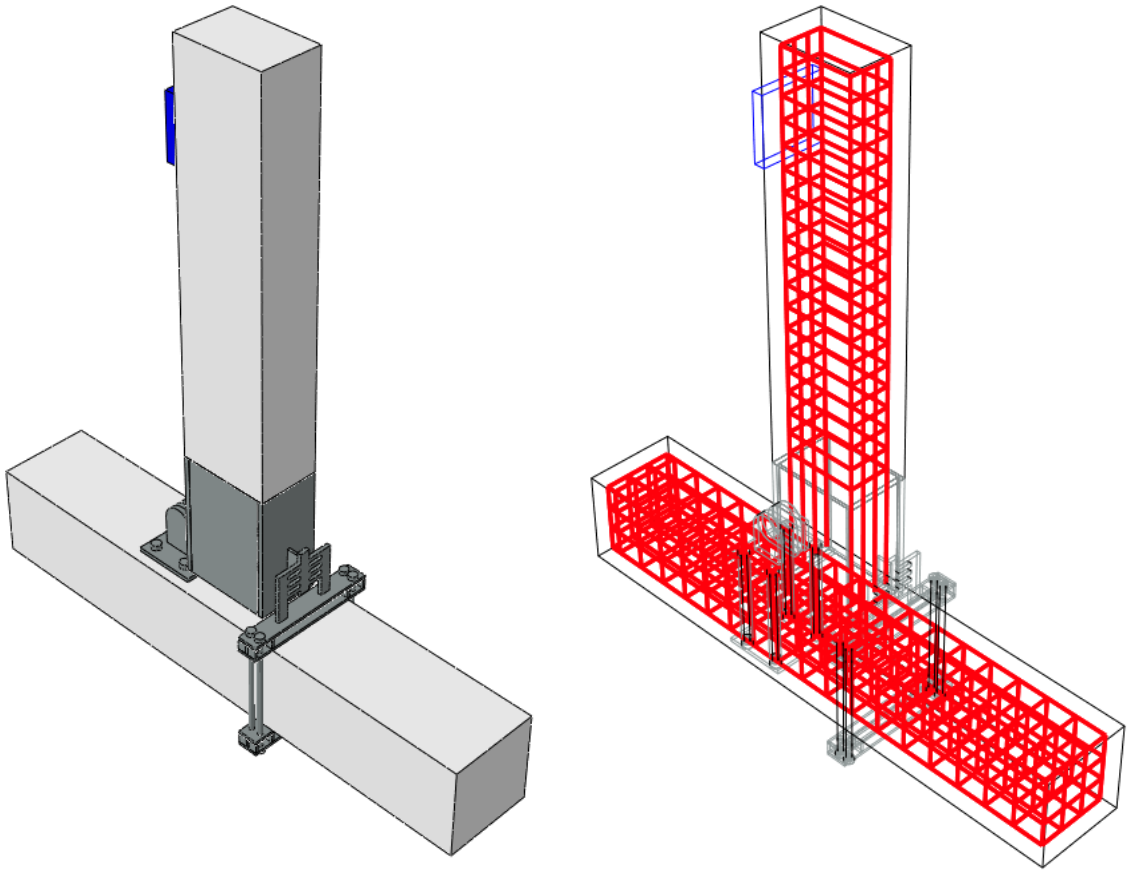

a) Concrete elements and connections b) Beam and column steel reinforcement

Figure 8-1. FEM of P-SD-0 in ABAQUS [7].

The loading plate was idealized as a solid element with infinite stiffness. Concrete elements were modeled as elastic with a modulus of elasticity equal to $2700\sqrt{f_c'} + 11000$ [41] where f'_c is equal to 43 MPa, measured from sample tests (see Chapter 6). A Poisson's ratio of 0.2 was used for the concrete material. The steel reinforcement material was considered to have an elastic-perfectly plastic behavior with a yield stress of 412 MPa and a Poisson's ratio of 0.3. The SD was modeled similarly with a yield stress of 325 MPa, obtained from coupon tests.

All concrete and structural steel components, including the SD, were modeled using C3D8R (8-node hexahedral 3D stress elements). Steel reinforcement was modeled using T3D2 (2-node linear 3D truss elements). The mesh was made with 50 mm elements for the concrete, steel box, and rebars; 25 mm elements for the steel connection components; and 12.5 mm elements for the SD.

An embedded region constraint was used for the steel reinforcement. Steel plates and other components were interconnected with tie constraints, meaning there were no relative movements between the connected surfaces. A contact-surface interaction was defined between the steel fastener and the concrete column to simulate the flexibility of the connection. The rotational hinge was idealized with four rounded steel plates without the pin between them, as shown in Figure 8-2. Modeling the pin would have been time-consuming and unnecessary. Instead, the outer plates were joined to the inner plates tying the nodes at the center of where the pin would have been, restricting the translational degrees of freedom of the tied nodes while allowing rotation.

The model was subjected to the same cyclic loading protocol applied to specimen P-SD-0. The effects of geometric non-linearity were considered. The results are presented below.

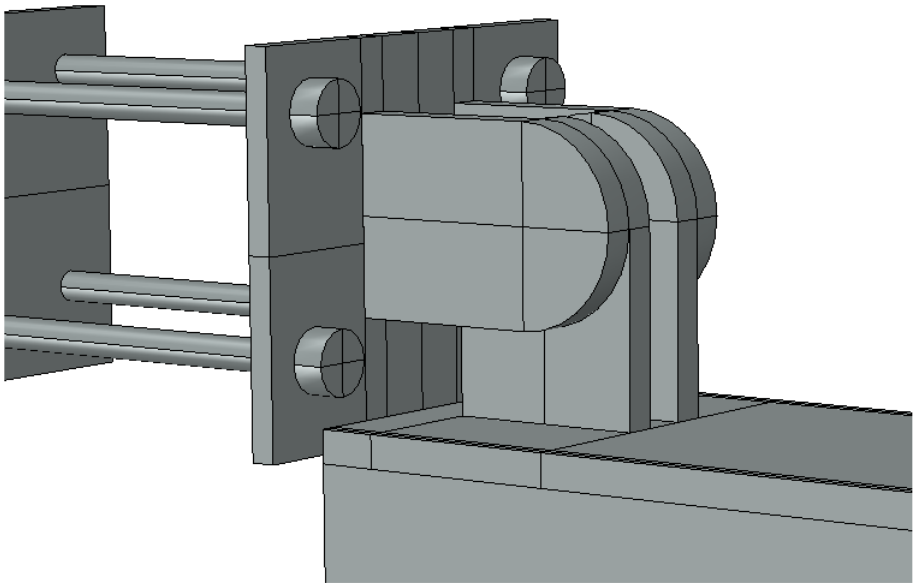

Figure 8-2. Rotational hinge.

8.2.2 Comparisons with test results

The experimental load-displacement curve is compared to that obtained from ABAQUS [7] in Figure 8-3. As can be seen, the cyclic response could be reasonably predicted. It must be mentioned that other models with different characteristics were attempted and were not successful. For example, the same model as that shown in Figure 8-1 was analyzed considering the cyclic hardening of the SD. In Chapter 7, it was shown that the combined isotropic-kinematic hardening model was adequate for predicting the cyclic response of isolated SDs. However, when the hardening model was used to predict the response of P-SD-0, the obtained lateral loads were significantly higher than those shown in Figure 8-3.

The model's response was also sensitive to mesh size and element shape. In some trials, the mesh size was reduced, or the element type of the solids was changed. Whichever the case, the post-elastic portion of the curve was flatter than that exhibited in Figure 8-3, simulating more an elastic-perfectly plastic behavior. Because of this, reproducing the experimental results had to be conducted on a trial-and-error basis of the mesh size, making the analysis method unreliable since experimental data is not readily available for different configurations of the system or different mechanical properties of the materials. More trials must be

conducted to determine practical methods of simulating the cyclic behavior of beam-column connections with SDs.

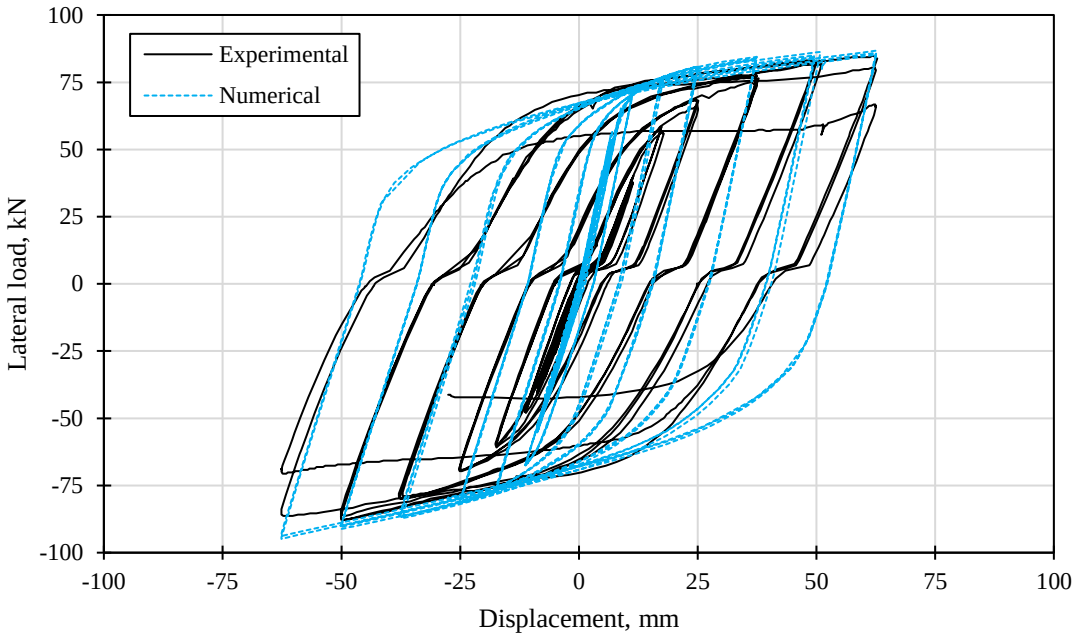

Figure 8-3. Comparison of results.

Despite the mentioned complications, the overall behavior of specimen P-SD-0 could be estimated. For example, the stress states of P-SD-0, at drift ratios of ±0.025 rad, shown in Figure 8-4, approximate the specimen's behavior. Stresses on the precast concrete elements were within an elastic range, with some small stress concentrations where tie constraints were defined. The reinforcing steel (not shown) was within the elastic range in all simulation stages, as observed during the experimental tests. The flexibility of the steel fastener was successfully represented. In the push direction, the flexural deformation of both accessories (top and bottom) can be observed, as well as the stress distribution within the components (see Figure 8-4). The tension in the threaded bars of the steel fastener can also be observed.

Regarding the damper, the stresses were mostly concentrated at the struts' ends, extending into the lateral elements. While in compression (push direction), most of the length of the struts was near yield. Also, higher stresses were concentrated on the lateral elements of the damper, extending into the connection region with the steel fastener. This demonstrates the

less stable behavior of the damper in compression, which could have been prone to buckling due to the slenderness of the lateral elements. For this reason, the lateral elements of specimen P-SD-1 were shorter and designed with revised capacity design concepts.

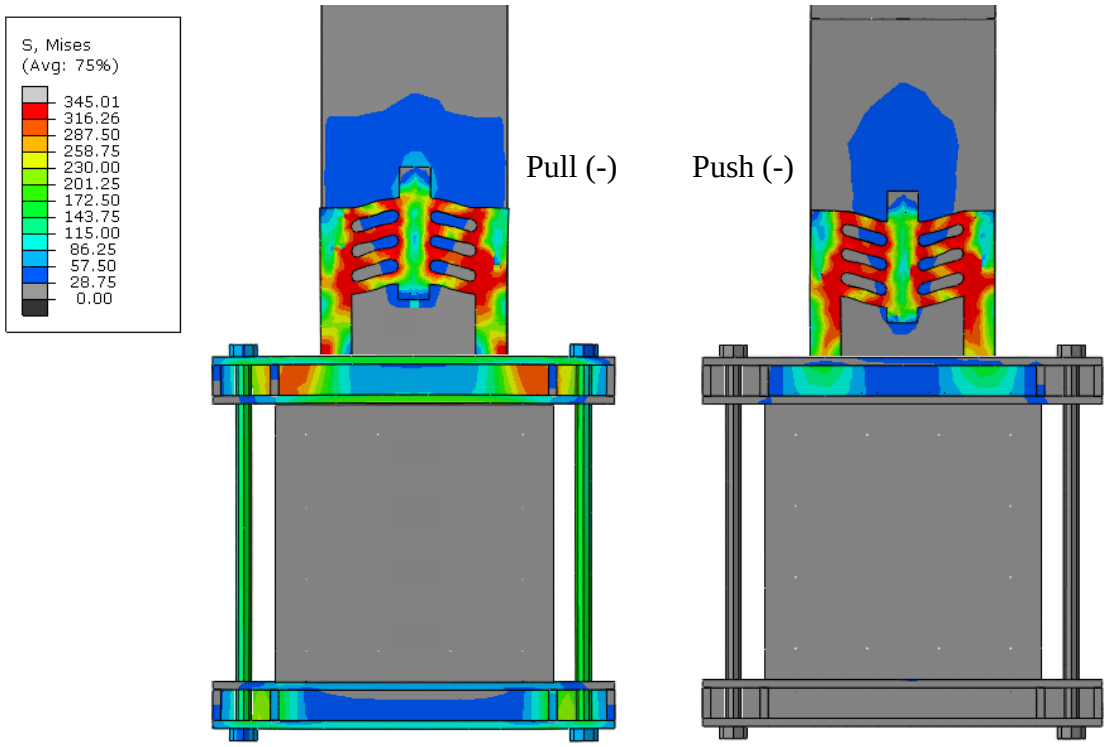

Figure 8-4. Stress states.

8.3 Specimen P-SD-1

8.3.1 Analysis method

Concrete elements were modeled as elastic with a modulus of elasticity equal to $2700\sqrt{f'_c} + 11000$ [41] where f'_c is equal to 70.8 MPa (see Chapter 6). A Poisson's ratio of 0.2 was used for the concrete material. In this case, the steel reinforcement was not modeled. From P-SD-0, it was observed that the reinforcement did not contribute to the response of the model. The SD was modeled with an elastic-perfectly plastic behavior with a yield stress of 342 MPa, obtained from coupon tests, a modulus of elasticity of 200000 MPa, and a Poisson's ratio of 0.3.

All concrete and structural steel components, excluding the SD, were modeled using C3D8R (8-node hexahedral 3D stress elements) with an approximate size of 50 mm. The damper was modeled with C3D10 (10-node quadratic tetrahedron) elements with an approximate size of 10 mm. The damper was modeled similarly to the models studied in Chapter 7, but without considering the cyclic hardening.

Steel plates and other components were interconnected with tie constraints. The steel bars embedded within the column were not modeled as they were observed to remain without damage during the experimental tests. The rotational hinge was connected through tie constraints to the beam and column. The model was subjected to the same cyclic loading protocol applied to specimen P-SD-1. The effects of geometric non-linearity were considered. The model is shown in Figure 8-5.

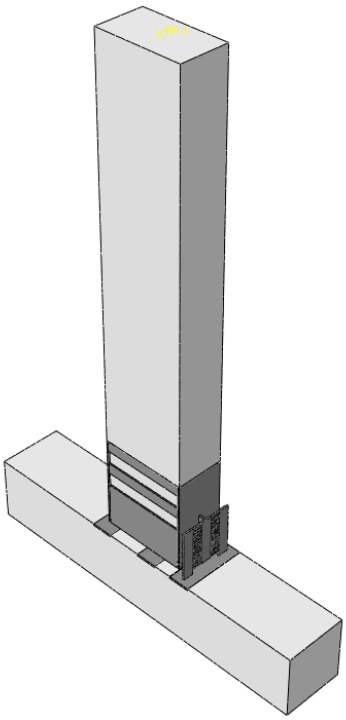

Figure 8-5. FEM model of P-SD-1 in ABAQUS [7].

8.3.2 Comparisons with test results

The experimental load-displacement curve is compared to the numerical results obtained from ABAQUS [7] in Figure 8-6. The numerical results are in good agreement with the

experimental curve up to target displacements of approximately 100 mm. After this, there was a significant asymmetry in the hysteresis loops when the FEM model changed from positive to negative direction. This is because a higher load was required to deform the numerical model to its original position, which didn't happen physically for specimen P-SD-1 as cracking had already occurred on multiple struts and the strength of the damper had decreased drastically.

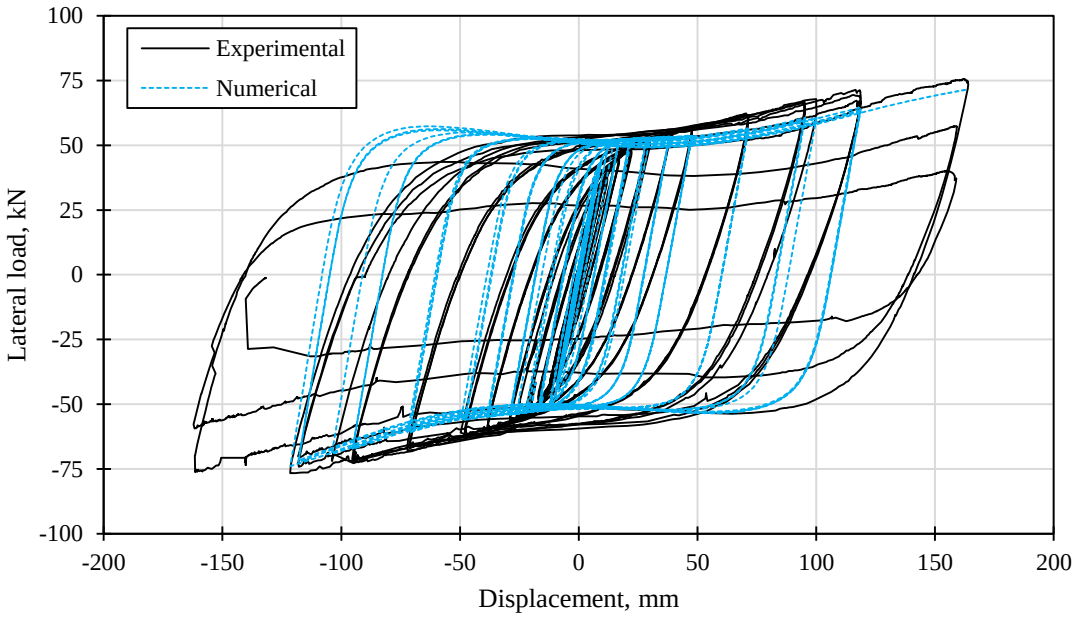

Figure 8-6. Comparison of the results.

The post-yield behavior could be reasonably predicted with the FEM model without including the combined isotropic-kinematic hardening model, which was adequate for the isolated dampers in Chapter 7. However, another trial model was studied, considering the cyclic hardening of the steel material. As was the case for specimen P-SD-0, the FEM model of P-SD-1 with cyclic hardening overestimated the strength of the beam-column connection significantly.

The possible reason the cyclic hardening model is suitable for the isolated dampers and not for the beam-column sub-assemblies is the unique boundary conditions of each experimental configuration. Although minimal, the out-of-plane deformations induced by the rotation of

the precast beam through the transfer plate may not have allowed the damper to fully develop the strain hardening that the isolated dampers did.

8.4 Conclusions

The results of nonlinear finite element analyses conducted in ABAQUS [7] simulating the behavior of precast beam-column connections equipped with slit dampers were presented in this chapter. Based on the results of this study, the following conclusions are offered:

1. Finite Element Modelling (FEM) is capable of predicting the cyclic behavior of precast beam-column connections with reasonable accuracy. Although the FEM models are relatively simple to do, with simple elastic and bilinear materials, the analysis time could be excessive. For example, specimen P-SD-1's FEM model analysis required over 80 hours to complete. This could be deemed appropriate for research purposes but unacceptable for practical aplications.
2. The cyclic response of specimen P-SD-0 could be predicted with reasonable accuracy using only elastic and elastic-perfectly plastic materials. The same model considering cyclic hardening of the SD gave lateral loads significantly higher than those obtained experimentally. The model's response was also sensitive to mesh size and element shape. Reproduction of the experimental results may be unreliable if experimental data is not readily available for different configurations of the system or different mechanical properties of the materials.
3. The FEM model of P-SD-1 exhibited a significant asymmetry in the hysteresis loops when direction changes occured. This is because a higher load was required to deform the struts of the model back to their place, which was not seen in specimen P-SD-1 as the strength of the damper was decreasing slowly due to crack initiation in the struts.
4. The combined isotropic-kinematic hardening model was not necessary to simulate the cyclic behavior of specimens P-SD-0 and P-SD-1. It is possible that the out-of-plane deformations induced by the rotation of the precast beam may not have allowed the damper to develop adequate strain hardening due to cyclic loading.
5. The effects of geometric non-linearity must be considered in the FEM models.

6. Strength degradation was not replicated with the FEM models. A damage model could be introduced into the current models to predict crack initiation of the steel damper; however, that was considered time-consuming and certainly out of the scope for validation purposes.

9

Conclusions and Further Work

9.1 Conclusions

This study aimed at developing innovative low-damage non-emulative precast concrete beam-column connections equipped with passive energy-dissipating devices that exploit the inherent advantages of precast construction, such as accelerated construction, while having superior seismic performance and predictable behavior. The extensive experimental program resulted in a new precast framing system equipped with steel slit dampers between the beam-column connections that possess superior deformation and energy-dissipating capacities.

The new precast system proposed here has different characteristics from the conventional cast-in-place or precast systems; therefore, comparing them is difficult. However, efforts were made to evaluate the performance of all the studied specimens in relative terms, such as: peak and cumulative ductility ratios and relative energy dissipation, etc. Specimen P-SD-1, the best representative of the proposed system with a slit damper, was superior to the rest of the specimens in nearly all respects, as described below.

Experimental studies on conventional cast-in-place and precast beam-column connections were conducted to assess their behavior under cyclic loading. In Chapter 3, four full-scale

exterior cast-in-place beam-column connections with low longitudinal reinforcement ratios and different levels of confinement were studied. Similarly, in Chapter 4, the behavior of four conventional precast beam-column connections with similar characteristics to the cast-in-place ones was studied. All of the tested specimens were subjected to reversible incremental cyclic loading applied quasi-statically. The hysteresis loops were broad and remained stable throughout most of the tests, with some pinching behavior at higher drift ratios for some specimens. Damage on the joint panels was minimal due to low demand/capacity ratios. The theoretical ultimate flexural strengths were achieved in all cases, and the load-carrying capacity remained reasonably stable even in the final stages of the tests. The overstrength developed by the cast-in-place specimens was, on average, 1.18. The overstrength developed by the U-beam specimens was, on average, 1.04, while the welded corbel system exhibited an overstrength of 1.28. Global ductility ratios (μ) were between 4.9 and 8.1 for the cast-in-place specimens and between 3.6 and 7.2 for the precast specimens. Maximum cumulative ductility ratios were around 100. In most cases, the tested specimens dissipated close to 40% of their idealized energy-dissipating capacity. Finally, equivalent viscous damping ratios were above 20% in all cases, with a maximum of 25% developed by specimens P-UB-1 and P-UB-3.

On the other hand, an extensive experimental program was conducted to develop innovative non-emulative precast systems. Multiple tests were conducted; however, the beam-column connection equipped with the slit damper was by far the most successful. Therefore, one small-scale and two full-scale exterior precast beam-column connections equipped with slit dampers were studied. They all had low ductility detailing and were subjected to reversible incremental cyclic loading, applied quasi-statically. A point-to-point comparison is described below; however, only the results of P-SD-1 and P-SD-2R are described as they are the most representative of the proposed system.

Hysteresis loops of specimen P-SD-1 were broad, stable, and symmetrical throughout most of the test, with no noticeable pinching behavior at higher target drift ratios. Specimen P-SD-2R exhibited significant slippage due to the tolerances provided to the bolted connections. This compromised the performance of the specimen in some respects; however, it still possessed superior energy-dissipating capacities than the cast-in-place and conventional

precast specimens. Damage on specimens P-SD-1 and P-SD-2R was minimal. No cracks appeared on the precast beam or joint region. Three vertical cracks with widths no larger than 0.1 mm appeared below the top plates of the dumbbell connections. Also, two cracks appeared adjacent to the top plate of the dumbbell-to-damper connection, one on each side of the plate, due to stress concentrations when the damper was in tension. These cracks had a width of 2.8 mm by the end of the test; however, they appeared on cover concrete with no structural consequences.

The theoretical yield strengths were achieved in both cases with the load-carrying capacity remained reasonably stable up to a target drift ratio of 0.035 rad. The ultimate strength was approximately 1.4 times the yield strength. The yield displacement and initial stiffness of specimen P-SD-1 could also be predicted with precision.

Global ductility ratios (μ) were, on average, 11.3 and 4.5 for specimens P-SD-1 and P-SD-2R, respectively. Maximum cumulative ductility ratios (P_y / δ_y) were around 300 and 100, respectively. That is, specimen P-SD-1 dissipated at least three times the cumulative hysteretic energy. Both specimens exhibited maximum relative energy dissipation ratios close to 75% and were above 50% at the end of the tests. This implies that the proposed system dissiapates significantly more energy than the cast-in-place and conventional precast specimens for the same drift ratios.

Finally, equivalent viscous damping ratios were close to 40% for a global ductility ratio of 5. Specimen P-SD-1 maintained this performance up to a ductility of approximately 12. These results, in general, mean that the proposed system showed superior deformation and energy dissipating capacities.

The proposed system has many other advantages, along with superior seismic performance. The precast elements can be fabricated as individual pieces to be later connected on-site, thus, minimizing cast-in-place concrete, excess use of formwork, and on-site labor and ultimately reducing assembly times significantly. The beam and the column can be connected with welding or bolted techniques. The proposed system's repairability was also validated as the damaged damper of specimen P-SD-1 was replaced, and the precast components were reused for specimen P-SD-2R. However, the welded components gave better results and better representation of the actual cyclic behavior of the damper.

Along with the above, one of the most important features of the proposed system is the predictability of its response. Structural parameters used for seismic design, such as the stiffness, strength and displacement at yield, could be accurately calculated. Since there is a gap between the beam and the column, moment-curvature relationships cannot be determined. However, moment-rotation relationships can be obtained and depend almost entirely on the structural characteristics of the slit damper and the inter-story drifts of the frame.

9.2 Further Work

Areas of further development have been identified and are described as follows:

1. *Experimental tests of cast-in-place and precast beam-column connections*. Emulative construction will still be the norm in Mexico and other countries for awhile. Therefore, more research must be done on conventional cast-in-place and precast beam-column connections considering different variables, such as higher reinforcement ratios on beams and columns. The good behavior of the studied specimens in Chapters 3 and 4 might be attributed to the low longitudinal reinforcement ratios and relatively adequate confinement. It is important to study specimens that accurately represent current practice. Fortunately, an experimental program on such matters is currently being developed in Mexico.
2. *Development of a seismic design methodology*. Although a method for designing beam-column connections was proposed, a performance based seismic design methodology for full precast structures equipped with slit dampers, that takes into account their nonlinear behavior, needs to be developed. Additionally, an optimal balance between strength, stiffness and energy dissipation can be found for these types of structures.
3. *Comparisons with other lateral resisting systems*. In this thesis, the superior deformation and energy-dissipating capacities of beam-column connections equipped with slit dampers was described extensibly. Building models comprised of moment-resisting frames equipped with slit dampers should be compared to conventional cast-in-place and precast moment-resisting frames to evaluate the benefits of the proposed system when located in actual structures. The comparative studies should include not

only dynamic responses, but aslo other important variables, such as: reparability, repair times, repair costs, lifecycles costs, probability of collapse, probability of loss of functionality, and carbon footprint, amongst others.

4. *FEM modeling*. FEM models must be conducted be conducted to represent accuratetly the cyclic behavior of precast beam-column connections with slit dampers when diverse properties are considered. Also, analysis times of the models are excessive currently. Simplification techniques should be developed to make the models more efficient and practical.

References

[1] Park R. Perspective on the seismic design of precast concrete structures in New Zealand. *PCI Journal* 40 (1995) 40–60. https://doi.org/10.15554/pcij.05011995.40.60.

[2] Khare R. Seismic performance and design of precast concrete building structures: an overview Seismic performance of existing brick masonry buildings. View project, Madras, 2011. https://www.researchgate.net/publication/286805123.

[3] VanGeem M. Achieving Sustainability with Precast Concrete. *PCI Journal*. 51 (2006) 42–61.

[4] Cheok G, Lew H. Performance of precast concrete beam-to-column connections subject to cyclic loading. *PCI Journal* 36 (1991) 56–67.

[5] Alcocer SM, Carranza R, Perez-Navarrete D, Martinez R. Seismic tests of beam-to-column connections in a precast concrete frame. *PCI Journal* 47 (2002) 70–89. https://doi.org/10.15554/pcij.05012002.70.89.

[6] Park R, Bull DK. Seismic resistance of frames incorporating precast prestressed concrete beam shells. *PCI Journal* 31 (1986) 54–93.

[7] ABAQUS. Analysis user's manual 6.11. Dassault Systems Simulia Corp. SIMULIA, Providence, IR, 2011.

[8] Elliot KS. Precast Concrete Structures. 2nd ed., Taylor & Francis Group, LLC, 2017.

[9] D'Arcy TJ, Nasser GD, Ghosh SK. Building code provisions for precast/prestressed concrete: A Brief History. *PCI Journal* (2003) 116–124.

[10] Kurama YC, Sritharan S, Fleischman RB, Restrepo JI, Henry RS, Cleland NM, Ghosh SK, Bonelli P. Seismic-Resistant Precast Concrete Structures: State of the Art. *Journal of Structural Engineering* 144 (2018) 03118001. https://doi.org/10.1061/(asce)st.1943-541x.0001972.

[11] Eom TS, Park HG, Hwang HJ, Kang SM. Plastic Hinge Relocation Methods for Emulative PC Beam–Column Connections. *Journal of Structural Engineering* 142 (2016). https://doi.org/10.1061/(asce)st.1943-541x.0001378.

[12] Englekirk RE. Seismic design of reinforced and precast concrete buildings. Wiley and Sons, Inc., 2003.

[13] Stanton JF, Stone WC, Cheok GS. A hybrid reinforced precast frame for seismic regions. *PCI Journal* 42 (1997) 20–32. https://doi.org/10.15554/pcij.03011997.20.23.

[14] Priestley MJN. Overview of PRESSS research program. *PCI Journal* 36 (1991) 50–57. https://doi.org/10.15554/pcij.07011991.50.57.

[15] Marriott D, Pampanin S, Bull D, Palermo A. Dynamic testing of precast, post-tensioned rocking wall systems with alternative dissipating solutions, Bulletin of the New Zealand Society for Earthquake Engineering 41 (2008) 90–103. https://doi.org/10.5459/bnzsee.41.2.90-103.

[16] ACI Committee 318. Building Code Requirements for Reinforced Concrete (ACI 318-63), American Concrete Institute, Detroit, MI, 1963.

[17] ACI Committee 318. Building code requirements for structural concrete (ACI 318-02), American Concrete Institute, Farmington Hills, Mich.

[18] ACI Committee 374. Acceptance criteria for moment frames based on structural testing and commentary (ACI 374.1-05), American Concrete Institute, Farmington Hills, Mich., 2005.

[19] ACI Committee 318. Building code requirements for structural concrete (ACI 318-08), American Concrete Institute, Farmington Hills, Mich.

[20] ACI Innovation Task Group 5. Acceptance criteria for special unbonded post-tensioned precast shear wall based on validation testing and commentary (ACI ITG 5.1-07), Farmington Hills, Mich., 2007.

[21] Rodriguez M. La prefabricación en la vivienda. In: V Simposio Nacional de Ingeniería Estructural En La Vivienda, 2007.

[22] Park R. The fib state-of-the-art report on the seismic design of precast concrete building structures. In: Pacific Conference on Earthquake Engineering, 2003.

[23] Fintel M. Performance of precast concrete structures during rumanian earthquake of march 4, 1977. *PCI Journal* 22 (1977) 10–15. https://doi.org/https://doi.org/10.15554/pcij.03011977.10.15.

[24] Fintel M. Performance of buildings with shear walls in earthquakes of the last thirty years. *PCI Journal* 40 (1995) 62–80. https://doi.org/https://doi.org/10.15554/pcij.05011995.62.80.

[25] Astiz L, Kanamori H. Source characteristics of earthquakes in the Michoacan seismic gap in Mexico, 1987.

[26] Fintel M. Performance of precast and prestressed concrete in Mexico earthquake. *PCI Journal* 31 (1986) 18–42.

[27] Rodríguez M. Comportamiento de estructuras prefabricadas de concreto reforzado para edificaciones en zonas sísmicas, innovaciones y tendencias en su empleo. Revista de Ingeniería Sísmica. 63, 1–34.

[28] Camba JL, Professor S. Case study of the performance of prestressed concrete buildings during the 1985 Mexico earthquake.

[29] Muguruma H, Nishiyama M, Watanabe F. Lessons learned from the Kobe earthquake a japanese perspective. *PCI Journal* 40 (1995) 28–42. https://doi.org/https://doi.org/10.15554/pcij.07011995.28.42.

[30] Ghosh SK. Observations on the performance of structures in the Kobe earthquake of January 17, 1995. *PCI Journal* 40 (1995) 14–22. https://doi.org/https://doi.org/10.15554/pcij.03011995.14.22.

[31] Preliminary reconnaissance report on damages to precast, prestressed concrete structures of the Hyogoken-Nanbu Earthquake. Japan Prestressed Concrete Engineering Association. (1995).

[32] Kam WY, Pampanin S. The seismic performance of RC buildings in the 22 February 2011 Christchurch earthquake. Structural Concrete 12 (2011) 223–233. https://doi.org/10.1002/suco.201100044.

[33] Megget LM. From Brittle to Ductile: 75 Years of Seismic Design in New Zealand.

[34] Lau DBN. Influence of precast/prestressed flooring on the seismic performance of reinforced concrete perimeter frame buildings. University of Auckland, 2007.

[35] Kam WY, Pampanin S, Elwood K. Seismic performance of reinforced concrete buildings in the 22 February Christchurch (Lyttelton) earthquake. Bulletin of the New Zealand Society for Earthquake Engineering 44 (2011).

[36] Park H, Im H, Kang S. An experimental study on beam-column connections with precast concrete U-shaped beam shells. Proceeding of the 14th World Conference on Earthquake Engineering, Beijing, China, 2008.

[37] Lee LH, Kim SH, Moon JH. An experimental study of the structural behavior on the precast concrete beam-column interior joint with splice type reinforcing bars. Journal of Architectural Institute of Korea, 20:10 (2004) 53-61.

[38] Ochs J, Ehsani M. Moment resistant connections in precast concrete frames for seismic regions. *PCI Journal* 38 (1993) 64–75.

[39] Ertas O, Ozden S, Ozturan T. Ductile connections in precast concrete moment resisting frames. *PCI Journal* 51 (2006) 66–76. https://doi.org/10.15554/pcij.05012006.66.76.

[40] RCDF. Mexico City building code and its complementary specifications. Mexico City, Mexico, 2020.

[41] NTC-C-2020. Normas técnicas complementarias para el diseño y construcción de estructuras de concreto. Gaceta Oficial de La Ciudad de México. (2020).

[42] Rodríguez ME, Torres-Matos M. Seismic behavior of a type of welded precast concrete beam-column connection. *PCI Journal* 58 (2013) 81–94. https://doi.org/https://doi.org/10.15554/pcij.06012013.81.94.

[43] Rodriguez ME, Rodriguez Asabay J. Se debe evitar la soldadura de barras de refuerzo en estructuras de concreto reforzado en zonas sísmicas de México. Revista de Ingeniería Sísmica (2006) 69–94.

[44] Parastesh H, Hajirasouliha I, Ramezani R. A new ductile moment-resisting connection for precast concrete frames in seismic regions: an experimental investigation. *Eng Struct* 70 (2014) 144–157. https://doi.org/10.1016/j.engstruct.2014.04.001.

[45] Cheok GS, Lew HS. Model precast concrete beam-to-column connections subject to cyclic loading. *PCI Journal* 38 (1993) 80–92. https://doi.org/10.15554/pcij.07011993.80.92.

[46] Uniform Building Code. International Conference of Building Officials, Whittier, CA, 1985.

[47] ACI-ASCE Committee 550. Design specification for unbonded post-tensioned precast concrete special moment frames satisfying ACI 374.1 (ACI 550.3-13) and commentary, American Concrete Institute. American Society of Civil Engineers, Farmington Hills, Mich., 2013.

[48] Nakaki SD, Englekirk RE, Plaehn JL. Ductile Connectors for a Precast Concrete Frame. *PCI Journal* 39 (1994) 46–59. https://doi.org/10.15554/pcij.09011994.46.59.

[49] Palmieri L, Saqan E, French C, Kreger M. Ductile connections for precast concrete frame systems. Special Publication (1996) 313–55.

[50] NTC-S-2020. Normas Técnicas Complementarias para Diseño por Sismo con Comentarios, Gaceta Oficial de La Ciudad de México (2020).

[51] ASCE/SEI 7-22. Minimum design loads and associated criteria for buildings and other structures, American Society of Civil Engineers, 2022.

[52] ACI committee 318. Building Code Requirements for Structural Concrete (ACI 318-19) Commentary on Building Code Requirements for Structural Concrete (ACI 318R-19), American Concrete Institute, Farmington Hills, Mich., 2019.

[53] Parker DE, Bullman PJM. Shear strength within reinforced concrete beam-column joints. *The Structural Engineer* 75 (1997).

[54] Seenivasan R, Sivanandam K. State-of-the-art report: various reinforcement techniques for monolithic cast-in-situ RC beam-column joint. *Innovative Infrastructure Solutions* 7 (2022). https://doi.org/10.1007/s41062-022-00854-4.

[55] Guerrero H, Ji T, Escobar JA, Teran-Gilmore A. Effects of Buckling-Restrained Braces on reinforced concrete precast models subjected to shaking table excitation. *Eng Struct* 163 (2018) 294–310. https://doi.org/10.1016/j.engstruct.2018.02.055.

[56] RCDF-2004. Reglamento de construcciones del Distrito Federal. Gaceta Oficial del Distrito Federal (2004).

[57] NTC-S-2004. Normas Técnicas Complementarias para Diseño por Sismo, Gaceta Oficial Del Distrito Federal (2004).

[58] NTC-C-2004. Normas Técnicas Complementarias para el Diseño y Construcción de Estructuras de Concreto, Gaceta Oficial Del Distrito Federal (2004).

[59] ACI-ASCE Committee 352. Recommendations for design of beam-column connections in monolithic reinforced concrete structures (ACI 352R-02). American Concrete Institute, Farmington Hills, Mich., 2002., (n.d.).

[60] CANACERO, NMX-B-506-CANACERO-2011 - Varilla Corrugada de Acero para Refuerzo de Concreto, Cámara Nacional de La Industria Del Hierro y Del Acero. (2011).

[61] Guerrero H, Rodriguez V, Escobar JA, Alcocer SM, Bennetts F, Suarez M. Experimental tests of precast reinforced concrete beam-column connections. *Soil Dynamics and Earthquake Engineering* 125 (2019) 105743. https://doi.org/10.1016/j.soildyn.2019.105743.

[62] Rodríguez V, Guerrero H, Alcocer SM, Tapia-Hernández E. Rehabilitation of heavily damaged beam-column connections with CFRP wrapping and SFRM casing. *Soil Dynamics and Earthquake Engineering* 145 (2021). https://doi.org/10.1016/j.soildyn.2021.106721.

[63] Ameli MJ, Parks JE, Brown DN, Pantelides CP. Seismic evaluation of grouted splice sleeve connections for reinforced precast concrete column-to-cap beam joints in accelerated bridge construction. *PCI Journal* 60 (2015) 80–103. https://doi.org/https://doi.org/10.15554/pcij.03012015.80.103.

[64] ACI Committee 374. Guide for testing reinforced concrete structural elements under slowly applied simulated seismic loads (ACI 374.2R-13), American Concrete Institute, Farmington Hills, Mich., 2013.

[65] Fema P-795. Quantification of building seismic performance factors: component equivalency methodology, 2011.

[66] Teran-Gilmore A, Avila E, Rangel G. On the use of plastic energy to establish strength requirements in ductile structures. *Eng Struct* 25 (2003) 965–980. https://doi.org/10.1016/S0141-0296(03)00040-3.

[67] Chopra AK. Dynamics of Structures: theory and applications to earthquake engineering, 4th ed., Prentice Hall, Upper Saddle River, NJ, 2014.

[68] Rosenblueth E, Meli R. The 1985 Mexico earthquake: causes and effects in Mexico city. *Concr Int* 8 (1986) 23–4.

[69] Meli R, Avila J. The Mexico earthquake of september 19, 1985 - analysis of building response. *Earthq Spectra* 5 (1989) 1–18.

[70] Meli R. Evaluation of performance of concrete buildings damaged by the september 19, 1985 earthquake. In: Cassaro MA, Martinez-Romero E, Editors. International Conference on the Mexico Earthquakes – 1985: Factors Involved and Lessons Learned. Mexico City: American Society of Civil Engineers (1986) 308–27.

[71] Galvis F, Miranda E, Heresi P, Davalos H, Silos JR. Preliminary statistics of collapsed buildings in Mexico city in the september 19, 2017 puebla-morelos earthquake. John A. Blume Earthquake Engineering Center, Stanford University. (2017).

[72] Weiser D, Hunt J, Jampole E, Gobbato M. EERI earthquake reconnaissance team report: M7.1 puebla, Mexico earthquake on september 19, 2017, Earthquake Engineering Research Institute (2018).

[73] Díaz A, Murren P, Walker S. 32 Years after michoacan: preliminary reconnaissance observations in the aftermath of the september 19, 2017 puebla-morelos earthquake. Skidmore, Owings and Merrill, LLP (2017).

[74] Krawinkler H, Miranda E. Performance-based earthquake engineering, In: Bozorgnia Y., Bertero V.V., Editors. Earthquake Engineering from Engineering Seismology to Performance-Based Engineering, CRC PRESS, 2004.

[75] Raynor DJ, Lehman DE, Stanton JF. Bond-slip response of reinforcing bars grouted in ducts. *ACI Struct J* 99 (2002) 568–576. https://doi.org/10.14359/12296.

[76] Priestley MJN, Sritharan SS, Conley JR, Pampanin S. Preliminary results and conclusions from the PRESSS five-story precast concrete test building. *PCI Journal* 44 (1999) 42–67. https://doi.org/10.15554/pcij.11011999.42.67.

[77] Girgin SC, Misir IS, Kahraman S. Experimental cyclic behavior of precast hybrid beam-column connections with welded components. *Int J Concr Struct Mater* 11 (2017) 229–245. https://doi.org/10.1007/s40069-017-0190-y.

[78] ASCE/SEI 7-16. Minimum design loads and associated criteria for buildings and other structures, American Society of Civil Engineers, 2017.

[79] Rodríguez V, Guerrero H, Alcocer SM, Tapia-Hernández E. Rehabilitation of heavily damaged beam-column connections with CFRP wrapping and SFRM casing. *Soil Dynamics and Earthquake Engineering* 145 (2021) 106721. https://doi.org/10.1016/j.soildyn.2021.106721.

[80] Tapia Hernández E, Rangel Torres G. Sobrerresistencia del material de perfiles IR de acero A992 con fines de diseño. In: Campeche (Ed.), XXI Congreso Nacional de Ingeniería Estructural, 2018. https://www.researchgate.net/publication/332470887.

[81] ASCE/SEI 41-17. Seismic evaluation and retrofit of existing buildings, American Society of Civil Engineers, 2017.

[82] Oh SH, Kim YJ, Ryu HS. Seismic performance of steel structures with slit dampers. *Eng Struct* 31 (2009) 1997–2008. https://doi.org/10.1016/j.engstruct.2009.03.003.

[83] Chan RWK, Albermani F. Experimental study of steel slit damper for passive energy dissipation. *Eng Struct* 30 (2008) 1058–1066. https://doi.org/10.1016/j.engstruct.2007.07.005.

[84] ACI-ASCE Committee 352. Recommendations for design of beam-column joints in monolithic reinforced concrete structures (ACI 352R-76). ACI Journal. Proceedings 1976; 73(7):375–93.

[85] International Code Council. 2021 International Building Code Illustrated Handbook, McGraw Hill. (2021).

[86] Javanmardi A, Ibrahim Z, Ghaedi K, Benisi Ghadim H, Hanif MU. State-of-the-art review of metallic dampers: testing, development and implementation. *Archives of Computational Methods in Engineering* 27 (2020) 455–478. https://doi.org/10.1007/s11831-019-09329-9.

[87] Chang KC, Soong TT, EERI M, Lai ML, Nielson EJ. Viscoelastic dampers as energy dissipation devices for seismic applications. *Earthquake Spectra* 9 (1993) 371–387.

[88] Jaisee S, Yue F, Ooi YH. A state-of-the-art review on passive friction dampers and their applications. *Eng Struct* 235 (2021). https://doi.org/10.1016/j.engstruct.2021.112022.

[89] Bergman DM, Goel SC. Evaluation of cyclic testing of steel-plate devices for added damping and stiffness. Report No. UMCE87-10, University of Michigan, Ann Arbor, Mich. (1987).

[90] Tsai K, Chen H, Hong C, Su Y. Design of steel triangular plate energy absorbers for seismic-resistant construction. *Earthquake Spectra* 9 (1993) 505–528.

[91] Saeedi F, Shabakhty N, Mousavi SR. Seismic assessment of steel frames with triangular-plate added damping and stiffness devices. *J Constr Steel Res* 125 (2016) 15–25. https://doi.org/10.1016/j.jcsr.2016.06.011.

[92] Kobori T, Miura Y, Fukusawa E, Yamada T, Takenake Y. Development and application of hysteresis steel dampers. In: Proceedings of 11th World Conference on Eaarthquake Engineering. (1992) 2341–2346.

[93] Clark P, Aiken I, Kasai K, Ko E, Kimura I. Design procedures for buildings incorporating hysteretic damping devices. 68th Annual Convention SEAOC (1999) 355–371. http://eqstory.skku.ac.kr/05-OPEN-INFORM/CONTROL/SEAOC-PAPER/Hysteretic.pdf.

[94] Maleki S, Mahjoubi S. Dual-pipe damper. *J Constr Steel Res* 85 (2013) 81–91. https://doi.org/10.1016/j.jcsr.2013.03.004.

[95] Javidan MM, Kim J. A ductile steel damper brace for low damage framed structures. *Steel and Composite Structures* 44 (2022). https://doi.org/https://doi.org/10.12989/scs.2022.44.3.311.

[96] Lee CH, Ju YK, Min JK, Lho SH, Kim SD. Non-uniform steel strip dampers subjected to cyclic loadings. *Eng Struct* 99 (2015) 192–204. https://doi.org/10.1016/j.engstruct.2015.04.052.

[97] Naeem A, Kim J. Seismic performance evaluation of a multi-slit damper. *Eng Struct* 189 (2019) 332–346. https://doi.org/10.1016/j.engstruct.2019.03.107.

[98] Park H, Oh S. Structural performance of beam system with T-stub type slit damper. *Eng Struct* 205 (2020) 109858. https://doi.org/10.1016/j.engstruct.2019.109858.

[99] Lee J, Kim J. Development of box-shaped steel slit dampers for seismic retrofit of building structures. *Eng Struct* 150 (2017) 934–946. https://doi.org/10.1016/j.engstruct.2017.07.082.

[100] Gandelli E, Chernyshov S, Distl J, Dubini P, Weber F, Taras A. Novel adaptive hysteretic damper for enhanced seismic protection of braced buildings. *Soil Dynamics and Earthquake Engineering* 141 (2021) 106522. https://doi.org/10.1016/j.soildyn.2020.106522.

[101] Dal Lago B, Biondini F, Toniolo G. Experimental tests on multiple-slit devices for precast concrete panels. *Eng Struct* 167 (2018) 420–430. https://doi.org/10.1016/j.engstruct.2018.04.035.

[102] Askariani SS, Garivani S. Introducing and numerical study of a new brace-type slit damper. *Structures* 27 (2020) 702–717. https://doi.org/10.1016/j.istruc.2020.06.019.

[103] Askariani SS, Garivani S, Aghakouchak AA. Application of slit link beam in eccentrically braced frames. *J Constr Steel Res* 170 (2020). https://doi.org/10.1016/j.jcsr.2020.106094.

[104] Naeem A, Maida Y, Koichi K, Javidan MM. Development and experimental verification of self-centering disc slit damper for buildings. *J Constr Steel Res* 201 (2023). https://doi.org/10.1016/j.jcsr.2022.107759.

[105] Javidan MM, Ali A, Kim J. A steel hysteretic damper for seismic design and retrofit of precast portal frames. *Journal of Building Engineering* 57 (2022). https://doi.org/10.1016/j.jobe.2022.104958.

[106] Koetaka Y, Chusilp P, Zhang Z, Ando M, Suita K, Inoue K, Uno N. Mechanical property of beam-to-column moment connection with hysteretic dampers for column weak axis. *Eng Struct* 27 (2005) 109–117. https://doi.org/10.1016/j.engstruct.2004.09.002.

[107] Inoue K, Suita K, Takeuchi I, Chusilp P, Nakashima M, Zhou F. Seismic-resistant weld-free steel frame buildings with mechanical joints and hysteretic dampers. *Journal of Structural Engineering* 132 (2006) 864–872. https://doi.org/10.1061/(asce)0733-9445(2006)132:6(864).

[108] Tagawa H, Nagoya Y, Chen X. Bolted beam-to-column connection with buckling-restrained round steel bar dampers. *J Constr Steel Res* 169 (2020) 106036. https://doi.org/10.1016/j.jcsr.2020.106036.

[109] Lor HA, Izadinia M, Memarzadeh P. Experimental and numerical study of I-shape slit dampers in connections. *Latin American Journal of Solids and Structures* 15 (2018). https://doi.org/10.1590/1679-78254416.

[110] Javidan MM, Nasab MSE, Kim J. Full-scale tests of two-story RC frames retrofitted with steel plate multi-slit dampers. *Steel and Composite Structures* 39 (2021) 645–664. https://doi.org/10.12989/scs.2021.39.5.645.

[111] Keykhosro Kiani B, Hosseini Hashemi B, Torabian S. Optimization of slit dampers to improve energy dissipation capacity and low-cycle-fatigue performance. *Eng Struct* 214 (2020) 110609. https://doi.org/10.1016/j.engstruct.2020.110609.

[112] Bae J, Lee CH, Park M, Alemayehu RW, Ryu J, Ju YK. Modified low-cycle fatigue estimation using machine learning for radius-cut coke-shaped metallic damper subjected to cyclic loading. *International Journal of Steel Structures* 20 (2020) 1849–1858. https://doi.org/10.1007/s13296-020-00377-7.

[113] Yoshida J, Abe M, Fujino Y, Watanabe H. Three-dimensional finite-element analysis of high damping rubber bearings. *J Eng Mech* 130 (2004) 607–620. https://doi.org/10.1061/(asce)0733-9399(2004)130:5(607).

[114] Madheswaran J, Tesfamariam S. Numerical analysis of steel slit dampers under cyclic loading. 6th International Conference on Engineering Mechanics and Materials 2 (2017) 667–676.